ATTENTION: The Singapore Copyright Act applies to the use of this document. Nanyang Technological University Library

DEVELOPMENT OF FAILURE ASSESSMENT METHODOLOGY FOR LEAD-FREE ELECTRONIC ASSEMBLY

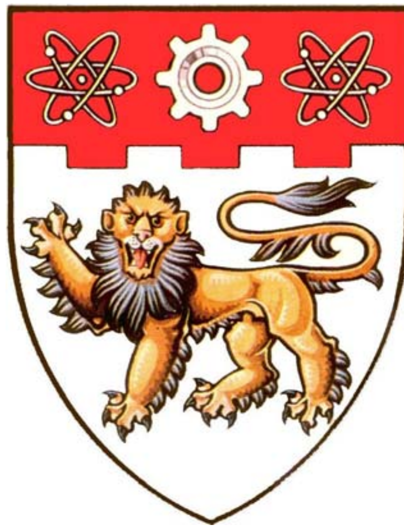

CHE FA XING

SCHOOL OF MECHANICAL & AEROSPACE ENGINEERING

NANYANG TECHNOLOGICAL UNIVERSITY

2006

ATTENTION: The Singapore Copyright Act applies to the use of this document. Nanyang Technological University Library

Development of Failure Assessment Methodology for Lead-Free Electronic Assembly

Che Fa Xing

School of Mechanical & Aerospace Engineering

A thesis submitted to Nanyang Technological University
in fulfillment of the requirement for the degree of
Doctor of Philosophy

2006

ATTENTION: The Singapore Copyright Act applies to the use of this document. Nanyang Technological University Library

To my parents, my wife

and my lovely son

ATTENTION: The Singapore Copyright Act applies to the use of this document. Nanyang Technological University Library

ACKNOWLEDGMENTS

I would like to acknowledge and express my earnest appreciation and gratitude to the following persons:

Associate Professor Pang Hock Lye, John, my thesis supervisor, for his invaluable direction, constant encouragement, and selfless help during this project.

Dr. Zhang Xueren, Mr. Low Tse Hoong, Dr. Xiong Bingshou, Mr. Xu Luhua for their helpful discussions, suggestion, and information.

Mr. Wong Foo Lam, Mr. Yeo Soo Pin, Mr. Joseph and Ms. Ng Kelin for their assistance in reliability tests.

All technicians and some research students in the Center for Advanced Numerical Engineering Simulations (CANES) for providing technical support.

Finally, I would like to express my gratitude and love to my parents and my wife, Ms. Wang Zhiying, for their support and dedication, to my lovely son, Che Luyang, for his birth and healthy growth bringing much more happiness and great encouragement.

ATTENTION: The Singapore Copyright Act applies to the use of this document. Nanyang Technological University Library

SUMMARY

The function and reliability of electronic product are very important concerns for customers and product users. Hence, methods to improve and predict the service life of electronic products are significant challenges for on-going research on design for reliability. Lead-free solders will replace tin-lead solders in electronic products due to European Union laws to restrict the use of lead (Pb) by July 1st, 2006. Solder is the weakest link material in electronic assemblies and failures are often caused by solder joint failures.

In this study, reliability test and analysis methodology for lead-free (Pb-free) soldered assemblies subjected to thermal cycling, cyclic bend, drop impact and vibration loadings are investigated. Finite element analysis (FEA) is used as a numerical modeling tool for simulating solder micro-deformation and integrated with solder fatigue failure analysis assessment. In this project, a failure assessment methodology for modeling Pb-free (and Pb-based) soldered assemblies is proposed.

A global-local submodeling finite element analysis technique is developed and compared with full 3D model results. The global-local FEA technique reduces computational effort and resources significantly (i.e. hard disk space, memory, and computational time). The global-local submodeling method results in good agreement with full 3D model results. A global-local beam (GLB) method is proposed for approximate application for vibration analysis. The global-local modeling technique is applied on reliability issue when electronic assembly subjected to different loadings such as thermal cycling, cyclic bending, drop impact and vibration.

ATTENTION: The Singapore Copyright Act applies to the use of this document. Nanyang Technological University Library

Thermal cycling reliability tests are conducted for electronic components (PBGA, TSSOP, PQFP) with tin-silver-copper (SnAgCu) Pb-free solder joints. The test results for mean-time-to-failure (MTTF) are determined based on Weibull failure distribution model and used for validation of numerical modeling and fatigue analysis results. FEA modeling and simulation are carried out for PBGA, TSSOP, and PQFP assemblies to investigate the stress-strain behavior of solder and solder fatigue life prediction results. Different cases and parameters are considered for simulation of the PBGA assembly, including 2D and 3D FE models, solder constitutive models, solder fatigue models, averaging volumes, solder mask definition (SMD) vs. no solder mask definition (NSMD), intermetallic compound (IMC) vs. no intermetallic compound. It is the first time to investigate different FE models effect on solder fatigue life systematically. The IMC consideration in FE model is also new. The ring volume for averaging fatigue damage parameter is presented for the first time.

Three-point and four-point cyclic bend tests are conducted for VQFN assemblies with SnAgCu Pb-free solder joints with OSP or Ni/Au finish. Correlation between three-point bend and four-point bend is developed and verified by test and simulation results for the first time. FEA simulations are performed for four-point bend fatigue test at isothermal conditions of 25°C and 125°C. It is the first time to conduct the cyclic bending test and FEA simulation for electronic assembly with Pb-free solder at high temperature of 125°C and present the bending fatigue model for SnAgCu solder.

Board-level drop impact tests are conducted for PBGA, PQFP and VQFN assemblies with different board finishes. Dynamic responses of specimen during drop impact are measured using high-speed camera, high strain-rate gauge, small profile accelerometer and in-situ resistance measuring instrument and are used to compare with numerical result. FEA simulations using explicit method (LS-DYNA) are

ATTENTION: The Singapore Copyright Act applies to the use of this document. Nanyang Technological University Library

performed considering three different simulation techniques containing full drop event modeling, Input-D (displacement) method and Input-G (acceleration) method. Different material behaviors are modeled for SnAgCu solder in FEA simulation for investigating their effect on stress-strain behavior of solder subjected to drop impact load. Bulk solder Charpy specimen and soldered Charpy specimen for copper and Ni/Au finish are tested to investigate the effect of different component types on failure mode and impact behavior. The strain rate dependent plastic model for SnAgCu solder is simulated in FEA modeling for the first time. The effect of IMC layer on stress strain behavior of solder under drop impact load is conducted in FEA modeling and simulation for the first time.

Sinusoidal vibration reliability tests for constant G-level and block G-level of 3G, 5G, and 10G are investigated. The quasi-static FEA modeling and simulation method is developed firstly for simulating forced vibration fatigue load applied on solder joints. Fatigue life predictions based on both quasi-static method and harmonic analysis are consistent with test result.

ATTENTION: The Singapore Copyright Act applies to the use of this document. Nanyang Technological University Library

CONTENTS

ACKNOWLEDGMENTS I

SUMMARY II

ABBREVIATIONS IX

NOMENCLATURE XI

LIST OF FIGURES XIII

LIST OF TABLES XVIII

CHAPTERS

1 INTRODUCTION 1

1.1 BACKGROUND 1
1.2 RELIABILITY PROBLEM OF ELECTRONIC ASSEMBLY 1
1.3 OBJECTIVE AND SCOPE 3
1.4 OUTLINE OF THE THESIS 6

2 LITERATURE REVIEW 9

2.1 MATERIALS PROPERTIES FOR ELECTRONIC ASSEMBLY 9
2.2 CONSTITUTIVE MODELS FOR SOLDER JOINTS 10
2.2.1 Creep Model 10
2.2.2 Viscoplastic Anand Model 12
2.2.3 Elastic-Plastic-Creep Model 13
2.2.4 Rate Dependent Plastic Model 15
2.3 SOLDER FATIGUE LIFE PREDICTION MODELS 17
2.3.1 Stress-Based Fatigue Models 19
2.3.2 Strain-Based Fatigue Models 20
2.3.3 Energy-Based Fatigue Models 25
2.3.4 Fracture Mechanics Approach 28
2.4 SOLDER JOINT RELIABILITY TESTS 29
2.4.1 Accelerated Thermal Cycling (ATC) Test 30
2.4.2 Bend Test 31
2.4.3 Drop Impact Test 32

ATTENTION: The Singapore Copyright Act applies to the use of this document. Nanyang Technological University Library

2.4.4 Vibration Test 33

3 FEA CALIBRATION STUDIES 35

3.1 INTRODUCTION 35
3.2 REVIEW OF FEA MODELING FOR SOLDER JOINTS 35
3.3 GLOBAL-LOCAL MODELING TECHNIQUE 37
3.3.1 Submodeling Method 38
3.3.2 Comparison of Submodel to Fine 3D Model Results 40
3.3.3 Global-Local-Beam Model 55
3.3.4 Comparison of the GLB Model to Fine 3D Model Results 55
3.3.5 Effective Solder Joint Model with Cubic Cross-Section 60
3.4 COMPARISON OF LEAD-FREE AND LEAD-BASED SOLDER 63
3.5 SUMMARY 65

4 THERMAL FATIGUE RELIABILITY TEST AND ANALYSIS 67

4.1 INTRODUCTION 67
4.2 THERMAL CYCLING TEST AND FAILURE ANALYSIS 69
4.3 FEA ANALYSIS OF THERMAL FATIGUE FOR SOLDER 73
4.3.1 Constitutive Models for Sn-Ag-Cu Solder 74
4.3.2 Fatigue Life Prediction Model Methodology 75
4.3.3 FEA Modeling and Analysis for PBGA, PQFP and TSSOP 77
4.3.4 Parametric Study for PBGA Solder Joints 88
4.4 SUMMARY 103

5 BEND FATIGUE TEST AND ANALYSIS FOR VQFN ASSEMBLY 105

5.1 INTRODUCTION 105
5.2 CYCLIC BEND TEST AND ANALYSIS 107
5.2.1 Test Vehicle and Fixture 107
5.2.2 Three-Point Bend Test and Analysis 110
5.2.3 Four-Point Bend Test and Analysis 111
5.3 FEA MODELING FOR BEND FATIGUE TEST 121
5.3.1 Validation of One-level and Two-level Submodeling Method 121
5.3.2 FEA Study for Three-Point Bend Fatigue Test 125
5.3.3 FEA Study for Four-Point Bend Fatigue Test 130
5.3.4 Correlation between Cyclic Bend and Thermal Cycling 139

ATTENTION: The Singapore Copyright Act applies to the use of this document. Nanyang Technological University Library

5.4 SUMMARY 141

6 DROP TEST AND ANALYSIS 143

6.1 INTRODUCTION 143
6.2 BOARD LEVEL DROP TEST AND ANALYSIS 146
6.2.1 Test Setup and Measurement 146
6.2.2 Dynamic Response and Failure Detection 148
6.2.3 Drop Impact Results and Discussion 150
6.3 FEA MODELING FOR DROP TEST 151
6.3.1 Drop Impact Modeling 151
6.3.2 FEA Study of Drop Test for PBGA Assembly 152
6.4 CHARPY IMPACT TEST AND ANALYSIS 161
6.5 SUMMARY 162

7 VIBRATION TEST AND ANALYSIS 164

7.1 INTRODUCTION 164
7.2 VIBRATION TEST 166
7.3 FINITE ELEMENT ANALYSIS FOR VIBRATION TEST 167
7.3.1 Modal Analysis of FCOB Assembly 167
7.3.2 Quasi-Static Analysis for Vibration Fatigue 168
7.3.3 Harmonic Response Analysis 174
7.4 SUMMARY 176

8 CONCLUSIONS 177

8.1 CONCLUSIONS 177
8.1.1 Global-Local Modeling Technique 177
8.1.2 Thermal Cycling Test and Analysis 178
8.1.3 Cyclic Bend Test and Analysis 180
8.1.4 Drop Test and Analysis 180
8.1.5 Vibration Test and Analysis 181
8.1.6 Design-for-Reliability and Failure Assessment 182
8.2 ACHIEVEMENTS AND RECOMMENDATIONS 183
8.2.1 Achievements and Contributions 183
8.2.2 Recommendations 186

REFERENCES 187

ATTENTION: The Singapore Copyright Act applies to the use of this document. Nanyang Technological University Library

APPENDIXES

A GLB MODELING TECHNIQUE A-1

A.1 EQUIVALENT BEAM STIFFNESS ANALYSIS A-1

A.2 CONSTRAIN EQUATION A-5

B AG CONTENT EFFECT ON FATIGUE LIFE OF FLIP CHIP SOLDER B-1

B.1 THERMAL CYCLING TEST FOR FCOB ASSEMBLY B-1

B.2 AG CONTENT EFFECT ON FATIGUE LIFE B-1

C DROP TEST AND SIMULATION C-1

C.1 DROP TEST AND ANALYSIS C-1

C.2 FEA SIMULATION FOR DROP TEST C-9

D VIBRATION TEST AND ANALYSIS D-1

D.1 VIBRATION TEST AND ANALYSIS D-1

D.2 MODAL ANALYSIS D-7

D.3 FATIGUE LIFE CALCULATION FOR VIBRATION TEST D-9

E PUBLICATIONS E-1

ATTENTION: The Singapore Copyright Act applies to the use of this document. Nanyang Technological University Library

ABBREVIATIONS

2D	Two-dimension
3D	Three-Dimension
AF	Acceleration Factor
Ag	Silver
ALT	Accelerated Life Test
AST	Accelerated Stress Test
ATC	Accelerated Thermal Cycling
Au	Gold
BGA	Ball Grid Array
CCGA	Ceramic Column Grid Array
CDI	Cumulative Damage Index
CSP	Chip Scale Package
CTE	Coefficient of Thermal Expansion
Cu	Copper
DFR	Design-For-Reliability
DNP	Displacement from Neutral Point
DOF	Degree Of Freedom
ENIG	Electroless Nickel Immersion Gold (Ni/Au)
EPC	Elastic-Plastic-Creep
FC	Flip Chip
FCOB	Flip Chip On Board
FE	Finite Element
FEA	Finite Element Analysis
FEM	Finite Element Method
FR-4	Fire Retardant
FTTF	First Time To Failure
GLB	Global-Local Beam
iNEMI	International Electronics Manufacturing Initiative
I/O	Input/Output
IC	Integrated Circuit
IMC	InterMetallic Compound

ATTENTION: The Singapore Copyright Act applies to the use of this document. Nanyang Technological University Library

MTTF	Mean Time To Failure
Ni	Nickel
NSMD	Non-Solder Mask Definition
OSP	Organic Solderability Preservative
Pb	Lead
PBGA	Plastic Ball Grid Array
PCB	Printed Circuit Board
PQFP	Plastic Quad Flat Package
PWB	Printed Wiring Board
RoHS	Reduction of Hazardous Substances
SAC	Sn-Ag-Cu
SEM	Scanning Electron Microscopy
SMA	Surface Mount Assembly
SMD	Solder Mask Definition
SMT	Surface Mounted Technology
S-N	Stress vs. Fatigue Life Curve
Sn	Tin
Sn/Pb	Tin-Lead
TC	Thermal Cycling
T_g	Glass Transition Temperature
T_m	Melting Temperature
TS	Thermal Shock
TSSOP	Thin Shrink Small Outline Package
VQFN	Very thin Quad Flat No lead package
WEEE	Waste Electrical and Electronic Equipment

ATTENTION: The Singapore Copyright Act applies to the use of this document. Nanyang Technological University Library

NOMENCLATURE

$\{a\}$	Acceleration vector
$[C]$	Damping matrix
D	Displacement (m)
D_0	Diffusion constant
da/dN	Crack growth
$d\gamma/dt$	Shear strain rate
E	Young's (Elastic) modulus (GPa)
E_p	Plastic hardening modulus (GPa)
E_{tan}	Tangent modulus (GPa)
f	Natural frequency (Hz), deflection (mm)
F	Force (N)
$\{F\}$	Nodal force vector
g, G	Acceleration of gravity (9.8m/s^2)
G	Shear modulus (GPa)
I	Moment of inertia
k	Boltzmann's constant (eV/K)
$[K]$	Stiffness matrix
M	Bending moment (N·m)
$[M]$	Mass matrix
N_f	Fatigue life (cycles)
p	Pressure (Pa)
Q	Activation energy (eV)
R	Electrical resistance (Ω)
T	Absolute temperature (K), transmissibility
t	Time (s), thickness (mm)
$\{u\}$	Nodal displacement vector
V	Volume (mm^3), voltage (volts)
α	Coefficient of thermal expansion (ppm/^{o}C)
β	Weibull model slope
γ	Shear strain (angle)
δ	Deflection (mm)

ATTENTION: The Singapore Copyright Act applies to the use of this document. Nanyang Technological University Library

ΔT	Temperature range (^{o}C)
ΔW_{ave}	Volume-averaged strain energy density (MPa)
ΔW_c	Creep strain energy density (MPa)
ΔW_p	Plastic strain energy density (MPa)
$\Delta \gamma_p$	Plastic shear strain range
$\Delta \varepsilon_p$	Plastic strain range
ε'_f	Fatigue ductility coefficient
ε_{cr}, ε_c	Creep strain
$\dot{\varepsilon}_c$	Creep strain rate
ε_{eff}	Equivalent von Mises strain
ε_{in}	Inelastic strain
ε_p	Plastic strain
$\dot{\varepsilon}_p$	Plastic strain rate
η	Characteristic life in Weibull model (cycles)
v, μ	Poisson's ratio
ρ	Density (kg/m^3), curvature
σ	Normal stress component (MPa)
σ_0	Initial yield strength (MPa)
σ'_f	Fatigue strength coefficient (MPa)
σ_a	Stress amplitude (MPa)
σ_{eff}	Equivalent von Mises stress (MPa)
σ_m	Mean stress (MPa)
σ_y	Normal yield stress (MPa)
τ	Shear stress component (MPa)
Ω	Natural circular frequency (radian)

ATTENTION: The Singapore Copyright Act applies to the use of this document. Nanyang Technological University Library

LIST OF FIGURES

1-1 The multidisciplinary approach in design for reliability methodology.................. 3
1-2 Schematic illustration for main work.. 6
3-1 Flowchart for global-local modeling technique... 38
3-2 Geometry size of the specimen for FEA calibration study (unit in mm)............. 40
3-3 Different 3D FEA models.. 42
3-4 Displacement of centre point on the solder interfaces from different models...... 43
3-5 Stress of centre point on the solder interfaces from different models.................. 43
3-6 Displacement interpolation on cut boundary for different submodels................. 44
3-7 Result comparison between fine model and hybrid submodels........................... 45
3-8 Result comparison between fine model and solder ball submodel...................... 46
3-9 Thermal cycling profile.. 49
3-10 Equivalent elastic strain comparison between fine 3D model and submodel...... 50
3-11 Equivalent plastic strain comparison between fine 3D model and submodel....... 50
3-12 Plastic work density comparison between fine 3D model and submodel............ 50
3-13 Equivalent plastic strain for underfill with constant material properties............. 53
3-14 Equivalent plastic strain for underfill with temperature dependent elastic modulus and CTE.. 53
3-15 Plastic work density for underfill with constant material properties.................. 54
3-16 Plastic work density for underfill with temperature dependent elastic modulus and CTE.. 54
3-17 Solder joint and corresponding two-node beam element.................................... 56
3-18 Relative displacement of two solder interfaces from different models................ 57
3-19 Maximum von Mises stress of solder joint for different models......................... 59
3-20 Von Mises stress distribution contour comparison.. 59
3-21 Solder ball and its effective solder joint with cubic cross section 60
3-22 Plastic work density from effective solder model for nonunderfill case............. 62
3-23 Plastic work density from effective solder model for underfill case.................. 62
3-24 Accumulated plastic work density per cycle for different models........................ 62
3-25 Accumulated plastic work density per cycle for different solder joints................ 64
3-26 Predicted fatigue life for Sn3.8Ag0.7Cu and Sn0.7Cu solder joints. 65

ATTENTION: The Singapore Copyright Act applies to the use of this document. Nanyang Technological University Library

4-1 Lead-free solder assembly specimen. 70
4-2 Actual and FEA-use thermal cycling profile. 70
4-3 Weibull plot of thermal fatigue life for PBGA316. 72
4-4 The cross section image of PBGA solder joint failure modes. 72
4-5 Finite element analysis procedure. 73
4-6 2D and 3D FEA models for PBGA assembly. 78
4-7 Effective quarter global FEA models for PBGA assembly. 78
4-8 Quarter global FEA models and submodels for PQFP assemblies. 80
4-9 Quarter FEA fine model for TSSOP assembly. 81
4-10 Averaged volumes located on component side for different assemblies. 81
4-11 Plastic work density accumulated in PBGA solder after fist thermal cycle. 82
4-12 Accumulated plastic work density per cycle for PBGA solder. 83
4-13 Accumulated plastic work densities for different PBGA FEA models. 83
4-14 Normalized fatigue life using different PBGA FEA models. 84
4-15 Normalized fatigue life for diagonal PBGA solders. 85
4-16 Normalized fatigue life of PQFP208 solder joints. 86
4-17 Normalized fatigue life of PQFP176 solder joints. 86
4-18 Normalized fatigue life of TSSOP48 solder joints. 87
4-19 Solder fatigue life for leaded components. 87
4-20 Solder fatigue life comparison for different assemblies. 88
4-21 Different averaging volumes for PBGA solder joint. 88
4-22 PBGA solder joint fatigue life based on different averaging volumes. 89
4-23 Accumulated plastic work density contour for different averaging volumes. 90
4-24 Inelastic strain energy density for different constitutive models. 91
4-25 Plot of strain energy density history for different constitutive models. 91
4-26 Fatigue life based on different solder constitutive and fatigue life models. 92
4-27 Fatigue life based on strain-base and energy-based fatigue models. 94
4-28 TC profiles of 4 different initial conditions used in FEA. 95
4-29 Solder fatigue life from different initial stress-free temperature conditions. 95
4-30 FEA model including IMC layer. 97
4-31 Nanoindentation results of CuNiSn layer. 98
4-32 IMC effect on solder fatigue life. 99
4-33 SMD FEA model vs. NSMD FEA model. 100
4-34 Fatigue life comparison between SMD and NSMD FEA models. 100

ATTENTION: The Singapore Copyright Act applies to the use of this document. Nanyang Technological University Library

4-35 Different thermal cycling profiles. 102
4-36 Fatigue life ratio for different temperature ranges. 102
5-1 Board size and layout of VQFN specimens. 108
5-2 Structure of VQFN package. 108
5-3 Three and four-point bending test fixtures. 109
5-4 Weibull plot of cycle to failure for three-point bend test. 110
5-5 Strain gage location on test board. 114
5-6 Strain measurement of different positions during cyclic bend. 114
5-7 Typical displacement and load profiles for four-point bend. 115
5-8 Typical in-situ resistance measurement during bend test. 116
5-9 Crack failure in solder joint of VQFN assembly. 117
5-10 Weibull plot of cycle to failure for OSP finish case tested at 25°C. 118
5-11 Weibull plot of cycle to failure for OSP finish case tested at 125°C. 119
5-12 Comparison of cycle to failure between Ni/Au and OSP finish cases. 119
5-13 Comparison of cycle to failure between 25°C and 125°C test condition. 120
5-14 Two-level submodeling method. 123
5-15 One-level submodeling method. 123
5-16 Global strain contour at displacement of 6mm. 124
5-17 Solder joint strains for different models. 125
5-18 Solder joint plastic strain energy density for different models. 125
5-19 Global simulation results for three-point bend. 126
5-20 Solder joint mesh and energy density contour for bottom and top layers. 127
5-21 Convergence history of accumulated strain energy density per cycle for the critical solder joint located at center row component case. 129
5-22 Convergence history of accumulated strain energy density per cycle for the critical solder joint located at right row component case. 129
5-23 Strain energy density accumulation percentage change each cycle for three-point bending load. 129
5-24 FEA result correlation between four-point bend and three-point bend. 130
5-25 Strain energy density accumulation of bottom layer for different cases. 131
5-26 FEA strain results of board surface at displacement of 0.432 to 2.16mm. 132
5-27 Deformation shape of specimen under different bending loads. 132
5-28 Accumulated energy density convergence for four-point bend at 25°C. 133
5-29 Relationship of displacement and accumulated energy density at 25°C. 134

ATTENTION: The Singapore Copyright Act applies to the use of this document. Nanyang Technological University Library

5-30 Accumulated energy density convergence for four-point bend at 125°C. 135

5-31 Relationship of displacement and accumulated energy density at 125°C. 136

5-32 Result comparison between bending simulation at 25°C and at 125°C. 136

5-33 Bending fatigue model for Sn-Ag-Cu solder at 25°C. 138

5-34 Bending fatigue model for Sn-Ag-Cu solder at 125°C. 138

5-35 Plastic strain energy density contour at the end of third cycle simulation. 140

5-36 Accumulated energy density per cycle from TC FEA simulation. 140

6-1 Drop test setup. 146

6-2 PCB specimen with three different packages... 147

6-3 Accelerations of PCB center. 148

6-4 Dynamic resistance measurement setup.. 149

6-5 Typical dynamic response during drop impact for leg2 specimen. 150

6-6 Quarter FEA model and boundary condition for PBGA assembly. 153

6-7 Input acceleration in drop impact FEA simulation for PBGA assembly. 154

6-8 Acceleration of PCB center node from FEA simulation. 155

6-9 Strain in drop direction for critical node on board and package sides. 155

6-10 Peel and 1st principal stress for critical node on board side. 156

6-11 Peel stress of critical node on board side from elastic and plastic models. 157

6-12 Von Mises stress from elastic model and plastic model. 157

6-13 Stress strain curves of SnAgCu solder under different strain rates.................... 158

6-14 Von Mises stress from different plastic models. 159

6-15 Effective plastic strain from different plastic models. 159

6-16 Effective plastic strain from bilinear plastic model for both with and without IMC consideration. 160

6-17 Effective plastic strain from rate dependent plastic model for both with and without IMC consideration. 160

6-18 Von Mises stress from rate dependent plastic model for both with and without IMC consideration. 161

6-19 Charpy specimens. 161

6-20 Fracture mode for different specimens. 162

7-1 Flip chip on board assembly and die number. 166

7-2 Schematic of the location for transmissibility measurement. 169

7-3 Transmissibility at natural frequency for 10G input test. 169

7-4 Global and local models for FCOB assembly. 170

ATTENTION: The Singapore Copyright Act applies to the use of this document. Nanyang Technological University Library

7-5 Plot of G_{out} vs. von Mises stress amplitude at natural frequency........................ 171

7-6 Plot of transmissibility vs. frequency for 3G level test...................................... 172

7-7 Eutectic Sn/Pb solder S-logN curve.. 173

7-8 CDI effect on fatigue life prediction... 174

7-9 Stress amplitudes at different frequencies for three G level tests....................... 175

ATTENTION: The Singapore Copyright Act applies to the use of this document. Nanyang Technological University Library

LIST OF TABLES

2-1 Material properties used for FE modeling of an electronic assembly.................... 9

2-2 Thermal environments for electronic products. 31

3-1 Comparison between fine model and submodel for FCOB without underfill. 46

3-2 Materials properties of FCOB assembly without underfill. 47

3-3 Anand’s constants for 62Sn36Pb2Ag solder [26]. 48

3-4 Plastic work density comparisons for different models*. 51

3-5 Temperature dependent materials properties for underfill. 52

3-6 Advantages of submodel compared to fine underfilled FCOB model. 55

3-7 Anand’s constants for different solders.. 63

4-1 TC test result for PBGA316, PQFP208, and PQFP176 (in cycles). 71

4-2 Weibull parameters, MTTF and FTTF for PBGA316 solder joints. 71

4-3 Material constants of creep model for Sn-Ag-Cu solders. 74

4-4 Material properties for PBGA assembly. 79

4-5 Temperature dependent material properties. 80

4-6 Element size and solving time comparison for different PBGA models. 85

4-7 Temperature dependent yield stress of solder joint.. 90

4-8 Material properties of IMCs.. 98

4-9 Thermal loading and fatigue life between TS and TC. 101

5-1 Weibull parameters and failure cycles for three-point bend test........................ 111

5-2 Fatigue life in cycles between three-point and four-point bend tests................. 116

5-3 Summary of four-point bend test conditions.. 118

5-4 Summary of failure data for all four-point bend tests. 121

5-5 Constitutive models for different materials in VQFN assembly........................ 124

5-6 Summary of results for four-point bend FEA simulations at 25°C. 133

5-7 Summary of results for four-point bend FEA simulations at 125°C. 136

5-8 FEA results and experimental data for four-point bend at 25°C. 137

6-1 Drop impact test results.. 151

6-2 Material properties of FEA drop model for PBGA assembly. 154

6-3 Strain rate dependent material properties of SnAgCu solder. 158

6-4 Impact toughness for different specimens.. 162

ATTENTION: The Singapore Copyright Act applies to the use of this document. Nanyang Technological University Library

7-1 Weibull parameters, MTTF and FTTF under vibration. 167
7-2 Comparison of the natural frequencies results. 168
7-3 Material properties used in FEA analysis for FCOB assembly. 170
7-4 Stress amplitudes for different G-level tests (at natural frequency). 171
7-5 Fatigue life comparisons for chip 3.. 173
7-6 Fatigue life comparison for test, quasi-static and harmonic analysis................. 175

ATTENTION: The Singapore Copyright Act applies to the use of this document. Nanyang Technological University Library

CHAPTER 1 INTRODUCTION

1.1 BACKGROUND

Electronic products are used in various industries and are expected to function reliably in service. Electronic packaging is the technology for fabricating physical electronic packages, assemblies and products. Electronic packages provide the structure for electrical interconnections, as well as the mechanical support structure for protecting the electronic circuitry [1]. Design-for-reliability (DFR) contributes to high quality and reliable electronic assemblies. Solder joint reliability tests such as thermal cycling, cyclic bend, drop impact and vibration tests provide useful failure assessment methods for electronic assembly reliability. Electronic assemblies are tested at higher stress conditions to accelerate failure for quicker understanding of product reliability. Such accelerated life test (ALT) methods shorten the cycle time for reliability design. Numerical modeling such as finite element analysis (FEA) further reduce the reliability failure assessment time and provide a comprehensive failure assessment and design-for-reliability methodology for electronic assemblies.

1.2 RELIABILITY PROBLEM OF ELECTRONIC ASSEMBLY

The reliability of a packaged microelectronic system is related to the probability that will be operational within acceptable limits for a given period of time [2]. Electronic assemblies are subjected to life cycle testing by thermal cycling (TC) or thermal shock (TS), cyclic bend, repeated drop impact, and sinusoidal and random vibration loadings. Failure mechanisms for electronic solders subjected to these different loadings need to

ATTENTION: The Singapore Copyright Act applies to the use of this document. Nanyang Technological University Library

be investigated. For microelectronic packages, surface mount technology (SMT) and soldering are used for assembly. The solder joint in the electronic assembly is often the weakest link and solder joint reliability becomes even more important with further minimization of electronic assemblies. The solder joint is particularly prone to fatigue failure due to power and temperature cycling loading [3]. Eutectic solder (63Sn/37Pb) is the current material used for soldering electronic components. However, lead (Pb) in electronic products will be banned in Europe from 1st July 2006 due to legislations to ban hazardous materials. The electronics industry is getting ready for implementing Pb-free solders. The Pb-free solder alloy recommended by the International Electronics Manufacturing Initiative (iNEMI) is Sn-3.9Ag-0.6Cu solder for reflow soldering and Sn-0.7Cu solder for wave soldering. Failure assessment methodology for electronic assemblies with SnAgCu Pb-free solder is urgently needed to be in place before year 2006.

Reliability testing often employs accelerated stress testing (AST), where stresses are applied to a product in excess of the specified operating limits to precipitate latent flaws to the point of detection via testing [4]. Thermal cycling and vibration tests are commonly used for characterization of solder joint failure assessment. Thermal cycling loads (high strain, low cycle fatigue) induce visco-plastic deformation in the solder joints. Vibration loads (low stress, high cycle fatigue) primarily induce elastic or elastic-plastic deformation in the solder joints. Drop impact test is used to investigate impact reliability of electronic assemblies for portable electronic products.

Numerical modeling with finite element analysis provide important understanding on the micro-deformation responses in solder joint subjected to reliability test conditions. Global-local finite element techniques, static/dynamic, and linear/nonlinear analyses are required for different solder joint reliability failure assessments. The

ATTENTION: The Singapore Copyright Act applies to the use of this document. Nanyang Technological University Library

combination of FEA and reliability tests provides a powerful and effective tool for design-for-reliability (DFR) application in electronic packaging design. It must be kept in mind that a multidisciplinary approach is required for electronic assembly failure assessments. Fig.1-1 shows the detailed consideration and methodology used in design-for-reliability.

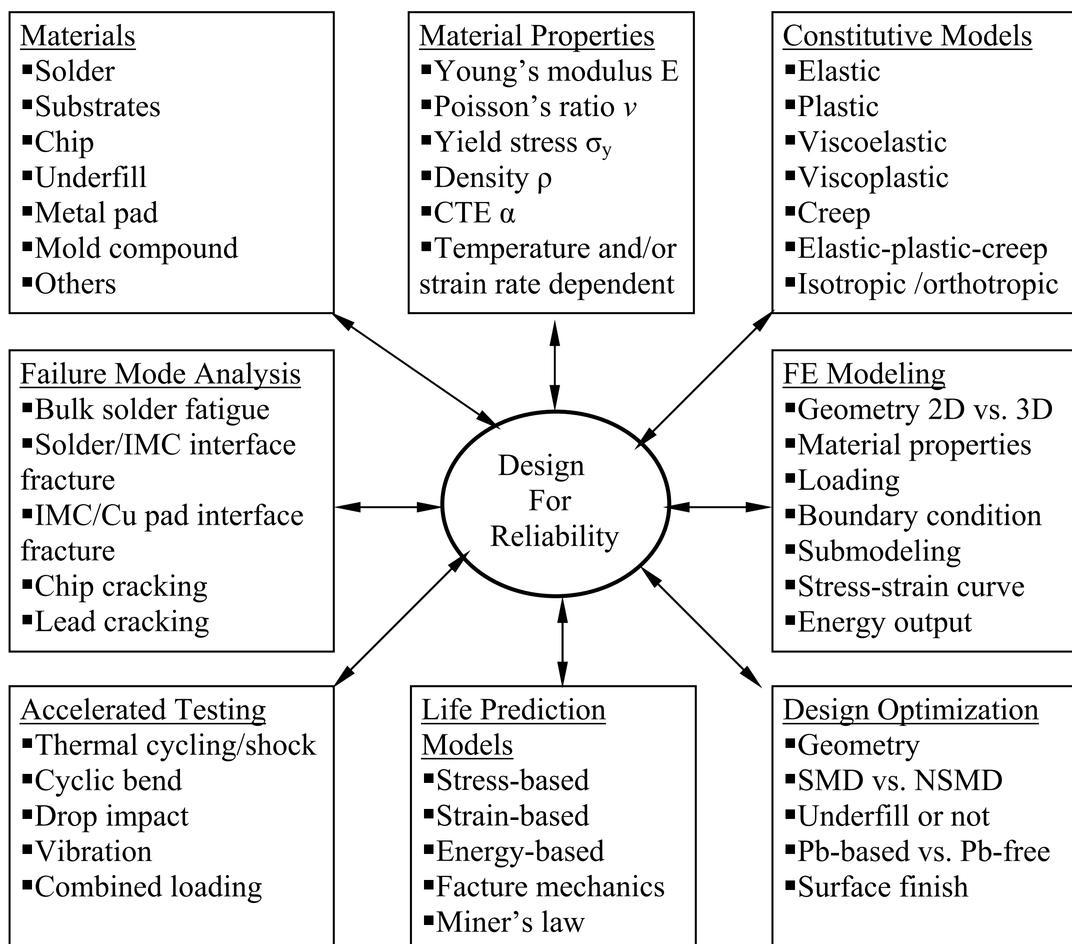

Fig. 1-1 The multidisciplinary approach in design for reliability methodology.

1.3 OBJECTIVE AND SCOPE

The main goal of this study is to develop a failure assessment methodology for soldered Pb-free electronic assemblies subjected to thermal cycling, cyclic bend, repeated drop impact, and vibration fatigue tests.

The specific research objectives and requirement for these objectives include:

ATTENTION: The Singapore Copyright Act applies to the use of this document. Nanyang Technological University Library

1) To develop a global-local FEA modeling technique for solder joint reliability assessment of electronic assemblies. Submodeling technique can also be found from existing literature. However, how to select appropriate cut boundary and how to quantify the error induced by submodel were not well documented from the limited literature. In this study, different cut boundaries were introduced for comparison and proper submodel and accuracy checking were proposed by comparing FEA results between submodel and full 3D model. Then submodeling technique developed in this study was used for solder joint reliability issue when subjected to different loadings such as thermal cycling, cyclic bend and vibration. In addition, a simple global-local model, called global-local-beam (GLB) model, was developed for board-level analysis such as modal analysis.

2) To develop a failure assessment methodology for solder joints of electronic assemblies under thermal cycling, cyclic bending, repeated drop impact and vibration reliability tests. Knowledge and understanding for Pb-free solder are still limited compared with Pb-based solder from published papers. The design-for–reliability (DFR) methodology will be developed for Pb-free solder considering different environmental conditions in this study.

3) To conduct parametric study of fatigue life of Pb-free solder subjected to thermal cycling. Numerous publications for reliability of electronic assembly are related to thermal fatigue analyses for Pb-free and Pb-based solders. FEA modeling and simulation in existing literatures are mostly used for verification of test results using certain solder constitutive model, fatigue model, and FE model. However, different models and other parameter effects on solder fatigue life were not clearly documented in existing literature. In this study, a series of parametric studies are reported using submodeling technique to investigate their impact on Pb-free solder

ATTENTION: The Singapore Copyright Act applies to the use of this document. Nanyang Technological University Library

fatigue life. Some studies are proposed for the first time, including modeling IMC effect, averaging volume effect.

4) To develop bending fatigue models for Pb-free solder at room temperature (25 ^{o}C) and high temperature (125°C). From existing literature, limited bend tests are related to Pb-free solder, and all bend tests reported were conducted at room temperature. It is necessary to understand how high temperature accelerates the bending fatigue failure of Pb-free solder. Therefore, bend tests at both 25°C and 125°C are reported in this study to investigate temperature effect on bending fatigue of Pb-free solder.

5) To investigate solder joint impact failure mode and mechanism based on FEA modeling and test results. Solder fatigue failure is dominant failure mode when subjected to thermal cycling, cyclic bend and vibration loads from existing literature. It is necessary to understand the impact failure mode and mechanism due to limited research related to this area. In this study, board surface effect on solder impact reliability and drop reliability comparison between Pb-free soldered and Pb-based soldered electronic assembly were investigated. Charpy impact tests for bulk solder and soldered specimens were carried out to compare and investigate impact failure mode and mechanism. The soldered Charpy specimens were designed for impact test considering two cases including solder on Cu and solder on Ni/Cu for the first time.

6) To evaluate the dynamic response of electronic assemblies subjected to drop impact and vibration reliability tests. Some vibration and drop tests and analyses can be found from existing literature. However, how to simulate dynamic response and drop induced solder stress strain behavior for Pb-free electronic assembly are new areas for research. Three simulation methods and different solder constitutive models were used in drop impact simulation in this study. The IMC effect on solder stress

ATTENTION: The Singapore Copyright Act applies to the use of this document. Nanyang Technological University Library

strain behavior was first investigated. The quasi-static FEA modeling method is developed to evaluate the solder response when subjected to vibration load. The cumulative damage law application is presented for predicting solder fatigue life when subjected to vibration test with frequency range around the natural frequency.

This project can be divided into three main parts such as experiment, FE modeling, and investigation, which are illustrated in Fig. 1-2.

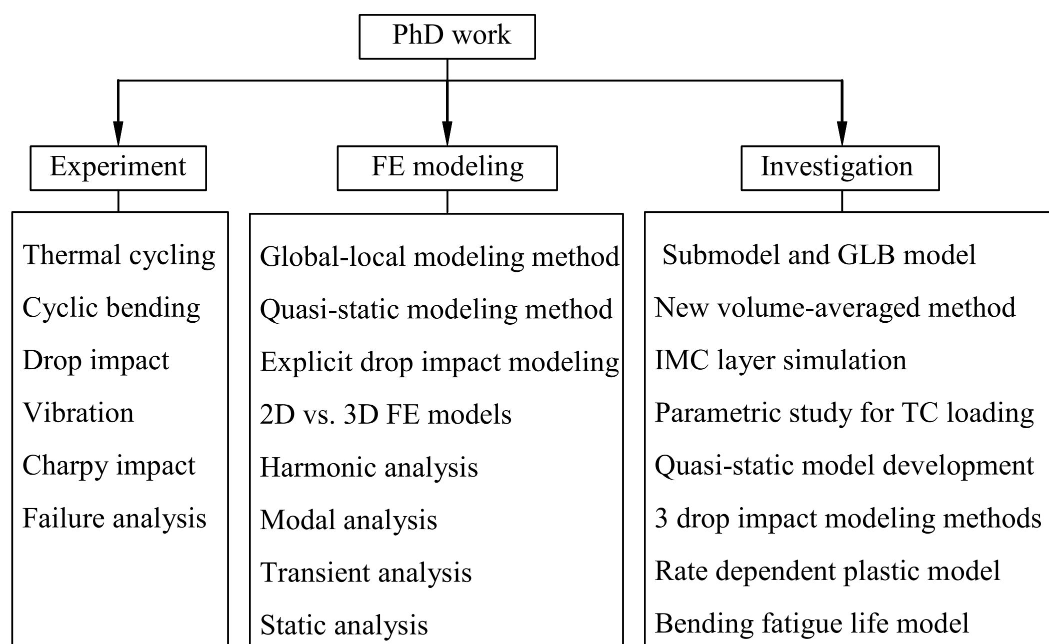

Fig. 1-2 Schematic illustration for main work.

1.4 OUTLINE OF THE THESIS

This thesis is organized into eight chapters. The content of each chapter is summarized as follows:

In Chapter 1, general research background and objectives are presented and mechanical reliability concerns in electronic assemblies are summarized.

In Chapter 2, techniques related to reliability of electronic assembly are reviewed. Different solder constitutive models such as elastic-plastic model, elastic-plastic-creep model, and viscoplastic Anand model are discussed. Different solder fatigue models

ATTENTION: The Singapore Copyright Act applies to the use of this document. Nanyang Technological University Library

such as stress-based fatigue model, strain-based fatigue model, energy-based fatigue model, fracture-based model relating to crack initiation and propagation concepts, and cumulative damage method are reviewed. Solder joint reliability test, such as thermal cycling, cyclic bend, drop impact and vibration tests are documented.

In Chapter 3, submodeling and global-local-beam (GLB) model techniques are developed and compared to conventional full 3D model results. The effects of underfill on the FCOB solder joint fatigue life are analyzed using submodeling method. Comparisons between Pb-free and Pb-based solders are conducted. Effects of shell or solid elements used in the GLB model on FEA results are investigated.

In Chapter 4, thermal cycling tests are conducted for PBGA, PQFP and TSSOP components with SnAgCu Pb-free solder joints. MTTF is determined from Weibull distribution model. FEA simulations for PBGA are conducted considering different conditions, such as 2D and 3D FEA models, IMC considerations, SMD vs. NSMD, solder constitutive models. Solder fatigue life is also predicted using different fatigue models and averaging volumes.

In Chapter 5, cyclic four-point bend tests are conducted for VQFN assembly with Ni/Au or OSP surface finish at 25^oC and 125^oC. Correlation between four-point bend and three-point bend is developed. FEA modeling and simulation are carried out using submodeling approaches. Bending fatigue models are proposed for VQFN component with SnAgCu Pb-free solder subjected to cyclic bend load.

In Chapter 6, board-level drop impact tests are conducted for different assemblies. Dynamic responses of specimen during drop impact are measured using different instruments. Explicit dynamic FEA analysis using Ansys/LS-DYNA is implemented. Three FEA modeling methods and different material properties of solder joint, including elastic, bilinear kinematic plastic, strain rate dependent plastic models, are

ATTENTION: The Singapore Copyright Act applies to the use of this document. Nanyang Technological University Library

investigated. IMC effect is also considered in FEA simulation. Charpy impact tests for bulk solder and soldered specimens are conducted.

In Chapter 7, sinusoidal vibration reliability tests for constant G-level and block G-level of 3G, 5G, and 10G are investigated. The quasi-static FEA modeling and simulation method is developed for simulating forced vibration fatigue load. Modal analyses using different approximate methods are performed. The quasi-static method could result in consistent fatigue life compared with harmonic analysis and experimental results.

In Chapter 8, conclusions based on key results relating to global-local modeling approach, thermal cycling, cyclic bend, repeated drop impact and vibration tests and analyses are summarized. Contributions made in this project and recommendations are also documented.

ATTENTION: The Singapore Copyright Act applies to the use of this document. Nanyang Technological University Library

CHAPTER 2 LITERATURE REVIEW

2.1 MATERIALS PROPERTIES FOR ELECTRONIC ASSEMBLY

Electronic packaging, materials and their properties influence the reliability of electronic assemblies [5]. In this study, only the thermomechanical properties and mechanics of material models will be reviewed. Thermo-mechanical properties include coefficient of thermal expansion (CTE) and glass transition temperature (T_g) for polymers. The mechanical properties include the modulus of elasticity, Poisson's ratio, shear modulus, yield stress, tangent modulus, creep strength, fracture toughness, and fatigue strength.

Table 2-1 Material properties used for FE modeling of an electronic assembly.

Materials	Young's Modulus (GPa)	Poisson's Ratio	CTE (ppm/^{o}C)
PCB (FR4)	xy: 12.2～22, z:1.6～10	0.19～0.39	xy: 13～18, z:60
Pad (copper)	120～130	0.3～0.36	16.5～17
Solder (63Sn37Pb)	24.8～31.7	0.32～0.4	23.9～25
Solder (Sn3.8Ag0.7Cu)	44.4～58.0	0.35～0.4	23.5～26
Substrate (BT resin)	19～26	0.18～0.39	13～14
Solder mask	2.5～4.9	0.3～0.48	30～95
Die (silicon)	106.9～169	0.22～0.35	2.3～2.7
Mold compound	12.5～16	0.25～0.35	20～25
Underfill	4.4～6	0.35～0.4	22～45
Die adhesive	3.45～7.4	0.27～0.35	45～100

The typical packaging materials include FR4 PCB substrate, eutectic Sn/Pb solder or lead-free solder, silicon chip, die adhesive, epoxy underfill, copper pad, mold compound, solder mask, BT resin substrate, etc. Many researchers [6-13] performed FEA simulations using different material properties. A summary for these material

ATTENTION: The Singapore Copyright Act applies to the use of this document. Nanyang Technological University Library

properties at room temperature is given in Table 2-1. Yao and Qu [14] gave a list of detailed temperature dependent properties for electronic materials in SMT assembly.

2.2 CONSTITUTIVE MODELS FOR SOLDER JOINTS

Solder is one of critical materials in electronic packaging. The suitable constitutive model for solder joints is needed to simulate solder stress-strain behavior when subjected to thermomechanical loading, cyclic bending, repeated drop impact and vibration loading.

2.2.1 Creep Model

Solder creep behavior is temperature and time dependent, and is typically important at 0.4 T_m and above, where T_m is the absolute melting temperature [15]. For eutectic Sn/Pb solder, the melting temperature is 456K (183°C +273°C), and the melting point for Sn3.8Ag0.7Cu lead-free solder is 490K (217°C+273°C) [16]. Therefore, even though at room temperature of 298K, the homologous temperature ratio (in Kelvin) is more than 0.5. Hence, creep behavior in electronic solders is important.

The steady-state creep strain rate is function of temperature and applied stress given in Eq. (2.1) [17, 18].

$$\dot{\varepsilon}_c = A\sigma^n \exp\left[\frac{-Q}{kT}\right] \tag{2.1}$$

where $\dot{\varepsilon}_c$ is the steady-state creep strain rate (s^{-1}), σ is the current stress (MPa), A is material constant $(MPa)^{-n}/s$, n is stress exponent, Q is activation energy for creep deformation process (eV), k is Boltzmann's constant (eV/K), and T is absolute temperature (K).

At high stresses, the simple power law creep behavior breaks down and the creep strain rate increases more quickly with applied stress, which is called power law

ATTENTION: The Singapore Copyright Act applies to the use of this document. Nanyang Technological University Library

breakdown creep behavior. In order to find a wider formulation for power law creep (low and medium stresses) and power law breakdown (high stresses), double power law and hyperbolic sine function have been widely used. The double power law model can be expressed as follows [19]:

$$\dot{\varepsilon}_c = A_1\left(\frac{\sigma}{\sigma_N}\right)^{n_1}\exp\left[\frac{-Q_1}{kT}\right] + A_2\left(\frac{\sigma}{\sigma_N}\right)^{n_2}\exp\left[\frac{-Q_2}{kT}\right] \tag{2.2}$$

The first term in Eq. (2.2) corresponds to the creep behavior at low stress level, where diffusion creep is dominant, and second term corresponds to the creep behavior at high stress level, where dislocation creep is dominant. This double power law model can be realized by using the provided models for primary and secondary creep simultaneously.

The Garofalo-Arrhenius steady-state creep behavior using hyperbolic sine function is used to model the power law break-down region at high stress region and is expressed as [20, 21]:

$$\frac{d\gamma}{dt} = C\frac{G}{T}\left[\sinh\left(\alpha\frac{\tau}{G}\right)\right]^n \exp\left[\frac{-Q}{kT}\right] \tag{2.3}$$

Eq. (2.3) is developed from shear creep test data. In multiaxial load condition, using equivalent creep strain rate, $\dot{\varepsilon}_c$, to replace the shear strain rate, $\frac{d\gamma}{dt}$, the general steady-state creep behavior can be expressed as:

$$\dot{\varepsilon}_c = C_1\frac{G}{T}\left[\sinh\left(\alpha\frac{\sigma}{G}\right)\right]^n \exp\left[\frac{-Q}{kT}\right] \tag{2.4}$$

Eq. (2.1) and (2.4) can be rewritten into Eq. (2.5) and (2.6), respectively, in the required format of input for implicit creep model in ANSYS^{TM} FEA software [22].

Power law: $$\dot{\varepsilon}_c = A_1\sigma^{A_2}\exp\left[\frac{-A_3}{T}\right] \tag{2.5}$$

ATTENTION: The Singapore Copyright Act applies to the use of this document. Nanyang Technological University Library

$$\text{Hyperbolic sine:} \quad \dot{\varepsilon}_c = C_1[\sinh(C_2\sigma)]^{C_3} \exp\left[\frac{-C_4}{T}\right] \tag{2.6}$$

where A_1, A_2, A_3 in power law and C_1, C_2, C_3, C_4 in hyperbolic sine equation are material constants, which can be determined from different temperature and stress level creep tests. Wiese et al. [19, 23] and Pang et al. [24] have published these material constants for lead-free bulk solder and solder joints.

2.2.2 Viscoplastic Anand Model

Creep deformation can be developed in any stress levels for solder alloy. Time independent plastic strain will become significant at stress levels above $\tau/G = 10^{-3}$, which is also the critical power law breakdown condition approximately [21]. The time-independent plastic strain and time-dependent creep strain are difficult to separate in higher stress level. From the non-linear deformation modeling point of view, the mechanism of the creep and plastic strain may be related to dislocation motion. In order to study the constitutive behavior using a state variable visco-plastic approach, the creep and plastic strain may be combined into inelastic strain.

A commonly used viscoplastic model for solder is Anand model [8, 13, 25, 26]. There are two basic features in this model. First, this model needs no explicit yield condition and no loading/unloading criterion. The plastic strain is assumed to take place at all nonzero stress level. Second, this model employs a single scalar as an internal variable, the deformation resistance s, to represent the averaged isotropic resistance to plastic flow. Anand model is broken down into a flow equation, and three evolution equations [27, 28]:

Flow equation:

$$\dot{\varepsilon}_p = A\left[\sinh\left(\frac{\xi\sigma}{s}\right)\right]^{1/m} \exp\left(\frac{-Q}{kT}\right) \tag{2.7}$$

ATTENTION: The Singapore Copyright Act applies to the use of this document. Nanyang Technological University Library

Evolution equations:

$$\dot{s} = \left\{ h_0 \left(|B| \right)^a \frac{B}{|B|} \right\} \dot{\varepsilon}_p \tag{2.8}$$

$$B = 1 - \frac{s}{s^*} \tag{2.9}$$

$$s^* = s^{\wedge} \left[\frac{\dot{\varepsilon}_p}{A} \exp\left(\frac{Q}{kT} \right) \right]^n \tag{2.10}$$

where $\dot{\varepsilon}_p$ is the effective plastic strain rate, σ is effective true stress (MPa), s is the deformation resistance (MPa), Q is the activation energy, k is Boltzmann's constant, T is the absolute temperature, A is the pre-exponential factor (1/sec), ξ is the stress multiplier, m is the strain rate sensitivity of stress, h_0 is the hardening constant (MPa), $\hat{s}$ is the coefficient for deformation resistance saturation value (MPa), n is the strain rate sensitivity of saturation value, and α is strain rate sensitivity of hardening. Nine constants in Anand model can be determined by curve-fitting the experimental data, such as creep tests and constant strain rate tensile tests. Cheng et al. [8] and Wang et al. [25] published these parameters for different lead-free and lead-based solder alloys. Anand model is a build-up model in ANSYS FEA software and has been widely used for simulation of the solder joint deformation under cyclic mechanical and thermomechanical loading with lower load frequency.

2.2.3 Elastic-Plastic-Creep Model

It is assumed in creep model that all inelastic strain is developed due to creep deformation, which is suitable for the condition that slow mechanical or thermomechanical loading is simulated. In viscoplastic model, plastic strain and creep strain cannot be separated distinctly and they are unified as inelastic strain. However, elastic-plastic-creep (EPC) model is realized by combining time independent elastic-

ATTENTION: The Singapore Copyright Act applies to the use of this document. Nanyang Technological University Library

plastic model and time dependent creep model. Plastic strain and creep strain are separated distinctly and their summation is called total inelastic strain:

$$\varepsilon_{in} = \varepsilon_c + \varepsilon_p \tag{2.11}$$

where ε_{in} is the total inelastic strain, ε_c is time dependent creep strain which can be obtained from creep model, ε_p is time independent plastic strain. At high stress deformation, time independent plastic strain can be expressed using following strain hardening law [26]:

$$\varepsilon_p = C_p\left(\frac{\sigma}{G}\right)^{m_p} \tag{2.12}$$

where G is shear modulus, C_p and m_p are material constants.

Plasticity theory provides a mathematical relationship that characterizes the elastoplastic response of materials. There are three ingredients in the rate-independent plasticity theory: the yield criterion, flow rule and the hardening rule. The yield criterion determines the stress level at which yield is initiated and von Mises yield criterion is widely used for metal and metal alloy. For multi-axes stress situation, the equivalent von Mises stress and strain can be expressed as [29]:

$$\sigma_{eff} = \frac{1}{\sqrt{2}}\sqrt{(\sigma_1-\sigma_2)^2+(\sigma_2-\sigma_3)^2+(\sigma_3-\sigma_1)^2} \tag{2.13}$$

$$\varepsilon_{eff} = \frac{\sqrt{2}}{3}\sqrt{(\varepsilon_1-\varepsilon_2)^2+(\varepsilon_2-\varepsilon_3)^2+(\varepsilon_3-\varepsilon_1)^2} \tag{2.14}$$

The flow rule determines the direction of plastic straining and plastic strains usually occur in a direction normal to the yield surface. The hardening rule describes the changing of the yield surface with progressive yielding, so that subsequent yielding can be established. Two hardening rules are available: work (or isotropic) hardening and kinematic hardening. In work hardening, the yield surface remains centered about its initial centerline and expands in size as the plastic strains develop. Kinematic

ATTENTION: The Singapore Copyright Act applies to the use of this document. Nanyang Technological University Library

hardening assumes that the yield surface remains constant in size and the surface translates in stress space with progressive yielding. In practical FE simulation when electronic assembly subjected to thermomechanical or mechanical load with lower strain rate, some simple plasticity forms after yield are used: perfectly plastic behavior, bilinear kinematic or work (isotropic) hardening plastic deformation, and multilinear kinematic or work hardening plastic deformation. The study done by Wiese et al. [19] shown that elastic-plastic-creep model can give more accurate result than elastic-creep model for the simulation of fast mechanical cycles (>0.1Hz) such as bend test.

Three models mentioned above are commonly used for solder joints when subjected to thermal cycling load. However, how these models affect the solder joint stress-strain behavior and life prediction have not been fully discussed from existing literature, especially for Pb-free solder reliability issue, so creep model, elastic-plastic model, Anand's model and EPC model are compared and discussed systematically in Chapter 4 by using them as the solder constitutive model for PBGA assembly when subjected to thermal cycling loading.

2.2.4 Rate Dependent Plastic Model

A typical application of rate dependent plastic model is the simulation of material deformation at high strain rate, such as impact. Some widely used rate dependent plastic models for metal and alloy are reviewed as below.

Plastic Kinematic Model considers isotropic, kinematic, or a combination of isotropic and kinematic hardening with strain rate dependency and failure. Isotropic and kinematic contributions may be varied by adjusting the hardening parameter β between 0 (kinematic hardening only) and 1 (isotropic hardening only). Strain rate is accounted for using the Cowper-Symonds model which scales the yield stress by the strain rate dependent factor as shown below [30]:

ATTENTION: The Singapore Copyright Act applies to the use of this document. Nanyang Technological University Library

$$\sigma_y = \left[1 + \left(\frac{\dot{\varepsilon}}{C}\right)^{\frac{1}{P}}\right]\left(\sigma_0 + \beta E_p \varepsilon_p^{eff}\right) \tag{2.15}$$

where σ_0 is the initial yield stress, $\dot{\varepsilon}$ is the strain rate, C and P are the Cowper-Symonds strain rate parameters, ε_p^{eff} is the effective plastic strain, and E_p is the plastic hardening modulus which is given by:

$$E_p = \frac{E_{\tan} E}{E - E_{\tan}} \tag{2.16}$$

where E is the Young's modulus and E_{tan} is tangent modulus.

Strain Rate Dependent Plasticity Model: In this model, a load curve is used to describe the initial yield strength, σ_0, as a function of effective strain rate. The yield stress for this material model is defined as:

$$\sigma_y = \sigma_0 \dot{\varepsilon}^{eff} + E_p \varepsilon_p^{eff} \tag{2.17}$$

where σ_0 is the initial yield strength, $\dot{\varepsilon}^{eff}$ is the effective strain rate, ε_p^{eff} is the effective plastic strain, and E_p is the plastic hardening modulus given by Eq. (2.16). This model also contains a simple mechanism for modeling material failure. In FE simulation, this option is activated by specifying a load curve ID defining the effective stress at failure as a function of strain rate. For solid elements, once the effective stress exceeds the failure stress, the element is deemed to have failed and is removed from the solution.

Rate Sensitive Power Law Plasticity Model follows a Ramberg-Osgood constitutive relationship of the form:

$$\sigma_y = k\varepsilon^m \dot{\varepsilon}^n \tag{2.18}$$

where ε is the strain, $\dot{\varepsilon}$ is the strain rate, k is the material constant, m is the hardening coefficient, and n is the strain rate sensitivity coefficient.

It is not found from existing literature that the strain rate dependent plastic model was used to model the solder joint behavior in FEA simulation for drop reliability of

ATTENTION: The Singapore Copyright Act applies to the use of this document. Nanyang Technological University Library

electronic assembly with Pb-free solder. In Chapter 6, different solder constitutive models such as elastic, bilinear plastic, and strain rate dependent plastic model are implemented respectively in FEA modeling and simulation for PBGA assembly with SnAgCu solder subjected to drop impact loading. Solder constitutive model effect on solder stress-strain dynamic response was documented for the first time. The strain rate dependent plastic model for SnAgCu solder was developed by our research group. In addition, the IMC effect on solder stress strain dynamic response was also investigated.

2.3 SOLDER FATIGUE LIFE PREDICTION MODELS

Solder joints are usually considered as the weakest part in the electronic assembly, therefore, the fatigue life of solder joint often limits the life of the electronic product. The main failure mechanisms of solder joints include fatigue, creep and fracture. The mechanism of damage and degradation, as well as determination of the fatigue life of solder joints have been discussed by de Kluizenaar [31, 32]. Eutectic or near eutectic Tin-Lead (Sn-Pb) solders are currently used in electronic assemblies and have a melting point of 183°C. In the coming year, lead-free solders will replace Sn/Pb solders because of legislations to ban hazardous materials like lead (Pb). The iNEMI has recommended 95.5Sn-3.9Ag-0.6Cu ($\pm$0.2%) alloys for solder reflow process and investigations on the properties of lead-free solders are needed [33, 34]. Miric and Grusd [16] reported some lead-free solder materials and their properties. Turbini et al. [35] discussed the existing problems for the lead-free soldering alternatives.

Solder fatigue failure characterizations are needed for lead-free solders. There are two approaches to develop a fatigue life prediction model for solder. One approach is developed by conducting displacement-controlled isothermal mechanical fatigue test using bulk solder material. The other is developed by using actual reliability test data

ATTENTION: The Singapore Copyright Act applies to the use of this document. Nanyang Technological University Library

and finite element simulation to estimate the fatigue driving parameter. For the first method, the bulk solder material is tested under displacement-controlled isothermal fatigue test condition. Inelastic strain energy density, inelastic strain and total strain in one cycle can be determined from stress-strain hysteresis loop. A fatigue failure criterion is usually set using 50% load drop based on load cell measurement. Then fatigue life model can be developed using Coffin-Manson strain-based model and/or Morrow's energy-based model. For the second method, in order to develop a life prediction model for solder joints, four steps are required. First, a constitutive equation and appropriate material properties need to be defined or chosen. Second, the constitutive equation is translated into FEA modeling and then using FEA analysis simulates stress-strain behavior of solder joints according to actual reliability test loading. Third, the volume-averaged numerical results such as strain or strain energy density from FEA simulation can be used as damage parameter in fatigue life prediction model. Fourth, actual thermal cycling test data (or Weibull failure distribution data) from different test conditions and different package types are used to correlate the FEA damage parameter with the Mean-Time-To-Failure (MTTF) cycles in the fatigue model. The coefficient and exponent in fatigue model can be determined by combining numerical result and actual reliability test data based on the Weibull cumulative failure distribution.

Lee et al. [36] divided fatigue models into five categories, namely, (a) stress-based, (b) plastic strain-based, (c) creep strain-based, (d) energy-based, and (e) damage accumulated based. Sometimes, plastic strain-based and creep strain-based models can be combined into inelastic strain-based model.

ATTENTION: The Singapore Copyright Act applies to the use of this document. Nanyang Technological University Library

2.3.1 Stress-Based Fatigue Models

The stress-based fatigue model, expressed by the S-N curve, is used for high-cycle fatigue failure assessment (>10^5 cycles) at low stress amplitude levels. This approach applies when plastic deformation is small or negligible. S-N curve data are usually presented on a log-log plot. The S-N curve expression is given as follows:

$$\sigma_a = \sigma_f^{'}(2N_f)^b = AN_f^{\ B} \tag{2.19}$$

where σ_a is stress amplitude, $\sigma_f^{'}$ is fatigue strength coefficient, b is fatigue strength exponent, $2N_f$ is reversals of failure (1 reversal = ½ cycle). When nonzero mean stress effect is considered for the fatigue life, Goodman criterion is generally used and expressed as follows:

$$\frac{\sigma_a}{\sigma_{ar}} + \frac{\sigma_m}{\sigma_f^{'}} = 1 \tag{2.20}$$

where σ_{ar} is stress amplitude for the case zero mean stress i.e. an equivalent completely reversed stress, σ_m is mean stress. Substituting σ_{ar} into Eq. (2.19), getting:

$$\sigma_a = \left(1 - \frac{\sigma_m}{\sigma_f^{'}}\right)\sigma_f^{'}(2N_f)^b = (\sigma_f^{'} - \sigma_m)(2N_f)^b \tag{2.21}$$

For a condition of variable amplitude loading, the Palmgren-Miner rule, also called the cumulative damage theory (CDT), states that fatigue failure is expected when summation of life fractions, N_i/N_{fi}, reaches unity expressed by:

$$\frac{N_1}{N_{f1}} + \frac{N_2}{N_{f2}} + \frac{N_3}{N_{f3}} + \cdots = \sum \frac{N_i}{N_{fi}} = 1 \tag{2.22}$$

where N_i is a number of cycles when a certain stress amplitude, σ_{ai}, is applied, N_{fi} is the number of cycles to failure from S-N curve at σ_{ai}. However, failure is often assumed to occur at a more conservative value such as 0.7 or lower for electronic

ATTENTION: The Singapore Copyright Act applies to the use of this document. Nanyang Technological University Library

equipment. High cycle fatigue is relevant to electronic assembly subjected to vibration loading. The cumulative damage index (CDI) approach has been used to predict the fatigue life of solder joint subjected to vibration loading [37-39].

2.3.2 Strain-Based Fatigue Models

When the electronic products are subjected to thermal cycling, low cycle fatigue ($<10^4$ cycles) failure occurs and the fatigue life can be predicted using strain-based approach. Strain-induced fatigue can be further divided into three groups, namely plastic strain, creep strain or total strain. Plastic strain deformation focuses on the time independent plastic effects, while creep strain accounts for the time dependent creep effects. Total strain considers all strain deformation due to not only inelastic deformation but also elastic deformation.

2.3.2.1 Plastic strain fatigue models

Plastic strain fatigue model applies to fatigue situations where cyclic plastic yielding of ductile materials lead to short fatigue lives hence low cycle fatigue behavior. The Coffin and Manson low cycle fatigue model is perhaps the best known and most widely used fatigue model currently in solder joint fatigue analysis and given by [40, 41]:

$$\varepsilon_p = \varepsilon_f{}^{'}\left(2N_f\right)^c \qquad (2.23)$$

where ε_p is plastic strain amplitude, N_f is total number of cycles to failure, $\varepsilon_f^{'}$ is fatigue ductility coefficient which is approximately equal to the true fracture ductility ε_f, and c is fatigue ductility exponent (varying between –0.5 and –0.7). Experimental data are required to determine the material constants. In order to account for the effect of frequency, a frequency-modified Coffin-Manson model was given by Shi et al. [42]:

$$\left[N_f \nu^{(k-1)}\right]^m \varepsilon_p = C \qquad (2.24)$$

ATTENTION: The Singapore Copyright Act applies to the use of this document. Nanyang Technological University Library

where ν is frequency, and k is a frequency exponent which can be determined from the relationship between fatigue life and frequency.

Solomon's low cycle fatigue model relating the plastic shear strain to fatigue life is expressed by [13]:

$$\Delta\gamma_p N_p^{\alpha} = \theta \tag{2.25}$$

where $\Delta\gamma_p$ is the plastic shear strain range, N_p is the number of cycles to failure, θ is the inverse of the fatigue ductility coefficient, and α is a material constant. This fatigue model has been applied to leaded PQFP package and underfilled Flip Chip by various authors with success [43]. However, since this model does not consider creep effect, it is limited in its practical use for solder joints subjected to thermal cycling load [44]. For multi-axes stress situation, the equivalent von Mises strain as shown in Eq. (2.14) is used to output the state of strain in the solder joint. Then fatigue life prediction models with shear strain component require conversion from equivalent strain. The relationship between equivalent strain and shear strain can be expressed as:

$$\gamma = \sqrt{3}\varepsilon_{eq} \tag{2.26}$$

2.3.2.2 Creep strain fatigue models

Creep strain fatigue models account strictly for the creep phenomenon involved in solder joints. Creep can be separated into two possible mechanisms: matrix creep and grain boundary creep. Knecht and Fox [45] proposed a simple matrix creep fatigue model relating to the solder microstructure and the matrix creep shear strain range:

$$N_f = \frac{C}{\Delta\gamma_{mc}} \tag{2.27}$$

where N_f is the number of cycles to failure, C is a material constant dependent on failure criteria and solder microstructure and $\Delta\gamma_{mc}$ is the shear strain range due to matrix creep.

ATTENTION: The Singapore Copyright Act applies to the use of this document. Nanyang Technological University Library

Syed [46] proposed creep strain fatigue models for SnPb and SnAgCu solders by partitioning creep strain into two parts corresponding to transient creep and steady-state creep stages:

$$\text{For SnPb:} \qquad N_f = \left(0.02\varepsilon_{cr}^{\mathrm{I}} + 0.063\varepsilon_{cr}^{\mathrm{II}}\right)^{-1} \tag{2.28}$$

$$\text{For SnAgCu:} \; N_f = (0.106\varepsilon_{cr}^{\mathrm{I}} + 0.045\varepsilon_{cr}^{\mathrm{II}})^{-1} \tag{2.29}$$

Syed [46] also presented creep strain fatigue model for SnAgCu using total accumulated creep strain by considering two different creep constitutive models of power law and hyperbolic sine creep model:

$$\text{Power law:} \qquad N_f = \left(0.0468\varepsilon_{cr}\right)^{-1} \tag{2.30}$$

$$\text{Hyperbolic sine:} \; N_f = \left(0.0513\varepsilon_{cr}\right)^{-1} \tag{2.31}$$

Schubert et al. [47] proposed creep strain fatigue model for SnPb and SnAgCu using total accumulated creep strain by experiments and simulations:

$$\text{For SnPb:} \qquad N_f = 0.69\varepsilon_{cr}^{(-1.80)} \tag{2.32}$$

$$\text{For SnAgCu:} \qquad N_f = 4.5\varepsilon_{cr}^{(-1.295)} \tag{2.33}$$

where ε_{cr} from Eq. (2.28) to (2.33) are accumulated creep strain per cycle calculated by volume averaging technique:

$$\Delta\varepsilon_{cr} = \frac{\sum_i^n \varepsilon_{cr2}^i \cdot V_2^i}{\sum_i^n V_2^i} - \frac{\sum_i^n \varepsilon_{cr1}^i \cdot V_1^i}{\sum_i^n V_1^i} \tag{2.34}$$

where ε_{cr2}^i, ε_{cr1}^i is the total accumulated creep strain in one element at the end point and start point of one certain cycle, respectively, V_2^i, V_1^i is the element volume at the end point and start point of one cycle, respectively, and n is the amount of selected elements to calculate averaged creep strain.

ATTENTION: The Singapore Copyright Act applies to the use of this document. Nanyang Technological University Library

Creep strain fatigue model provides a more comprehensive approach because it can consider dwell time and strain amplitude in thermal cycling load. However, one limitation of creep strain fatigue model is the absence of plastic strain effects. Plastic strain effects can be neglected only if the strain rate is low enough, thus resulting in a constant stress-situation and the strain is indeed time dependent.

2.3.2.3 Total strain fatigue models

In this model, total strain including elastic, plastic and creep strain is considered as damage parameter. Sometimes, just inelastic strain including plastic and creep strain is used as fatigue damage parameter. These two cases here are all called total strain fatigue models.

Coffin-Manson equation (2.23) is often combined with the stress-based approach to account for elastic deformation as well. The resulting equation is known as the total strain fatigue model:

$$\varepsilon_a = \varepsilon_{ea} + \varepsilon_{pa} = \frac{\sigma_f^{'}}{E}\left(2N_f\right)^b + \varepsilon_f^{'}\left(2N_f\right)^c \tag{2.35}$$

where all the material constants explanation can be referred to Eq. (2.19) and (2.23).

Engelmaier [48] proposed a solder joint fatigue life prediction model based on the total shear strain range considering thermal cycling loading frequency effect:

$$N_f = 0.5\left(\Delta\gamma_T / 2\varepsilon_f^{'}\right)^{1/c} \tag{2.36}$$

where $c = -0.442 - 6\times10^{-4}\,T_m + 1.74\times10^{-2}\ln(1+f)$, T_m is mean cyclic temperature (°C), f is cyclic frequency ($1 \le f \le 1000$ cycles/day), $2\varepsilon_f^{'} \cong 0.65$ is the fatigue ductility coefficient. The maximum shear strain range, $\Delta\gamma_T$, in the solder joint subjected to thermal cycling can be estimated briefly by equation below:

$$\Delta\gamma_T = \frac{L}{h}\left(\alpha_b - \alpha_c\right)\left(T_{\max} - T_{\min}\right) \tag{2.37}$$

ATTENTION: The Singapore Copyright Act applies to the use of this document. Nanyang Technological University Library

where L is DNP or the distance of the outermost solder joint from the neutral point, h is the height of the solder joint, α_b is the coefficient of the thermal expansion (CTE) of the FR4 PCB, α_c is the CTE of the chip or BT substrate, $T_{\max}$ is the maximum temperature, and $T_{\min}$ is the minimum temperature. This fatigue model improves upon Solomon's and Coffin-Manson models by including cyclic frequency effects, temperature effects, and elastic-plastic strains. However, when package has complicated structure or underfill is used in package, the shear strain calculation based on Eq. (2.37) will result in more errors.

Shi et al. [49] developed a temperature and frequency-dependent fatigue life prediction model using the total strain range in the frequency-modified low cycle fatigue relationship:

$$N_f \nu^{(k-1)} = \left[\frac{C}{\Delta\varepsilon_t} \right]^{\frac{1}{m}} \tag{2.38}$$

It is shown that fatigue life of solder actually follows a different trend when frequencies change over at 10^{-3} Hz, which is expressed as follows [49]:

$$\nu^{(k-1)} = \begin{cases} \nu^{k_1-1} & 10^{-3} \le \nu \le 1Hz \\ \left[\dfrac{\nu}{10^{-3}} \right]^{k_2-1} \left(10^{-3}\right)^{k_1-1} & 10^{-4} \le \nu \le 10^{-3}\,Hz \end{cases} \tag{2.39}$$

where the parameters of k_1, k_2, m and C can be determined by polynomial expression fitting from temperature dependent experimental data, as follows [49]:

$$k_1 = 0.919 - 1.765\times10^{-4}T - 8.634\times10^{-7}T^2 \tag{2.40a}$$

$$k_2 = 0.437 - 3.753\times10^{-4}T - 8.04\times10^{-7}T^2 \tag{2.40b}$$

$$m = 0.731 - 1.63\times10^{-4}T + 1.392\times10^{-6}T^2 - 1.151\times10^{-8}T^3 \tag{2.40c}$$

$$C = 2.122 - 3.57\times10^{-3}T + 1.329\times10^{-5}T^2 - 2.502\times10^{-7}T^3 \tag{2.40d}$$

ATTENTION: The Singapore Copyright Act applies to the use of this document. Nanyang Technological University Library

Practical applications at high temperature often involve both creep and fatigue, and these phenomena may act together in a synergistic manner. One simple approach is to sum the life fractions due to both creep and fatigue. By applying Miner's linear superposition principle, both plastic and creep strain can be accounted for in strain-based fatigue model [29]:

$$\frac{1}{N_f} = \frac{1}{N_p} + \frac{1}{N_c} \tag{2.41}$$

where N_p refers to the number of cycles to failure due to plastic fatigue and is obtained directly from the plastic strain fatigue model, ad N_c refers to the number of cycles to failure due to the creep fatigue and is obtained from the creep strain fatigue model. However, this approach is an approximate method as the physical processes of creep and fatigue can have an interaction effect.

2.3.3 Energy-Based Fatigue Models

The energy-based fatigue model is the newest models in use today, and is based on calculating the overall stress-strain hysteresis energy of solder joint. The Morrow energy-bases fatigue model is widely used for solder joint fatigue life prediction [24]:

$$N_f^m W_p = C \tag{2.42}$$

where m is fatigue exponent, and C is material ductility coefficient. W_p is plastic strain energy density. Typically, the hysteresis loop is observed to stabilize after a few cycles. The plastic strain energy density is determined from the area within the stable hysteresis loop. However, it should be noted that the fatigue life strongly depends on the test frequency at any given strain energy density value. Solomon and Tolksdorf [50, 51] adopted a different approach by introducing a frequency-modified energy-based fatigue model, which incorporates both the frequency-modified strain energy density and the frequency-modified fatigue life, as shown below:

ATTENTION: The Singapore Copyright Act applies to the use of this document. Nanyang Technological University Library

$$\left[N_f \nu^{(k-1)}\right]^m \frac{W_p}{\nu^n} = C \tag{2.43}$$

where v is load frequency, k is a frequency exponent like in Eq. (2.38), and n is another frequency exponent which is determined from the relationship between strain energy density and frequency.

A modified energy-based fatigue model for eutectic SnPb solder was proposed by Shi et al. [42] and given below:

$$\left[N_f \nu^{(k-1)}\right]^m \frac{W_p}{2\sigma_f} = C \tag{2.44}$$

where σ_f is called flow stress which is averaged values of yield point and highest point in the stress-strain curve in a hysteresis loop. The averaged material constants for eutectic SnPb were: m=0.70, C=1.69, (1-k) = 0.1 for $v>10^{-3}$ Hz or (1-k) = 0.59 for $v<10^{-3}$ Hz.

Syed [46] proposed energy-based fatigue models for SnAgCu solder using creep strain energy as fatigue damage parameter based on simulations and test data from different BGA specimens:

$$N_f = (0.0019 W_{cr})^{-1} \tag{2.45}$$

Schubert et al. [47] proposed creep strain energy-based fatigue model for SnPb and SnAgCu using total accumulated creep strain energy by simulations and experiments using PBGA, FCOB with/without underfill as samples:

For SnPb: $$N_f = 210 W_{cr}^{(-1.20)} \tag{2.46}$$

For SnAgCu: $$N_f = 345 W_{cr}^{(-1.02)} \tag{2.47}$$

where W_{cr} from Eq. (2.45) to (2.47) is accumulated creep strain energy density per cycle calculated by volume averaging technique.

ATTENTION: The Singapore Copyright Act applies to the use of this document. Nanyang Technological University Library

Darveaux [26] proposed a solder life prediction model for 62Sn36Pb2Ag solder based on the plastic strain energy density accumulated per cycle. Based on Darveaux's model, the fatigue life consists of two parts, one for crack initiation, and the other for crack propagation. Crack initiation and crack growth are given as follows:

$$N_0 = K_1 \Delta W_{ave}{}^{K_2} \tag{2.48}$$

$$\frac{da}{dN} = K_3 \Delta W_{ave}{}^{K_4} \tag{2.49}$$

where K_1, K_2, K_3, K_4 are constants for all the various modeling methodologies employed. The plastic work unit volume, or plastic strain energy density, ΔW_{ave} is averaged cross the elements along the solder joint surface where the crack initiates and propagates:

$$\Delta W_{ave} = \frac{\sum \Delta W \cdot V}{\sum V} \tag{2.50}$$

Based on the above equations, the fatigue life can be predicted as:

$$N_f = N_0 + \frac{a}{da/dN} \tag{2.51}$$

where a is the solder joint diameter at interface between solder ball and substrate or chip side. This method is sensitive to the mesh size and model form. In order to obtain accurate results, the elements near the interface used to calculate averaged plastic work must be fine enough.

Akay et al. [52] presented a fatigue life model of thermally loaded solder joints based on total strain energy using a volume-weighted average method:

$$N_f = \left(\frac{\Delta \overline{W}_{total}}{W_0} \right)^{1/k} \tag{2.52}$$

where N_f is the mean cycles to failure related to the corresponding experimental data,

ATTENTION: The Singapore Copyright Act applies to the use of this document. Nanyang Technological University Library

$\Delta \overline{W}_{total}$ is total strain energy calculated from the volume-weighted averages over one cycle, W_0 and k are load-independent material constants obtained by a least-squares curve-fitting analyses and W_0 =0.385N·mm and k =-0.8165 were given for eutectic SnPb solder. It was conclusion that the energy criterion is more accurate than the maximum strain range criterion since the strain energy contains both stress and strain information, the effects of cycle period, hold time, and strain rate are more directly represented in the hysteresis loop. In addition, total strain energy includes the effects of geometry and volume of solder joint and becomes a more reliable parameter for the prediction of fatigue life.

Numerous solder fatigue models have been developed from publications. However, how to apply these models to predict accurate fatigue life and how these models affect on solder fatigue life are not discussed from existing literature. In Chapter 4, discussion on solder fatigue life prediction using different fatigue models are presented. In addition, new averaging volume was proposed for solder fatigue life prediction. The IMC effect on solder fatigue life was also investigated for the first time.

2.3.4 Fracture Mechanics Approach

Many failures in electronic products exhibit the crack fracture of the interface between solder and substrate or chip. Many researchers [53-56] studied this phenomenon by observing microstructures of solder joint using Scanning Electron Microscope (SEM).

At high stress/strain amplitude, initiation life may be relatively short compared to propagation life. Propagation life is determined in terms of fatigue crack growth rate of *da/dN*, which is related to stress intensity factor range, ΔK_I. The Paris law, a power law relationship, is frequently used to determine *da/dN*:

$$\frac{da}{dN} = C(\Delta K_I)^m \tag{2.53}$$

ATTENTION: The Singapore Copyright Act applies to the use of this document. Nanyang Technological University Library

where C and m are constants which are influenced by material properties, temperature, environment, cyclic load frequency, waveform and load ratio, $\Delta K = F\Delta S\sqrt{\pi a}$ and F is a dimensionless function of geometry. The value of the stress ratio R affects the growth rate in a manner analogous to the effects observed in S-N curves for different values of R or mean stress. Therefore, fatigue life can be estimated for constant amplitude loading by integrating above equation:

$$N_{if} = \int_{ai}^{af} \frac{da}{C(\Delta K)^m} = \int_{ai}^{af} \frac{da}{C\left(F\Delta S\sqrt{\pi a}\right)^m} = \frac{a_f^{1-m/2} - a_i^{1-m/2}}{C\left(F\Delta S\sqrt{\pi}\right)^m\left(1-\frac{m}{2}\right)}, (m \neq 2) \quad (2.54)$$

where N_{if} is fatigue life of crack propagating from a_i of initial crack length to a_f of final crack length.

2.4 SOLDER JOINT RELIABILITY TESTS

Reliability tests of electronic assemblies are very important concerns to ensure long-term reliability of electronic products. In service, electronic products failures can occur within a year but often much longer. Therefore, it is not practical to test at service load level and it is uneconomical with respect to test time and cost. Accelerated life testing (ALT) methods are employed for the purpose of accelerating reliability test results.

Reliability tests aim at revealing and understanding the physics of failure. Another objective of reliability tests is to accumulate representative failure statistics [57]. Accelerated tests use elevated stress levels and/or higher stress-cycle frequency to precipitate failures over a much shorter time. Stress loading includes constant stress, step stress, progressive stress and random stress [58]. Typical accelerating stresses are temperature, mechanical load, thermal cycling or thermal shock, cyclic bend, drop impact and vibration. Such tests can facilitate physics of failure for reliability tests that

ATTENTION: The Singapore Copyright Act applies to the use of this document. Nanyang Technological University Library

cost effectively, shorten the product process and improve long-term product reliability.

Accelerated tests can be performed at any level, such as part level, component level, board level, equipment level and system level. The degree of stress acceleration is usually determined by an acceleration factor. This factor is defined as the ratio of lifetime under normal service conditions to the lifetime under accelerated conditions.

2.4.1 Accelerated Thermal Cycling (ATC) Test

When accelerated thermal cycling (ATC) tests were carried out, the acceleration factor (AF) given by Norris and Landzberg [59] has been used to relate test conditions to field conditions for lead based solder:

$$AF = \left(\frac{\Delta T_t}{\Delta T_f}\right)^{1.9} \left(\frac{f_f}{f_t}\right)^{1/3} \exp\left[1414\left(\frac{1}{T_{\max.f}} - \frac{1}{T_{\max.t}}\right)\right] \tag{2.55}$$

where $\Delta T_t, \Delta T_f$ are temperature ranges at test and field conditions; f_t, f_f are the cyclic frequencies at test and field conditions; $T_{max.t}$, $T_{max.f}$ are the highest temperature in K at test and field conditions, respectively. When the accelerated factor, AF, is determined and reliability test data are known, the life distribution, reliability function, and failure rate for field condition can be calculated using best-fit Weibull life distribution model considering linear acceleration case in which the Weibull plots of the field condition and testing condition have the same Weibull slope [60]:

$$F_f(x_f) = 1 - \exp\left(-\left(x_f / AF \cdot \theta_t\right)^{\beta_t}\right) \tag{2.56a}$$

$$R_f(x_f) = \exp\left(-\left(x_f / AF \cdot \theta_t\right)^{\beta_t}\right) \tag{2.56b}$$

$$h_f(x_f) = \left(\beta_t / AF \cdot \theta_t\right)\left(x_f / AF \cdot \theta_t\right)^{\beta_t - 1} \tag{2.56c}$$

where x_f, F_f, R_f, and h_f are time-to-failure, life distribution, reliability function and failure rate at field condition, respectively, β_t, θ_t are shape parameter and characteristic life at testing condition, respectively, and AF is accelerated factor.

ATTENTION: The Singapore Copyright Act applies to the use of this document. Nanyang Technological University Library

The two common ATC tests for solder joint reliability used in industry are the thermal cycling (TC) [61] and thermal shock (TS) [62] tests. TC has a ramp rate varying from 8°C/min to 33°C/min, whereas TS condition has a ramp rate between 33°C/min and 55°C/min. Dwell time is included at the cycle extremes to allow for creep and stress relaxation process to take place. Different temperature ranges are shown in Table 2-2 for different service environments for electronic products.

Table 2-2 Thermal environments for electronic products.

Use condition	Temperature range (°C)
Consumer Electronics	0 to 60
Telecommunications	-40 to 85
Commercial Aircraft	-55 to 95
Military Aircraft	-55 to125
Space	-40 to 85
Automotive-Passenger	-55 to 65
Automotive-Under the Hood	-55 to 150

2.4.2 Bend Test

Bend load is commonly encountered load for electronic devices, especially for handhold products, such as mobile phone, PDA, MP3, when consumers press the keypad. Two commonly used bend tests are three-point and four-point bend tests with cyclic or monotonic load. Cyclic bend test can evaluate the fatigue reliability of electronic package, while monotonic bend test is intended to characterize the fracture strength of electronic interconnection. Three-point bend test is an ideal choice for generating reliability model because multiple packages can be tested under multiple load levels in a single test. While four-point bend test is an ideal choice for testing a large sample size of packages because packages between loading span will subject to same stress level due to pure bending condition.

ATTENTION: The Singapore Copyright Act applies to the use of this document. Nanyang Technological University Library

Shetty et al. [63, 64] had conducted cyclic three-point bend tests from zero curvature to maximum curvature for Chip Scale Packages (CSP) mounted on both sides of PCB. Before cyclic bend test, overstress monotonic three-point bend test was conducted to determine the overstress limits for CSP assembly. Fatigue life and fracture of solder joints of a stacked CSP under three-point bending load have been investigated by Wu et al. [65] and parametric study, such as PCB and Substrate thickness effect on fatigue life were also reported. Skipor and Leicht [66] conducted mechanical bending fatigue test for BGA and wafer level CSP by introducing new support method, which was, the specimen was suspended at three simply hinged support points and load cell was centrally located over the specimen center. Mercado et al. [67] introduced four-point bend fixture with capability of two-sided bend test from positive to negative deflections and investigated the effect of loading frequency of 1Hz, 3Hz and 5Hz and deflection levels of 1.5mm, 2mm, 3mm, and 4mm on fatigue reliability of handheld components. Correlation between four-point and three-point bend was also developed by Mercado et al. [67]. Geng et al. [68] conducted effect of strain rate on PBGA solder joint reliability using four-point bend test with three different loading speeds of 2.54mm/min, 25.4mm/min and 254mm/min. All bend tests were conducted at room temperature from existing literature. In this study, the cyclic bend tests were conducted for the first time at high temperature of 125°C to investigate the temperature accelerating factor for solder joint bending fatigue (see Chapter 5).

2.4.3 Drop Impact Test

Reliability testing of soldered assemblies subjected to drop impact is critical, especially for handhold or portable telecommunication devices such as mobile phone and Personal Digital Assistant (PDA) because these products are prone to accidental drop resulting in failure. Drop tests are increasingly required for personal electronic

ATTENTION: The Singapore Copyright Act applies to the use of this document. Nanyang Technological University Library

products. There are mainly three types of drop tests in the electronic industry: (a) free fall product level; (b) free fall board level; and (c) controlled pulse drop at board level. Board level drop test is convenient to characterize the solder joint performance, as it is more controllable than product level drop test. Some researchers had conducted board level drop tests to understand the response of solder joint to impact loading using different boundary conditions such as 4 or 6 screw support [69, 70], clamped-clamped boundary condition [71, 72] and free fall drop [73, 74]. Some researchers [75, 76] had conducted product level drop tests due to real drop events. The maximum acceleration of PCB can reach to more than 1000G when subjected to drop impact, but the displacement and strain of the PCB is relatively small. Suhir [77] stated that it is dynamic stress, not the acceleration, which is a true criterion of the dynamic strength. Keltie and Falter [78] proposed an approximate method to simulate different parameters effects, such as mass ratio, stiffness ratio, pulse width ratio, and rotational stiffness ratio, on response analysis of electronic assemblies using a simple structure consisting of a mass attached to a beam.

Lead-free solder usually exhibits less drop impact life than lead-based solder from many test results [70, 72]. Amagai et al. [79, 80] proposed that the number of drop to failure decreased with Ag content increasing for SnAgCu solder and the drop failure performance could be improved by adding some optimum Indium and Nickel to SnAgCu solder.

2.4.4 Vibration Test

Vibration test is intended to evaluate and determine the ability of electronic components to withstand vibration load as a result of motion produced by transportation or field operation. There are two methods for delivering vibration energy to units under tests by electrodynamic shakers and repetitive shock machines.

ATTENTION: The Singapore Copyright Act applies to the use of this document. Nanyang Technological University Library

Sinusoidal vibration is useful in the test laboratory, but will not be encountered in the real world. This sine vibration test is mainly used to perform modal investigations. Random vibration has instantaneous magnitudes that cannot be predicted. When a structure receives a broad-spectrum vibration, all of its modal states will be excited simultaneously. There are two major reasons for using random vibration for testing purpose [4]: (1) random vibration is more representative of the real service loading, and (2) simultaneous excitation of all resonance is much more likely to reveal design or manufacturing flaws.

Generally, the linear system is implemented when making a numerical simulation of dynamic response of electronic packaging. This assumption can give rise to errors at some conditions. He and Fulton [81] proposed a nonlinear laminated theory applicable for PCB dynamic response modeling and analysis. Nonlinear phenomena were found in harmonic vibration test using clamped-clamped boundary condition by Che et al. [82] for FCOB assemblies, by Perkins and Sitaraman [83] for CCGA assemblies and by Yang et al. [84] for PBGA assemblies.

Under vibration testing, fatigue failure is the predominant failure mechanism in solder joints. High-cycle fatigue life prediction method using stress or strain as damage parameter was employed to predict the fatigue life of soldered electronic assemblies under vibration load [37, 85, 86].

In this study, a new vibration fatigue test method using constant G-level tests to predict variable G-level test results was proposed. A quasi-static analysis method has been developed to calculate the solder joint stress strain behavior.

ATTENTION: The Singapore Copyright Act applies to the use of this document. Nanyang Technological University Library

CHAPTER 3 FEA CALIBRATION STUDIES

3.1 INTRODUCTION

The finite element method (FEM) developed from advances in aircraft structural analysis, where the term of finite element was first used by Clough [87]. The basis of the finite element method is the representation of a structure by an assemblage of subdivisions called finite elements. These elements are considered interconnected at joints, which are called nodes or nodal points. Shape functions are chosen to approximate the distribution or variation of the displacements over each finite element.

A variational principle of mechanics, such as the principle of minimum potential energy, is usually used to obtain the set of equilibrium equations. The equilibrium equations of the entire body are then obtained by combining the equations for the individual elements in such a way that continuity of displacements is preserved at the interconnecting nodes. These equations are modified for the given displacement boundary conditions and then solved to obtain the unknown displacements. When the displacements are known, the strain and stress can then be calculated.

3.2 REVIEW OF FEA MODELING FOR SOLDER JOINTS

Manufacturers of electronic products face with demands for design with high reliability and performance at lower costs. Computational modeling can reduce the product development time to market in a competitive electronic product sector. Commercial finite element analysis (FEA) software, such as ANSYS, ABQUS, MARC, and NASTRAN, have been used extensively to simulate reliability test, design

ATTENTION: The Singapore Copyright Act applies to the use of this document. Nanyang Technological University Library

and service operation loads on electronic components, board assemblies and product systems. By using FEA simulations, industry can minimize the requirement for extensive and time-consuming physical testing. This can reduce product development costs, increase reliability and reduce the product time to market.

Further miniaturizations of IC component size and higher I/O counts are expected trends in electronic packaging applications. Thus, conventional application of finite element modeling technique will become more difficult as the geometry features become smaller and require higher number of elements so that FEA simulation will require higher speed computing, larger memory size and hard disk storage space. These critical requirements can limit the use of full 3D model applications for finite element reliability analysis of the electronic assemblies. In order to reduce the element size in the FEA simulation for solder joint reliability, some reduced models were used by researchers, including slice model [13, 88, 89], one-eighth model [13, 29, 54, 89-92], and 2D model [88, 89]. Some trade-off in accuracy is expected in these simple models. In this study, a global-local modeling technique was developed. The coarse-mesh global model was used to model the 3D effect while the fine-mesh local model was used to compute accurate results for the desired elements for the solder joints.

Cheng et al. [93] proposed a three-dimensional local model with equivalent beam for ball grid array (BGA) packaging. Two types of equivalent beams with different cross sections were investigated. One was a solid round beam; the other was thin-walled round pipe with a uniform thickness. Yuan and Chiang [94] proposed an equivalent beam method based on the micro-macro technique with multi-point constraint method for thermomechanical simulation of wafer level packaging in order to significantly reduce the simulation CPU time. The used equivalent beam consists of three/five sections to simulate the three-dimensional solder joint with different

ATTENTION: The Singapore Copyright Act applies to the use of this document. Nanyang Technological University Library

upper/lower pad size and the total length of beam is equal to the stand-of-height of the realistic solder joint. An effective finite element method was proposed by Yu et al. [95] to analyze the stress of the leads and the solder joints in the surface-mount assembly (SMA) using an influence function method to obtain the stiffness matrix of the solder joints. The global-local modeling method with coarse global model and fine submodel was reported by researchers [7, 91, 96, 97] for BGA assemblies subjected to thermal or mechanical loadings. Some simplified models for stress-strain analysis of BGA assemblies subjected to thermal cycling or vibration loads, where the solder connections were considered as an effective beam element with stiffness, were employed by researchers [98, 99].

3.3 GLOBAL-LOCAL MODELING TECHNIQUE

In this study, the ANSYS FEA software [22] was used to simulate the board-level assembly model. For the board-level simulation, an efficient modeling method is required intensively because many components are attached on the board or substrate. The global-local model is a good choice for this simulation. In this study, two types of global-local models were introduced. One is submodeling, in which a coarse global model was used to simulate the whole model and the fine local model was used to simulate the critical area of the whole model. The other is global-local-beam (GLB) model, in which the interconnections were replaced by an equivalent beam with effective stiffness based on classical beam theory. The results from global-local model simulation were compared to those from full 3D model simulation for calibration of global-local modeling method. The detailed procedure and calibration of submodeling and GLB model were developed in the following sections. The development work for global-local modeling was summarized in Fig. 3-1.

ATTENTION: The Singapore Copyright Act applies to the use of this document. Nanyang Technological University Library

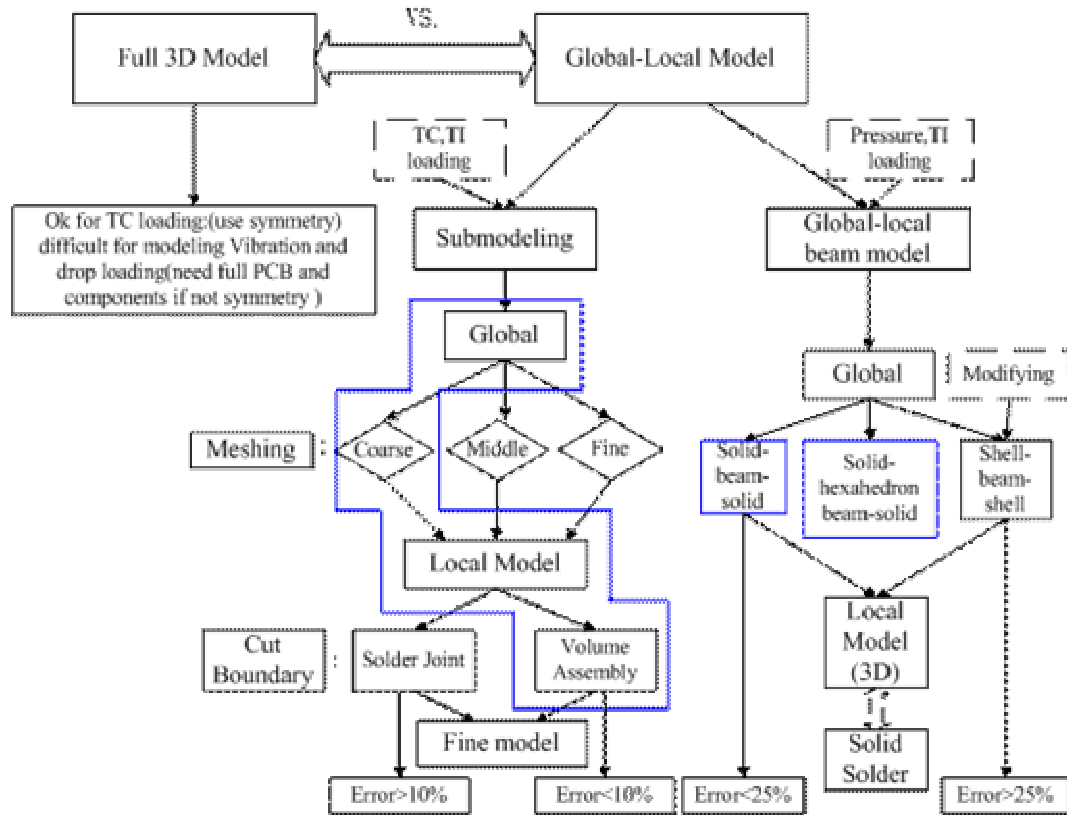

Fig. 3-1 Flowchart for global-local modeling technique.

3.3.1 Submodeling Method

Submodeling is a FEA technique used to get more efficient results in a local region of model. The global finite element mesh may be coarser to produce satisfactory results at a region of interest such as a stress concentration region. To obtain more accurate results in such case, there are two options: (a) reanalyze the entire model with greater mesh refinement but this will cause the model too large and costly to solve, (b) use submodeling technique to generate an independent submodel in region of interest and transfer the effective loading from the global to the submodel.

Submodeling is also known as the cut-boundary displacement method. The cut boundary is the boundary of the submodel, which represents a cut through the coarse global model. Displacements calculated on the cut boundary of the coarse global model are transferred as boundary conditions to the fine submodel. Submodeling

ATTENTION: The Singapore Copyright Act applies to the use of this document. Nanyang Technological University Library

technology is based on St. Venant's principle, which states that if an actual distribution of forces is replaced by a statically equivalent system, the distribution of stress and strain is altered only near the regions of load application. This implies that stress concentration effects are localized around the concentration; therefore, if the boundaries of submodel are far enough away from the stress concentration, reasonably accurate results can be calculated in the submodel.

Aside from the obvious benefit of giving more accurate results in a region of model, the submodeling technique can reduce, or even eliminate, the need for complicated transition regions in solid finite element models. The procedure for submodeling consists of the following steps:

1. Create and analyze the coarse global model for the entire structure.

2. Create the submodel for the region of interest. The location of the submodel must be the same as the corresponding portion of the global model with respect to the global origin.

3. Perform cut boundary interpolation. This is the key step in submodeling. The nodes along the cut boundaries firstly are identified and then the program calculates the degree of freedom (DOF) values at those nodes by interpolating global model results. For each node of the submodel along the cut boundary, the program uses the appropriate element from the coarse mesh to determine the DOF values. These values are interpolated onto the cut boundary nodes using the element shape functions.

4. Analyze the submodel. In this step, analysis type and options were defined, the interpolated DOF values were applied onto cut boundary, other loads, boundary conditions and load step options were specified, then submodel was solved.

5. Verify that the distance between the cut boundaries and the stress concentration is adequate.

ATTENTION: The Singapore Copyright Act applies to the use of this document. Nanyang Technological University Library

3.3.2 Comparison of Submodel to Fine 3D Model Results

In this study, submodeling was developed using the flip chip on board (FCOB) assembly as FEA calibration study. The geometry size mismatch among FCOB assemblies gives rise to more difficulties in numerical modeling. So the submodeling technique is a good choice to reduce the model size significantly.

Before using submodeling technology, the verification was first conducted to validate the feasibility and accuracy of submodeling as well as the appropriate cut boundary. The silicon chip or die was connected onto PCB by four corner solder balls as shown in Fig. 3-2 for benchmark study in order to reduce element size. The chip size is 8.5mm×8.5mm×0.65mm. For calibration study, the material of 62Sn36Pb2Ag was selected for solder joint with a standoff height of 0.1mm. The FR-4 PCB has the size of 30mm×10mm×1.13mm. In order to determine the underfill effect on the fatigue life of the electronic product, two cases are studied including FCOB assembly with and without underfill between the die and PCB. In order to simplify the analysis, the fillet of the underfill is not considered, that is, underfill only locates underneath the die. For convenient, copper pad and UBM material used in actual FCOB assembly are not considered because of just validation study for submodeling technique.

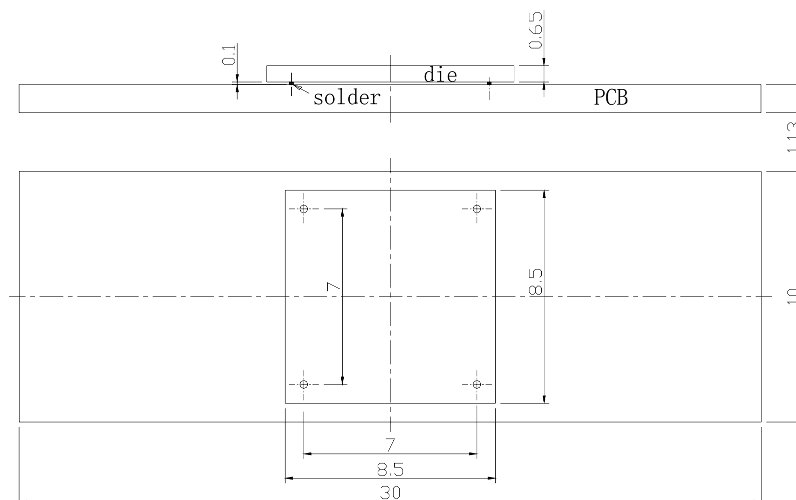

Fig. 3-2 Geometry size of the specimen for FEA calibration study (unit in mm).

ATTENTION: The Singapore Copyright Act applies to the use of this document. Nanyang Technological University Library

3.3.2.1 FCOB assembly without underfill subjected to temperature increment

In this section, the main purpose was to find the reasonable cut boundary and compare the results between the submodel and conventional full 3D model. The full 3D model was considered as a reference model, or benchmark model. When the results from submodel agreed with those from reference model, the submodel and corresponding cut boundary were regarded satisfactory. The temperature increment of 20°C was applied to the FCOB assembly firstly to obtain the appropriate grid size and cut boundary condition. Due to the symmetry, only the quarter part of the assembly was modeled in order to reduce the element size without losing accuracy.

The 3D quarter meshed models are shown in Fig. 3-3. The fine model as shown in Fig. 3-3(a) could give the accurate results, so it was used as a reference model in which the grid size was considered as standard grid size. The medium model with 2 times standard grid size and coarse model with 3 times standard grid size are shown in Fig. 3-3(c) and (b), respectively. All the materials were assumed having elastic behavior. For calibration study, displacement and stress in the solder joint interfaces were selected as the compared items. The displacement results of the center nodes on the solder/die interface labeled as T (top), and solder/substrate interface labeled as B (bottom), are shown in Fig. 3-4 for different models, where the label of F, M, and C represent fine, medium, and coarse models as shown in Fig.3-3, respectively. The mark of R in Fig. 3-4 indicates the relative displacements of the center nodes on the top and bottom interfaces. The displacement component, labeled as Abs_R, was obtained from the following equation:

$$Abs_R = \sqrt{UX_R^2 + UY_R^2 + UZ_R^2} \tag{3.1}$$

where UX_R, UY_R and UZ_R are relative displacement between center nodes of top and bottom interfaces in x, y and z direction, respectively.

ATTENTION: The Singapore Copyright Act applies to the use of this document. Nanyang Technological University Library

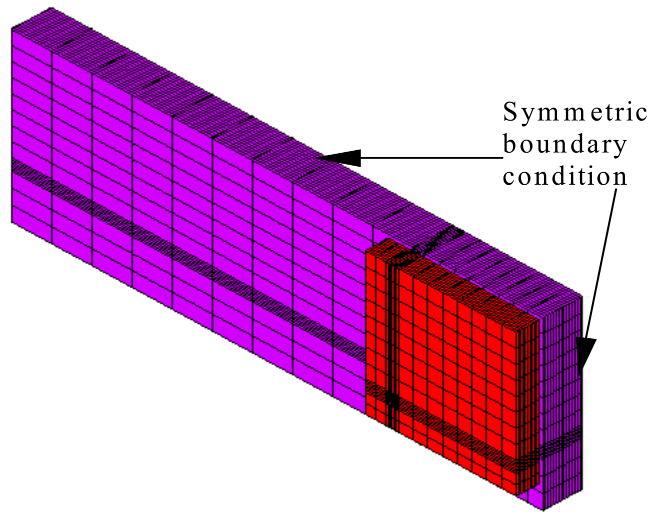

a) Fine model (F)

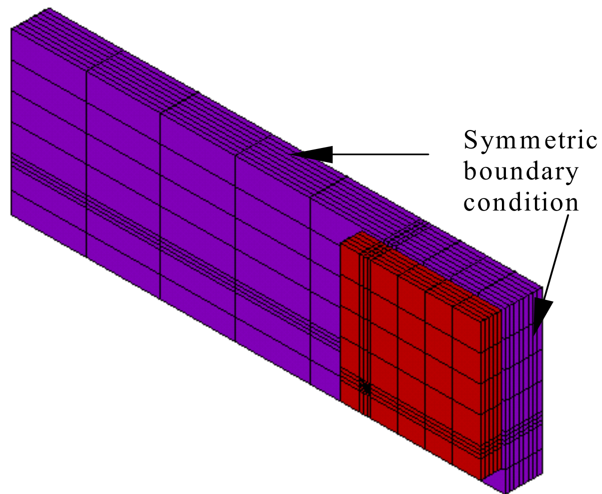

b) Medium model (M)

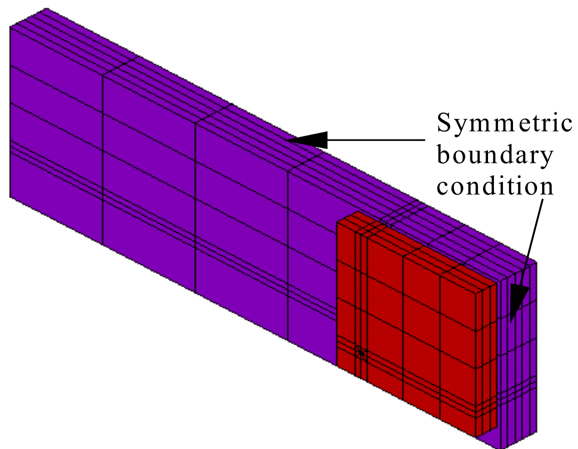

c) Coarse model (C)

Fig. 3-3 Different 3D FEA models.

ATTENTION: The Singapore Copyright Act applies to the use of this document. Nanyang Technological University Library

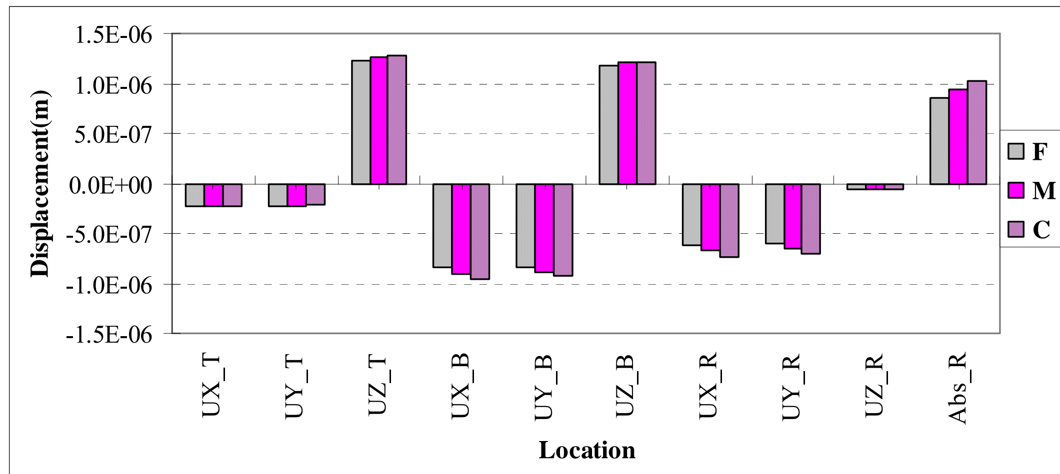

Fig. 3-4 Displacement of centre point on the solder interfaces from different models.

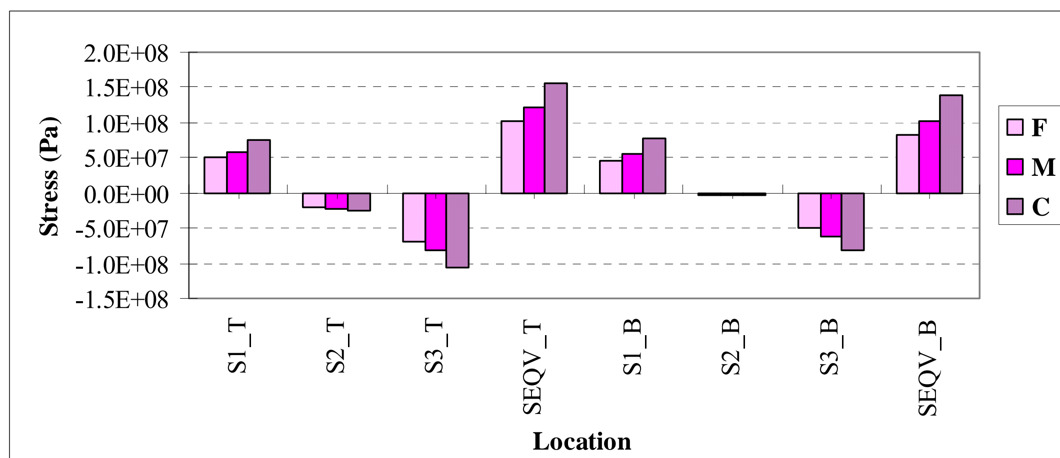

Fig. 3-5 Stress of centre point on the solder interfaces from different models.

It can be seen from the Fig. 3-4 that displacement increases with the grid size increasing. It means that the coarser the model, the lower the accuracy. The stress results for different models are shown in Fig. 3-5. It can be seen that the changing trend of the stresses for different models is the same as that of displacements. Therefore, finely meshed model is required for the traditional FEA model in order to obtain accurate results. When the model is very complicated, FEA simulation becomes difficult because more elements and computational resource are required. Therefore, the submodeling technique is a good choice for this problem.

According to the procedure of the submodeling technology mentioned above, the

ATTENTION: The Singapore Copyright Act applies to the use of this document. Nanyang Technological University Library

submodel was used to simulate the same specimen as shown in Fig. 3-2. The models shown in Fig. 3-3(b) and (c) were chosen as the global model which was solved to obtain DOF results. After that, the displacement interpolation was conducted. Two types of cut boundary were selected as shown in Fig. 3-6 to determine the reasonable cut boundary. Fig. 3-6(a) shows hybrid submodel with a cut boundary far enough away from solder joint interfaces and Fig. 3-6(b) shows a submodel of solder ball. The grid size of the submodel is same as that the fine 3D model as shown in Fig. 3-3(a).

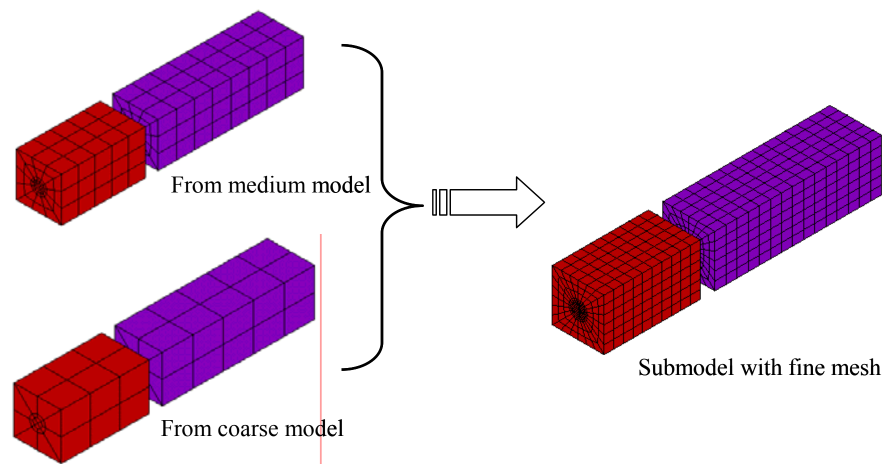

(a) Hybrid submodel (Die + Solder ball + PCB).

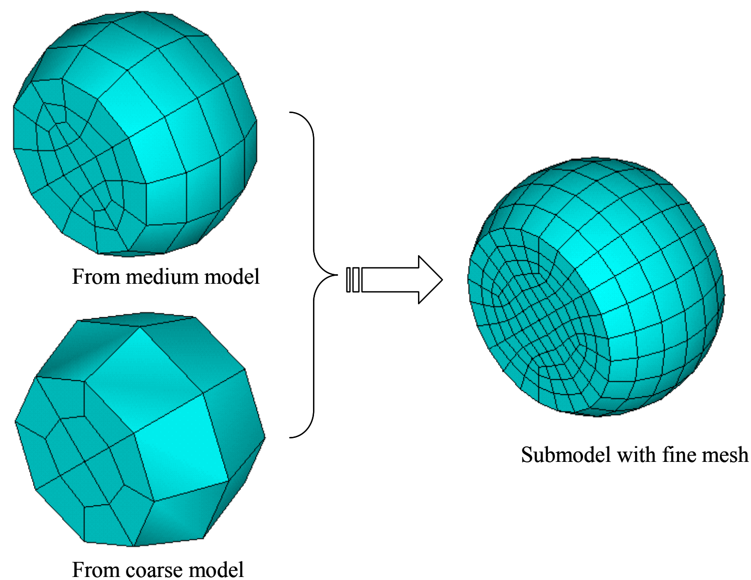

(b) Solder ball submodel.

Fig. 3-6 Displacement interpolation on cut boundary for different submodels.

ATTENTION: The Singapore Copyright Act applies to the use of this document. Nanyang Technological University Library

The DOF values (displacements) at nodes along the cut boundaries of submodel as shown in the right hand side of Fig. 3-6 were calculated by interpolating results from the global model as shown in the left hand side of Fig. 3-6. Then the submodel was analyzed. The results from submodel were compared with those from the fine 3D model. The Von Mises stress was compared because it is commonly used in the reliability analysis of the electronic assembly. The stress comparisons between the fine model and submodel with hybrid cut boundary of Fig. 3-6 (a) are shown in Fig. 3-7, where the legends of submodel_M and submodel_C indicate that interpolating DOFs were obtained from the medium global model of Fig. 3-3(b) and coarse global model of Fig. 3-3(c), respectively. It can be seen that the results from the submodel agree with those from fine 3D model very well. Submodels with DOFs interpolation from global models with different grid sizes induce close results, which means that the submodeling method is less mesh sensitive than full 3D model. Therefore, coarse global model can be used so that element size and computational time can be saved.

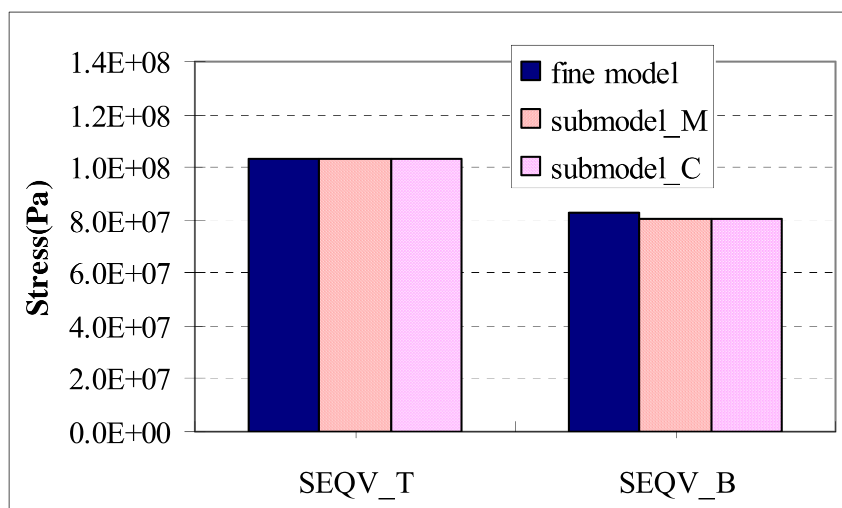

Fig. 3-7 Result comparison between fine model and hybrid submodels.

The result comparisons between the fine 3D model and submodel with the cut boundary of Fig. 3-6(b) are shown in Fig. 3-8. The difference between submodel and fine 3D model is distinct and significant. Therefore, the cut boundary in Fig. 3-6(a) can

ATTENTION: The Singapore Copyright Act applies to the use of this document. Nanyang Technological University Library

lead to better results than that in Fig. 3-6(b). Usually, cut boundary width for hybrid submodel equals the pitch of the solder joints.

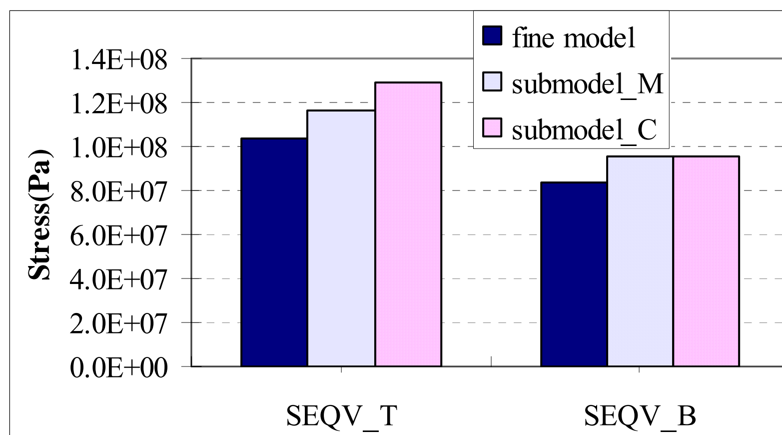

Fig. 3-8 Result comparison between fine model and solder ball submodel.

Some conclusions can be obtained from the above analyses. Firstly, for FCOB without underfill, the submodeling technique can induce the accurate results so that elements size and computational time, as listed in Table 3-1, can be reduced significantly. Secondly, the cut boundary of submodel has a great effect on the results, so it is very important to select reasonable and suitable cut boundary. Usually, for BGA or FCOB assemblies, the appropriate submodel contains a whole solder joint, component and substrate on one pitch-width volume. Finally, the submodel technique has a less mesh sensitivity compared to full 3D model. Thus, submodeling method allows users to conduct the FEA simulation with less elements size without losing accuracy.

Table 3-1 Comparison between fine model and submodel for FCOB without underfill.

Items		Elements	Nodes	Computational Time (minutes)
Submodeling	Coarse Model (1)	530	793	3.3
	Submodel (2)	5148	5816	109
Fine 3D Model (3)		12928	14872	300
Factor (3)/(1+2)		2.28	2.25	2.67

ATTENTION: The Singapore Copyright Act applies to the use of this document. Nanyang Technological University Library

3.3.2.2 FCOB assembly without underfill subjected to thermal cycling

In reliability test and service operation, electronic assemblies are usually subjected to thermal cycling load. Solder fatigue is the main failure mechanism resulting from thermal cycling where cyclic stresses or strains occur in the solder joints. In this section, the solder joints were modeled with viscoplastic material properties while the other parts of the FCOB assembly remained elastic. The PCB was assumed to exhibit orthotropic material properties. The elastic modulus of solder was temperature dependent while other materials were assumed with constant properties as given in Table 3-2.

Table 3-2 Materials properties of FCOB assembly without underfill.

Materials	Young's Modulus (GPa)	Shear Modulus (GPa)	Poisson's Ratio	CTE (ppm/°C)
PCB (FR-4)	$E_x=E_y=22$ $E_z=9.8$	$G_{xy}=3.5$ $G_{xz}=G_{yz}=2.5$	$\nu_{xy}=0.11$ $\nu_{xz}=\nu_{yz}=0.28$	$\alpha_x=\alpha_y=18$ $\alpha_z=50$
Die (Si)	131	-	0.3	2.3
Solder (62Sn36Pb2Ag)	75.97-0.152T (K)	-	0.35	24.5

ANSYS has an option for viscoplastic analysis using Anand's model to describe rate-dependent material behavior with Visco107 element, for three-dimensional large strain solid model. Anand's constitutive model is expressed by a flow and three evolution equations:

Flow equation:

$$\frac{d\varepsilon_p}{dt} = A\left[\sinh\left(\frac{\xi\sigma}{s}\right)\right]^{1/m} e^{(-Q/kT)} \tag{3.2}$$

Evolution Equations:

$$\frac{ds}{dt} = \left\{h_0\left(|B|\right)^a \frac{B}{|B|}\right\} = \frac{d\varepsilon_p}{dt} \tag{3.3}$$

ATTENTION: The Singapore Copyright Act applies to the use of this document. Nanyang Technological University Library

$$B = 1 - \frac{s}{s^*} \tag{3.4}$$

$$s^* = s\hat{}\left(\frac{1}{A}\frac{d\varepsilon_p}{dt}e^{Q/kT}\right)^n \tag{3.5}$$

Darveaux [26] reported the solder joint life prediction based on the plastic work dissipated in crack initiation and crack propagation to failure. Darveaux also proposed that the calculated strain energy density increases as element size in the solder joint decreases. Hence a volume weight technique was used to reduce this sensitivity to meshing. The averaged viscoplastic work density accumulated per cycle for the interface elements, ΔW_{ave}, can be calculated by following equation:

$$\Delta W_{ave} = \frac{\sum \Delta W \cdot V}{\sum \Delta V} \tag{3.6}$$

where ΔW is the viscoplastic work density per cycle of each element, and V is the volume of each element. The values of ΔW and V can be obtained in ANSYS FEA simulation and are important parameters in calculation of fatigue life.

Table 3-3 Anand's constants for 62Sn36Pb2Ag solder [26].

ANSYS	Parameter	Definition	Value
C1	S_0 (MPa)	Initial value of deformation resistance	12.41
C2	Q/k (K)	Q = Activation energy, k = Boltzmann's constant	9400
C3	A	Pre-exponential factor	4.0e6
C4	ξ	Multiplier of stress	1.5
C5	m	Strain rate sensitivity of stress	0.303
C6	h_0 (MPa)	Hardening / softening constant	1379
C7	s^ (MPa)	Coefficient for deformation resistance saturation value	13.79
C8	n	Strain rate sensitivity of saturation (deformation resistance) value	0.07
C9	a	Strain rate sensitivity of hardening or softening	1.3

ATTENTION: The Singapore Copyright Act applies to the use of this document. Nanyang Technological University Library

The temperature profile as shown in Fig. 3-9 specifies the temperature range from –40°C to 125°C. Two thermal cycles were simulated in the FEA for validation of submodeling technique. The stress free state condition of the thermal cycling load is room temperature (25°C). The fine 3D quarter model as shown in Fig. 3-3(a) was used as a reference model. For submodeling simulation, the global model of Fig. 3-3(c) and submodel of Fig. 3-6(a) were used. The cut boundary interpolation for the multiload steps simulation in DOF interpolation steps was performed by code programming so that the DOF interpolation can be carried out automatically and correctly.

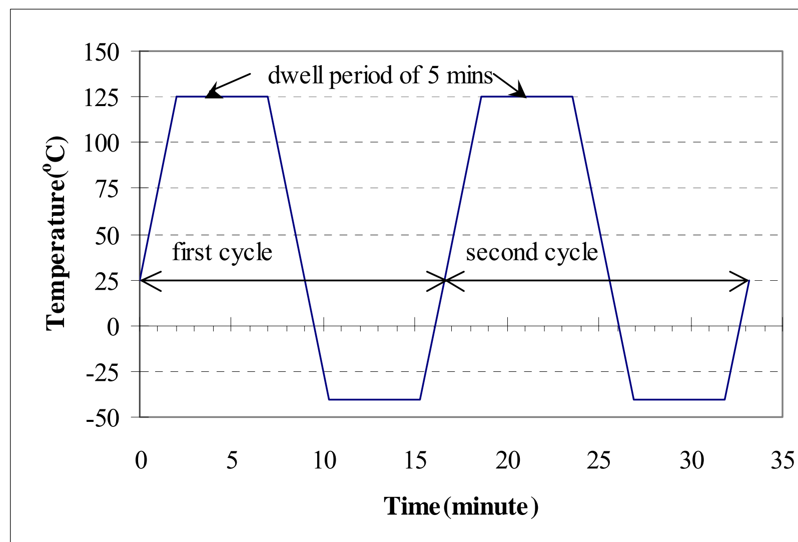

Fig. 3-9 Thermal cycling profile.

The equivalent elastic strain, plastic strain and plastic work density extracted form the center node on the solder/die interface were compared as shown in Fig. 3-10, Fig. 3-11 and Fig. 3-12, respectively. It can be seen from Fig. 3-10 to Fig. 3-12 that submodel results have a very good consistency with fine 3D model results for the FCOB assembly without underfill case. It also can be seen from Fig. 3-10 and Fig. 3-11 that the plastic strain is dominant compared with elastic strain when the solder joint is considered as viscoplastic material under thermal cycling, which accelerates the failure of solder joint.

ATTENTION: The Singapore Copyright Act applies to the use of this document. Nanyang Technological University Library

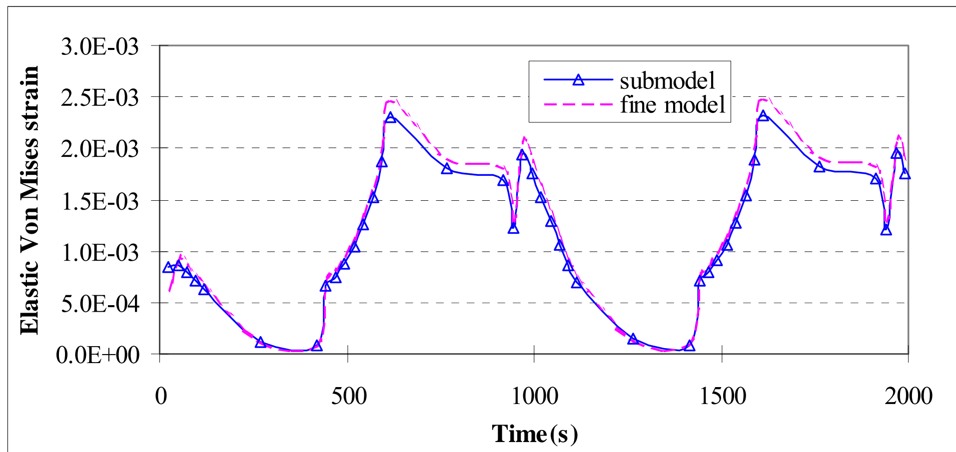

Fig. 3-10 Equivalent elastic strain comparison between fine 3D model and submodel.

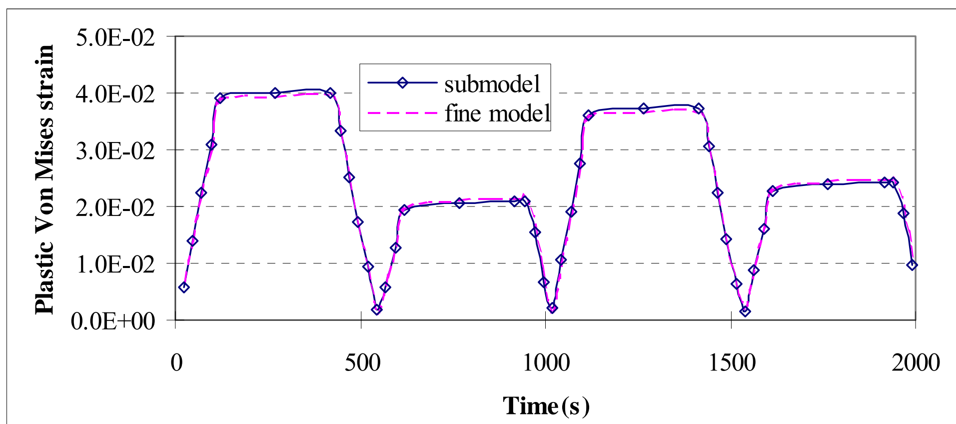

Fig. 3-11 Equivalent plastic strain comparison between fine 3D model and submodel.

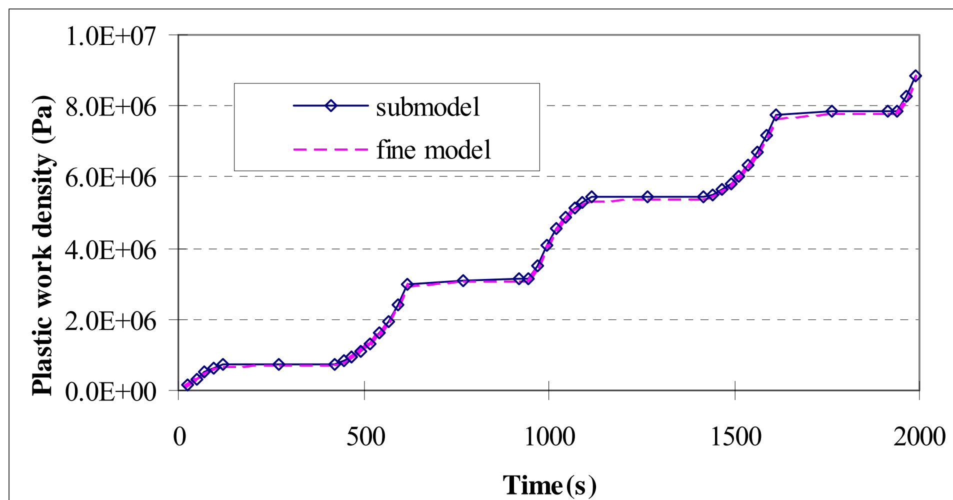

Fig. 3-12 Plastic work density comparison between fine 3D model and submodel.

ATTENTION: The Singapore Copyright Act applies to the use of this document. Nanyang Technological University Library

The average plastic work density accumulated per cycle was calculated according to Eq. (3.6). Table 3-4 lists the volume-averaged plastic work density for different models. Some conclusions can be obtained from the Table 3-4. Firstly, the submodel can induce more accurate results than one-level coarse model, and it can save more computational resource compared with fine 3D model. Secondly, the volume-averaged plastic strain energy density in the die side is higher than that in PCB side, so the first failure site in solder joints is often close to interface between solder joint and die.

Table 3-4 Plastic work density comparisons for different models*.

Element location		Solder/die interface	Solder/PCB interface
Fine Model	ΔW_{ave} (MPa)	6.19	5.61
Submodel	ΔW_{ave} (MPa)	6.22	5.55
	Difference	0.44%	-1.02%
Coarse model	ΔW_{ave} (MPa)	5.28	5.29
	Difference	-14.75%	-5.70%

* For nonunderfill specimen

3.3.2.3 FCOB assembly with underfill subjected to thermal cycling

In FCOB assembly, underfill encapsulation is used to improve the solder joint reliability. The submodeling technique developed earlier for FCOB assembly without underfill was applied to the case with underfill. The material properties are same as those given in Table 3-2 with the addition of the underfill material. In the FEA simulation, underfill was assumed to exhibit the elastic behavior. Chen et al. [100] had conducted the study on effect of underfill material properties on thermomechanical behaviors of flip chip package by considering three cases: elastic underfill with constant Young's modulus and CTE, elastic underfill with temperature dependent Young's modulus and CTE, and underfill with viscoelastic behavior. They concluded from FEA simulation that the plastic strain range in solder joint is larger in viscoelastic model of underfill than those in constant elastic model and temperature dependent

ATTENTION: The Singapore Copyright Act applies to the use of this document. Nanyang Technological University Library

elastic model so that the elastic models of underfill overestimate the thermal fatigue life of flip chip solder joints. However, results from temperature dependent elastic model is slightly less than those from viscoelastic model, so the viscoelastic underfill model can be replaced by temperature dependent elastic model for the purpose of simplicity. In this study, two cases are considered for the elastic underfill model: underfill with constant material properties as listed in Table 3-5 at room temperature (25°C), and underfill with temperature dependent Young's modulus and coefficient of thermal expansion (CTE) as given in Table 3-5.

Table 3-5 Temperature dependent materials properties for underfill.

Temperature (^{o}C)	-50	0	25	80	125
Young's modulus (MPa)	6400	6000	5600	4500	2300
Poisson's ratio	0.35	0.35	0.35	0.35	0.35
CTE (ppm/ ^{o}C)	40	45	50	60	80

The equivalent plastic strains of the center node on the die/solder interface are shown in Fig. 3-13 for underfill with constant material property and in Fig. 3-14 for underfill with temperature dependent Young's modulus and CTE, respectively. It can be seen that equivalent plastic strain is higher for underfill with temperature dependent material property case than underfill with constant material property case. Comparing plastic strains for flip chip solder joint between FCOB without underfill as shown in Fig. 3-11 and FCOB with underfill as shown in Fig. 3-13 and Fig. 3-14, it can be seen that plastic strain in the solder joint reduces significantly when underfill is used in FCOB assembly. Thus solder joint reliability of the FCOB assembly can be improved by using underfill. The good consistency between fine 3D model and submodel result can be observed from Fig. 3-13 and Fig. 3-14.

ATTENTION: The Singapore Copyright Act applies to the use of this document. Nanyang Technological University Library

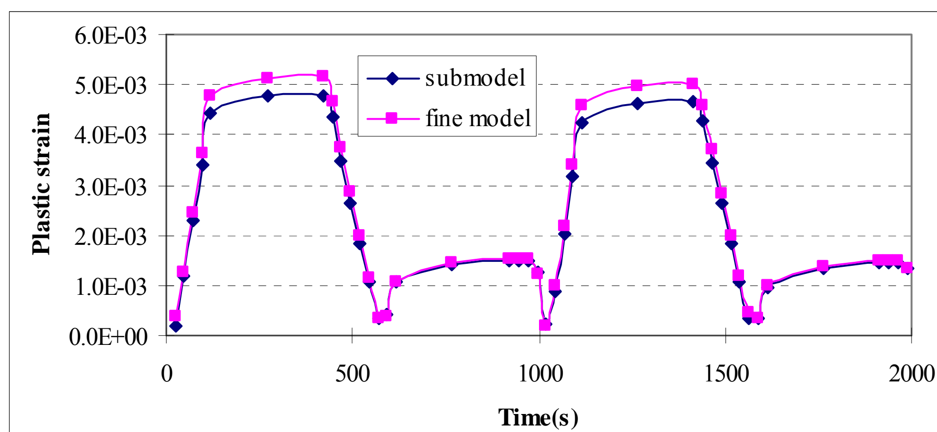

Fig. 3-13 Equivalent plastic strain for underfill with constant material properties.

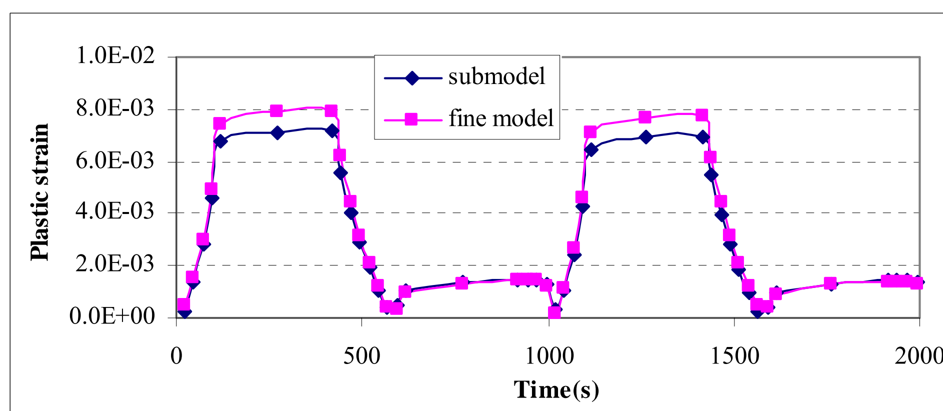

Fig. 3-14 Equivalent plastic strain for underfill with temperature dependent elastic modulus and CTE.

The accumulated plastic work densities are shown in Fig. 3-15 for underfill with constant material properties and Fig. 3-16 for underfill with temperature dependent material properties, respectively. Compared with the nonunderfill case as shown in Fig. 3-12, the difference of the plastic work density becomes larger when underfill was considered. However, the difference between submodel and fine 3D model is less than 10% from results as shown in Fig. 3-15 and Fig. 3-16 and this error is acceptable for numerical simulation results. Therefore, submodeling technique can be used to accurately simulate FCOB assembly with underfill when subjected to thermal cycling load.

ATTENTION: The Singapore Copyright Act applies to the use of this document. Nanyang Technological University Library

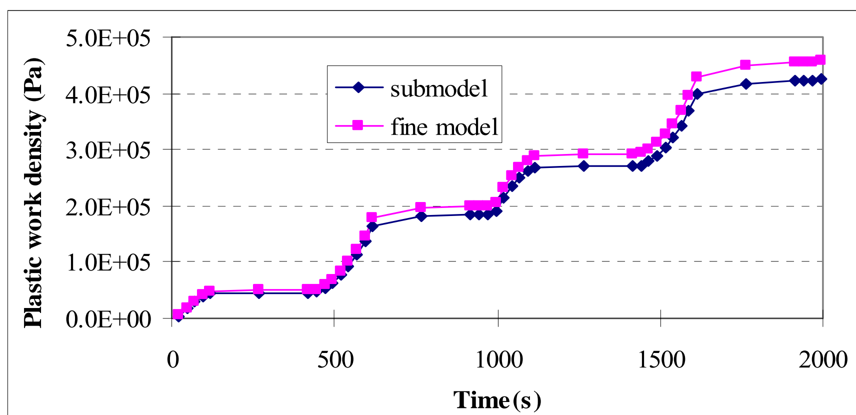

Fig. 3-15 Plastic work density for underfill with constant material properties.

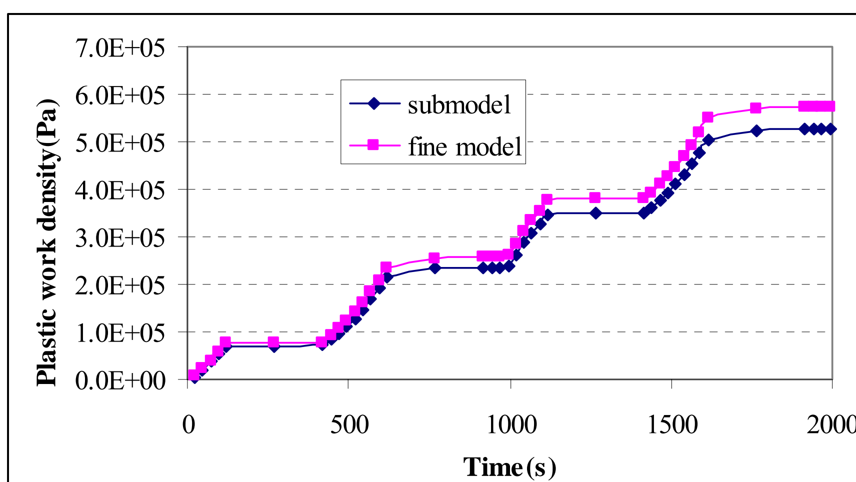

Fig. 3-16 Plastic work density for underfill with temperature dependent elastic modulus and CTE.

The error of results obtained from submodeling technology is less than 10% compared with conventional full 3D model for both assemblies with and without underfill cases due to appropriate cut boundary application in submodel. The advantages of submodeling technique include computational time saving, the hard disc space saving, less memory requirement, and less element size, which can be easily observed form Table 3-6. In this study, simple specimen of FCOB with only four corner solder joints was used for the validation of submodeling method. In real condition of many solder joints used between component and PCB, submodel is a good choice and its advantages will become more significant.

ATTENTION: The Singapore Copyright Act applies to the use of this document. Nanyang Technological University Library

Table 3-6 Advantages of submodel compared to fine underfilled FCOB model.

Items		Elements	Nodes	Computational time (Minutes)	Result file (MB)
Submodeling	Coarse model (1)	845	1144	12	113
	Submodel (2)	5580	6176	84	650
Fine 3D model (3)		22905	25408	671	2730
Factor (3)/(1+2)		3.56	3.47	6.99	3.58

3.3.3 Global-Local-Beam Model

Symmetry boundary condition can be employed in FEA modeling of an electronic assembly subjected to thermal load. However, vibration and drop analysis sometimes need a full model due to non-symmetry condition. A full detailed model of a SMA with numerous solder joints and many components is difficult to model. The submodeling technique mentioned earlier can reduce the mesh complexity, but can be still too complex with many components. In this section, a two-level global-local technique is developed, which is named global-local-beam (GLB) technique in order to distinguish from submodel method. The key technique in this method is the use of simple elements, such as beam elements with effective stiffness matrix, to represent solder joints, thus the number of elements needed to model the entire structure can be reduced significantly. This method consists of three steps: stiffness extraction analysis of a single solder joint; deformation analysis of the entire structure; and stress strain analysis of solder joint.

3.3.4 Comparison of the GLB Model to Fine 3D Model Results

In this section, the global-local-beam (GLB) model was verified by comparing the results of the GLB model with those of fine 3D model. The used specimen is same as that for submodeling calibration study as shown in Fig. 3-2.

ATTENTION: The Singapore Copyright Act applies to the use of this document. Nanyang Technological University Library

3.3.4.1 Equivalent beam stiffness analysis (see Appendix A for details)

The solder joint can be replaced by a simple two-node beam element as shown in Fig. 3-17. The two-node beam element has 12 DOFs, three translational and three rotational at each end, marked by node 1 and 2. The relation between the generalized nodal force vector $\{F\}$ and the generalized nodal displacement vector $\{u\}$ of beam is expressed in matrix form as follows:

$$\{F\} = \{K\}\{u\} \tag{3.7}$$

where $[K]$ is the 12×12 stiffness matrix of two-node beam.

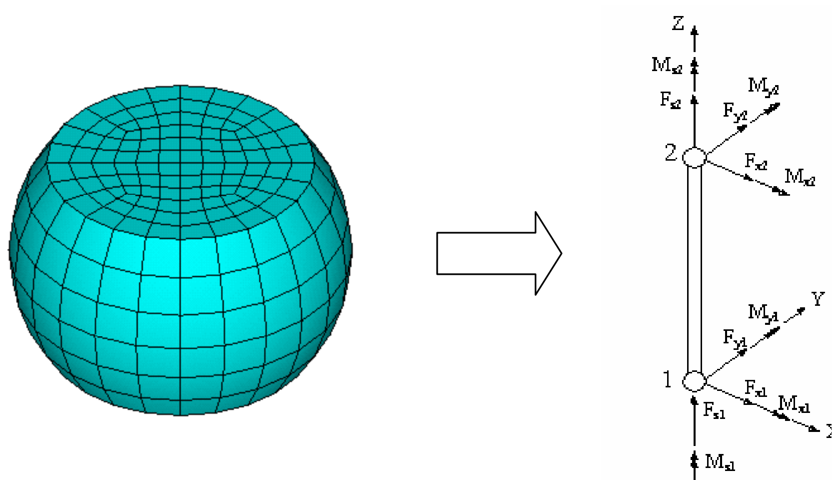

Fig. 3-17 Solder joint and corresponding two-node beam element.

In order to extract the stiffness of the solder joint, unit translational and rotational displacement were applied on the surface of the solder joint as a boundary condition. After 12 different boundary value problems with unit displacement were solved, all the terms in the stiffness matrix can be obtained (see Appendix A).

3.3.4.2 Deformation analysis of the entire structure

In this process, the solder joints were modeled as two-node beam elements with the effective stiffness matrix established in above analysis. In this study, two types of elements containing solid and shell elements were used to model chip and PCB,

ATTENTION: The Singapore Copyright Act applies to the use of this document. Nanyang Technological University Library

respectively. For shell element case, called shell-beam-shell model or shell model, nodes in both beam element and shell element can be directly connected due to same DOFs. For solid case, called solid-beam-solid model or solid model, the constraint equation should be used to solve the DOF inconsistent problem when connecting beam element to solid element (see Appendix A) because the node in solid model and shell model has 3 DOFs and 6 DOFs, respectively. In ANSYS software, the element type of MATRIX27 represents an arbitrary two-node element whose geometry is undefined but its elastic kinematic response can be specified by stiffness coefficients. The stiffness matrix constants were input as real constants in the simulation.

Two types of load were considered in this study. For the first case, the pressure of 0.1MPa was applied on the IC chip while the two shorter opposite sides of PCB were fixed. For the second case, the uniform load of temperature increment of 20°C was imposed onto the whole model. The absolute translational displacement between two beam nodes obtained from entire model was extracted to compare with that of center nodes of two solder interfaces in the fine 3D model. It can be seen from Fig. 3-19 that the solid model gives rise to better results than shell model. The error between fine model and GLB model is less for thermal load case than for mechanical load case.

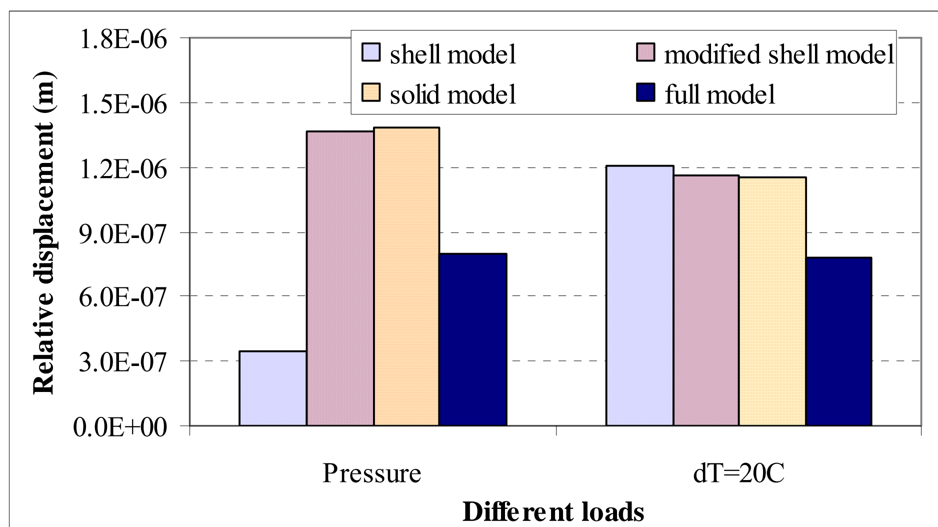

Fig. 3-18 Relative displacement of two solder interfaces from different models.

ATTENTION: The Singapore Copyright Act applies to the use of this document. Nanyang Technological University Library

In FEA simulation, the shell element is usually represented by the middle surface of the structure. When the structure thickness is very small, for example, one-twentieth of the edge length or below, the rotary effects of the shell can be ignored so that the assumption of same displacement value for the top and bottom surfaces as middle surface of shell is reasonable. In the electronic product, the PCB and chip cannot be assumed as perfect thin shell element because thickness of PCB and IC chip usually do not satisfy the assumption of the thin shell. Therefore, the thick shell element should be considered in the GLB method. According to the theory of thick plate element, the displacements parallel to the middle surface are given by [101]:

$$\begin{aligned} u(x,y,z) &= z\theta_y(x,y) \\ v(x,y,z) &= z\theta_x(x,y) \end{aligned} \tag{3.8}$$

where θ_x , θ_y are the rotations about the x and y axes, z is the coordinate in thickness direction. It can be seen from Fig. 3-18 that the modified shell model can give rise to similar results as solid model.

3.3.4.3 Stress strain analysis of solder joint

After the deformation analysis, the weakest solder joint should be selected as the one that has the largest stress. In the present approach, the relative deformations between two nodes of the beam elements were used as an index to determine the weakest solder joint. Then the nodal displacements at both ends of the beam element were applied on the detailed model as prescribed displacement boundary condition. The translational displacements were applied directly on the nodes of two end surfaces of solder joint. The rotations were transferred to the translational displacements considering the location of each node on the surface and then imposed on the corresponding nodes. For the modified shell element method, the modified translational displacements were superposed on the solder joint surface nodes.

ATTENTION: The Singapore Copyright Act applies to the use of this document. Nanyang Technological University Library

Fig.3-19 shows the comparisons of maximum Von Mises stress in the solder joint from different models. It can be seen that solid model used in GLB model gives rise to more accurate result than shell model for two loading cases. The difference induced by GLB solid model is about 25% compared to the fine 3D model. The difference induced by GLB shell model is larger than GLB solid model, especially for non-modified GLB shell model. In some papers [98, 99], shell elements were used in the GLB approach with the large discrepancy. In order to further verify the data validation from the solid element used in GLB model, the Von Mises stress distribution contour of the solder joint is shown in Fig. 3-20. It can be seen that the stress distribution contour is similar between fine 3D model and GLB solid model, which verifies that solid-beam-solid model is an acceptable modeling method.

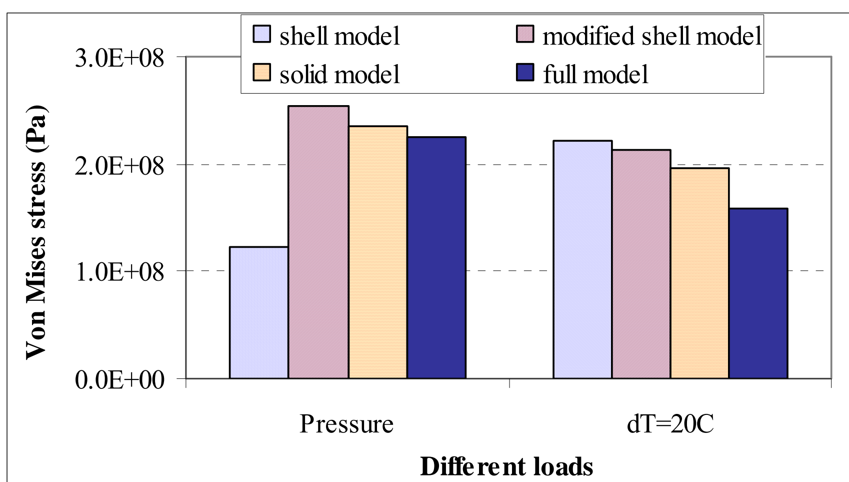

Fig. 3-19 Maximum von Mises stress of solder joint for different models.

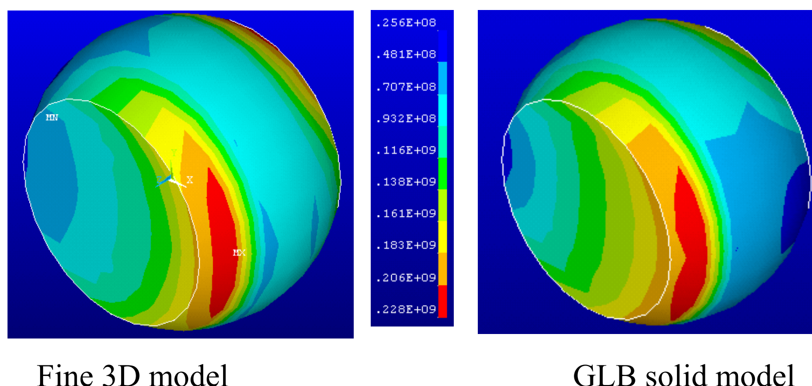

Fine 3D model GLB solid model

Fig. 3-20 Von Mises stress distribution contour comparison.

ATTENTION: The Singapore Copyright Act applies to the use of this document. Nanyang Technological University Library

3.3.5 Effective Solder Joint Model with Cubic Cross-Section

Through analyses for submodeling and GLB model technique mentioned above, it was known that submodeling could lead to more accurate results than GLB model but with more element size and computational resources. It is difficult for GLB model to consider plastic behavior of solder ball because the stiffness of effective beam model for solder joint just considers the elastic deformation of solder ball when extracting stiffness matrix of solder ball. For FCOB and BGA assemblies with many ball-shape solder joints, large element size is also needed for submodeling technique because ball shape solder joint cannot be meshed with fewer elements without loss of accuracy. In order to reduce element size significantly, an effective solder joint modeling method was developed by combining submodeling and GLB modeling techniques. In effective solder joint model, the ball shape solder joint was replaced by an effective hexahedron shape solder joint with cubic cross section and the same height as solder ball as shown in Fig. 3-21. According to GLB modeling technique, the cross section area of effective solder joint can be determined by making solder ball and effective solder joint having equivalent stiffness in axial tension/compression and shear direction because tension/compression and shear force are dominant for solder joint when subjected to thermomechanical or mechanical loads.

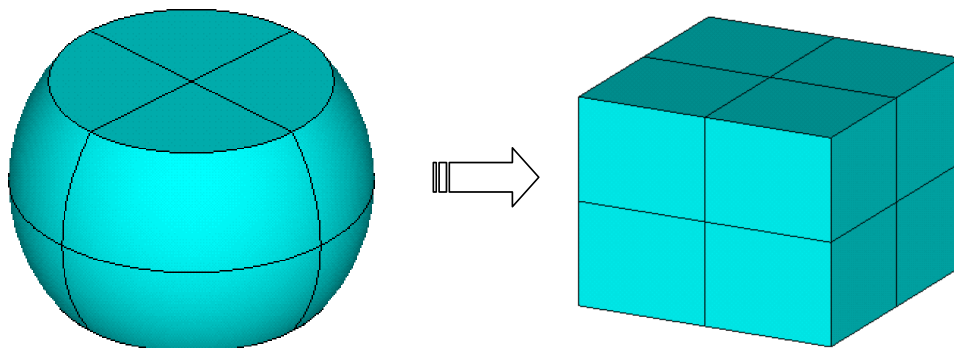

Fig. 3-21 Solder ball and its effective solder joint with cubic cross section.

ATTENTION: The Singapore Copyright Act applies to the use of this document. Nanyang Technological University Library

In global model, the effective solder joint can be used with fewer elements and plastic deformation can also be considered by effective solder joint. After results from global model with effective solder joint were obtained, submodel with detailed solder joint geometry and fine mesh can be solved by transferring and interpolating displacement results from global model to cut boundary of submodel as boundary condition. In order to verify the effective solder joint model, result comparison between effective solder ball model and fine 3D model were conducted considering two cases: FCOB with underfill and without underfill subjected to thermal cycling load as shown in Fig. 3-9. The specimen used for effective solder model was the same as that used for submodeling and GLB model method. Result comparisons of plastic work density of center node on solder/die interface between effective solder joint model and fine 3D model are shown in Fig. 3-22 for FCOB without underfill case and Fig. 3-23 for FCOB with underfill with temperature dependent material properties, respectively. It can be seen that effective solder joint model can lead to accurate results compared with submodeling method as shown in Fig. 3-12 and Fig. 3-16. Accumulated plastic work density per cycle based on solder/die interface volume averaged method is shown in Fig. 3-24. It can be seen that effective solder joint model can lead to consistent result with submodel and fine 3D model for both underfill and nonunderfill cases, which means effective solder joint model can be used for FEA simulation accurately for FCOB with/without underfill and BGA assemblies. The practical use of effective solder joint model is that all the ball shape solder joints are modeled as effective solder joint with cubic cross section except critical solder joints for which the detailed ball shape meshing was used, and then submodel is created and simulated based on the critical solder joint.

ATTENTION: The Singapore Copyright Act applies to the use of this document. Nanyang Technological University Library

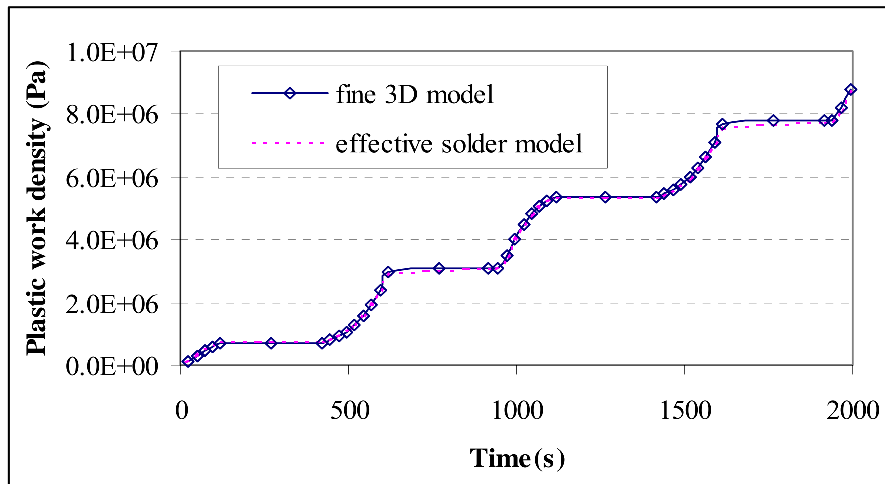

Fig. 3-22 Plastic work density from effective solder model for nonunderfill case.

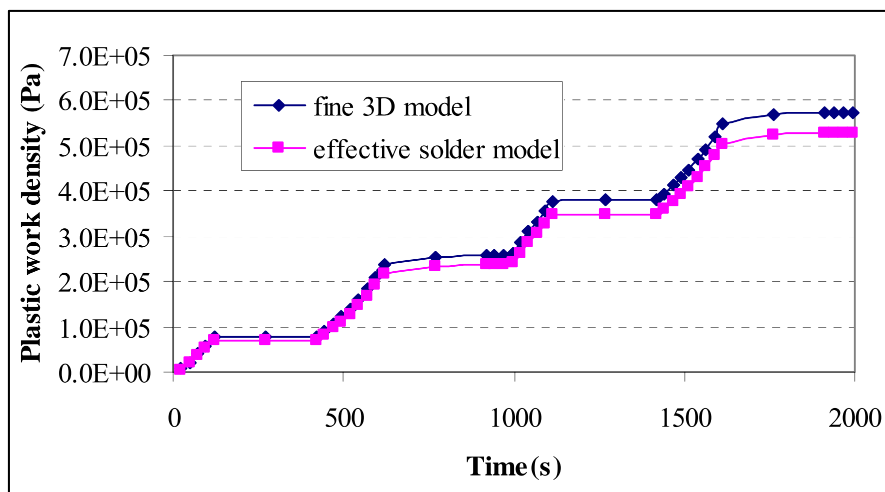

Fig. 3-23 Plastic work density from effective solder model for underfill case.

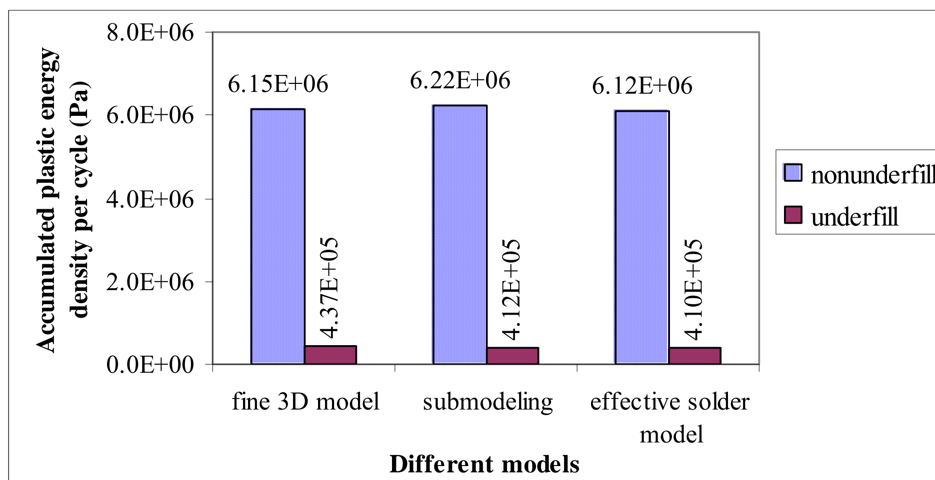

Fig. 3-24 Accumulated plastic work density per cycle for different models.

ATTENTION: The Singapore Copyright Act applies to the use of this document. Nanyang Technological University Library

3.4 COMPARISON OF LEAD-FREE AND LEAD-BASED SOLDER

Lead-free solders are increasingly used in electronic packaging industries due to lead contamination. The Sn3.8Ag0.7Cu, Sn0.7Cu, and 96.5Sn3.5Ag are widely used lead-free solder alloys. In order to take comparison between lead-based and lead-free solders, some lead-based solders are also selected, including high lead solders such as 92.5Pb5Sn2.5Ag, 97.5Pb2.5Sn and near eutectic Sn/Pb solders such as 60Sn40Pb, 62Sn36Pb2Ag. The used specimen was the same as that as shown in Fig. 3-2. The submodeling technique in section 3.3 is used to take FEA simulation for FCOB with different solder joints. The Anand's viscoplastic model in Eq. (3.2) to Eq. (3.5) is used for solder materials. The nine Anand's constants for different solders are listed in Table 3-7 [8, 25, 26]. The Anand's constants for 95.5Sn3.8Ag and 99.3Sn0.7Cu solders have been developed by our research group and implemented in FEA modeling in this study. However, the details of these data are not given due to IP restrictions. In FEA simulation, thermal cycle loading as shown in Fig. 3-9 was used and the underfill was considered with temperature dependent material properties as shown in Table 3-5.

Table 3-7 Anand's constants for different solders.

Solders	62Sn36Pb 2Ag	92.5Pb5Sn 2.5Ag	60Sn 40Pb	96.5Sn 3.5Ag	97.5Pb 2.5Sn	95.5Sn3.8Ag 0.7Cu*	99.3Sn 0.7Cu*
S_0 (MPa)	12.41	33.07	56.33	39.09	15.09	S_{01}	S_{02}
Q/k (^{o}K)	9400	11010	10830	8900	15583	k_1	k_2
A	4.00E+06	1.05E+05	1.49E+07	2.23E+04	3.25E+12	A_1	A_2
ξ	1.5	7	11	6	7	ξ_1	ξ_2
m	0.303	0.241	0.303	0.182	0.143	m_1	m_2
h_0 (MPa)	1379	1432	2640.75	3321.15	1787.02	h_{01}	h_{02}
s^ (MPa)	13.79	41.63	80.42	73.81	72.73	$s\hat{}_1$	$s\hat{}_2$
n	0.07	0.002	0.0231	0.018	0.00437	n_1	n_2
a	1.3	1.3	1.34	1.82	3.73	a_1	a_2

* details restricted from publication due to IP restrictions.

ATTENTION: The Singapore Copyright Act applies to the use of this document. Nanyang Technological University Library

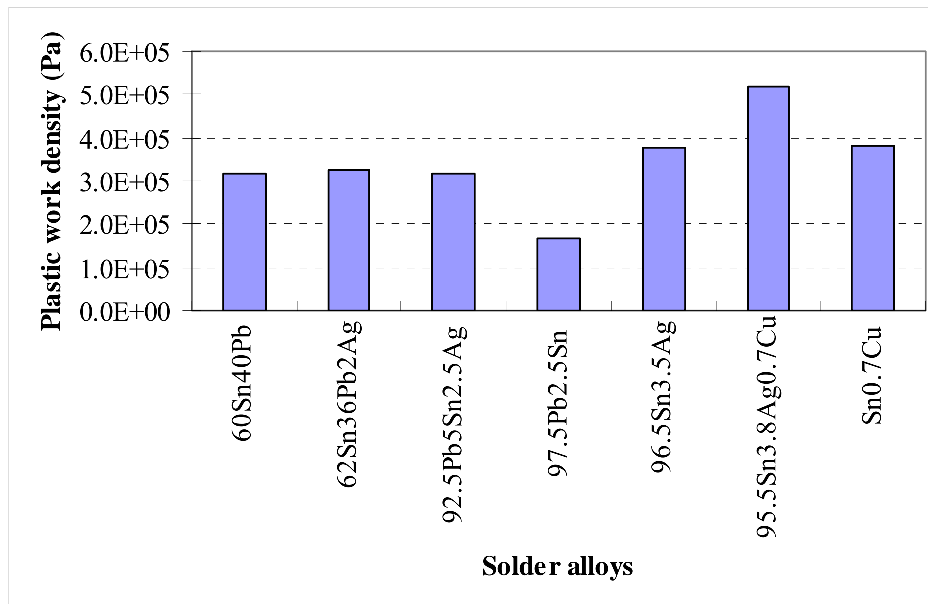

Fig. 3-25 Accumulated plastic work density per cycle for different solder joints.

A volume-averaged technique was used to calculate plastic work density accumulated per cycle for the solder/die interface elements by Eq. (3.6). Plastic work density accumulated per cycle was compared for different solder joints as shown in Fig. 3-25. It can be seen that plastic work density accumulated per cycle is similar for near eutectic solder of 60Sn40Pb and 62Sn36Pb2Ag. The high Pb solder, 97.5Pb2.5Sn, has a lowest plastic work density. Lead–free solders have higher plastic work density than lead-based solders.

Plastic work density accumulated per cycle is usually selected as a damage parameter to predict the solder fatigue life. Morrow's energy-based model is often used to predict the low cycle fatigue life due to thermal cycling load. The predicted fatigue life in terms of plastic work density can be expressed as follows:

$$N_f^n W_p = A \tag{3.9}$$

where fatigue exponent n, and material ductility coefficient A, for Sn3.8Ag0.7Cu solder are 0.897 and 311.7MPa [24], for Sn0.7Cu are 0.733 and 38.6 MPa [102], respectively. Fig. 3-26 shows the predicted fatigue life based on Eq. (3.9) for

ATTENTION: The Singapore Copyright Act applies to the use of this document. Nanyang Technological University Library

Sn3.8Ag0.7Cu and Sn0.7Cu solders. It can be seen that the predicted fatigue life of Sn3.8Ag0.7Cu solder is more than that of Sn0.7Cu solder. The fatigue life of FCOB solder joint with underfill joints is 10 times that of FCOB without underfill, which is consistent with thermal reliability test results conducted by Chen et al. [100] for flip chip packages with/without underfill.

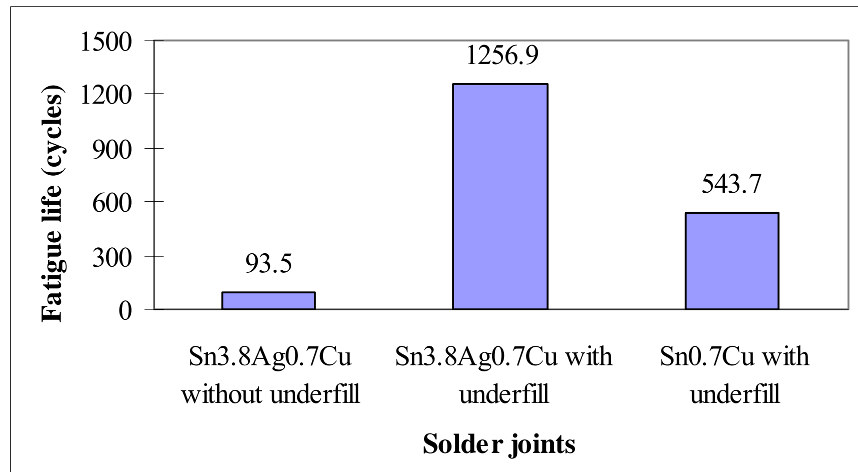

Fig. 3-26 Predicted fatigue life for Sn3.8Ag0.7Cu and Sn0.7Cu solder joints.

3.5 SUMMARY

In this chapter, global-local modeling method containing submodeling and GLB modeling technique was developed and calibration for these models was also conducted. Based on global-local modeling technique, reliability analyses for lead-free and lead-based solder joints were compared.

Reasonable submodel with hybrid solid including solder joint, PCB and component can lead to more accurate result than submodel with only solder joint when compared to fine 3D reference model because cut boundary of hybrid submodel is far enough away from stress concentration region of solder/component or solder/PCB interface. The submodel technology has a less mesh sensitivity compared with full 3D model in which the grid size has a great effect on FEA results. Submodeling technique

ATTENTION: The Singapore Copyright Act applies to the use of this document. Nanyang Technological University Library

can give rise to accurate results for FCOB assembly without underfill as well as with underfill case when subjected to thermal cycling. Submodeling method allows users to conduct the FEA simulation with less elements size without losing accuracy so that computer resource required can be reduced significantly.

The global-local-beam (GLB) modeling method was developed. The GLB model is a simpler FEA simulation method than submodeling technology because the solder joint in GLB model is replaced by one two-node beam element with effective stiffness, thus leading to more error for the GLB model than submodel. Solid-beam-solid GLB model can lead to more accurate results for stress analysis of critical solder joint than shell-beam-shell GLB model. When shell-beam-shell model is used in the GLB model, modified shell elements gives less error than non-modified shell elements. GLB model is reasonable for small deformation problem and modal analysis because only elastic deformation behavior is considered for solder joint in deformation analysis of entire structure. Based on GLB modeling theory, the ball shape solder joint can be replaced by effective solder joint with cubic cross-section assuming that they have similar stiffness. The effective solder joint model can lead to accurate result with solder joint plastic deformation consideration.

Lead-free and lead-based solder stress analyses were conducted using submodeling method. It was shown that lead-free solders have higher plastic work density accumulated per cycle than lead-based solders when subjected to thermal cycling load because lead-free solders are usually harder than lead-based solders. Underfill can improve fatigue life of FCOB assembly significantly when subjected to thermal cycling load.

ATTENTION: The Singapore Copyright Act applies to the use of this document. Nanyang Technological University Library

CHAPTER 4 THERMAL FATIGUE RELIABILITY TEST AND ANALYSIS

4.1 INTRODUCTION

Thermal cycling (TC) or thermal shock (TS) tests are used for accelerated testing of electronic assemblies. Cyclic stress-strain will deform the solder material when subjected to TC or TS test due to CTE mismatch in different electronic materials, thus inducing thermal fatigue failure in solder joints.

Surface mounted components such as Plastic Ball Grid Array (PBGA), Plastic Quad Flat Package (PQFP), Thin Shrink Small Outline Package (TSSOP), and Flip Chip On Board (FCOB) are commonly used in electronic assemblies. In these components, the solder joints are very important parts for the integrity of electronic products as they are prone to fatigue failure at test or field condition. Lead-free solders are rapidly replacing lead-based solders as the EU legislations on RoHS (Reduction of Hazardous Substances) and WEEE (Waste Electrical and Electronic Equipment) take effective in July 2006. The Pb-free solder alloy recommended by the iNEMI, Sn-3.9Ag-0.6Cu, is gaining wide use with a narrow range Sn-(3-4)Ag-(0.5-1)Cu. However, understanding of these new materials in failure assessment is still in its infant period compared to lead-containing solders and further researches are needed. In this study, thermal fatigue test from -40°C to 125°C and FEA simulation of PBGA, PQFP and TSSOP with Sn-3.8Ag-0.7Cu solder were investigated. Weibull distribution analysis was conducted for test results and mean time to failure (MTTF) was used for validation of FEA simulation result.

ATTENTION: The Singapore Copyright Act applies to the use of this document. Nanyang Technological University Library

Solder creep behavior is temperature and time dependent, and is typically important at 0.4 T_m and above, where T_m is the absolute melting temperature. The melting point of Sn-3.8Ag-0.7Cu solder is around 490K (217°C) [16]. Therefore, even though at room temperature of 298K, the homologous temperature ratio is more than 0.5. Hence, creep behaviors in SnAgCu Pb-free solders are important properties. The steady-state creep model of solder is of major concern. The Garofalo-Arrhenius steady-state creep constitutive model and viscoplastic Anand's model for solder are widely used by researchers [8, 13, 20, 26]. In this study, these two solder constitutive models will be used in FEA simulation for comparison.

Finite element modeling and simulation is powerful tool and takes an important role in fatigue life prediction for solder joints. In order to reduce the element size in the FEA simulation for solder joint reliability, some reduced models were used by researchers, including slice or strip model [13], one-eighth or octant model [29, 88], 2D model containing 2D plane strain [103], 2D plane stress [14] and axisymmetric models [100]. Some trade-off in accuracy is expected in these simple models. In this study, the FEA result comparison was conducted for 2D and 3D models considering 3D quarter model with submodeling approach as a reference model.

An important function of FEA simulation is to find the critical solder joint location and extract the fatigue damage parameter at the critical solder joint for subsequent fatigue life prediction. Volume averaging method is often used for extracting fatigue life prediction strain or energy parameter. Typically, the whole interface layer of elements was averaged and this may lead to lower averaged value of strain or energy thus overestimates the fatigue life of solder joint. In this study, alternative averaging volumes containing outer two rings and outermost ring elements were proposed and employed with energy-based solder fatigue models.

ATTENTION: The Singapore Copyright Act applies to the use of this document. Nanyang Technological University Library

Fatigue life of solder joints can be affected by many factors such as thermal cycling profile, solder joint material, geometry and design, intermetallic compound (IMC). In order to understand these effects better, FEA simulations of the intermetallic layer effect (IMC materials with two different thicknesses); solder mask definition (SMD) versus non-solder mask definition (NSMD) in design; different stress free state conditions at –40°C, 25°C, 125°C, and 150°C; thermal cycling versus thermal shock loadings; different temperature ranges were investigated. In addition, effect of Ag content in SnAgCu solder on reliability of flip chip solder joint was also investigated using FEA simulation by comparing predicted results to test results by Terashima et al. [104] for FCOB assembly with Sn-xAg-0.5Cu solder (see Appendix B for details).

4.2 THERMAL CYCLING TEST AND FAILURE ANALYSIS

The test specimen is shown in Fig. 4-1. Four different components were investigated: PBGA316 with 316 solder balls, pitch of 1.27mm, solder ball height of 0.58mm and die size of 7.6mm×7.6mm×0.41mm; PQFP208 with 208 leads, pitch of 0.5mm and die size of 10mm×10mm×0.16mm; PQFP176 with 176 leads, pitch of 0.5mm and die size of 8mm×8mm×0.125mm; TSSOP48 with 48 leads, pitch of 0.5mm and die size of 3mm×3mm×0.125mm. These four components were mounted on the FR4 PCB of 210mm×150mm×1.63mm using Sn-3.8Ag-0.7Cu Pb-free solder. Three different surface finishes with ENIG (electroless nickel immersion gold or Ni/Au), immersion Ag and OSP (organic solderability preservative) were used on board side, respectively. Six test boards for each finish case were tested giving a total of 18 specimens. This sample size used in this test was determined by considering the thermal chamber space limit and minimal level for getting an approximate result. Thermal cycling test with –40°C /125°C temperature range and cycle time of one hour was conducted in a three-

ATTENTION: The Singapore Copyright Act applies to the use of this document. Nanyang Technological University Library

zone temperature cycling chamber. The thermal cycling (TC) profile is shown in Fig. 4-2. The test started from room temperature, and then ramped up to maximum temperature of 125°C at which dwell time of 15 minutes is used, then temperature ramped down to minimum temperature of –40°C with dwell time of 15 minutes. Only one daisy chain connects all the solder joints for each component used for in-situ resistance monitoring using data logger. Failure of the component is defined when the resistance is larger than a failure criterion set at 300Ω.

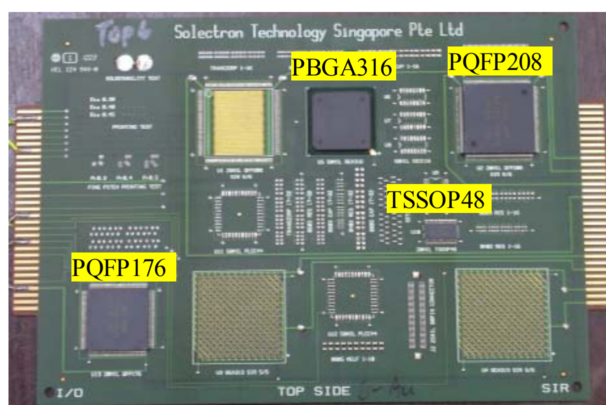

Fig. 4-1 Lead-free solder assembly specimen.

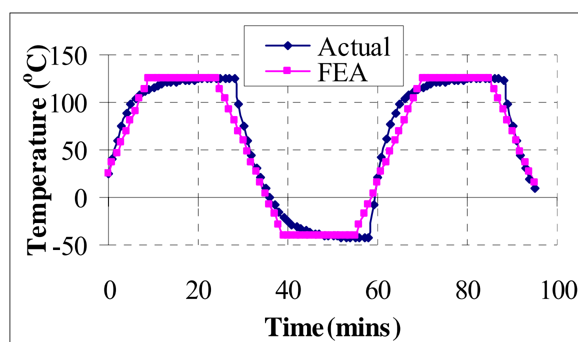

Fig. 4-2 Actual and FEA-use thermal cycling profile.

The TC test was stopped after completing 3400 cycles. The test results are given in Table 4-1. No failures were recorded for all TSSOP, for PQFP208 with Ni/Au finish and for PQFP176 with Ni/Au and immersion Ag finishes. Thus, TSSOP and PQFP components have higher thermal cycling fatigue resistance than PBGA component. Components with Ni/Au finish exhibit higher thermal fatigue life compared to other

ATTENTION: The Singapore Copyright Act applies to the use of this document. Nanyang Technological University Library

finishes. The failure data fit the two-parameter Weibull failure distribution model as shown in Fig. 4-3. The Weibull parameters of characteristic life and slope are given in Table 4-2. It can be seen that longer characteristic life and larger slope for PBGA with Ni/Au finish were noted compared to OSP and Ag finish cases. From cross section observation of solder joint after thermal cycling test, voids closed to PCB side were found in solder balls for PBGA component with Ag and OSP finishes. This is the reason of the fact that the fatigue life was lower for PBGA components with Ag or OSP finishes than that with Ni/Au one. In addition, microstructure of solder interface close to PCB side or component side affects the solder fatigue life. The thermal fatigue data of PBGA with Ni/Au finish would be used for validation of FEA results.

Table 4-1 TC test result for PBGA316, PQFP208, and PQFP176 (in cycles).

Finishes	Ni/Au	Ag	OSP
PBGA316	2131	1048	1236
	2745	1309	1680
	2892	1347	1931
	2972	1432	2661
	3053	2127	2987
PQFP208	No failures	2304	876
		2976	1766
			1942
PQFP176	No failures	No Failures	1024
			2586
			2828
TSSOP48	No failures	No failures	No failures

Table 4-2 Weibull parameters, MTTF and FTTF for PBGA316 solder joints.

Finish	Ni/Au	Ag	OSP
Slope (β)	7.69	4.42	2.96
Char. Life (η)	2917	1579	2360
MTTF (cycles)	2742	1439	2105
FTTF (cycles)	2131	1048	1236

ATTENTION: The Singapore Copyright Act applies to the use of this document. Nanyang Technological University Library

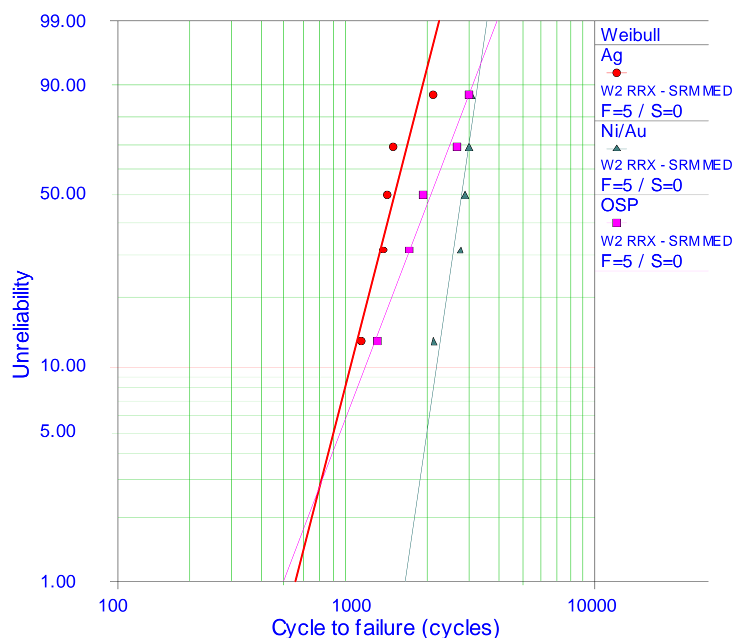

Fig. 4-3 Weibull plot of thermal fatigue life for PBGA316.

Failure analysis was conducted for PBGA component to observe failure site and mode using cross sectioning and optical microscope or Scanning Electron Microscopy (SEM). Fig. 4-4 shows the cross section images of some typical solder joint failure sites. It can be seen that the observed failure mode was fatigue cracks initiating from the solder joint corner and propagating through the solder adjacent to the solder-to-IMC interface. Cracks occur at the corner of the solder joint at the component side more often than board side, which is consistent with theoretical fact that larger strain occurs in solder interface close to the component side due to larger CTE mismatch at solder-to-component location.

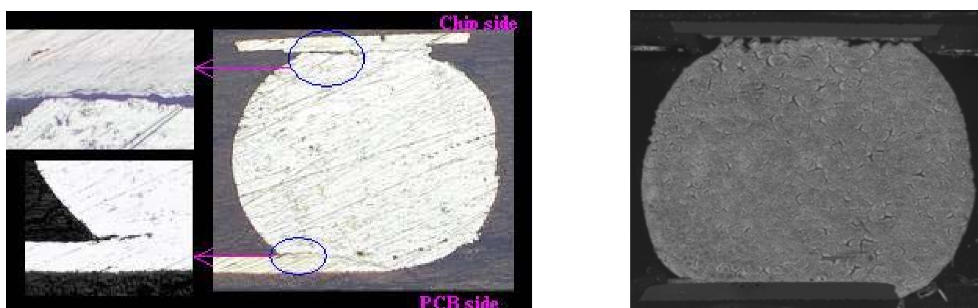

(a) Cracks at component and PCB sides (b) Crack at component side

Fig. 4-4 The cross section image of PBGA solder joint failure modes.

ATTENTION: The Singapore Copyright Act applies to the use of this document. Nanyang Technological University Library

4.3 FEA ANALYSIS OF THERMAL FATIGUE FOR SOLDER

The combination of accelerated testing and FEA simulation is a useful way to assess the reliability of electronic assemblies. Fig. 4-5 shows the requirements of input (preprocessing) and desired output results (postprocessing). In preprocessing, the important input issue is good material properties and constitutive model, especially for solder material. In this study, different solder constitutive models containing Anand's viscoplastic model, elastic-creep model, elastic-plastic model and elastic-plastic-creep model were used for comparison. Strain and strain energy density output from FEA results are very commonly used damage parameters in solder fatigue life prediction. In this study, two different fatigue life prediction models, containing energy-based and strain-based fatigue life models extracted from isothermal bulk solder fatigue test or combination of FEA simulation and thermal cycling reliability test, were used for comparison. Different volume averaging methods based on whole top layer, outer two rings and outermost ring elements were used in fatigue life prediction for comparison.

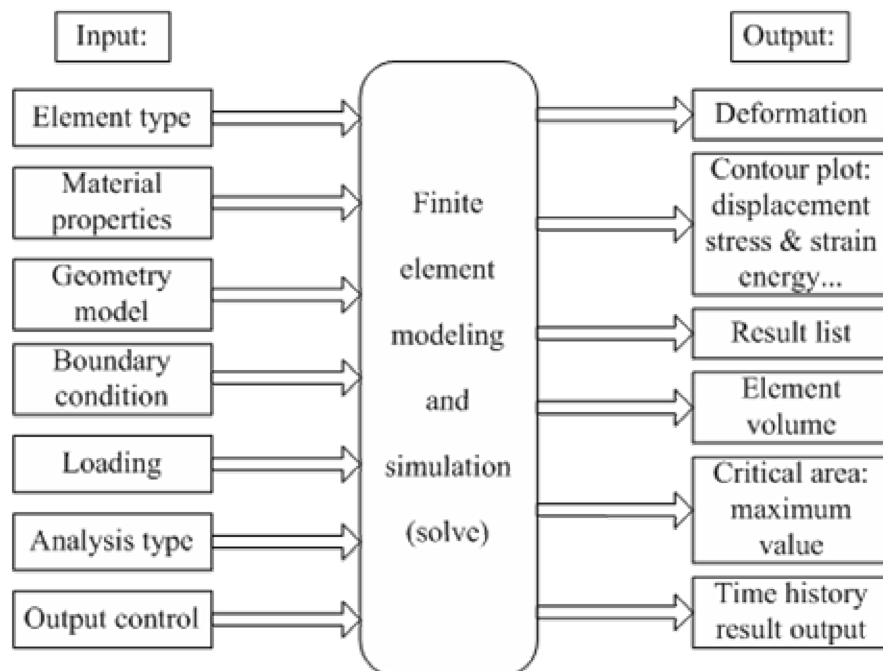

Fig. 4-5 Finite element analysis procedure.

ATTENTION: The Singapore Copyright Act applies to the use of this document. Nanyang Technological University Library

4.3.1 Constitutive Models for Sn-Ag-Cu Solder

It was known that solder creep behavior is temperature and time dependent, and plays a very important role in deformation of solder in thermal cycling tests. Therefore, the time- and temperature-dependent deformation behavior of solder material must be modeled in FEA simulation of TC loading test. These models include single creep equations with power-lower or hyperbolic sine functions [46], elastic-plastic and elastic-plastic-creep models [13] and viscoplastic Anand's model [8].

In elastic-plastic-creep (EPC) model, the solder is modeled as an elastic-plastic-creep material with temperature dependent Young's modulus and yield stress. The solder is assumed to exhibit elastic, bilinear kinematic hardening plastic behavior after yield. The creep behavior of solder is modeled using hyperbolic sine creep equation:

$$\dot{\varepsilon}_c = C_1 \frac{G}{T}\left[\sinh\left(\alpha \frac{\sigma}{G}\right)\right]^n \exp\left[\frac{-Q}{kT}\right] \tag{4.1}$$

This equation is then re-written into Eq. (4.2) in the required format for implicit creep model (TBOPT = 8) in ANSYS [22]. Table 4-3 lists the constants C1, C2, C3 and C4 for Sn-Ag-Cu solder. The EPC model can be realized in ANSYS by combining bilinear kinematic hardening plasticity with implicit creep (TB, BKIN +TB, CREEP).

$$\dot{\varepsilon}_c = C_1[\sinh(C_2\sigma)]^{C_3} \exp^{-C_4/T} \tag{4.2}$$

Table 4-3 Material constants of creep model for Sn-Ag-Cu solders.

Solders	C1	C2	C3	C4
Sn-3.8Ag-0.7Cu	32000	0.037	5.1	6524.7
Sn-1Ag-0.5Cu	57370	0.084	3.8	7726

Fatigue damage parameter such as inelastic strain or inelastic strain energy density can be expressed as follows:

$$\varepsilon_{in} = \varepsilon_c + \varepsilon_p \tag{4.3}$$

ATTENTION: The Singapore Copyright Act applies to the use of this document. Nanyang Technological University Library

$$W_{in} = W_c + W_p \tag{4.4}$$

where subscript *in*, *p* and *c* represent inelastic, plastic and creep, respectively. Some researchers [46, 47] just considered creep behavior of solder without considering the plastic part in FEA simulation of thermal cycling.

It is difficult separating the creep and plastic components in Eq. (4.3) and (4.4) in TC test condition and using a viscoplastic analysis is often preferred. Viscoplastic Anand's model expressed by Eq. (2.7) to (2.10) is commonly used for viscoplastic deformation analysis of solder. There are nine constants in Anand's model, which can be determined directly from the experimental data, such as creep test and constant strain rate tensile tests [105, 106].

4.3.2 Fatigue Life Prediction Model Methodology

There are two different approaches to develop a life prediction model for solder joint. One approach is to develop fatigue model by conducting displacement-controlled isothermal mechanical fatigue test using bulk solder material. The other is to develop fatigue model by combining actual reliability test data and FEA simulation results.

For the first method, Coffin-Manson strain-based model and Morrow's energy-based model have been reported by Pang et al. [24]:

$$N_f^m \Delta\varepsilon_{in} = C \tag{4.5}$$

$$N_f^n W_p = A \tag{4.6}$$

The fatigue ductility coefficient, *C* and *A*, and the fatigue exponent, *m* and *n* for Sn-3.8Ag-0.7Cu can be obtained from strain-life and energy-life curves at different test conditions such as at 25°C, 75°C and 125°C with 0.1 Hz, 0.01Hz or 0.001Hz., Temperature changes from –40°C to 125°C with 1 hour per cycle during thermal cycling test. The highest temperatures of 125°C and strain rate (low frequency at

ATTENTION: The Singapore Copyright Act applies to the use of this document. Nanyang Technological University Library

0.001Hz) in thermal cycling test have significant effect on solder joint fatigue failure. Hence, the isothermal test condition at temperature 125°C with 0.001Hz frequency was selected for further fatigue analysis. The m, n, C, and A are 0.853, 0.897, and 9.2, 311.7MPa (at 125°C with 0.001Hz), respectively reported by Pang et al. [24].

For the second method, the coefficient and exponent in fatigue model can be determined by combining numerical result and actual test data based on a damage mechanism. Schubert et al. [47] proposed fatigue model for Sn-Ag-Cu solder determined by creep strain criteria and creep strain energy-based method based on FEA results and actual reliability test data (300Ω as a failure criterion) from different assemblies such as FCOB with or without underfill and PBGA with Ni/Au board finish under different thermal cycling conditions:

$$N_f = 4.5\varepsilon_{cr}^{(-1.295)} \tag{4.7}$$

$$N_f = 345W_{cr}^{(-1.02)} \tag{4.8}$$

Syed [46] proposed fatigue model for Sn-Ag-Cu solder determined by using FEA results and actual reliability test data (300Ω as a failure criterion) from different BGA assemblies with Ni/Au plating on component side and OSP board finish such as PBGA, Ceramic BGA and fleXBGA under different thermal cycling conditions:

$$N_f = (0.0513\varepsilon_{cr})^{-1} \tag{4.9}$$

$$N_f = (0.0019W_{cr})^{-1} \tag{4.10}$$

Hyperbolic sine constitutive creep model for solder was used in FEA simulation and fatigue damage parameter calculation averaged over whole solder/component interface was used in determining fatigue constants in Schubert's and Syed's models.

When elastic-plastic-creep constitutive model for solder was used in FEA simulation, the inelastic strain includes two part, plastic strain and creep strain. In

ATTENTION: The Singapore Copyright Act applies to the use of this document. Nanyang Technological University Library

order to predict solder fatigue life using above fatigue models, some treatments can be made as follows. When creep part is dominant, fatigue life can be predicted by substituting creep strain or creep strain energy into above equations. When plastic part is dominant, fatigue life can be predicted by using plastic strain or plastic strain energy as fatigue damage parameter. Otherwise, fatigue life prediction also can be done using total inelastic parameter including creep and plastic parts as fatigue damage parameter. In addition, a combined creep-fatigue life prediction model for solder was proposed by Pang et al. [13, 29] as given below:

$$\frac{1}{N_f} = \frac{1}{N_p} + \frac{1}{N_c} \tag{4.11}$$

In this study, fatigue life models shown in Eq. (4.5) to Eq. (4.11) will be used to predict PBGA solder fatigue life for comparison, respectively.

4.3.3 FEA Modeling and Analysis for PBGA, PQFP and TSSOP

4.3.3.1 Finite element modeling and simulation for PBGA assembly

Fig. 4-6 shows all FEA models for PBGA assembly including quarter, octant, slice and 2D models, respectively. Quarter model was obtained by cutting along two symmetric centerline planes. Octant model was obtained by cutting along diagonal and centerline planes using geometry symmetric property. Slice models were extracting from two different areas such as centerline (S3model) and diagonal for comparison. Two different geometry slice models along diagonal were also considered, one was obtained by cutting plane through the diagonal solder ball center (S2), and the other slice model contains all diagonal integrated solder balls (S1). Due to the complexity of octant and quarter models, submodeling method was used in these two models. Two different cut planes were considered for 2D model, one is from center of component with distance of normal pitch between adjacent solder balls (2DC) while the other is

ATTENTION: The Singapore Copyright Act applies to the use of this document. Nanyang Technological University Library

from diagonal with distance of diagonal pitch (√2 times normal pitch) between adjacent solder balls (2DD). For diagonal 2D model, 2DD strain, 2DD stress (unit thickness is default value in analysis), 2DD stress with pitch thickness and 2DD axisymmetric models were considered. For centerline 2D model, 2DC strain and 2DC axisymmetric models were performed.

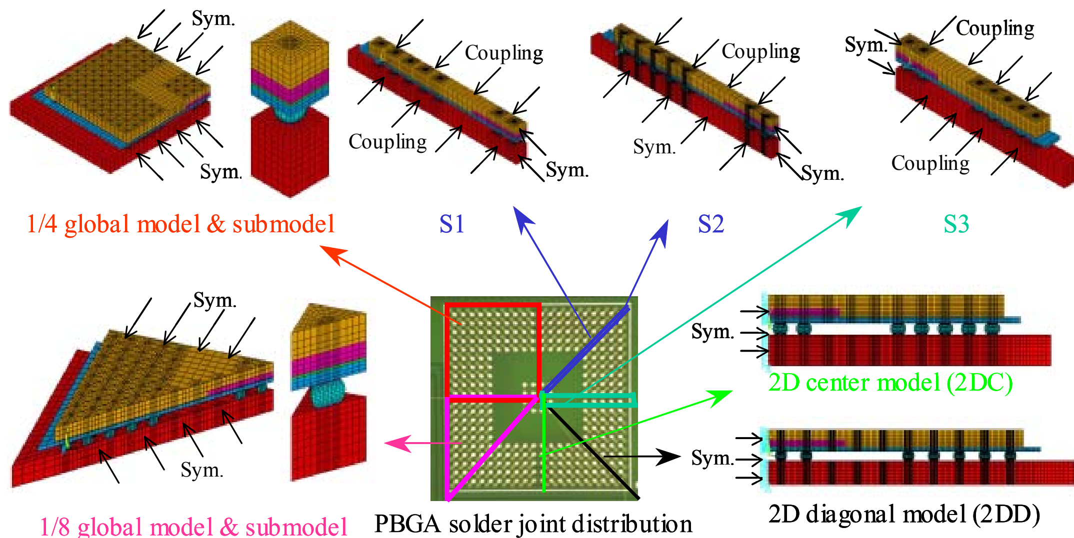

Fig. 4-6 2D and 3D FEA models for PBGA assembly.

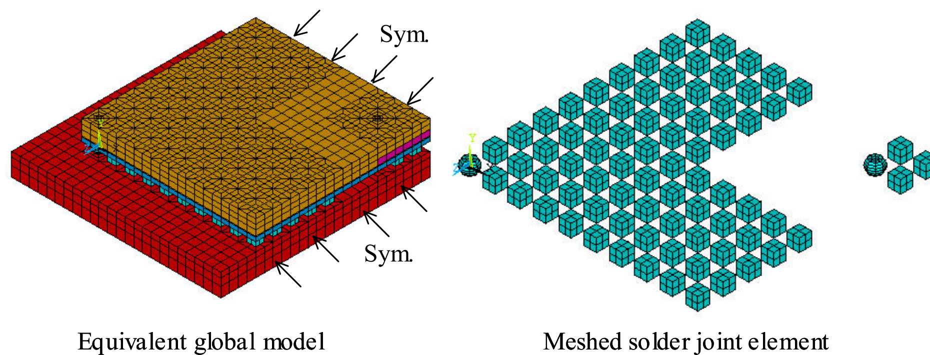

Fig. 4-7 Effective quarter global FEA models for PBGA assembly.

According to effective solder model presented in Chapter 3, the ball-shape solder joint can be replaced by cuboid-shape solder joint with the same height and effective tensile and shear stiffness because the tension-compression and shear loads are major loads of electronic component subjected to thermal cycling load. Fig. 4-7 shows the meshed solder joints in equivalent global quarter model. The critical solder joints, for

ATTENTION: The Singapore Copyright Act applies to the use of this document. Nanyang Technological University Library

example, solder joints under chip or component corner shown in Fig. 4-7, were modeled as real shape solder ball and others were modeled as equivalent cuboid-shape solder joints. The submodel in effective solder joint model is same as that in quarter model as shown in Fig. 4-6. The effective global model with cuboid-shape solder joints reduces the elements size compared to global model with all ball-shape solder joint meshes. The proper symmetric and/or coupling boundary conditions were used for different FEA models. In this study, all FEA models possibly encountered in FEA simulation for electronic packaging reliability study were carried out systematically for comparison. Error arise from different models can be determined qualitatively and quantitatively considering results from quarter model as a benchmark.

Tables 4-4 and 4-5 list the material properties [107, 108] used in FEA simulation for PBGA assembly. In FEA simulation, three thermal cycles were simulated because it is enough to obtain converged strain or strain energy density results accumulated per cycle [109] and 28 load steps were implemented for each cycle. Thermal cycling profile used in FEA simulation is given in Fig. 4-2 and it can simulate actual thermal cycling load accurately. Room temperature of 25°C was selected as initial condition or stress-free state temperature. Viscoplastic Anand's model was used for solder material. Multilinear kinematic hardening plasticity model was used for copper material.

Table 4-4 Material properties for PBGA assembly.

Materials	Young's Modulus (GPa)	Poisson's ratio	CTE (ppm/^{o}C)
Solder	Table 4-5	0.35	24.5
Copper	155.17	0.34	Table 4-5
FR4 PCB	(x,z):20 (y):9.8	x,z: 0.28; y: 0.11	x,z: 18; y: 50
BT Substrate	x,z: 26 y: 11	x,z: 0.39 y: 0.11	x,z: 15 y: 52
Die	Table 4-5	0.278	Table 4-5
Adhesive	7.38	0.3	52
Mold	16	0.25	15

ATTENTION: The Singapore Copyright Act applies to the use of this document. Nanyang Technological University Library

Table 4-5 Temperature dependent material properties.

Temperature (°C)	-40	25	50	125
Solder modulus (GPa)	54.43	41.73	36.84	22.19
Copper CTE (ppm/ °C)	15.3	16.4	16.7	17.3
Die modulus (GPa)	192.1	191	190.6	190
Die CTE (ppm/ °C)	1.5	2.6	2.8	3.1

4.3.3.2 FEA models for PQFP and TSSOP assemblies

Figs. 4-8 and 4-9 show quarter FEA models for PQFP and TSSOP assemblies, respectively. Submodeling technique was used for PQFP assemblies due to complicated geometry. For TSSOP assembly, only one-level quarter fine model was implemented. Material properties used in PQFP and TSSOP assemblies were same as those listed in Table 4-4 and 4-5 except BT and Die adhesive materials.

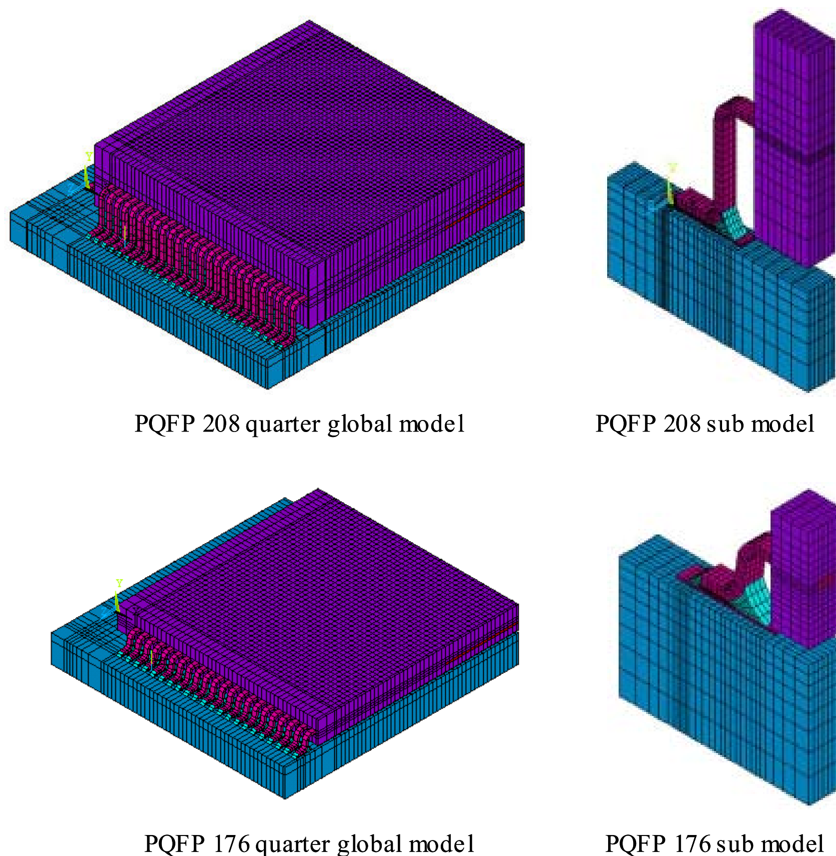

Fig. 4-8 Quarter global FEA models and submodels for PQFP assemblies.

ATTENTION: The Singapore Copyright Act applies to the use of this document. Nanyang Technological University Library

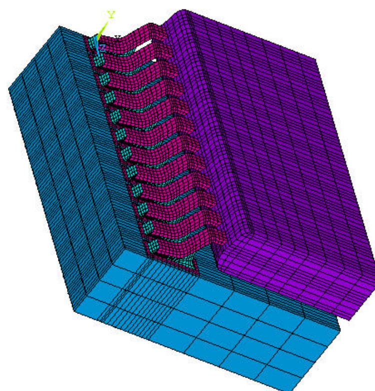

Fig. 4-9 Quarter FEA fine model for TSSOP assembly.

4.3.3.3 Results and Discussions

1) Plastic work density calculation

In FEA result, plastic work density or plastic strain energy density accumulated per cycle was extracted from numerical result as a damage parameter for fatigue life prediction. The volume-averaged method was used for plastic work density calculation as shown in following equation:

$$\Delta W_{ave} = \frac{\sum \Delta W \bullet V}{\sum V} \tag{4.12}$$

It can be seen from Eq.(4.12) that the averaged plastic work density is sensitive to elements selected for volume averaging. Generally, elements involved in interface layer between solder/component and/or solder/PCB were selected for averaging as shown in Fig. 4-10.

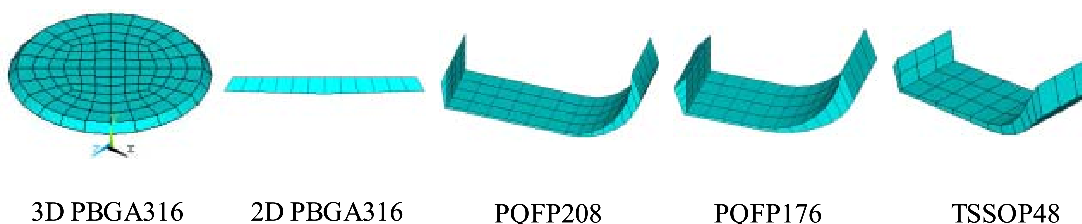

Fig. 4-10 Averaged volumes located on component side for different assemblies.

Fig. 4-11 shows the plastic strain energy density accumulation for PBGA solder after first thermal cycle from quarter model results. It can be seen from Fig. 4-11 that

ATTENTION: The Singapore Copyright Act applies to the use of this document. Nanyang Technological University Library

the critical solder joint for PBGA component under thermal cycling loading was close to die corner other than component corner due to large CTE mismatch around die corner area, which is consistent with crack site from cross-section result. The submodel, therefore, will be modeled based on critical solder joint.

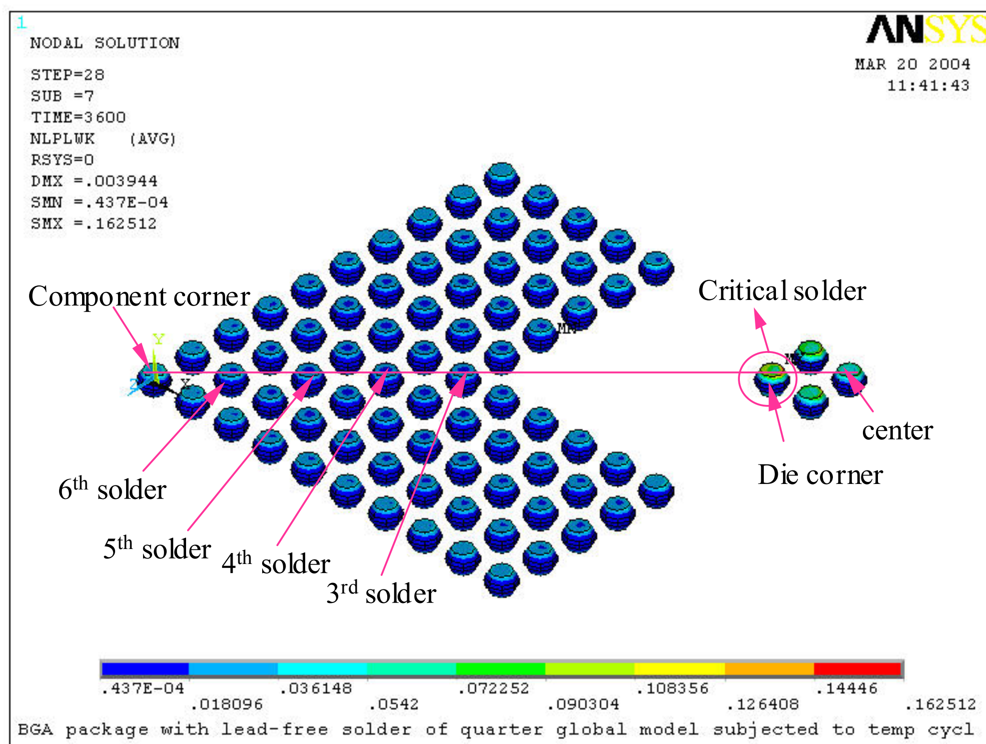

Fig. 4-11 Plastic work density accumulated in PBGA solder after fist thermal cycle.

Fig. 4-12 shows the accumulated plastic work density per cycle averaged at interface elements of solder/component and solder/PCB for three different cycles. It can be seen that accumulated plastic work density converges at third thermal cycle not only for die side elements but also for PCB side element. Therefore, three thermal cycles is enough in FEA modeling and simulation. The accumulated plastic work density is larger on solder/component interface than on solder/PCB interface so that solder failure will first occur on component side which has been verified by failure mode analysis as shown in Fig. 4-4. The following fatigue life analysis, therefore, will focus on component side interface.

ATTENTION: The Singapore Copyright Act applies to the use of this document. Nanyang Technological University Library

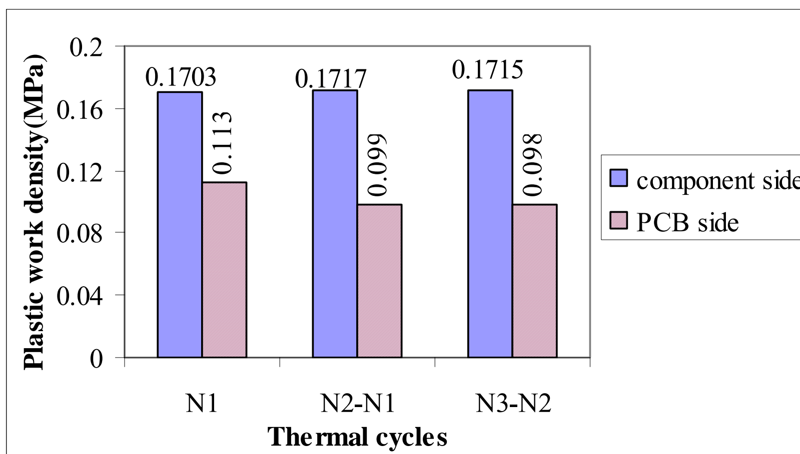

Fig. 4-12 Accumulated plastic work density per cycle for PBGA solder.

2) Results comparison for different PBGA FEA models

From FEA result, all different models predict the same critical solder joint close to chip corner and solder/component interface is more prone to failure than solder/PCB interface. Volume-averaged plastic strain energy densities accumulated per cycle based on component/solder interface elements are shown in Fig. 4-13.

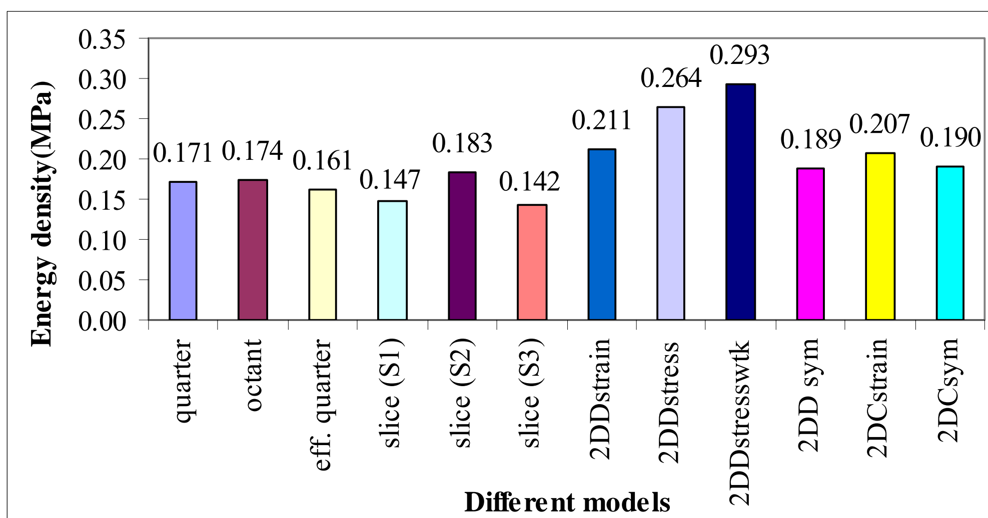

Fig. 4-13 Accumulated plastic work densities for different PBGA FEA models.

Some conclusions can be obtained from Fig. 4-13. First, 2DD stress models result in highest plastic strain energy density, while slice models such as S1 and S2 result in lowest plastic strain energy density due to more assumptions made on geometry and boundary condition in these models compared to real condition. Second, for 2D

ATTENTION: The Singapore Copyright Act applies to the use of this document. Nanyang Technological University Library

axisymmetric and strain models, plastic strain energy density values from 2DD models are similar to that from 2DC models. Finally, octant, equivalent quarter, S2 slice, 2D axisymmetric models can give accurate results compared to quarter benchmark model.

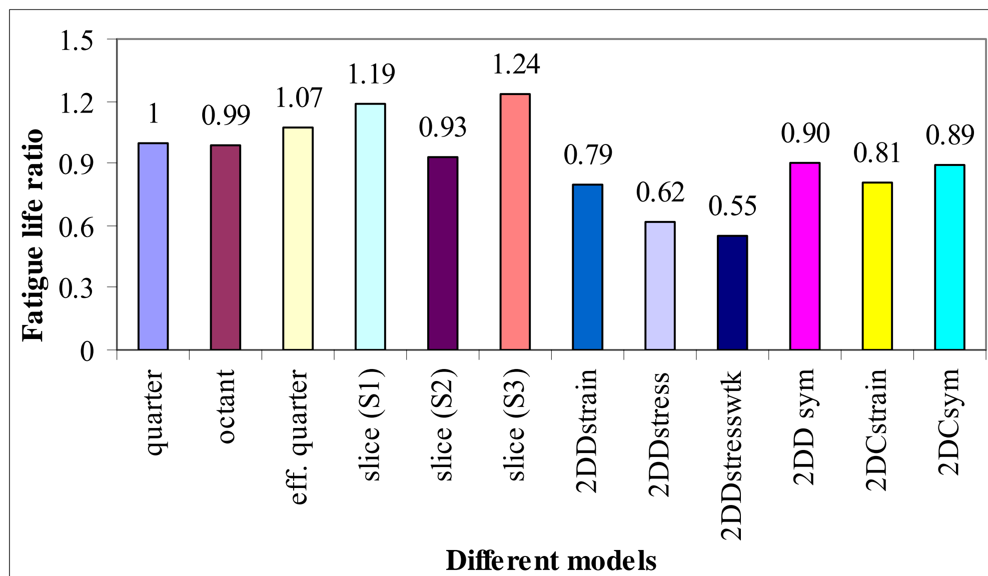

Fig. 4-14 Normalized fatigue life using different PBGA FEA models.

Solder fatigue life predictions base on different FEA models were conducted using energy-based fatigue model of Eq. (4.6). For convenience, normalized fatigue life or called fatigue life ratio as shown in Fig. 4-14 was calculated considering fatigue life predicted from quarter benchmark model as unity. It can be seen that all 2D models underestimate the PBGA solder fatigue life, especially for 2D stress with half fatigue life of quarter model. Octant, effective quarter, S2 slice and 2D symmetric models can result in accurate fatigue life predictions with error less than 10% compared to quarter benchmark model.

Table 4-6 lists comparison of element size and solving time for different PBGA FEA models and the solving time was based on computer with 2.2GHz CPU and 2GB RAM memory. It can be seen that 2D FEA model has smallest elements and shortest solving time. Therefore, 2D axisymmetric FEA model also can be used in parametric study where relative results are desirable.

ATTENTION: The Singapore Copyright Act applies to the use of this document. Nanyang Technological University Library

Table 4-6 Element size and solving time comparison for different PBGA models.

FEA models		2D	Quarter		Octant		Slice			Eff. Quarter	
			Global	Local	Global	Local	S1	S2	S3	Global	Local
Elements	Solder	1008	5688	1296	2844	648	9072	4032	9072	760	1296
	Total	5120	26564	5388	13544	2694	32640	16272	31500	10168	5388
Solving time(min.)		50	1090	330	630	140	1380	720	1320	405	330

Fig. 4-15 shows the normalized fatigue life for solder joints along PBGA diagonal considering fatigue life of critical solder ball at die corner as unity. It can be seen that solder joints under die and solder joint under component corner in PBGA component are easy to fail when subjected to thermal cycling loading. The fatigue life of the different solder joint locations labeled in Fig. 4-11 shows a normalized fatigue life of 1.57 for the solder joint at the component corner, a life ratio of 1.66 for the solder joint at the center under the silicon die. The other solder joints numbered 3, 4, 5 and 6 have a life ratio of 2.15, 2.44, 2.39 and 2.17, respectively.

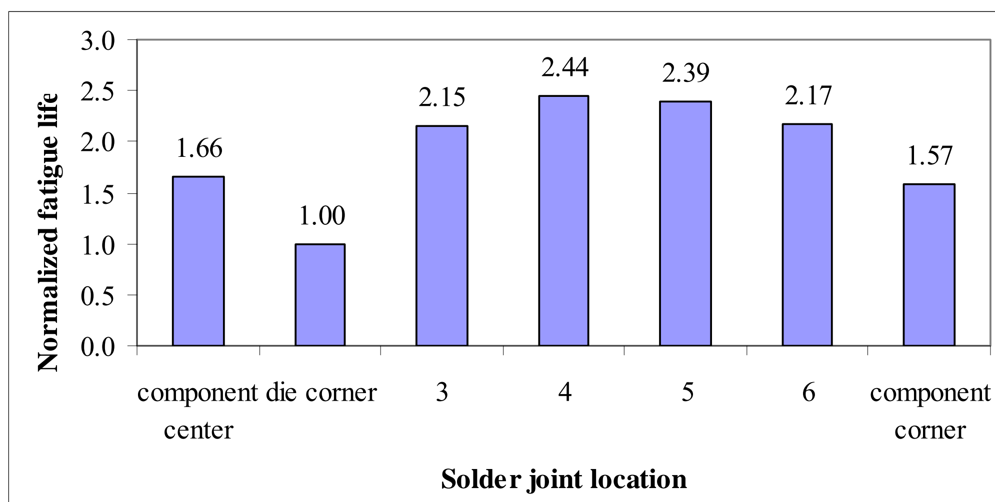

Fig. 4-15 Normalized fatigue life for diagonal PBGA solders.

3) Fatigue life prediction for PQFP and TSSOP assemblies

From FEA results, the critical solder joint is located or close to component corner for PQFP component because leads and solder joints are distributed on four peripheral

ATTENTION: The Singapore Copyright Act applies to the use of this document. Nanyang Technological University Library

sides of component which leads to larger deformation acting on corner lead and solder joint when subjected to thermal cycling loading. However, the critical solder joint is located or close to component center or die corner for TSSOP component because leads and solder joints are distributed along two longer opposite sides of component and larger deformation occurs at the lead and solder joint close to die position. Fig. 4-16 to Fig. 4-18 show the normalized fatigue life of solder joints for PQFP208, PQFP176 and TSSOP48 assemblies, respectively. The corner solder joint was selected as reference one for PQFP assembly while the center solder joint was selected as reference one for TSSOP assembly. It can be seen from Fig. 4-16 to Fig. 4-18 that the differences of solder fatigue life were 17%, 42% and 7% for PQFP208, PQFP176 and TSSOP48 components, respectively.

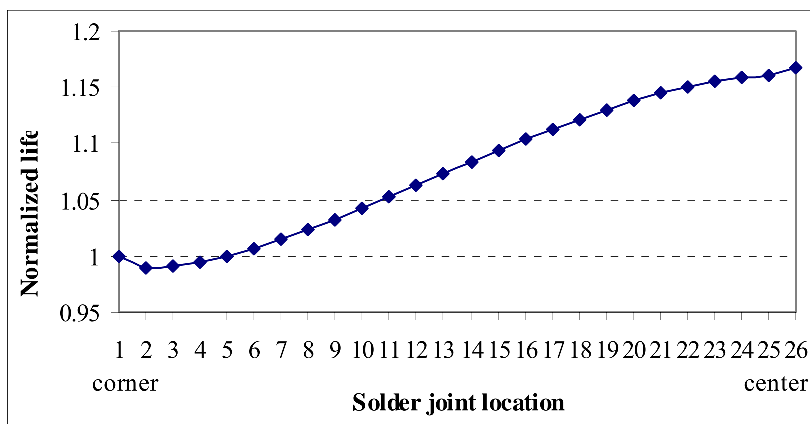

Fig. 4-16 Normalized fatigue life of PQFP208 solder joints.

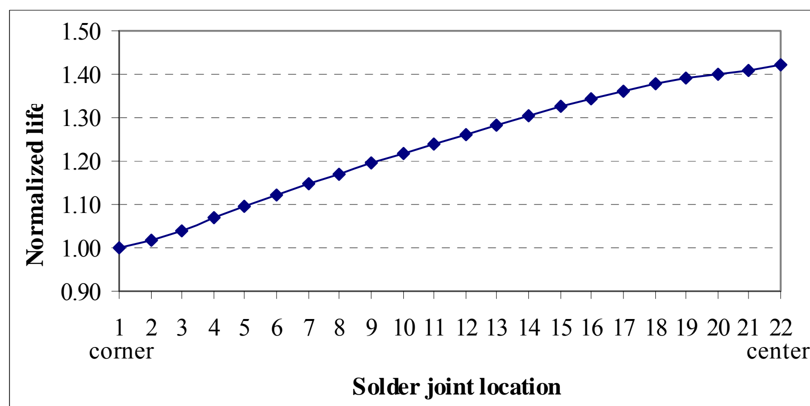

Fig. 4-17 Normalized fatigue life of PQFP176 solder joints.

ATTENTION: The Singapore Copyright Act applies to the use of this document. Nanyang Technological University Library

Fig. 4-18 Normalized fatigue life of TSSOP48 solder joints.

4) Fatigue life comparison for different components

Fig. 4-19 shows the fatigue life for leaded components including PQFP 208, PQFP176 and TSSOP48 using energy-based fatigue model of Eq. (4.6). The predicted solder fatigue life for three leaded components is more than 12000 cycles, which is consistent with test result in which no failure was found for TSSOP and a fraction of PQFP components failed after 3400 thermal cycles.

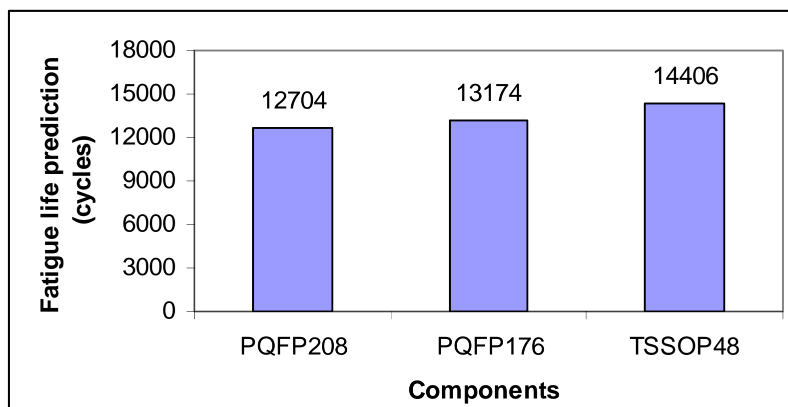

Fig. 4-19 Solder fatigue life for leaded components.

Fig. 4-20 also shows the fatigue life comparison for different assemblies considering fatigue life of PBGA316 as unity. It can be seen that the fatigue lives of PQFP assemblies are about 3 times of PBGA assembly. TSSOP assembly has longest fatigue life in four different assemblies. These simulation results are consistent with thermal cycling experimental results. Therefore, when subjected to thermal cycling

ATTENTION: The Singapore Copyright Act applies to the use of this document. Nanyang Technological University Library

loading, leaded assemblies usually have longer fatigue life compared to PBGA assemblies due to more flexible for lead in leaded assemblies than solder ball in PBGA assemblies.

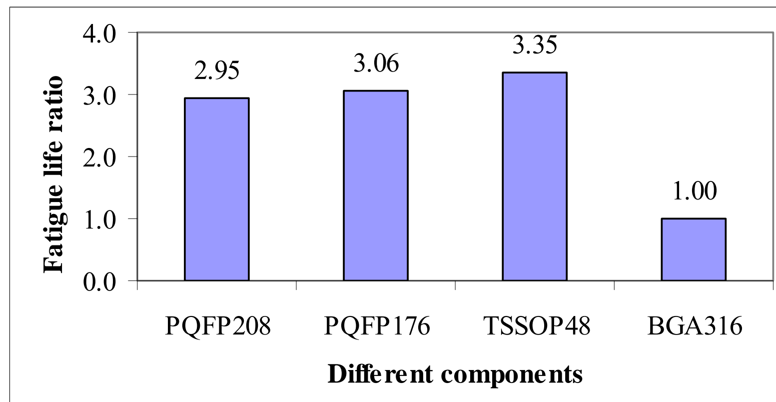

Fig. 4-20 Solder fatigue life comparison for different assemblies.

4.3.4 Parametric Study for PBGA Solder Joints

4.3.4.1 Averaged volume effect on fatigue life of PBGA solder joints

Volume averaging technique is frequently introduced for calculating plastic work density in order to minimize the effect of mesh sensitivity and stress concentration on fatigue life prediction. However, how to select suitable elements for volume-averaged plastic work density estimation is very important as it affects the fatigue life result significantly. Fig. 4-21 shows the different solder/component interface layer elements such as whole layer elements with thickness of about 1/20 stand-off height of solder ball, outer two rings elements with radius of 1/2 radius of interface circle and outermost ring elements with radius of 1/3 radius of interface circle.

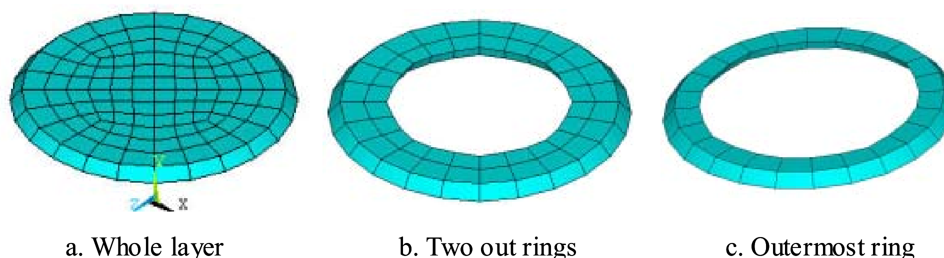

a. Whole layer b. Two out rings c. Outermost ring

Fig. 4-21 Different averaging volumes for PBGA solder joint.

ATTENTION: The Singapore Copyright Act applies to the use of this document. Nanyang Technological University Library

Fig. 4-22 shows the predicted fatigue life of solder joint based on different averaged-volumes using fatigue model of Eq. (4.6). It can be seen that fatigue life based on outermost ring elements has a good agreement with test result for specimens with OSP and Ni/Au board finish cases. From cross section analysis, many voids occur in solder joint interface for PBGA with ImAg finish due to solderability and manufacturing problem. Therefore, the test results from PBGA with Ni/Au and OSP finishes would be chosen for FEA result validation in the following studies. During thermal cycling test, the crack always initiates at the outer area of interface between solder and die due to strain concentration near this area. Then, the crack propagates along the interface so that the stress concentration area will move toward the interface center. Therefore, averaging the whole top layer volume will underestimate the plastic strain energy density and overestimate the fatigue life.

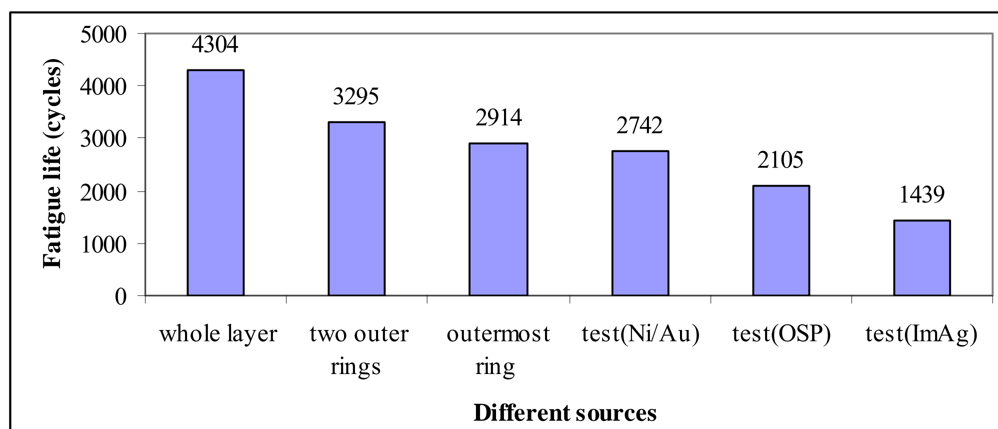

Fig. 4-22 PBGA solder joint fatigue life based on different averaging volumes.

In order to explain why outermost ring elements can result in desired fatigue life, the nonuniformity factor is introduced, which is defined as a ratio of maximum plastic work density to minimum one among selected elements. Fig. 4-23 shows the contour of plastic work density for different averaged-volumes. The nonuniformity factors of plastic work density are 10.2, 5.1 and 2.9 for whole layer, outer two rings, and outermost ring elements, respectively. Therefore, plastic work density averaged on

ATTENTION: The Singapore Copyright Act applies to the use of this document. Nanyang Technological University Library

whole layer elements results in lower magnitude which leads to higher fatigue life. In practice, crack generates around solder joint outer ring due to higher stress. Therefore, outermost ring elements are a desirable averaged-volume for fatigue life prediction.

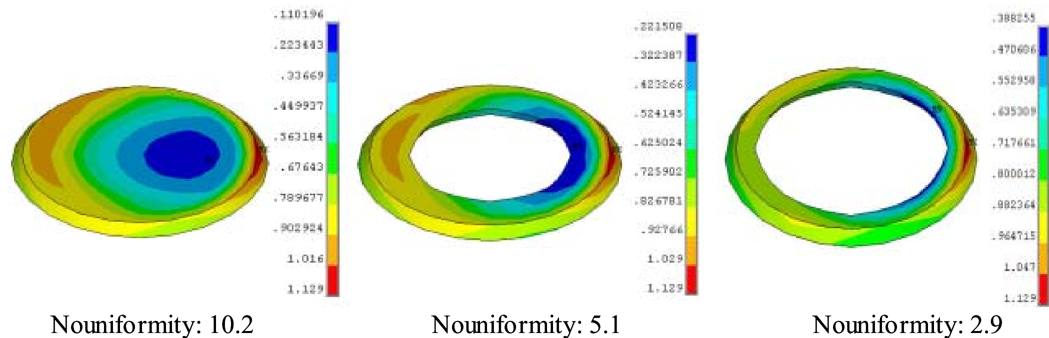

Fig. 4-23 Accumulated plastic work density contour for different averaging volumes.

4.3.4.2 Effect of constitutive models and fatigue models on solder fatigue life

In this section, elastic-plastic (EP), elastic-plastic-creep (EPC), elastic-creep (Creep) and viscoplastic (Anand) constitutive models for Sn-Ag-Cu discussed above were used in FEA simulation for PBGA assembly, respectively. For solder joint plastic behavior, the temperature dependent yield stress as listed in Table 4-7 was used.

Table 4-7 Temperature dependent yield stress of solder joint.

Temperature (^{o}C)	-40	25	50	125
Yield stress (MPa)	45.8	22.7	18.4	12.4

Based on whole interface layer volume-averaged method, accumulated strain energy densities per cycle were extracted from FEA results with different solder constitutive models. Fig. 4-24 shows the energy density results for different constitutive models. It was shown that the energy density obtained from EPC model, Creep model and Anand's model have consistent values. In EPC model, total inelastic strain energy was separated into two parts: creep part and plastic part. It can be seen from Fig. 4-24 that the creep part is dominant (EPC creep) in total inelastic energy

ATTENTION: The Singapore Copyright Act applies to the use of this document. Nanyang Technological University Library

density value (EPC total) when using EPC model for PBGA solder joint.

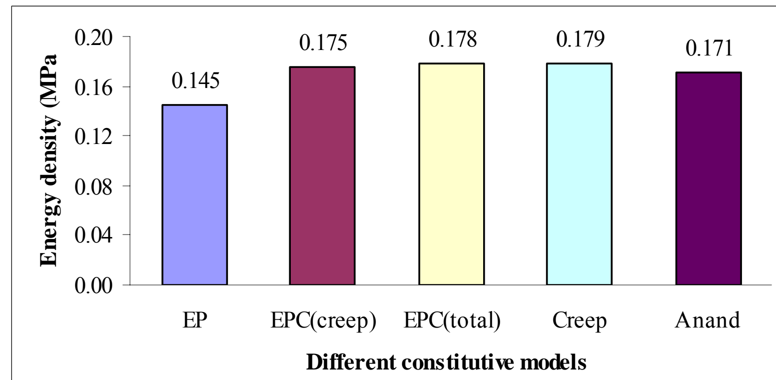

Fig. 4-24 Inelastic strain energy density for different constitutive models.

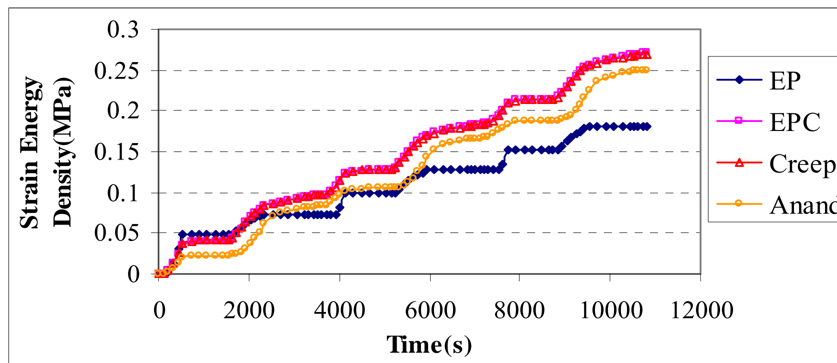

Fig. 4-25 Plot of strain energy density history for different constitutive models.

In Anand's model, plastic and creep strain energy density cannot be separated and they were unified as inelastic strain energy density. In Creep model, time-dependent creep behavior was considered and it can be developed in any stress level. In EP model, time-independent plastic behavior was considered but time-dependent creep behavior was not considered. Therefore, the energy density calculated from EP model is lower than that from the other models. These phenomena can be illuminated from Fig. 4-25 where the strain energy density was extracted from central node of solder/component interface. The data curve for EP model shows some flat lines without strain energy density increase during temperature dwell period, while strain energy density from the other models exhibit slight increase during temperature dwell due to creep behavior consideration. Therefore, EP model is not suitable in thermal cycling simulation for

ATTENTION: The Singapore Copyright Act applies to the use of this document. Nanyang Technological University Library

solder material because it cannot account for creep behavior in temperature dwell time.

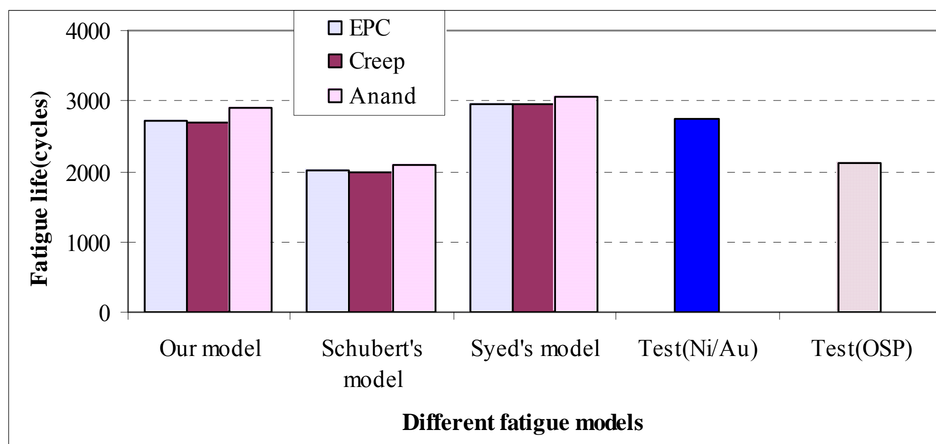

(Note: our model refers to Pang et al [24])

Fig. 4-26 Fatigue life based on different solder constitutive and fatigue life models.

In order to investigate the effect of different fatigue models on solder fatigue life, fatigue life prediction was conducted by substituting accumulated strain energy results shown in Fig. 4-24 into energy-based fatigue models such as Schubert's model of Eq. (4.8) and Syed's model of Eq. (4.10). Fatigue life was predicted based on outmost ring volume-averaged strain energy density accumulation when using our model of Eq. (4.6). Fatigue life predictions were shown in Fig. 4-26. It was shown that for selected fatigue life model, different solder constitutive models can lead to similar trend in prediction of fatigue life. Syed's model was developed by combining experimental results from different BGA package types with OSP board finish and FEA simulation results where the fatigue damage parameter was averaged based on whole solder/component interface layer elements. Schubert's model has similar trend compared with Syed's model except that different surface mount package types such as PBGA, FCOB with and without underfill has Ni/Au board finish. Therefore, fatigue life predicted by Syed's model should be compared to test result for OSP finish case while Schubert's model should be used for Ni/Au finish case. It can be seen from comparison that Syed's model results in life prediction with 40% error, Schubert's

ATTENTION: The Singapore Copyright Act applies to the use of this document. Nanyang Technological University Library

model with error of -27% and our model [24] ranges from 2% to 28% error. Therefore, all three different fatigue models give acceptable result for PBGA solder fatigue life prediction when subjected to thermal cycling. It should be noted that whole layer averaging method is reasonable in fatigue life prediction when using Syed's model of Eq. (4.10) and Schubert's model of Eq. (4.8), while outermost ring averaging method is desirable when using our fatigue model of Eq. (4.6).

Energy-based and strain-based fatigue models are widely used fatigue model for low cycle thermal fatigue life prediction. Fatigue life predictions mentioned above are all calculated using energy-based fatigue model. Now the fatigue life was predicted by energy-based and strain-based fatigue for comparison using accumulated creep strain energy density and creep strain from FEA result with solder using creep constitutive model, respectively. The accumulated creep strain per cycle was calculated by volume averaging technique:

$$\Delta\varepsilon_{cr} = \frac{\sum_{i}^{n} \varepsilon_{cr2}^{i} \cdot V_2^i}{\sum_{i}^{n} V_2^i} - \frac{\sum_{i}^{n} \varepsilon_{cr1}^{i} \cdot V_1^i}{\sum_{i}^{n} V_1^i} \tag{4.13}$$

where ε_{cr2}^{i}, ε_{cr1}^{i} is the total accumulated creep strain in one element at the end point and start point of one certain cycle, respectively, V_2^i, V_1^i is the element volume at the end point and start point of one cycle, respectively, and n is the amount of selected elements to calculate averaged creep strain. Whole solder interface layer averaging method is used for Schubert's model and Syed's model while outermost ring averaging method is used for our fatigue model.

Fatigue life results are shown in Fig. 4-27. Strain-based fatigue models used in life prediction are from Eq. (4.5) for our model [24], Eq. (4.7) for Schubert's model [47] and Eq. (4.9) for Syed's model [46]. It can be seen from Fig. 4-26 that all strain-based

ATTENTION: The Singapore Copyright Act applies to the use of this document. Nanyang Technological University Library

fatigue models predict lower fatigue life compared to energy-based models and test result. For the strain-based fatigue model, fatigue damage parameter is just inelastic strain but stress effect is not considered. In the energy-based fatigue model, the accumulated energy per cycle is calculated from stress-strain hysteresis loop in which both strain and stress are considered. Solder is a ductile material for which the energy control failure is reasonable. Therefore, the energy-based fatigue model is a better choice for solder fatigue life prediction than strain-based fatigue model.

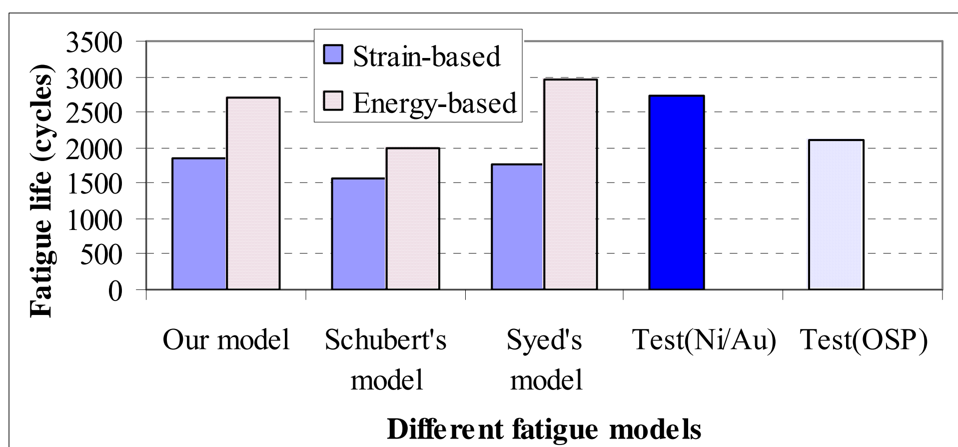

(Note: our model refers to Pang et al [24])

Fig. 4-27 Fatigue life based on strain-base and energy-based fatigue models.

4.3.4.3 Effect of different initial stress-free state conditions on solder fatigue life

In the thermomechanical FEA analysis, setting the initial conditions is important. The solder joint is formed at soldering temperature with a relatively stress-free state. When the assembly is cooled to room temperature, stresses will be developed in the assembly. Many investigators assumed a stress-free temperature at room temperature or some other arbitrary temperatures. This assumption is based on the belief that any stresses will relax due to the creep characteristics of solder. In this study, 4 different initial stress-free state temperatures as shown in Fig. 4-28, i.e. -40°C of extreme low dwell temperature, 25°C of room temperature, 125°C of extreme high dwell temperature and 150°C of mold compound curing temperature, were considered.

ATTENTION: The Singapore Copyright Act applies to the use of this document. Nanyang Technological University Library

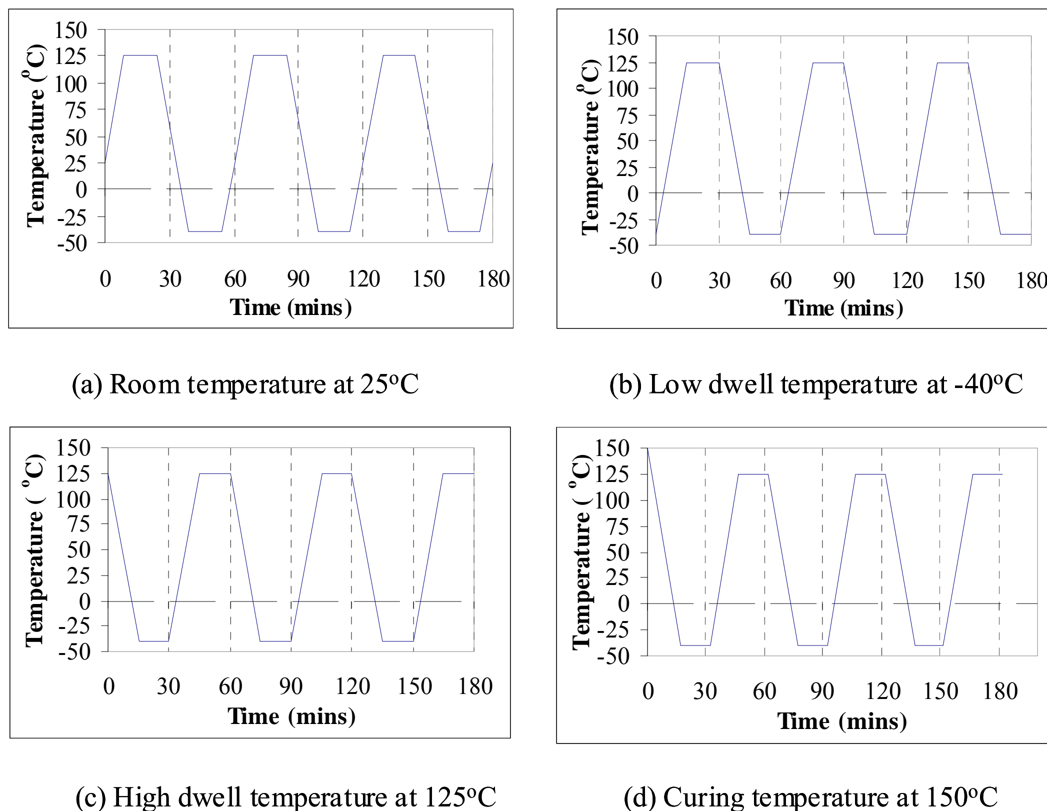

Fig. 4-28 TC profiles of 4 different initial conditions used in FEA.

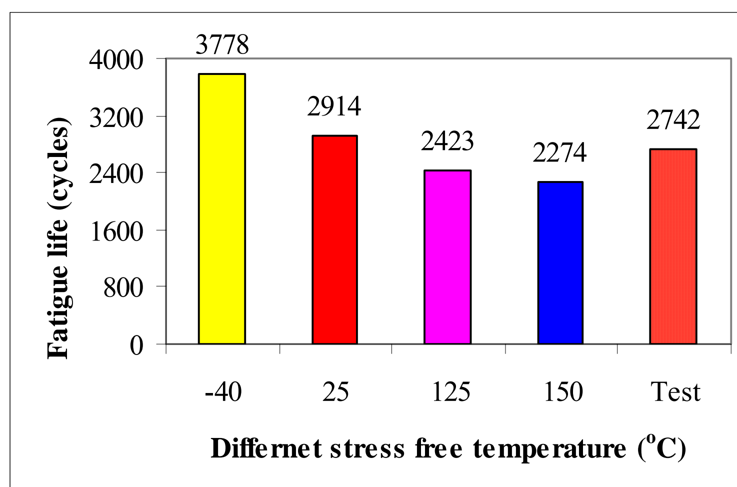

Fig. 4-29 Solder fatigue life from different initial stress-free temperature conditions.

Viscoplastic Anand's model was used in FEA simulation for solder constitutive model. In fatigue life prediction, energy-based fatigue model of Eq. (4.6) and outermost ring elements volume-averaged method were used. Fig. 4-29 shows fatigue life prediction comparison for different initial conditions cases. It can be seen that

ATTENTION: The Singapore Copyright Act applies to the use of this document. Nanyang Technological University Library

fatigue life of solder decreases with reference temperature increasing. Compared with test result, setting room temperature (25°C) as initial condition results in more accurate fatigue life than other initial conditions as electronic assembly will be in stress-free state at room temperature due to long time stress relaxation after soldering. Therefore, room temperature can be used as initial condition, which is widely used by researchers.

4.3.4.4 Intermetallic compound effect on solder fatigue life

The Cu_3Sn and Cu_6Sn_5 IMCs are formed between Cu-pad and solder joints during reflow and thermal cycling [54, 110]. When Ni/Au surface finish on Cu pad is used in package design, usually Ni_3Sn_4 IMC layer occurs at interface of solder/pad for Sn/Pb solder and tertiary IMC of CuNiSn will be formed at interface for Sn-Ag-Cu Pb-free solder during reflow and thermal cycling load. Three different IMCs of Cu_6Sn_5, Ni_3Sn_4 and CuNiSn were simulated in this study in order to investigate IMCs effect on solder fatigue life. The IMC thickness increases with the number of thermal cycle increasing and the relationship between thickness of IMC layer and time can be expressed by

$$h = \sqrt{Dt} \tag{4.14}$$

where h is IMC layer thickness and t is temperature hold time at high extreme temperature. The diffusion coefficient D is given by an Arrhenius expression [54]:

$$D=D_0\, exp(-Q/kT) \tag{4.15}$$

where D_0 is the diffusion constant, Q is the activation energy, k is Boltzmann' constant and T is the absolute temperature. The thickness of IMC layer is around 3 to 7 micron after 2000 thermal cycles from –40°C to 125°C. It is obvious that the IMC thickness increases with aging time. However, it cannot be realized in finite element modeling to model the IMC growth dynamically. Therefore, two constant IMC thicknesses of 3μm and 6μm were chosen in FEA study (see Fig. 4-30) to investigate the IMC thickness effect on solder fatigue life, thus can mimic the IMC growth effect on solder fatigue

ATTENTION: The Singapore Copyright Act applies to the use of this document. Nanyang Technological University Library

life approximately. From authors' review for previous publications of investigation for solder fatigue life using numerical simulation method, there are not considerations for the IMC effect on solder fatigue life. It was expected that solder fatigue life will be predicted more accurately when considering the IMC layer in FEA model.

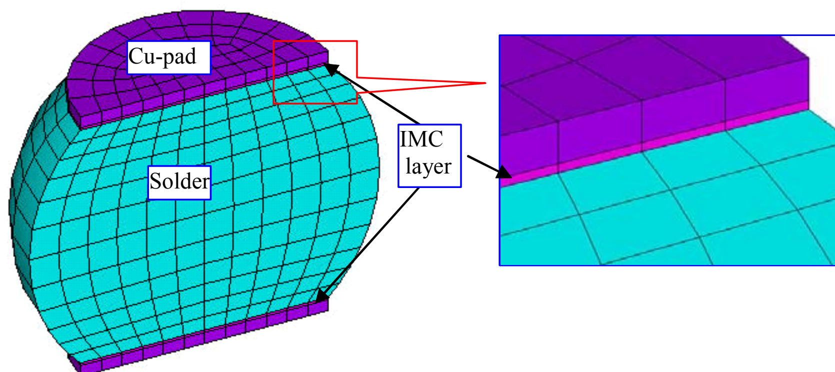

Fig. 4-30 FEA model including IMC layer.

Material properties of Cu_6Sn_5, Ni_3Sn_4 IMCs can be obtained from reported publications [111, 112]. However, material properties of tertiary IMC of CuNiSn are limited from existing literature. In this study, the Young's modulus of CuNiSn was measured by nanoindentation test using a continuous stiffness measurement technique. This technique consists of applying a small harmonic, high frequency amplitude force during loading, and measuring the contact stiffness of the specimen from the displacement response at the excitation frequency. The Young's modulus of the material is then derived from the contact stiffness. Fig. 4-31 shows the nanoindentation results of CuNiSn layer containing force vs. displacement and Young's modulus vs. displacement. The Young's modulus can be obtained from the plateau region in the figure, where the modulus is independent of depth. Table 4-8 listed Young's modulus and CTE for different IMCs used in FEA simulation. The isotropic elastic constitutive model was used for IMC layers in FEA simulation because IMC is a brittle material with very high yield stress more than 1GPa [113]. Other material models are shown in Table 4-4 and 4-5.

ATTENTION: The Singapore Copyright Act applies to the use of this document. Nanyang Technological University Library

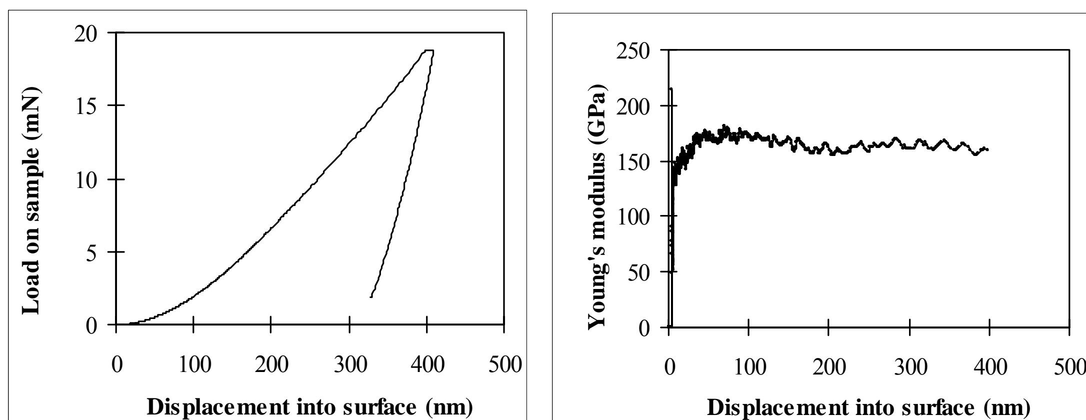

Fig. 4-31 Nanoindentation results of CuNiSn layer.

Table 4-8 Material properties of IMCs

IMC	Young's modulus (GPa)	CTE (ppm/^{o}C)	Poisson's ratio
Cu_6Sn_5	86	16.3	0.25
Ni_3Sn_4	133.3	13.7	0.25
CuNiSn	160	15.3	0.25

Anand's model was used for solder material and energy-based fatigue model of Eq. (4.6) was used for fatigue life prediction based on outermost ring elements volume averaging plastic strain energy density. The fatigue life comparisons for different IMC layers are shown in Fig. 4-32. It can be seen that IMC layer reduces the solder joint fatigue life compared to the case without considering IMC layer. Thicker IMC layer results in lower solder fatigue life. The fatigue life of solder was reduced by Ni_3Sn_4 layer more significantly than by CuNiSn and Cu_6Sn_5 layers. This is because the CTE mismatch between Ni_3Sn_4 and solder material is more significant than that between Cu_6Sn_5 or CuNiSn and solder material, which will introduce more deformation in solder/IMC interface during thermal cycling. The fatigue life of solder reduced slightly by Cu_6Sn_5 layer with different thickness compared with the case without simulating IMC layer. However, from the numerical simulation view of point, the IMC effect on solder fatigue life is distinct with fatigue life prediction error varying from 2.3% to

ATTENTION: The Singapore Copyright Act applies to the use of this document. Nanyang Technological University Library

10.8% for the case of simulating IMCs compared to without simulating IMC layer. Therefore, without considering IMC layer in FEA analysis predict slightly higher solder fatigue life compared to the case of modeling IMC layer.

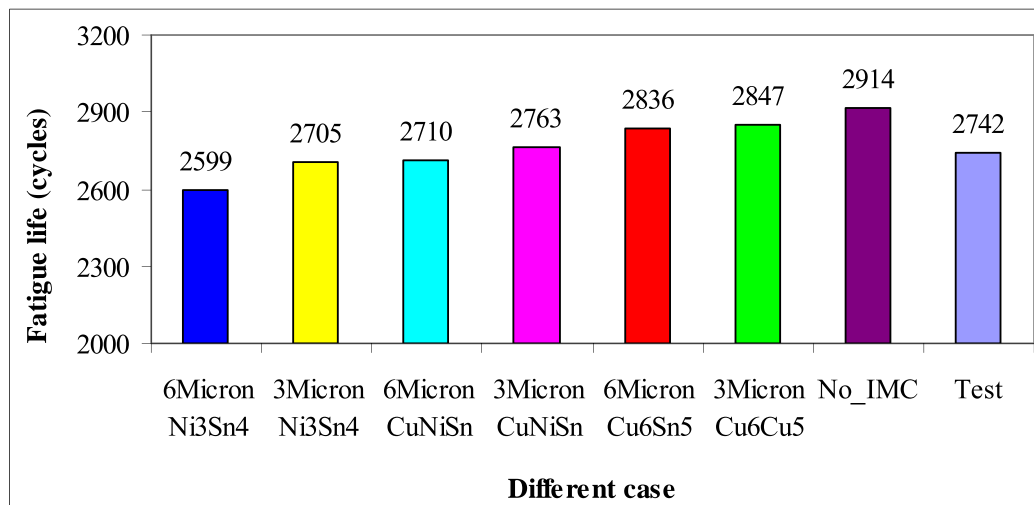

Fig. 4-32 IMC effect on solder fatigue life.

4.3.4.5 NSMD vs. SMD

Solder mask defined, SMD, and non-solder mask defined, NSMD are two typical package design in electronic assembly. In FEA modeling and simulation, NSMD and SMD models are widely used for BGA assembly. In this study, two different models were considered in FEA simulation in order to compare the effect of SMD on fatigue life of solder joint. Fig. 4-33 shows typical solder joint cross-section and two different FEA models. The height of solder ball is same for two FEA models. The solder mask material properties such as CTE have a significant effect on solder fatigue life. Two different solder masks were simulated in this study. One solder mask is called SMD1 with Young's modulus of 2GPa, Poisson's ratio of 0.35 and CTE of 30ppm/^{o}C [114]. The other solder mask is called SMD2 with Young's modulus of 4.9GPa, Poisson's ratio of 0.4 and CTE of 70ppm/^{o}C. Viscoplastic Anand's model was used for solder material and fatigue life was predicted based on our energy-based fatigue model [24] and outermost ring volume averaging method.

ATTENTION: The Singapore Copyright Act applies to the use of this document. Nanyang Technological University Library

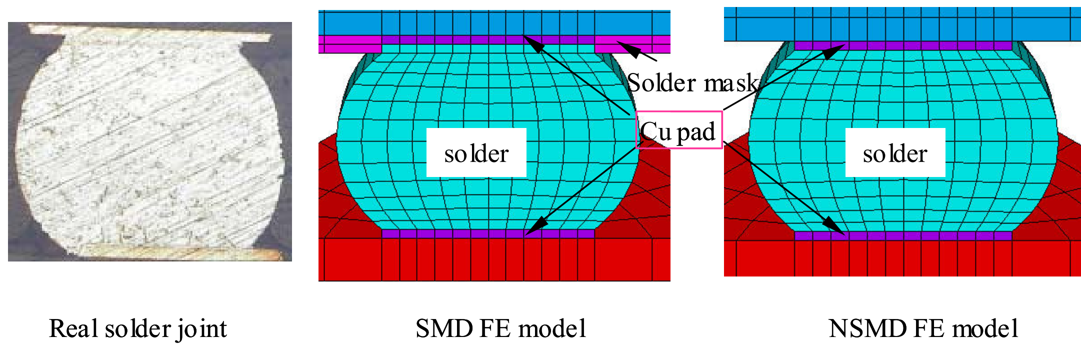

Fig. 4-33 SMD FEA model vs. NSMD FEA model.

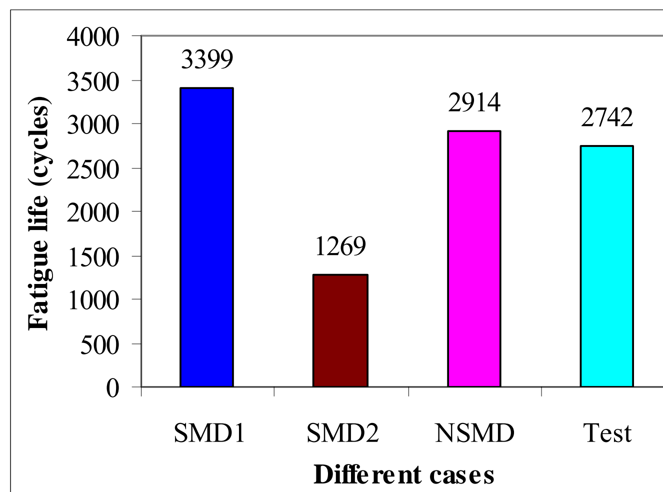

Fig. 4-34 Fatigue life comparison between SMD and NSMD FEA models.

Fig. 4-34 shows the SMD effect on solder joint fatigue life. It can be seen that the SMD1 used on package side can increase 9.5% fatigue life of solder joint compared to NSMD case. However, SMD2 reduces fatigue life of solder by 58%. This different effect of SMD on fatigue life of solder is due to different CTE values of solder mask material. SMD1 has solder mask with CTE of 30ppm/^{o}C close to solder CTE of 24.5ppm/^{o}C, thus the solder mask can protect solder/package interface by reducing deformation acting on solder joint. However, CTE mismatch is significant between solder mask of SMD2 (70ppm/^{o}C) and solder material (24.5ppm/^{o}C), which can increase deformation of solder during thermal cycling leading to shorter fatigue life of solder joint. Therefore, it is important to select suitable solder mask material properties, especially CTE value, when using solder mask design in electronic packaging.

ATTENTION: The Singapore Copyright Act applies to the use of this document. Nanyang Technological University Library

4.3.4.6 Thermal shock (TS) vs. thermal cycling (TC)

Generally, the definition of TS and TC tests are based on temperature ramp rate. TS profile has high ramp rate, for example, more than 30°C /min, and TC profile has low ramp rate. The main advantage of TS test is for saving time. In this study, FEA simulation was used to investigate the temperature ramp rate effect on fatigue life of solder. Table 4-9 shows the detailed information for TS and TC profiles. Fatigue life of solder was calculated based on energy-based fatigue model and outermost ring element volume averaged plastic strain energy density as shown in Table 4-9. It can be seen that fatigue life under TS condition is slightly less than that under TC condition. This result is consistent with those given by Pang et al. [115] in which TC and TS tests were carried out for FCOB assembly with 96.5Sn-3.5Ag solder joint. It was recommended from FEA result that TS test is the first choice due to timesaving when testing machine is available.

Table 4-9 Thermal loading and fatigue life between TS and TC.

Profile	Ramp time (Mins)	Dwell time (Mins)	Ramp rate (°C/min)	Cycle time (Mins)	W_p (MPa)	Fatigue life (cycles)	Life ratio (TS/TC)
TS	3.3	5	50	16.6	0.248	2858	98.1%
TC	15	15	11	60	0.243	2914	

4.3.4.7 Temperature range effect on solder fatigue life

Electronic products can be subjected to thermal cycling with different temperature ranges that result in different fatigue life of solder joint. JEDEC standard of temperature cycling provides different test conditions, where condition G (-40~125°C), J (0~100°C), K (0~125°C), L (-55~110°C), and M (-40~150°C) as shown in Fig. 4-35 can be used with frequency of 1 cycle/hour and soak time of 15minutes.

ATTENTION: The Singapore Copyright Act applies to the use of this document. Nanyang Technological University Library

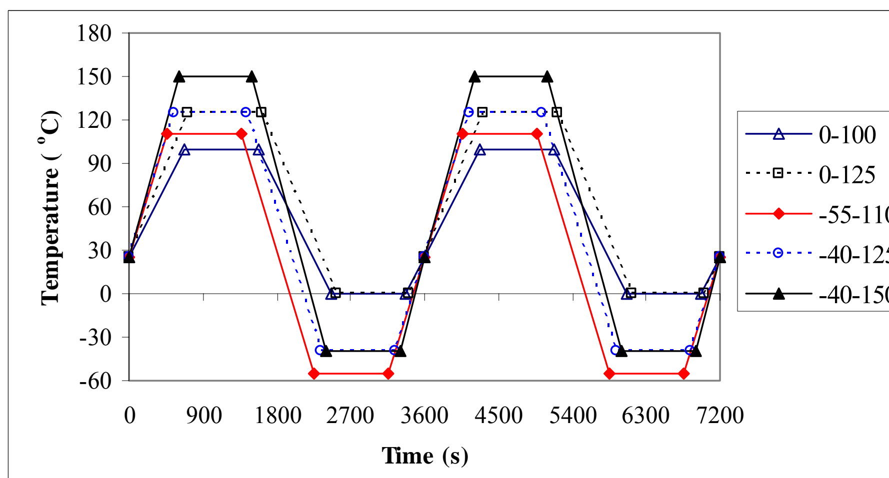

Fig. 4-35 Different thermal cycling profiles.

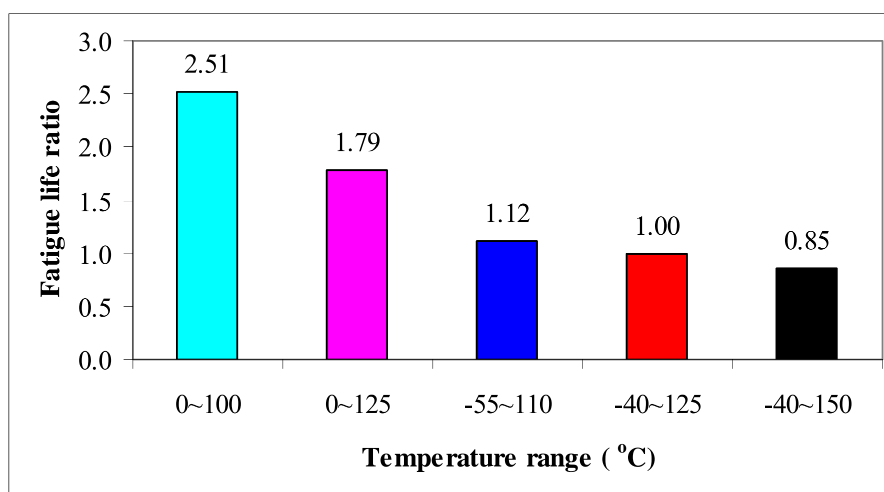

Fig. 4-36 Fatigue life ratio for different temperature ranges.

These test conditions have different temperature ranges and same cycle frequency. In order to investigate the temperature range effect on solder fatigue life, these test conditions were simulated using FEA, respectively. For convenience, 2D axisymmetric FEA model and Anand constitutive model were used for PBGA assembly. For different conditions, the stress-free state of room temperature was employed. Accumulated plastic work density per cycle based on volume-averaged method was selected as damage parameter for solder fatigue life prediction. For convenience, the normalized fatigue life was calculated considering fatigue life under condition G (-40~125°C) as reference life. Fig. 4-36 shows the fatigue life comparison

ATTENTION: The Singapore Copyright Act applies to the use of this document. Nanyang Technological University Library

for different temperature range conditions. It can be seen that fatigue life increases when temperature range decreases. Conditions G (-40~125°C) and L (-55~110°C) have same temperature range but different maximum temperature values. Condition G with higher maximum temperature induces lower fatigue life than condition L with lower maximum temperature because solder joint exhibits larger deformation under higher maximum temperature. These results have similar trend with that from Eq. (2.55) of calculating accelerated factor. In terms of Eq. (2.55), accelerated factor increases with temperature range decreasing in field condition and with maximum temperature decreasing in field condition. The study of temperature range effect on solder fatigue life can help engineers to select suitable test condition for specified specimen.

4.4 SUMMARY

Thermal cycling reliability test and FEA simulation were conducted for Pb-free electronic assemblies. PBGA assembly is more sensitive to thermal cycling than leaded assemblies such as PQFP and TSSOP, which was verified by test and FEA results. From failure analysis for PBGA component, failure mode exhibits solder fatigue failure with failure site very close to solder/IMC interface and more cracks occur at component side than board side.

In FEA simulations for PBGA assembly, 3D Quarter model or octant model can give more accurate results than 2D model and 3D slice model. Similar results can be obtained for different solder constitutive models such as elastic-plastic-creep model, elastic-creep model and viscoplastic Anand’s model. Elastic-plastic model is not suitable for thermomechanical FEA simulation because creep behavior cannot be considered. When using EPC model, plastic strain is very small compared to creep

ATTENTION: The Singapore Copyright Act applies to the use of this document. Nanyang Technological University Library

strain for PBGA assembly.

Solder fatigue life decreases with stress-free temperature increasing and selecting room temperature as stress-free state is reasonable. Solder fatigue life decreases with IMC layer thickness increasing. Fatigue life under thermal shock condition is less than that under thermal cycling condition slightly. Fatigue life decreases with temperature range increasing, and for same temperature range, fatigue life with higher maximum temperature is less than that with lower maximum temperature.

Fatigue damage parameter based on averaging whole interface volume method is reasonable when using Syed's and Schubert's fatigue models, while result based on outermost ring volume averaging method is reasonable and proper in solder fatigue life prediction when using our fatigue model [24]. Energy based fatigue models predict more accurate fatigue life than strain based fatigue models.

ATTENTION: The Singapore Copyright Act applies to the use of this document. Nanyang Technological University Library

CHAPTER 5 BEND FATIGUE TEST AND ANALYSIS FOR VQFN ASSEMBLY

5.1 INTRODUCTION

Bend loading is encountered for handphone board-level keypad loading test. Three-point and four-point bend tests with cyclic or monotonic loading may be used. Cyclic bend test can evaluate the fatigue reliability of electronic assembly, while monotonic bend test is intended to characterize the fracture strength and overstress of solder joints. Three-point bend test is useful for generating reliability data for multiple packages tested under different load levels (bending moments) in a single test. While four-point bend test is suitable for testing large sample size of packages at similar loading condition (same bending moments) between the inner load span region.

Shetty et al. [63, 64] reported cyclic three-point bend tests from zero curvature to maximum curvature for Chip Scale Packages (CSP) mounted on both sides of PCB. Before cyclic bend test, overstress monotonic three-point bend tests were conducted to determine the overstress limits for CSP assembly. Fatigue life was developed based on bending strain and failure data. However, bending strain of PCB measured during bend test is not a useful fatigue damage parameter for determining solder fatigue failure because bending strain can be affected by many factors such as PCB thickness and material properties, load profile, support span and load span, package type, etc. Fatigue damage parameters for solder fatigue failure should be used and the solder stress (S-N) or strain (ε-N) or energy (W_p-N) fatigue life approach needs to be developed and is reported in this chapter.

ATTENTION: The Singapore Copyright Act applies to the use of this document. Nanyang Technological University Library

Skipor and Leicht [66] conducted mechanical bending fatigue test for BGA and wafer level CSP by introducing a new support method, that was, the specimen was suspended at three simply hinged support points and load cell was centrally located over the specimen center. Coffin-Manson fatigue model was used to correlate the peeling inelastic strain and fatigue cycle. Numerical analysis for the influence of package substrate material on bend fatigue was studied. It was shown that solder fatigue life would be enhanced due to significant reduction of inelastic strain when Young's modulus of substrate material decreases. It was also found that a thinner substrate is preferred when the Young's modulus of substrate is high, while a thicker substrate results in lower solder strain when the modulus of substrate is lower.

Mercado et al. [67] introduced a four-point bend fixture capable of two-sided bend test from positive to negative deflections and investigated the effect of loading frequency with 1Hz, 3Hz and 5Hz and deflection levels with 1.5mm, 2mm, 3mm, and 4mm on fatigue reliability of handheld components. Correlation between four-point and three-point bend was also developed.

Geng et al. [68] studied the effect of loading rate on PBGA solder joint reliability using four-point bend test with three different loading speeds of 2.54mm/min, 25.4mm/min and 254mm/min. It was shown that solder joint fatigue failure is dependent on bend loading rate. At high loading rate, solder joint failed at less board deflection. Therefore, traditional quasi-static bending test is not sufficient to quantify solder joint failure under shock load.

All the bend tests from above reported literature were conducted at room temperature (25°C) and were for tin-lead (Sn-Pb) solder joints. In this study, SnAgCu solder joints were investigated at both 25°C and 125°C. Four-point bend test at 125°C is presented in this study for the first time in terms of literature review. VQFN

ATTENTION: The Singapore Copyright Act applies to the use of this document. Nanyang Technological University Library

assembly with peripheral solder joint with Sn-Ag-Cu lead-free solder was tested under three-point and four-point cyclic bending load at room temperature (25°C) and high temperature (125°C). The correlation between three-point bend and four-point bend was developed and verified by test results. Temperature effect on bending fatigue life was evaluated and accelerated factor was presented. Validation of one-level submodeling method transiting from board-level model to solder-level model was carried out. Fatigue model was created based on FEA results and fatigue test data using strain energy density as a fatigue damage parameter.

5.2 CYCLIC BEND TEST AND ANALYSIS

5.2.1 Test Vehicle and Fixture

VQFN (Very thin Quad Flat No lead package) assembly with Sn-Ag-Cu Pb-free solder was selected for cyclic bend test in this study. The specimen size as shown in Fig. 5-1 follows JEDEC standards [117, 118]. Two different board side surface finishes including Ni/Au and OSP were investigated in order to study surface finish effect on fatigue failure of VQFN component under cyclic bending load. For specimen with OSP finish, two types of test boards as shown in Fig. 5-1 were used: one type of test board has 5 components and the other type of test board has 15 components. For specimen with Ni/Au finish, one type of test board with 5 components was used. The structure of VQFN component is shown in Fig. 5-2. VQFN package with geometry size of 7mm×7mm×0.8mm was mounted on the FR-4 PCB with size of 132mm×77mm×1mm (L×W×H) by 48 Sn-Ag-Cu solder joints with 0.1mm thickness. Silicon die has the size of 3mm×3mm×0.254mm. One daisy chain loop containing all 48 solder joints was designed for each VQFN component in order to take in-situ measurement of resistance.

ATTENTION: The Singapore Copyright Act applies to the use of this document. Nanyang Technological University Library

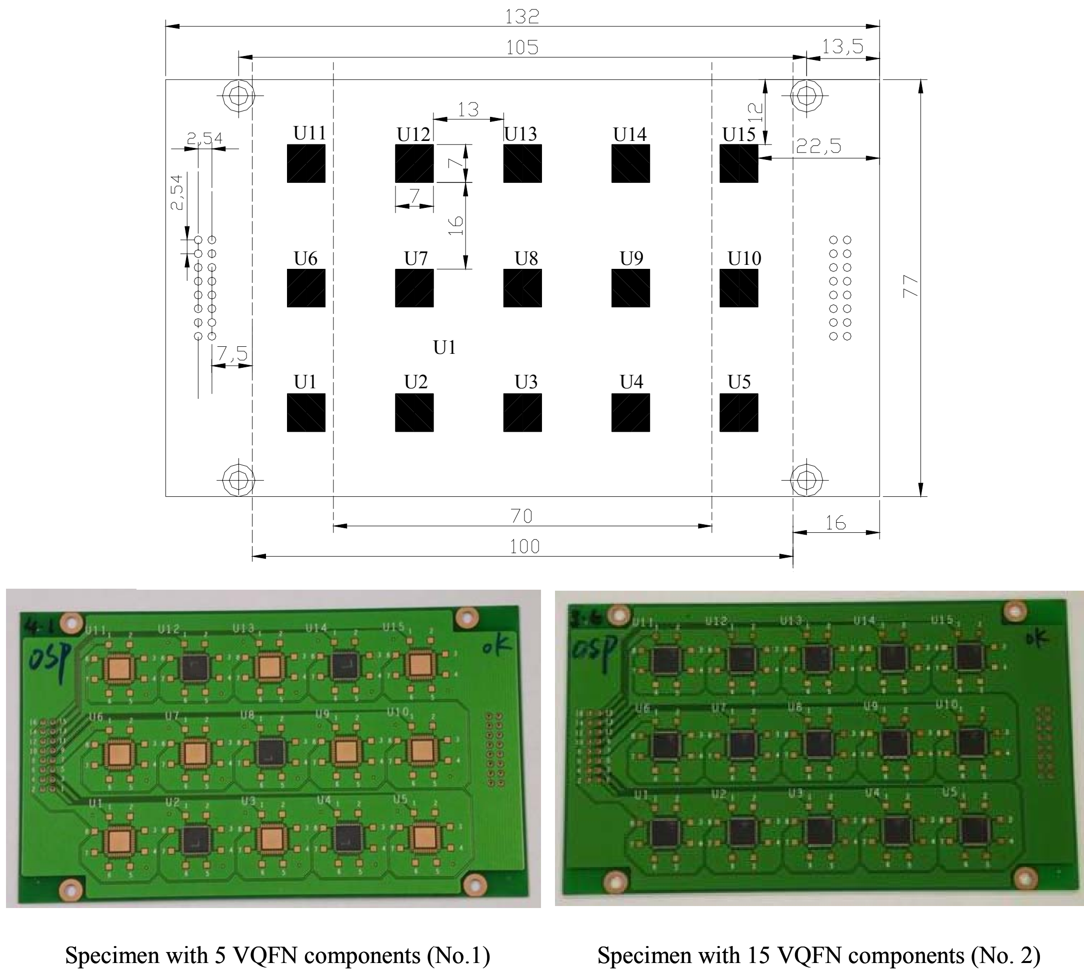

Specimen with 5 VQFN components (No.1)　　Specimen with 15 VQFN components (No. 2)

Fig. 5-1 Board size and layout of VQFN specimens.

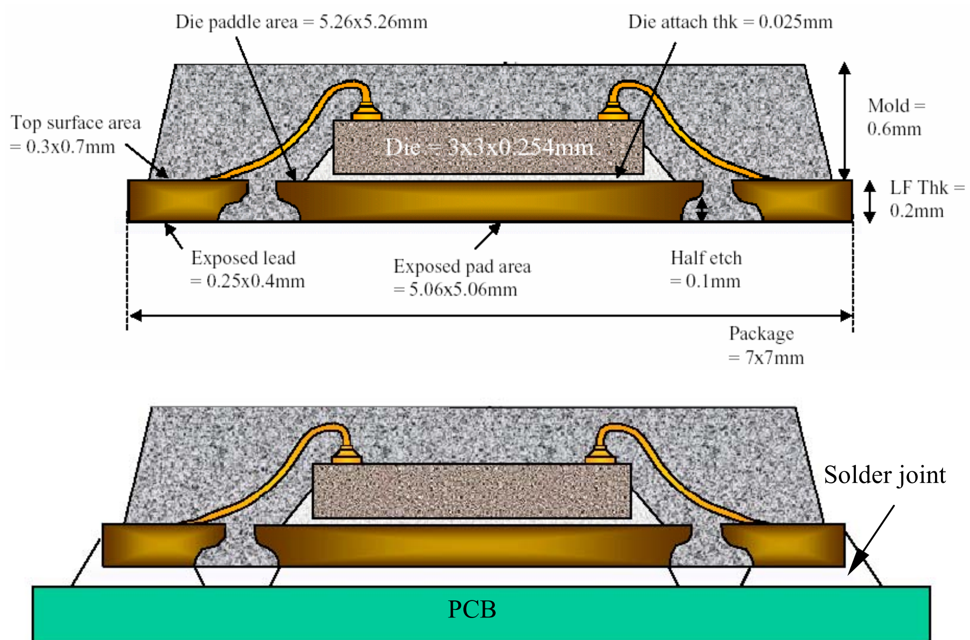

Fig. 5-2 Structure of VQFN package.

ATTENTION: The Singapore Copyright Act applies to the use of this document. Nanyang Technological University Library

Bend fatigue tests of specimen were accomplished by using an Instron test machine with thermal chamber. The failure event was detected when resistance greater than 300 ohms lasting for 0.1second or longer. Four-point and three-point bend tests were conducted in order to make correlation between them. Fig. 5-3 shows fixture for four-point bend and three-point bend. Anvil radius and length of fixture satisfy requirement of bend test given by IPC/JEDEC-9702 standard [118]. The support span of 100mm and load span of 70mm as shown in Fig. 5-1 were used for four-point bend test. For three-point bend test, support span of 100mm was also used. Constant bending moment can be obtained between load head in four-point bend test so that all the samples within the load span are subjected to the same stress level (bending moment or curvature), which significantly increase the sample size suitable for Weibull analysis. Therefore, in four-point bend test, all five components are used for test board No.1 and nine components along three center rows for test board No.2 are used.

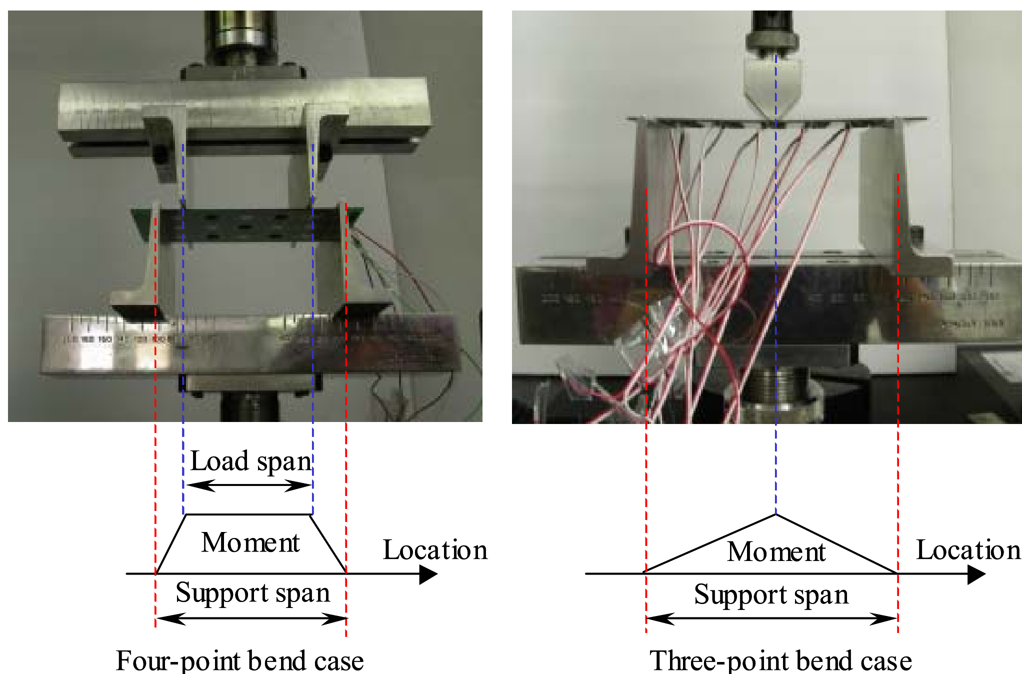

Fig. 5-3 Three and four-point bending test fixtures.

ATTENTION: The Singapore Copyright Act applies to the use of this document. Nanyang Technological University Library

5.2.2 Three-Point Bend Test and Analysis

Three-point cyclic bend test was widely used by researchers in order to investigate mechanical bend fatigue of electronic packages. In this study, VQFN assembly with OSP finish was used in three-point bend test using displacement control. Displacement range from 1mm to 5 mm with a frequency of 1Hz was applied to specimen center with chip down condition as shown in Fig. 5-3, which gives a positive to positive curvature fatigue test. Three components (U3, U8 and U13) located at the center row of specimen as shown in Fig 5.1 have the same stress level (bending moment). Three components at right row (U2, U7 and U12) and three components at left row (U4, U9 and U14) have the same stress level (bending moment) due to symmetry. Failure data of component at right and left rows satisfy Weibull distribution as shown in Fig. 5-4. Mean-time-to-failure (MTTF) was calculated from Weibull distribution model.

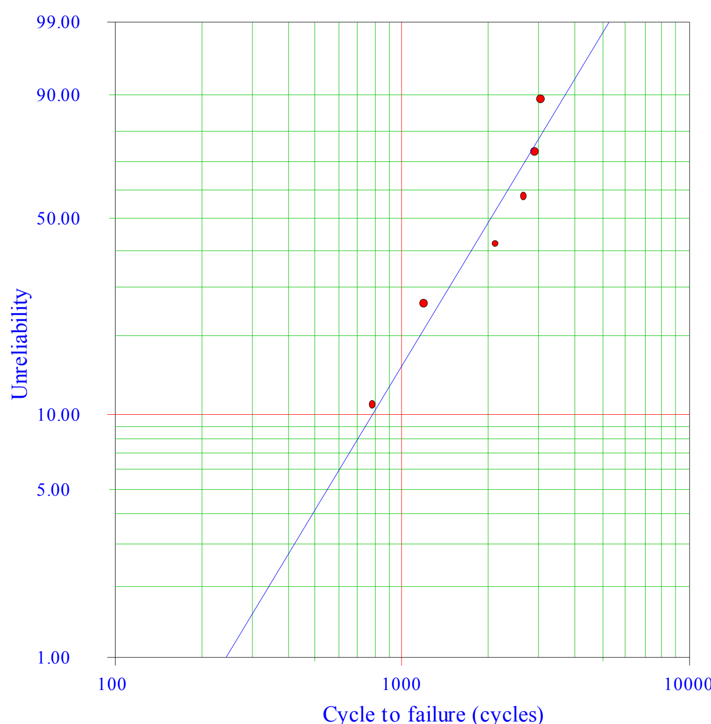

Fig. 5-4 Weibull plot of cycle to failure for three-point bend test.

Table 5-1 shows the failure data for three-point bend test. No Weibull parameters were shown for center row component failure due to limited sample size. Arithmetical

ATTENTION: The Singapore Copyright Act applies to the use of this document. Nanyang Technological University Library

average of fatigue cycles for all components under the same stress level was also calculated. It can be seen that averaged life and MTTF are close. The fatigue life of components at center row is less than that at right and left rows dramatically due to different stress levels. It is one major disadvantage of three-point bend test that failure is dependent of component locations, which reduce the number of components subjected to the same stress level. Moreover, the limited sample size and large board-to-board variation will result in larger variation in failure data for three-point bend.

Table 5-1 Weibull parameters and failure cycles for three-point bend test.

Component location	Slope	Char. life	MTTF	Averaged life	Life range
Right and left row	2.0	2432	2155	2111	787~3033
Center row	-	-	-	512	422~563

5.2.3 Four-Point Bend Test and Analysis

In the four-point bend test, failures of components between loading anvils are independent of component locations due to uniform stress strain region, which can increase the sample size for reliability analysis. The correlation between three-point bend and four-point bend was carried out firstly. From limited literature review, no bend tests at high temperature, say, 125°C, were reported. In this study, four-point bend tests were conducted at room temperature and high temperature of 125°C in order to investigate high temperature effect on bending fatigue failure.

5.2.3.1 Correlation between three-point bend and four-point bend

Correlation between three-point bend and four-point bend was performed considering components in four-point bend test subjected to the same bending moment value as components of center row, right and left rows in three-point bend test. Based on classic beam theory, the maximum deflection for three-point bend with centered loading

ATTENTION: The Singapore Copyright Act applies to the use of this document. Nanyang Technological University Library

condition can be expressed as:

$$f = \frac{pl^3}{48EI} \tag{5.1}$$

where p is the load applied on specimen, l is support span (100mm in this study), E and I are Young's modulus and moment of inertia of specimen, respectively. For centered loading case, the maximum deflection and maximum moment occur at centered loading point. The maximum moment can be obtained by:

$$M_C = M_{\max} = \frac{pl}{4} \tag{5.2}$$

where M_C is moment applied on components of center row in three-point bend test. Substituting Eq. (5.1) to Eq. (5.2), yield:

$$M_C = \frac{12EIf}{l^2} \tag{5.3}$$

The moment value of M_R applied on components of right row can be obtained considering specimen layout as shown in Fig. 5.1

$$M_R = \frac{3}{5} M_C = \frac{36EIf}{5l^2} \tag{5.4}$$

Pure bend condition occurs between loading anvils in four-point bend test. The following equation can be derived from classic beam theory when any effects due to the packages and the Poisson's ratio effect of a plate in bending are ignored:

$$\delta = \frac{\varepsilon(L_S - L_L)(L_S + 2L_L)}{6t} \tag{5.5}$$

where δ is displacement of loading anvil, ε is global PCB strain, L_S is support span of 100mm, L_L is load span of 70mm, and t is PCB thickness of 1mm. The global strain of PCB surface is a function of curvature expressed as:

$$\varepsilon = \frac{y}{\rho} \tag{5.6}$$

ATTENTION: The Singapore Copyright Act applies to the use of this document. Nanyang Technological University Library

where y is distance of PCB surface to middle plane, equating to half thickness of PCB. The curvature can be expressed as follows:

$$\frac{1}{\rho} = \frac{M}{EI} \tag{5.7}$$

Combining above three equations and substituting known value, the relationship between moment and displacement of loading anvil can be obtained as follows:

$$M_4 = \frac{\delta EI}{600} \tag{5.8}$$

The same moment value leads to the same global stress strain level. Therefore, in order to use four-point bend test to simulate stress level of center row components in three-point bend test, let moment value of Eq. (5.3) equal to that of Eq. (5.8), getting:

$$\delta_{4C} = 0.72 f_3 \tag{5.9}$$

where δ_{4C} and f_3 are displacement of loading anvil in four-point bend and three-point bend tests, respectively. Similarly, let moment of Eq. (5.4) equal to that of Eq. (5.8), the relationship of displacement in four-point bend and three-point bend can be obtained in order to use four-point bend to simulate the same stress level of right row components in three-point bend:

$$\delta_{4R} = 0.432 f_3 \tag{5.10}$$

VQFN assemblies with OSP surface finish were selected for four-point bend tests in order to take comparison between four-point bend and three-point bend. Displacement range from 0.72mm to 3.6mm and from 0.432mm to 2.16mm was used in four-point bend tests to simulate stress level of center row components and right row components in three-point bend test with displacement rang from 1mm to 5mm, respectively. Three uniaxial strain gauges as shown in Fig. 5-5 were mounted on test board according to requirement of JEDEC standard [118]. Strain gage mounted on opposite side of PCB as component and positioned at package center was used to

ATTENTION: The Singapore Copyright Act applies to the use of this document. Nanyang Technological University Library

measure the local stiffening effect of VQFN package. Strain gage mounted on opposite side of PCB as component and positioned at package corner was used to measure the maximum PCB strain. Strain gage mounted on same side of PCB as component and centered between package edge and anvil centerline was used to measure the global PCB strain. The sensing direction of all strain gages was aligned with the longitudinal board direction, which is coincident with PCB principal strain angle. The measured strain value can also be used for verification of finite element result.

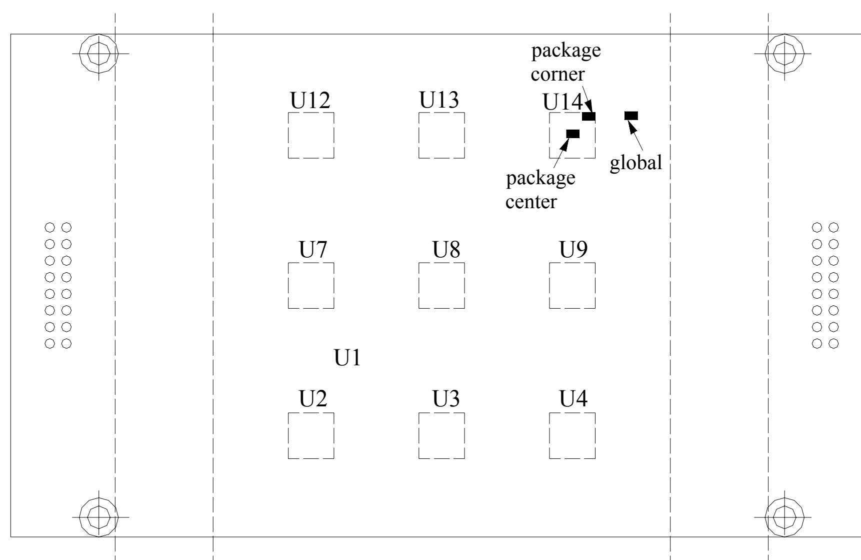

Fig. 5-5 Strain gage location on test board.

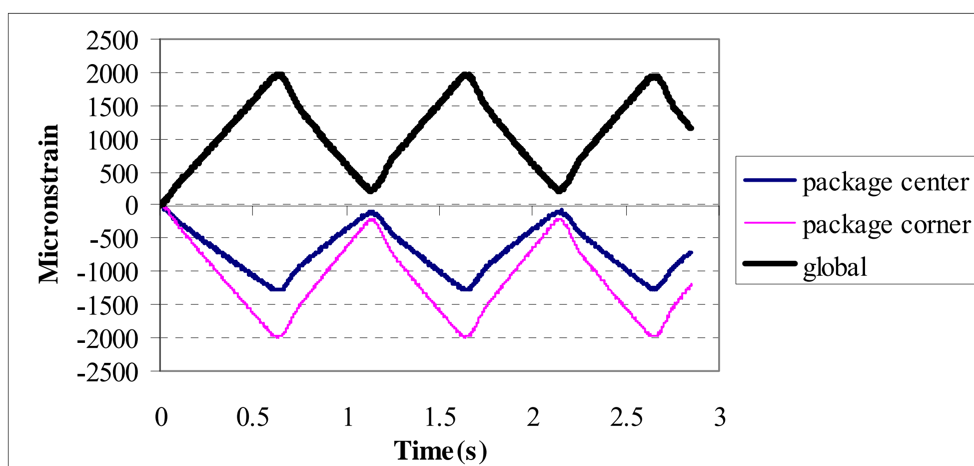

Fig. 5-6 Strain measurement of different positions during cyclic bend.

Fig. 5-6 shows the strain values measured by three strain gages during cyclic four-

ATTENTION: The Singapore Copyright Act applies to the use of this document. Nanyang Technological University Library

point bend test at 25°Cwith displacement from 0.432mm to 2.16mm. The maximum strains are 2000με, 1960με and 1280με for package corner, global and package center strain gages, respectively. Therefore, the local stiffening effect of VQFN package on global PCB strain is obvious. The package corner strain is slightly more than global PCB strain.

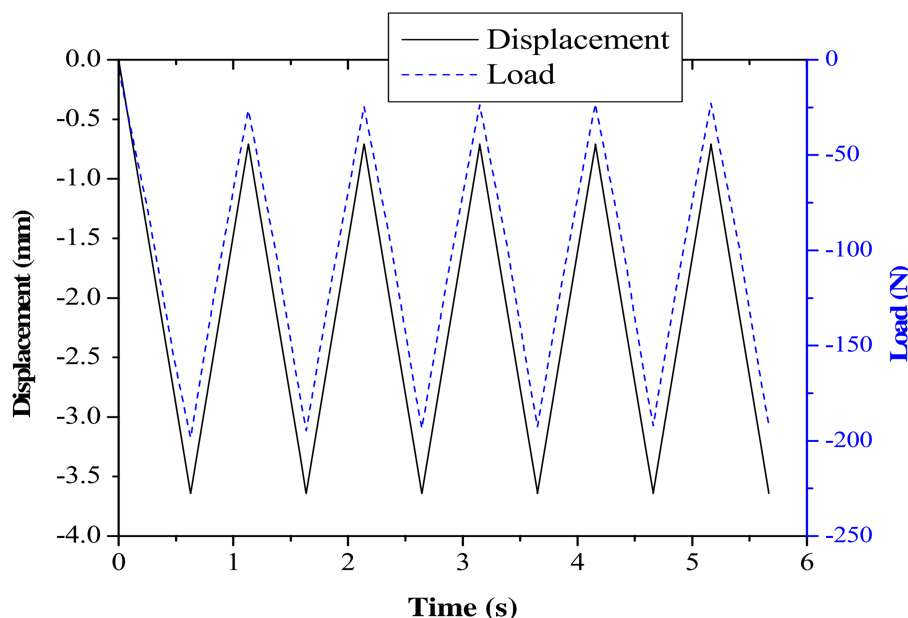

Fig. 5-7 Typical displacement and load profiles for four-point bend.

Fig. 5-7 shows the loading and displacement profile during four-point bend test with displacement control from 0.72mm to 3.6mm. The maximum load is about 190N at maximum displacement of 3.6mm. Some researchers [63, 64] correlated global displacement, strain or loading and solder fatigue failure to develop the solder fatigue model. Solder fatigue life, however, is controlled by stress strain behavior of solder itself not by global displacement or loading even though solder stress strain is related to global load. Many parameters such as support/load span, anvil displacement, package type and layout, PCB thickness and material properties, etc. could affect solder fatigue life at same displacement or loading condition. In this study, general solder fatigue model was developed based on different bend test data and FEA results

ATTENTION: The Singapore Copyright Act applies to the use of this document. Nanyang Technological University Library

using strain energy density of solder joint as damage parameter. The package failure was detected when resistance of daisy chain was more than 300ohms.

Fig. 5-8 shows the typical resistance change of daisy-chained current loop with cycles during four-point bend test with displacement from 0.72mm to 3.6mm.

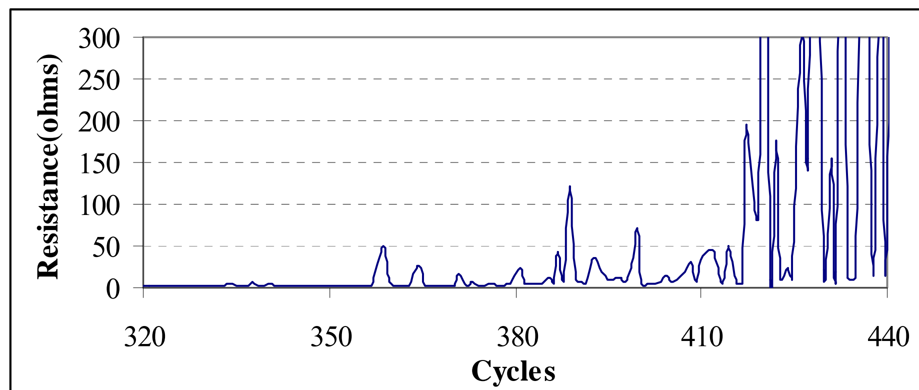

Fig. 5-8 Typical in-situ resistance measurement during bend test.

Table 5-2 Fatigue life in cycles between three-point and four-point bend tests.

Bend type	Conditions	Char. life	MTTF	Averaged life	Life range
Three-point	Center row	-	-	512	422~563
Four-point	0.72~3.6mm	485	440	444	317~678
Three-point	Right/left row	2432	2155	2111	787~3033
Four-point	0.432~2.16mm	2458	2237	2249	1363~3426

The fatigue comparison between three-point bend and four-point bend is listed in Table 5-2. It can be seen that fatigue lives of package in four-point bend tests with displacement from 0.72mm to 3.6mm and from 0.432mm to 2.16mm are consistent with that of center row components and right/left rows components in three-point bend test with displacement from 1mm to 5mm, which verify the correlation between three-point bend and four-point bend developed in this section. It was shown by failure mode analysis using cross-section and microscopy that exhibit solder failure as shown in Fig. 5-9. The failure site is close to component and/or board side, which is similar to result reported by Shetty et al. [63, 64]. More cracks occur on solder joints located at

ATTENTION: The Singapore Copyright Act applies to the use of this document. Nanyang Technological University Library

component corner or peripheral side parallel to loading edge in which the solder joints are subjected to larger stress level due to local stiffness and moment effect.

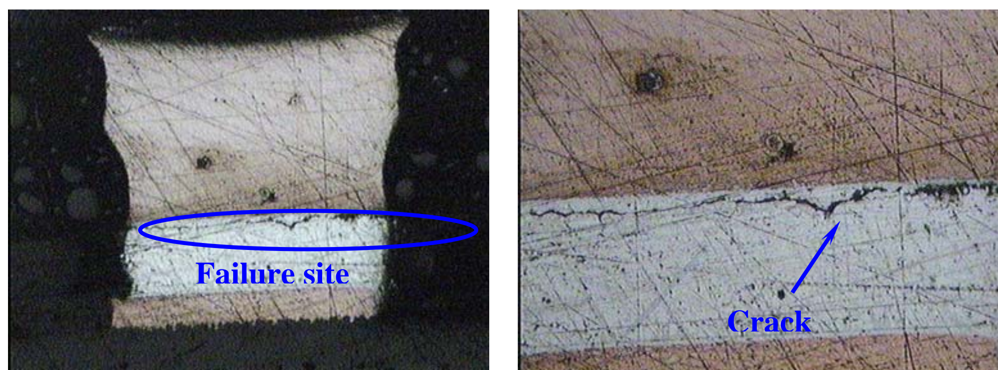

Fig. 5-9 Crack failure in solder joint of VQFN assembly.

5.2.3.2 Four-point bend tests at 25°C and 125°C

Different displacement ranges were used in four-point bend tests in order to develop bending fatigue life model of VQFN solder. Two different surface finishes containing Ni/Au and OSP were selected for VQFN assembly in order to investigate finish effect on bending fatigue life. All cyclic bend tests reported in limited literatures were conducted at room temperature of 25°C. In this study, bend tests was also conducted at high temperature of 125°C in order to investigate acceleration factor of fatigue life at high temperature condition compared to room temperature condition. Typical thermal cycling test was carried out with temperature range from -40°C to 125°C. Therefore, correlation between bend test at high temperature of 125°C and thermal cycling test from -40°C to 125°C was carried out. All four-point bend test conditions are listed in Table 5-3. For convenience, one term was given for each test condition, for example, Ni/Au-25_3.6 indicates that specimen with Ni/Au finish was tested at room temperature of 25°C with maximum displacement of 3.6mm. The minimum displacement was selected as one fifth of maximum displacement for all displacement ranges used in four-point bend tests.

ATTENTION: The Singapore Copyright Act applies to the use of this document. Nanyang Technological University Library

Table 5-3 Summary of four-point bend test conditions.

Test temperature	Surface finish	Displacement range (mm)	Notation
25°C	Ni/Au	0.72~3.6	Ni/Au-25_3.6
		0.432~2.16	Ni/Au-25_2.16
	OSP	0.72~3.6	OSP-25_3.6
		0.432~2.16	OSP-25_2.16
		0.3~1.5	OSP-25_1.5
		0.25~1.25	OSP-25_1.25
125°C	Ni/Au	0.432~2.16	Ni/Au-125_2.16
		0.3~1.5	Ni/Au-125_1.5
		0.2~1	Ni/Au-125_1
	OSP	0.432~2.16	OSP-125_2.16
		0.3~1.5	OSP-125_1.5
		0.25~1.25	OSP-125_1.25
		0.2~1	OSP-125_1

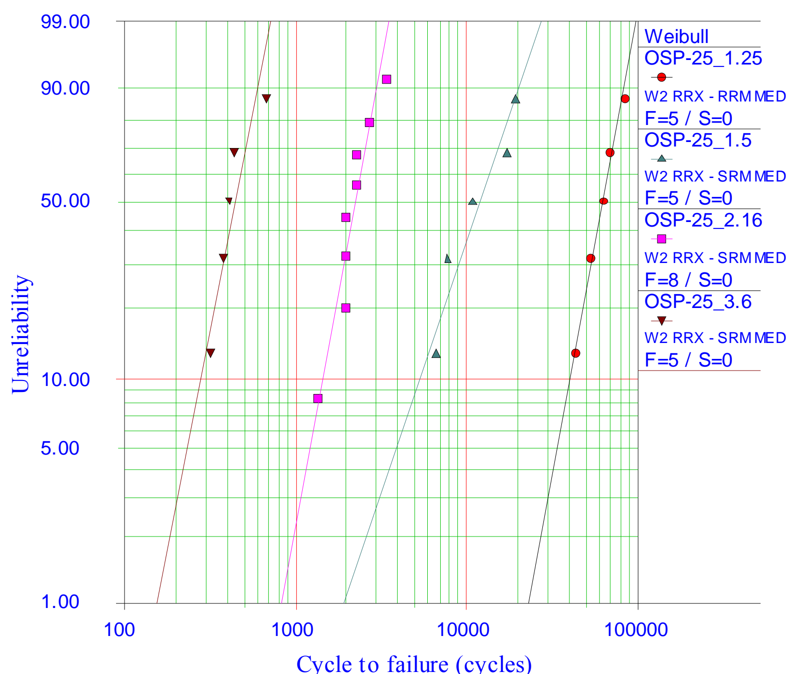

Fig. 5-10 Weibull plot of cycle to failure for OSP finish case tested at 25°C.

Fig. 5-10 and Fig. 5-11 show the Weibull plots of cycle to failure for VQFN assembly with OSP finish under four-point bent tests conducted at 25°C and 125°C, respectively. It can be seen that failure data satisfy the Weibull distribution very well.

ATTENTION: The Singapore Copyright Act applies to the use of this document. Nanyang Technological University Library

The cycle to failure increases significantly with displacement range decreasing for both bend tests at 25°C and 125°C. However, Weibull slopes of all test conditions have similar value. These phenomena are also fit for failure data of VQFN assembly with Ni/Au finish.

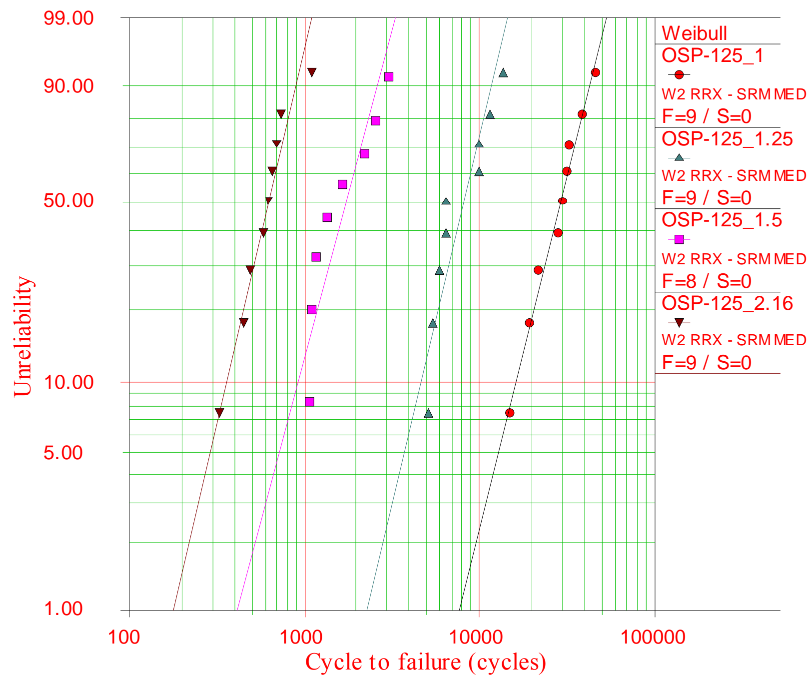

Fig. 5-11 Weibull plot of cycle to failure for OSP finish case tested at 125°C.

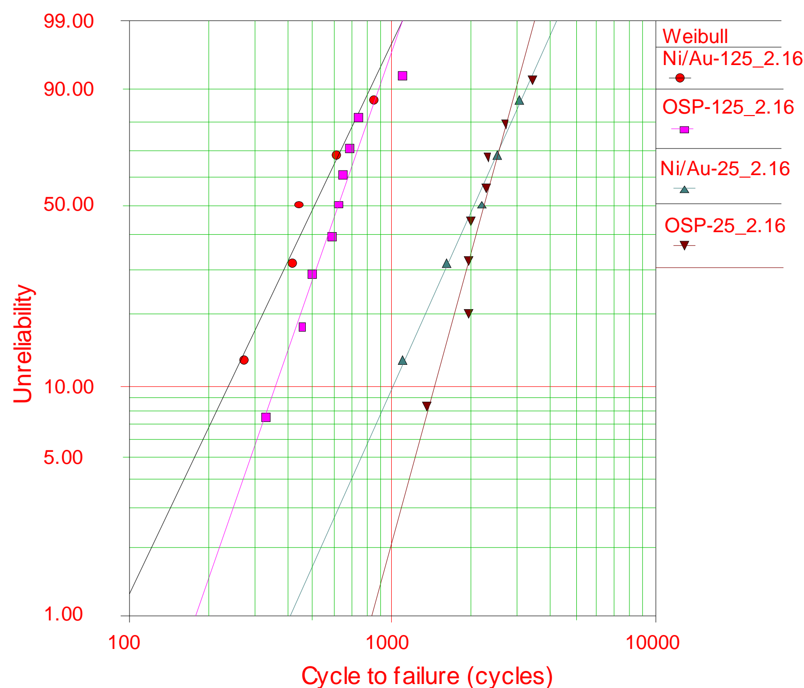

Fig. 5-12 Comparison of cycle to failure between Ni/Au and OSP finish cases.

ATTENTION: The Singapore Copyright Act applies to the use of this document. Nanyang Technological University Library

Fig 5-12 shows the comparison of failure data for VQFN with Ni/Au and OSP finishes. It can be seen from Fig. 5-12 that the characteristic life and MTTF for OSP finish case are slightly more than those for Ni/Au finish case under mechanical bend fatigue test.

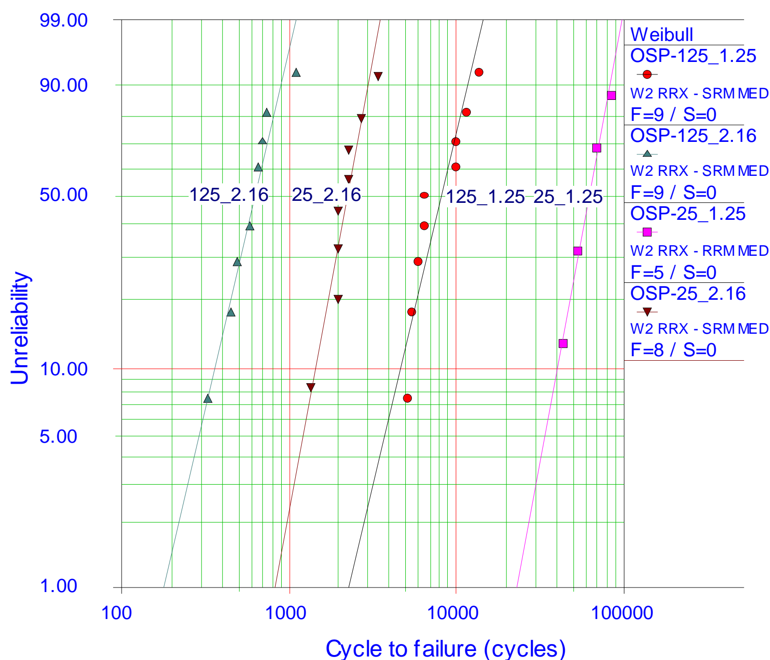

Fig. 5-13 Comparison of cycle to failure between 25°C and 125°C test condition.

Fig. 5-13 shows the failure data comparison for OSP finish case tested at room temperature of 25°C and high temperature of 125°C. It was shown that high temperature (125°C) accelerates the failure of VQFN assembly compared to room temperature (25°C) in four-point bend test with same displacement range because the solder fatigue resistance would be reduced and simultaneously solder joint deformation become larger at 125°C compared to 25°C. The acceleration factor of cycle to failure due to high temperature effect (125°C vs. 25°C) is around 4 to 7 times compared to room temperature case for cyclic bend test. All bending fatigue life data were summarized in Table 5-4. Some conclusions can be made from this table. The VQFN assemblies with OSP finish have slightly longer fatigue life than VQFN assemblies with Ni/Au finish for all test conditions. The MTTF is almost same as

ATTENTION: The Singapore Copyright Act applies to the use of this document. Nanyang Technological University Library

averaged fatigue life. The Weibull slope is larger when life range is smaller.

Table 5-4 Summary of failure data for all four-point bend tests.

Test conditions	Slope	Char. life	MTTF	Averaged life	Life range
Ni/Au-25_3.6	1.76	447	398	388	158~691
Ni/Au-25_2.16	2.62	2375	2110	2089	1103~3034
OSP-25_3.6	4.04	485	440	444	317~678
OSP-25_2.16	4.27	2458	2237	2249	1363~3426
OSP-25_1.5	2.31	14097	12489	12434	6735~19331
OSP-25_1.25	4.16	69058	62739	62914	43553~84640
Ni/Au-125_2.16	2.47	590	523	520	272~854
Ni/Au-125_1.5	3.99	1509	1368	1374	984~1920
Ni/Au-125_1	5.24	31932	29400	29526	21372~36102
OSP-125_2.16	3.38	699	628	631	330~1098
OSP-125_1.5	2.93	1968	1756	1778	1076~3062
OSP-125_1.25	3.3	9185	8239	8331	5131~13895
OSP-125_1	3.15	32949	29488	29455	14880~46175

5.3 FEA MODELING FOR BEND FATIGUE TEST

In this section, FEA modeling for bend fatigue tests were conducted in order to investigate the stress strain behavior of solder joint. Based on fatigue test data and FEA results, fatigue life prediction models were proposed for VQFN solder fatigue with OSP finish subjected to cyclic bend load at 25°C and at 125°C. Submodeling technique was used for board-level FEA simulation in order to save computing resource. Firstly, two-level submodeling and one-level submodeling were compared in order to investigate mesh effect on FEA results of solder joint.

5.3.1 Validation of One-level and Two-level Submodeling Method

Solder joint is the critical part in VQFN assembly so that stress strain in solder is very important in order to assess the reliability of VQFN package under cyclic bend load.

ATTENTION: The Singapore Copyright Act applies to the use of this document. Nanyang Technological University Library

Conventional 3D FEA model for board-level simulation is not desirable due to larger element size and high-level computing resource requirement. Therefore, submodeling technique is a desirable choice. In this study, two submodeling methods were implemented to study the mesh effect of global model on submodel results. One is called two-level submodeling method as shown in Fig. 5-14 where the global board-level quarter model was solved firstly. Then DOF results were transferred and interpolated to cut boundary in first-level package submodel with medium mesh. Finally, the DOF results from first-level submodel were transferred and interpolated to cut boundary in second-level submodel with fine mesh. In two-level submodeling method, the package-level FEA model is a transitional model, which is a submodel relative to the board-level global model while it becomes the package-level global model relative to second-level submodel. This method can satisfy requirement of elements transferring from much coarser mesh to much finer mesh. It was expected that two-level submodeling method leads to more accurate results but complicated procedure is needed due to twice DOF interpolations. The other method is called one-level or traditional submodeling as shown in Fig. 5-15. In this method, global model and submodel are the same as board-level global model and second-level submodel used in two-level submodeling method, respectively. The DOF results from global model were transferred to final submodel directly without using package-level submodel as transitional model. However, it maybe give arise to more error because DOF results were interpolated and transferred from too coarse mesh in board-level global model to finer mesh in submodel. In this study, these two submodeling methods were performed to find a desirable method. For convenience, the monotonic four-point bending load was used in this validation procedure. Validation will be done by comparing numerical results from different modeling method.

ATTENTION: The Singapore Copyright Act applies to the use of this document. Nanyang Technological University Library

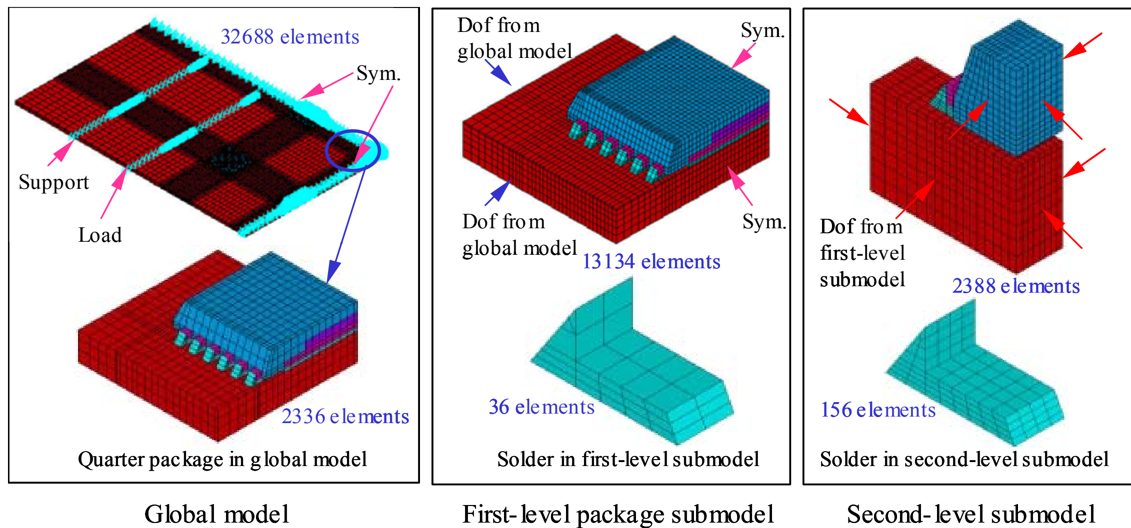

Fig. 5-14 Two-level submodeling method.

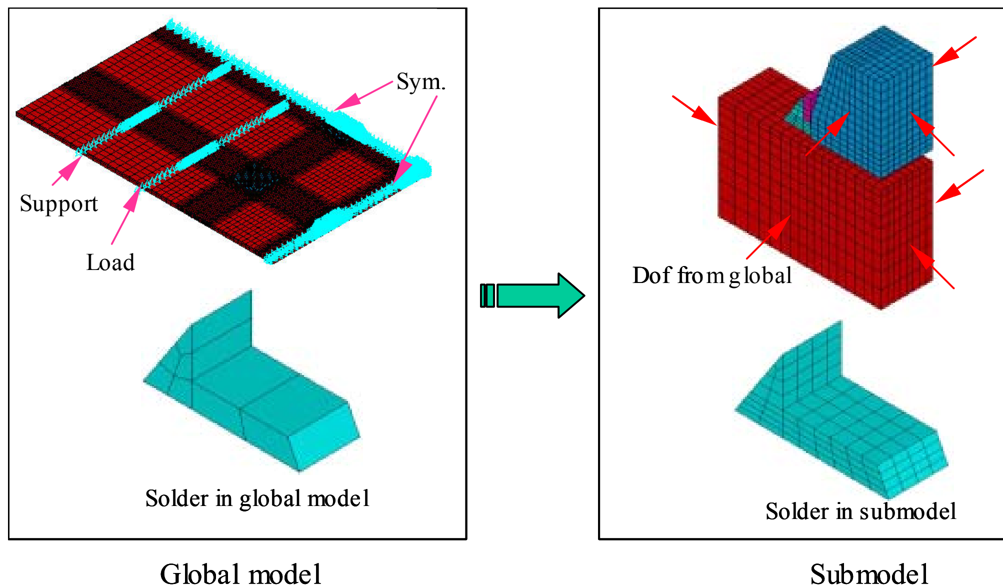

Fig. 5-15 One-level submodeling method.

The displacement range from zero to 6mm was added on loading position of global model in 1 second using 6 load steps in FEA simulation. The material constitutive models used in VQFN assembly are shown in Table 5-5. Viscoplastic Anand model was used for solder material. Fig. 5-16 shows the global strain contour with direction normal to load and support anvil at the displacement of 6mm. It is shown that all packages are subjected to same strain level in four-point bending load case. Strain value close to package corner is more than global strain due to localized

ATTENTION: The Singapore Copyright Act applies to the use of this document. Nanyang Technological University Library

stiffening effect of package. Outmost corner solder joints of VQFN package were prone to failure and submodel was created based on corner solder joint accordingly. Transitional package model in two-level submodeling method can be selected from any package location and it was modeled based on center package in this study.

Table 5-5 Constitutive models for different materials in VQFN assembly.

Materials	Constitutive model
SnAgCu solder	Viscoplastic Anand model, isotropic
Cu pad	Multilinear kinematic hardening plastic, isotropic
PCB	Elastic, orthotropic
Die	Elastic, isotropic
Die adhesive	Elastic, isotropic
Mold compound	Elastic, isotropic

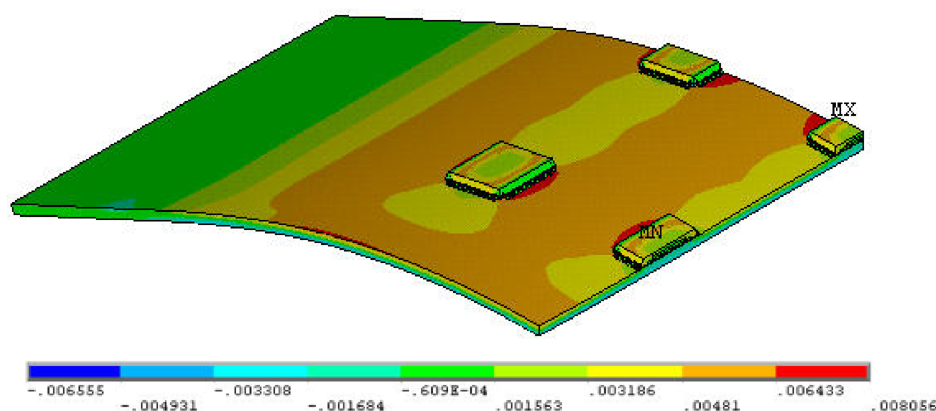

Fig. 5-16 Global strain contour at displacement of 6mm.

Fig. 5-17 and Fig. 5-18 show the volume-averaged von Mises strain and plastic strain energy density at the last load step with displacement of 6mm for different models considering whole solder joint as averaging volume, respectively. It can be seen that one-level submodel and two-level submodel result in almost the same von Mises strain and plastic strain energy density. Therefore, one-level submodeling method is effective and sufficient for FEA modeling and simulation of VQFN assembly subjected to bending load. The important advantage of one-level

ATTENTION: The Singapore Copyright Act applies to the use of this document. Nanyang Technological University Library

submodeling exists in saving time and computing resource compared to two-level submodeling and providing more accurate results compared to coarse global model, especially for simulating cyclic bending test with more load steps.

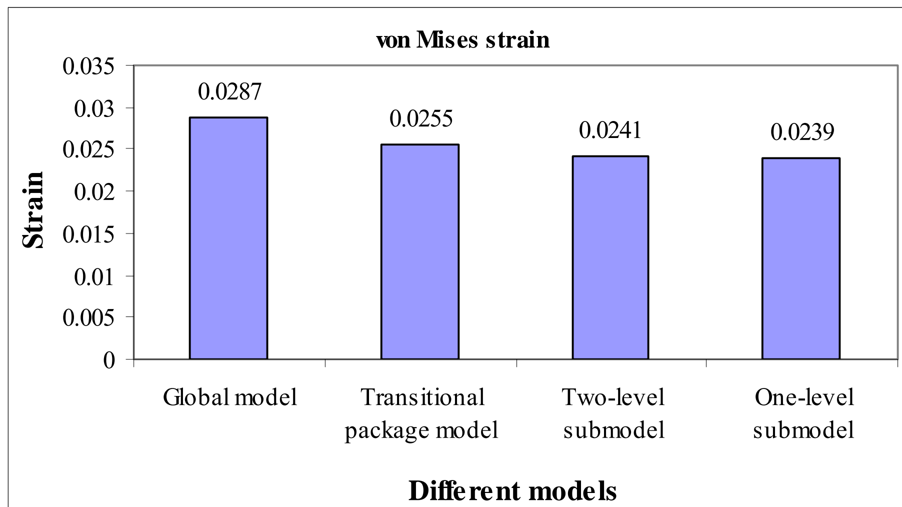

Fig. 5-17 Solder joint strains for different models.

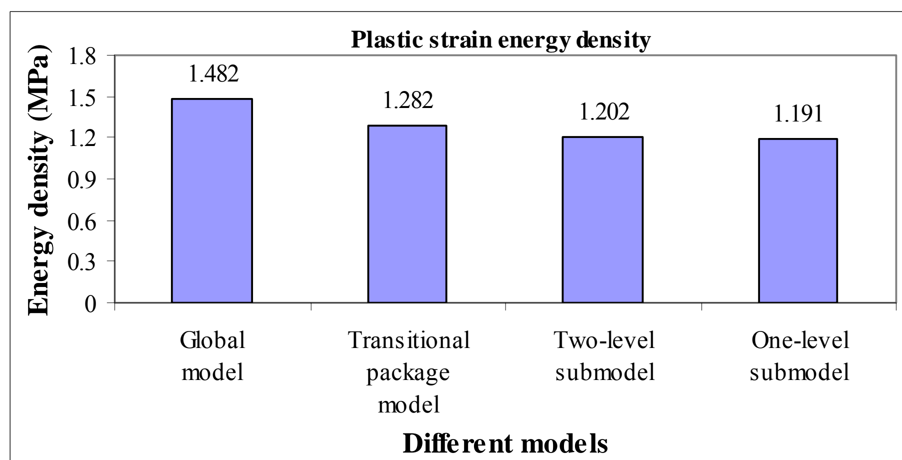

Fig. 5-18 Solder joint plastic strain energy density for different models.

5.3.2 FEA Study for Three-Point Bend Fatigue Test

One level global-local modeling approach discussed above was used to simulate the three-point bend test using ANSYS FEA software. Quarter model was used to model the board-level assembly due to symmetry of geometry and load. The materials used in global model and corresponding constitutive model are listed in Table 5-5. According

ATTENTION: The Singapore Copyright Act applies to the use of this document. Nanyang Technological University Library

to the test conditions, board-level global model was constrained at both symmetry planes and fixed in the out-of-plane direction at the support edge. In three-point bend test, a displacement range from 1mm to 5mm was applied at the centerline of specimen and repeated with a frequency of 1Hz and without dwell time. For convenience, only four load steps with equal displacement increment were specified for both loading and unloading periods to facilitate the DOF transfer between the global model and submodel.

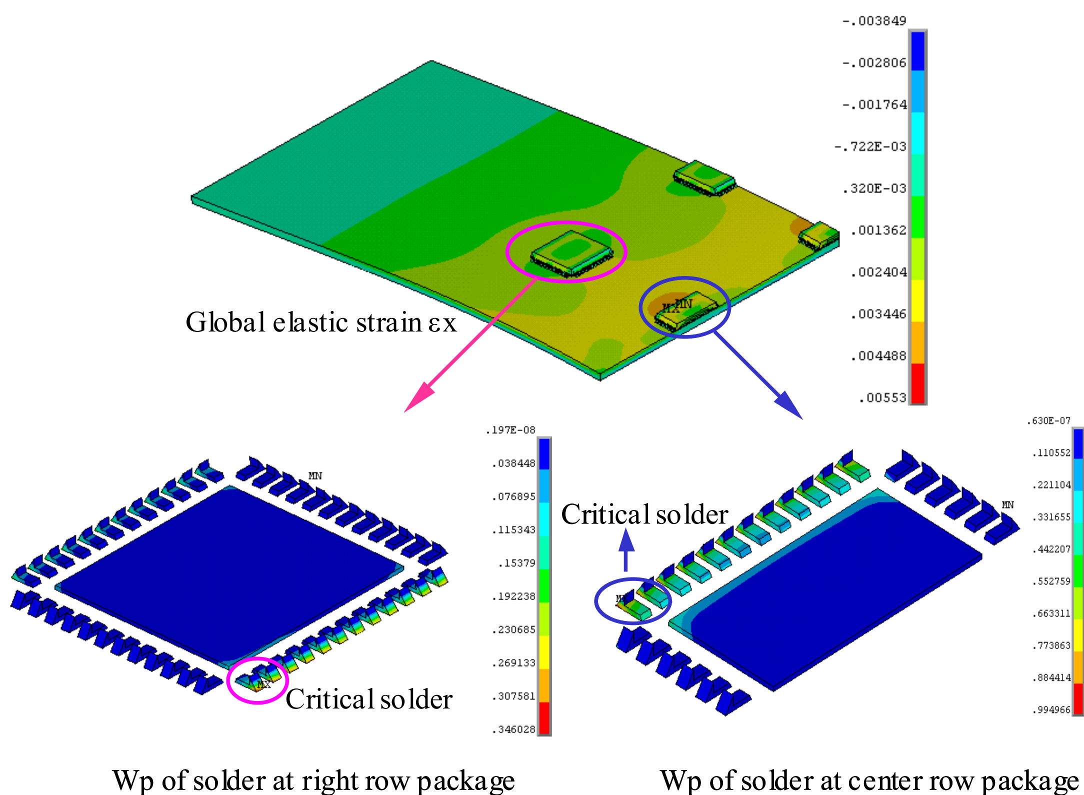

Fig. 5-19 Global simulation results for three-point bend.

Fig. 5-19 shows the result contour of global strain with direction normal to support/load edge and energy density contour of solder joints at different component rows. The global strain distribution shows very strong location effect and package localized stiffening effect. The global strain increases with location close to load edge of centerline of specimen, which verifies the fact that packages at different locations are subjected to different stress levels in three-point bend test. The stress levels for

ATTENTION: The Singapore Copyright Act applies to the use of this document. Nanyang Technological University Library

packages at the same row show similar value even though they are not exactly same due to free edge effect. Therefore, it is assumed that all packages in the same row are subjected to the same stress level and only one submodel is created for packages at the same row in order to simplify the simulation without loss of generalization. It can be seen from strain energy density contour that the critical solder joint is located at component corner for both center row and right row packages. The solder joint edge containing critical solder joint is parallel to support/load edge and close to loading edge for right row component. Then the submodel was modeled based on the critical solder joint.

The submodel contains one critical solder joint and PCB, copper pad, mold compound in one pitch volume as shown in Fig. 5-15. Solder joint was modeled with Anand's viscoplastic behavior. Displacement results from global model was interpolated and transferred to corresponding nodes of cut boundary in submodel step by step. The accurate results can be obtained from detailed submodel with fine mesh. Usually, strain energy density is used as damage control parameter for solder joint. For Anand's model, unified plastic strain energy density can be output.

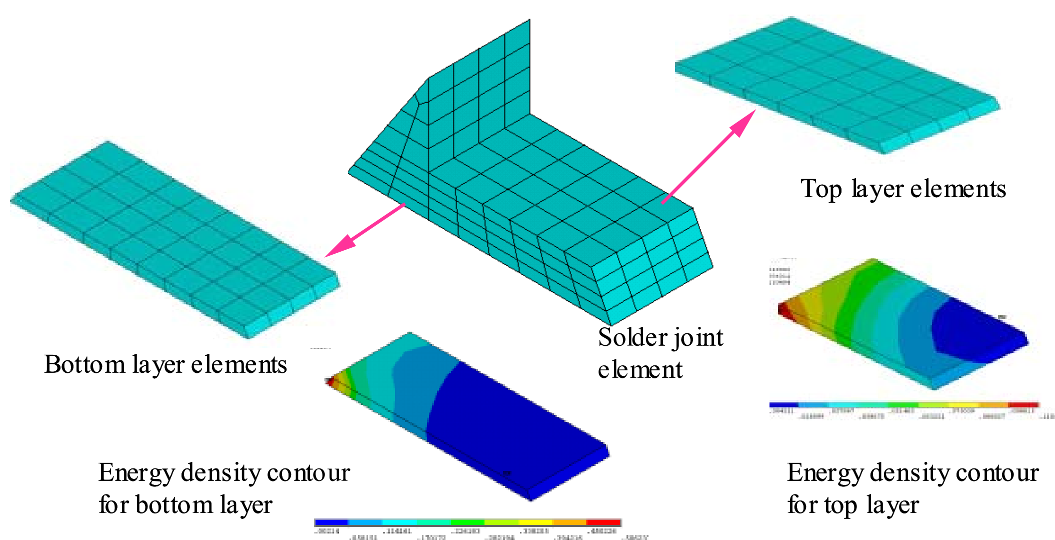

Fig. 5-20 Solder joint mesh and energy density contour for bottom and top layers.

Fig. 5-20 shows the solder joint mesh in submodel and plastic strain energy

ATTENTION: The Singapore Copyright Act applies to the use of this document. Nanyang Technological University Library

contour for top and bottom layer elements. It can be seen that maximum energy value was located at corner node of bottom side or top side due to stress concentration and localized stiffening effect, which exactly is crack initiation site. In order to reduce stress concentration effect, volume-averaged approach was used to calculate strain energy density based on top or bottom layer elements.

Generally, mechanical loading is much faster than thermal cycling loading with cycle time from several minutes to hours. Therefore, it takes only a few simulation cycles, for example three cycles [109], to reach convergence for thermomechanical loading. However, for mechanical loading with frequency around 1Hz, it always takes more simulation cycles to obtain the converged results because the creep of solder material cannot fully develop during short cycle period. Usually, 10 to 15 simulation cycles are needed to obtain converged results for bending load with 1Hz frequency [64]. In this study, fifteen cycles were simulated for both global and local models.

Fig. 5-21 and Fig. 5-22 show the accumulated strain energy density per cycle averaged on top or bottom elements from submodel results for center row and right row cases, respectively. It was shown that strain energy density value is larger for center row component case than for right row component case, which is consistent with test results where center row components fail faster than right/left row components. At high stress level of center row component case, strain energy density at bottom layer converges faster than top layer due to larger plastic deformation. At low stress level of right row component case, strain energy density convergence is similar for bottom and top layers. After 10 cycles, volume-averaged strain energy densities are close in bottom and top layers for both high stress and low stress levels. FEA simulation by Shetty and Reinikainen [64] showed that strain energy density appeared to be nearly same on top and bottom BGA solder interfaces.

ATTENTION: The Singapore Copyright Act applies to the use of this document. Nanyang Technological University Library

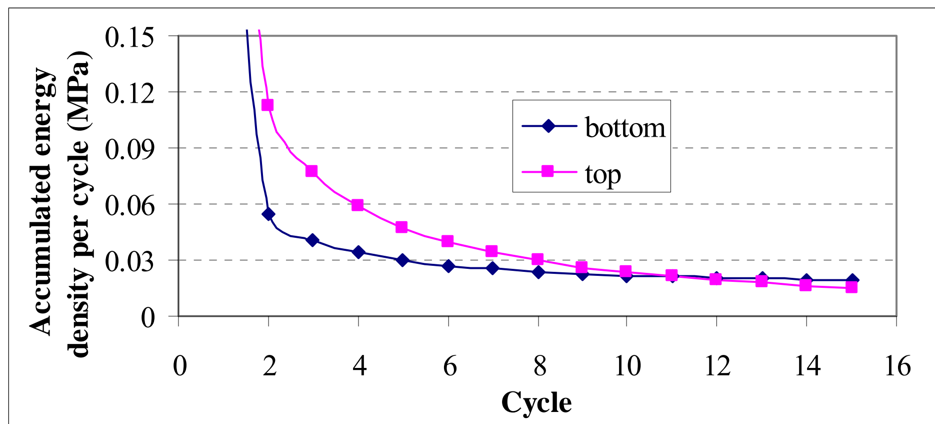

Fig. 5-21 Convergence history of accumulated strain energy density per cycle for the critical solder joint located at center row component case.

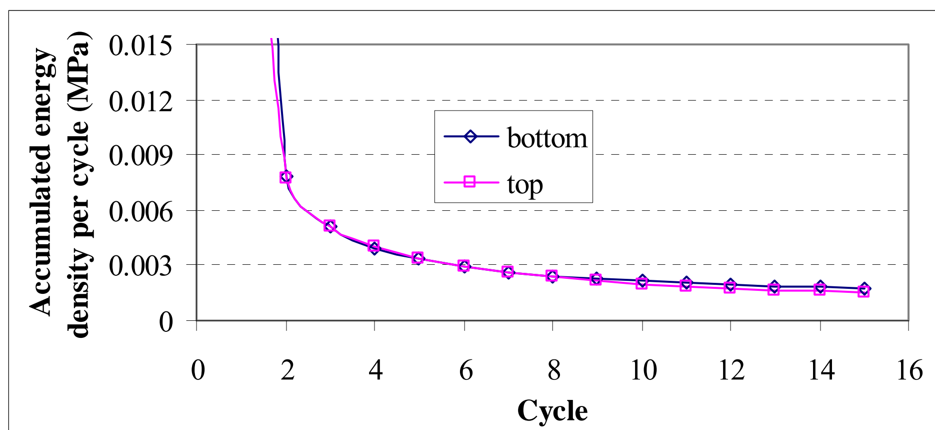

Fig. 5-22 Convergence history of accumulated strain energy density per cycle for the critical solder joint located at right row component case.

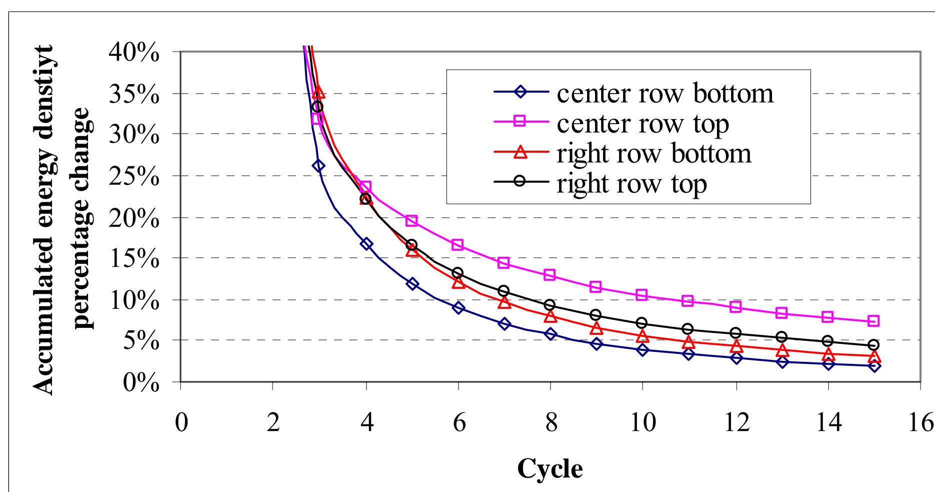

Fig. 5-23 Strain energy density accumulation percentage change each cycle for three-point bending load.

ATTENTION: The Singapore Copyright Act applies to the use of this document. Nanyang Technological University Library

In order to explain strain energy convergence further, relative strain energy density percentage changes were calculated based on energy density difference between two consecutive cycles and plotted in Fig. 5-23. It was verified that FEA result convergence for mechanical loading is slower than thermomechanical loading. It was shown that 15 cycles simulation was enough to obtain a 5% energy density percentage change between two consecutive cycles based on bottom layer volume averaging, which was considered a convergence criterion in this FEA study.

5.3.3 FEA Study for Four-Point Bend Fatigue Test

5.3.3.1 FEA result correlation between three-point bend and four-point bend

The global-local modeling procedure and FEA models in four-point bend simulation are same as that in three-point bend simulation except displacement loading position and value. Displacement load was applied on centerline of specimen in three-point bend while it was added on loading span position in four-point bend. Four-point bend with displacement loading from 0.72mm to 3.6mm was simulated to correlate FEA results between four-point bend and center row components in three-point bend.

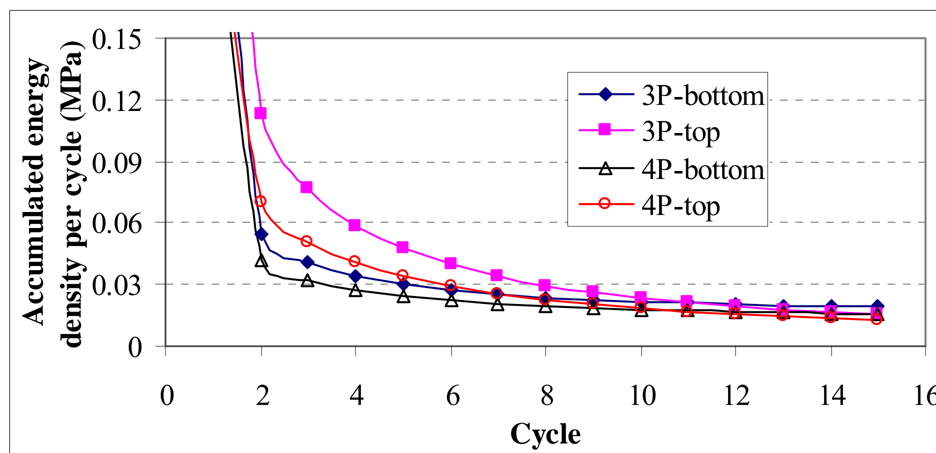

Fig. 5-24 FEA result correlation between four-point bend and three-point bend.

Fig. 5-24 shows the energy density accumulation comparison between three-point bend and four-point bend. It can been seen that energy density accumulation values

ATTENTION: The Singapore Copyright Act applies to the use of this document. Nanyang Technological University Library

appear to be similar for four-point bend and three-point bend after 10 cycles, which is consistent with four-point bend and three-point bend test results.

5.3.3.2 FEA result discussion at room temperature (25°C)

In four-point bend FEA simulation, it was shown that components are subjected to almost the same stress level, so global board-level simulation can be conducted just considering one center component. Global board-level quarter model with full VQFN components as shown in Fig. 5-15 has 32688 elements while global quarter model just with center VQFN component (named U8 in Fig. 5-1) has 8195 elements. The simulation time used by global model with full VQFNs is 10 times of that used by global model with one VQFN.

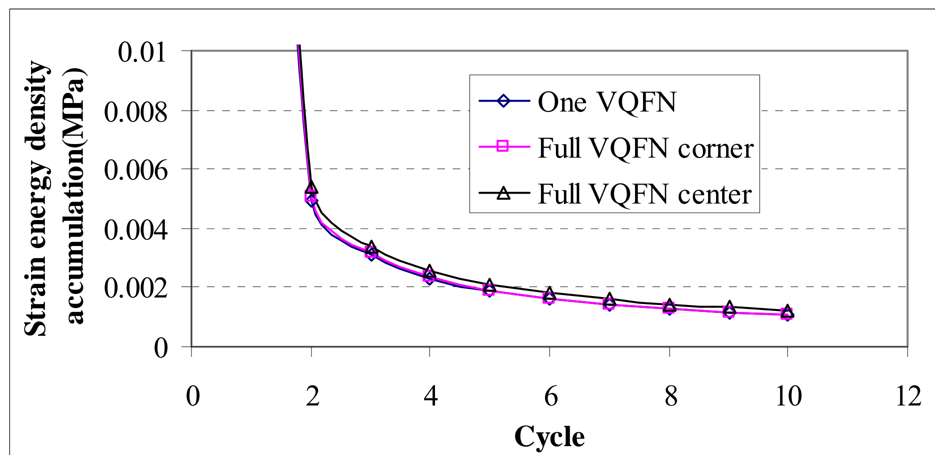

Fig. 5-25 Strain energy density accumulation of bottom layer for different cases.

Fig. 5-25 shows the strain energy density accumulations of bottom layer from submodel results with DOF transferred from different global models. It was shown that energy density accumulations are nearly the same for different cases. Different components on specimen result in almost the same energy density, which verifies the assumption of different components subjected to the same stress level under four-point bending load. The stiffening effect of one component on another component can be neglected. Therefore, global model with one center VQFN is equivalent to global

ATTENTION: The Singapore Copyright Act applies to the use of this document. Nanyang Technological University Library

model with full VQFNs. Therefore, the global model with one center VQFN would be used in following FEA study in order to save solving time without loss of accuracy.

Fig. 5-26 shows the strain results from FEA simulation for four-point bend with displacement from 0.432mm to 2.16mm. FEA simulation results as shown in Fig. 5-26 are consistent with experimental results as shown in Fig. 5-6.

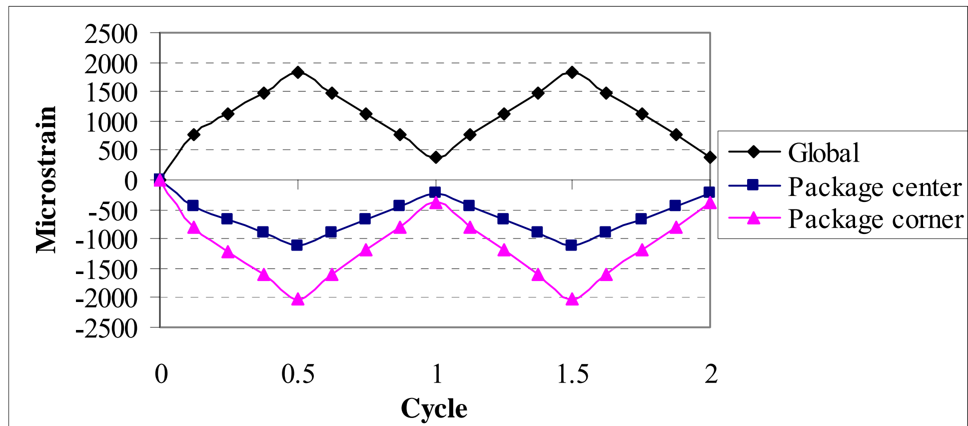

Fig. 5-26 FEA strain results of board surface at displacement of 0.432 to 2.16mm.

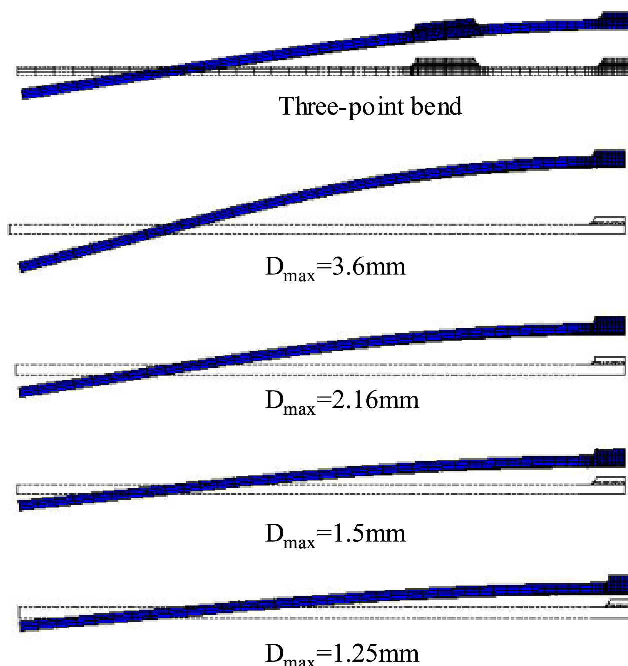

Fig. 5-27 Deformation shape of specimen under different bending loads.

Fig 5-27 shows the deformation shape of specimen at different maximum displacements. It was found that the curvature and deflection at specimen centerline

ATTENTION: The Singapore Copyright Act applies to the use of this document. Nanyang Technological University Library

increase with displacement increasing, thus accelerating the failure of components.

Fig. 5-28 shows the plastic strain energy density accumulation convergence history of bottom layer for different four-point bending loads at room temperature. It was shown that all energy density accumulations reach a convergence after 15 simulation cycles with 5% difference between two consecutive cycles. The energy density values converge faster for larger displacement, which are consistent with results from three-point bend FEA simulation.

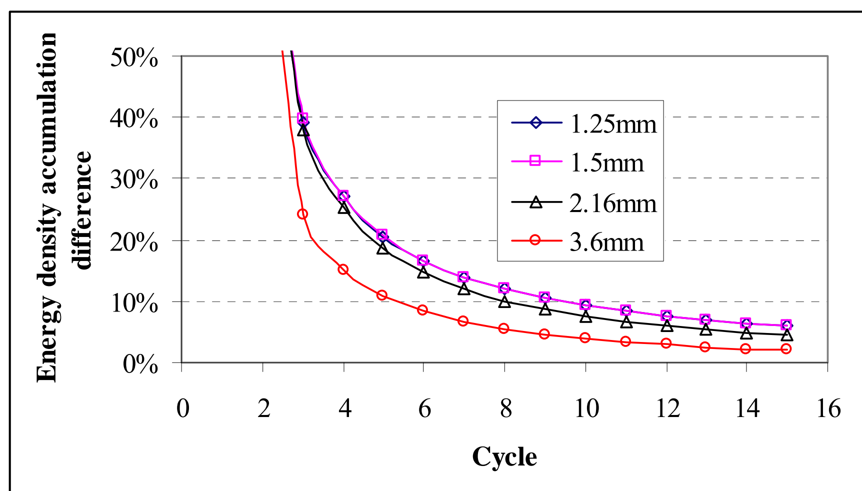

Fig. 5-28 Accumulated energy density convergence for four-point bend at 25°C.

Table 5-6 Summary of results for four-point bend FEA simulations at 25°C.

Maximum displacement	1.25mm	1.5mm	2.16mm	3.6mm
Energy density at bottom layer (MPa)	1.27e-04	2.10e-04	8.08e-04	1.56e-02
Energy density at top layer (MPa)	8.53e-05	1.76e-04	7.75e-04	1.25e-02
Energy density factor (Bottom/Top)	1.49	1.19	1.04	1.25
Relative energy density (bottom)	1	1.65	6.34	122.64
Relative displacement	1	1.20	1.73	2.88

Table 5-6 lists energy density accumulations at 15th simulation cycle for different displacement loads. It can be seen that volume-averaged energy density accumulation value on bottom layer is larger than that on top layer. The energy density increases significantly with displacement load increasing. The relationship between

ATTENTION: The Singapore Copyright Act applies to the use of this document. Nanyang Technological University Library

displacement and energy density accumulation can be expressed by a power law equation as shown in Fig. 5-29. Therefore, once one displacement load and its corresponding energy density accumulation are known, energy density accumulation can be easily estimated for another displacement load using following equation:

$$\frac{W_{kn}}{W_{un}} = \left(\frac{D_{kn}}{D}\right)^{4.581} \tag{5.11}$$

where D_{kn} and W_{kn} are known displacement and corresponding energy density accumulation, respectively. Unknown W_{un} can be obtained when D is known.

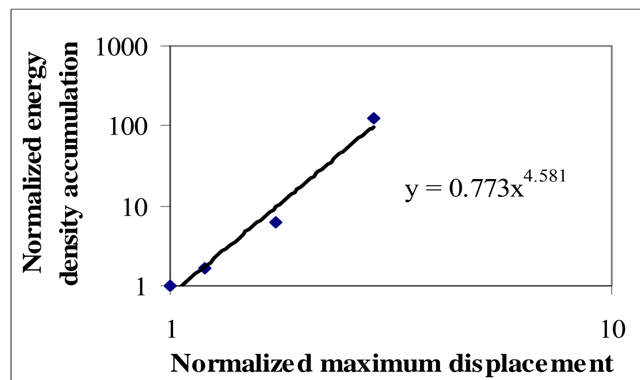

Fig. 5-29 Relationship of displacement and accumulated energy density at 25°C.

5.3.3.3 FEA result discussion at high temperature (125°C)

FEA modeling and simulation for four-point bend at high temperature (125°C) were also conducted. The geometry solid model of high temperature bend is the same as that of room temperature bend. The difference is that some material properties used in high temperature bend simulation are temperature-dependent like those used in thermal cycling simulation for PBGA assembly in Chapter 4. Before applying mechanical bending load, temperature ramp up from 25°C to 125°C was simulated with time period of 10 minutes, which was consistent with physical bend test condition. Then cyclic bending load was simulated with frequency of 1 Hz and dwell temperature of 125°C. Anand viscoplastic model was used for solder material. Fifteen bending cycles

ATTENTION: The Singapore Copyright Act applies to the use of this document. Nanyang Technological University Library

were simulated to obtain converged results. It was found that accumulated energy density on top layer is slightly higher than that on bottom layer due to high residual stress effect close to top solder interface after temperature ramp up to high dwell temperature, while higher volume-averaged energy density accumulation occurs on bottom layer at room temperature bend. Fig. 5-30 shows the energy density accumulation convergence history based on top layer volume averaging for different four-point bends at 125°C. It is similar to room temperature bend simulation that convergence of 5% difference between two continue cycles can be obtained after 15 cycles for high temperature bend FEA simulation.

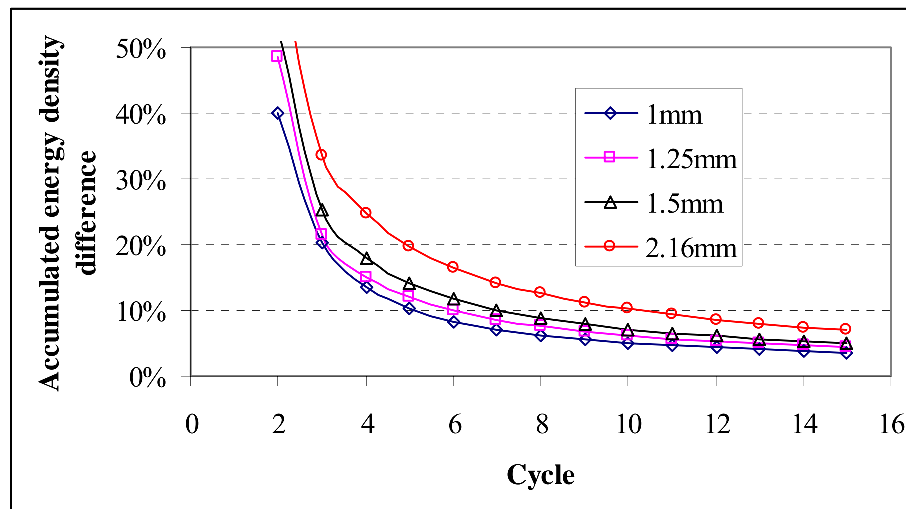

Fig. 5-30 Accumulated energy density convergence for four-point bend at 125°C.

Table 5-7 lists converged energy density accumulation results for different displacement loads at 125°C. It can be seen that volume-averaged energy density accumulation value on top layer is nearly twice that on bottom layer. The relationship between displacement and energy density accumulation as shown in Fig. 5-31 can be fitted by power law curve. Energy density accumulation in four-point bend at 125°C can be calculated using following equation refer to Eq. (5.11) for bending load at 25°C.

$$\frac{W_{kn}}{W_{un}} = \left(\frac{D_{kn}}{D}\right)^{2.669} \tag{5.12}$$

ATTENTION: The Singapore Copyright Act applies to the use of this document. Nanyang Technological University Library

Table 5-7 Summary of results for four-point bend FEA simulations at 125°C.

Maximum displacement	1mm	1.25mm	1.5mm	2.16mm
Energy density at bottom layer (MPa)	4.45e-04	8.31e-04	1.41e-03	3.52e-03
Energy density at top layer (MPa)	8.25e-04	1.60e-03	2.80e-03	6.45e-03
Energy density factor (Top/Bottom)	1.85	1.92	1.99	1.83
Relative energy density (Top)	1	1.94	3.40	7.82
Relative displacement	1	1.25	1.5	2.16

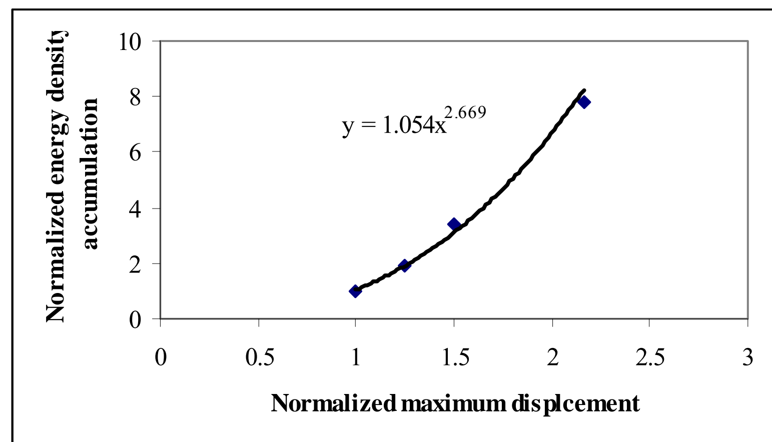

Fig. 5-31 Relationship of displacement and accumulated energy density at 125°C.

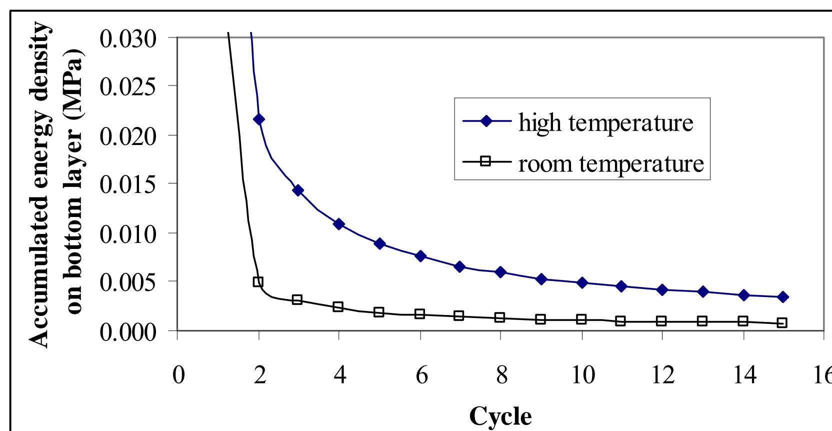

Fig. 5-32 Result comparison between bending simulation at 25°C and at 125°C.

The result comparison between bending simulation at 25°C and at 125°C with the same displacement load of 2.16mm is shown in Fig. 5-32. It is clear that accumulated energy density per cycle at high temperature is more than that at room temperature significantly, which indicates that higher temperature accelerates bending fatigue

ATTENTION: The Singapore Copyright Act applies to the use of this document. Nanyang Technological University Library

failure of solder joint. The simulation results are consistent with experimental data.

5.3.3.4 Fatigue model development for cyclic bending load

Some literatures showed fatigue life curves with the fatigue life as a function of board strains, or even board deflections and reaction loads. These fatigue models cannot be extended when board or package parameters change. In fact, the solder fatigue model should correlate fatigue life to damage parameter extracted from solder material. Skipor and Leicht [66] developed a bending fatigue model for PBGA SnPb solder joint using inelastic strain as damage parameter. Mercado et al. [67] proposed a total energy-based bending fatigue model for CSP with eutectic SnPb solder. All bending fatigue models were developed at room temperature from literatures. Based on limited literature, bending fatigue model for Sn-Ag-Cu solder was not documented. In this section, bending fatigue models were presented for VQFN with Sn-Ag-Cu solder at both conditions of room temperature and high temperature.

Strain energy density was selected as damage parameter because it is a comprehensive factor considering both stress and strain effects. The strain energy density results shown in above section are all plastic strain energy density from Anand's model. The total energy density accumulation on bottom layer was also calculated and listed in Table 5-8 for room temperature bending simulations. It can be seen that plastic energy density is dominant. For high temperature case, the ratio of plastic energy density to total energy density is more than 99% from FEA results.

Table 5-8 FEA results and experimental data for four-point bend at 25°C.

Displacement	1.25mm	1.5mm	2.16mm	3.6mm
Total strain energy density (MPa)	1.34e-04	2.24e-04	8.56e-04	1.56e-02
Plastic strain energy density (MPa)	1.27e-04	2.10e-04	8.08e-04	1.55e-02
Ratio (plastic/total)	95.3%	93.8%	94.4%	99.7%
MTTF (cycles)	67073	12489	2237	440

ATTENTION: The Singapore Copyright Act applies to the use of this document. Nanyang Technological University Library

Fig. 5-33 shows the relationship of MTTF from test and plastic strain energy density from FEA simulation for room temperature (25°C) bending load. The power law function can fit data well. Therefore, bending fatigue life at room temperature (25°C) can be predicted from these new bending fatigue models:

$$N_f = 6.025(\Delta W_P)^{-0.946} \tag{5.13}$$

$$N_f = 5.725(\Delta W_T)^{-0.959} \tag{5.14}$$

where ΔW_P, ΔW_T are plastic strain energy density and total strain energy density accumulations per cycle, respectively. The power law exponents are –0.946 and –0.959 for plastic energy-based and total energy-based fatigue models, respectively. These exponents are quite close due to plastic deformation dominant.

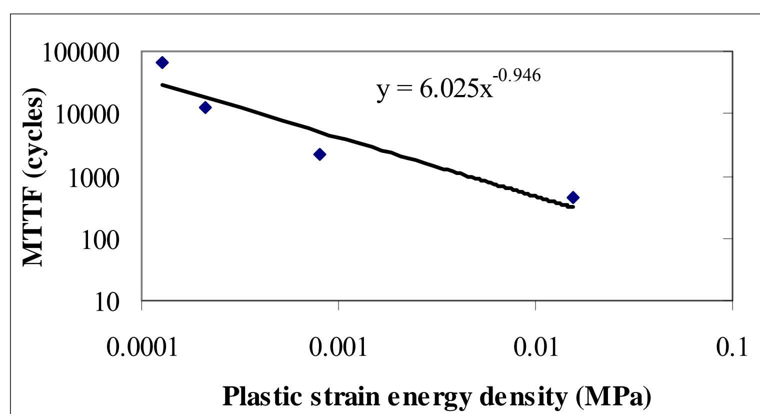

Fig. 5-33 Bending fatigue model for Sn-Ag-Cu solder at 25°C.

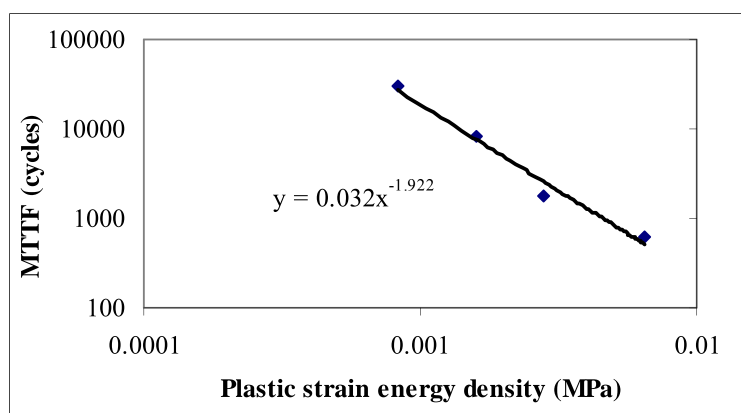

Fig. 5-34 Bending fatigue model for Sn-Ag-Cu solder at 125°C.

ATTENTION: The Singapore Copyright Act applies to the use of this document. Nanyang Technological University Library

Fig. 5-34 shows the power law relationship between MTTF and plastic strain energy density for high temperature bending load. As plastic energy density is as high as 99% of total energy density, plastic energy-based fatigue model is equivalent to total energy-based fatigue model. Therefore, bending fatigue life at high temperature (125°C) can be predicted from following fatigue model:

$$N_f = 0.032(\Delta W_P)^{-1.922} \tag{5.15}$$

It was found that the power law exponent of high temperature bending fatigue model is about twice the exponent of room temperature bending fatigue model, which indicates that acceleration factor of cycle to failure is higher in high temperature bending fatigue than in room temperature bending fatigue.

5.3.4 Correlation between Cyclic Bend and Thermal Cycling

Thermal cycling test with temperature range from –40°C to 125°C and 1 hour per cycle was conducted for the VQFN assembly. The test was terminated after 1000 cycles without failure. FEA simulation was performed for the VQFN component using submodeling technique considering three thermal cycles. Fig. 5-35 shows the energy density contour for whole solder joint, top layer and bottom layer elements. It can be seen that energy density at bottom layer is higher than that at top layer, which is different from PBGA component with higher energy density occurring at chip side interface layer. Fig. 5-36 shows the accumulated energy density per cycle for bottom and top layers. It can be seen that energy density accumulation converges at third cycle and is slightly higher on bottom layer than on top layer. Fatigue life of VQFN solder joint can be predicted using Eq. (4.8) based on energy density result on bottom layer and the predicted life is more than 6000 cycles which is related to bending fatigue life at displacement of 1.25mm at 125°C. However, energy density accumulation per cycle under thermal cycling is significantly more than that under cyclic bending load. Creep

ATTENTION: The Singapore Copyright Act applies to the use of this document. Nanyang Technological University Library

deformation is important in thermal cycling with long cycle period while it cannot be fully developed in cyclic bending load with very shorter cycle period. Correlation or difference of failure mode and mechanism of solder between TC load and bending load are needed to be further investigated. If relationship between TC and bending tests was found, the bend test having an experimental time of several hours or days is desirable compared to thermal cycling test with several months of experimental time.

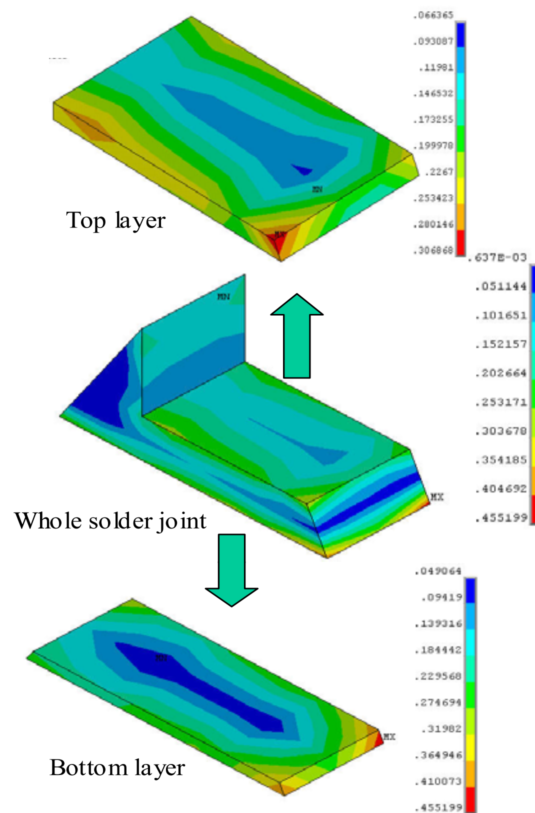

Fig. 5-35 Plastic strain energy density contour at the end of third cycle simulation.

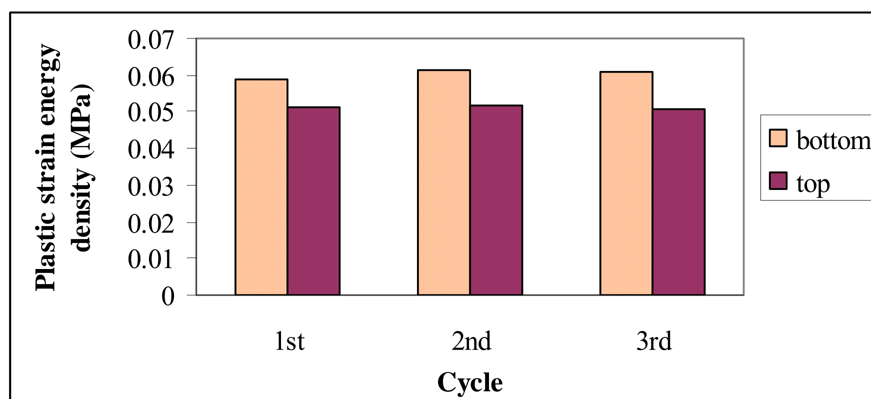

Fig. 5-36 Accumulated energy density per cycle from TC FEA simulation.

ATTENTION: The Singapore Copyright Act applies to the use of this document. Nanyang Technological University Library

5.4 SUMMARY

Cyclic four-point and three-point bend tests were performed for reliability assessment of VQFN assembly. The correlation between three-point bend and four-point bend was developed and validated by test and simulation results. Four-point bend tests were conducted at 25°C and at 125°C for VQFN with Ni/Au or OSP surface finish, respectively. Failure data satisfy Weibull distribution very well. The cycle to failure increases significantly with displacement ranges decreasing for both bend tests at 25°C and at125^{o}C. Fatigue resistance of VQFN with OSP finish is slightly better than that of Ni/Au finish case from test data. The acceleration factor of cycle to failure due to high temperature effect is higher than that due to room temperature effect.

FEA modeling and simulation were performed for different testing conditions. Before cyclic bend simulation, monotonic bending load was simulated using one-level and two-level submodeling methods. Based on FEA result comparison, one-level submodeling method is effective and sufficient for FEA simulation with the advantage of saving time and computing resource. Fifteen simulation cycles are needed for cyclic bending load in order to obtain converged results. Simulation results show the location dependent global strain for three-point bend and location independent global strain for four-point bend. Strain results from FEA simulation are consistent with testing results and localized stiffening effect due to package is also found for four-point bend. Volume-averaged energy density accumulation on bottom layer is slightly higher than that on top layer for room temperature bend while it is higher on top layer than bottom layer for bend simulation at 125°C. The relationship between displacement and energy density accumulation fits power law curve for both bends at 25°C and 125°C. Accumulated energy density per cycle at 125°C is more than that at 25°C significantly, which indicates that higher temperature accelerates bending fatigue failure of solder.

ATTENTION: The Singapore Copyright Act applies to the use of this document. Nanyang Technological University Library

Energy-based fatigue models were developed for Sn-Ag-Cu Pb-free solder subjected to cyclic bending load at 25°C and 125°C. It was found that the power law exponent of bending fatigue model at 125°C is about twice the exponent of bending fatigue model at 25°C, which indicates that acceleration factor of cycle to failure is higher in bending fatigue at 125°C than in bending fatigue at 25°C. Initial study of correlation between thermal cycling fatigue and bending fatigue were performed.

ATTENTION: The Singapore Copyright Act applies to the use of this document. Nanyang Technological University Library

CHAPTER 6 DROP TEST AND ANALYSIS

6.1 INTRODUCTION

Portable electronics devices like mobile phone, personal digital assistant (PDA), and laptop have to be designed to withstand repeated drops because it is common for them to be subjected to accidental drop impacts resulting in damage and hence failures. Therefore, the reliability characterization of electronic assembly subjected to drop impact is a major concern. When an electronic product drops on the ground, impact force is transmitted to the PCB, solder joints and the packages. The packages are susceptible to solder joint failures induced by a combination of PCB bending and inertial force during impact.

Drop tests are often substituted in qualification testing of microelectronic devices by shock tests [119]. In shock tests, a short-term load with the given magnitude (i.e. a constant or half-sine load with the given maximum value of G) and duration is applied to the support structure of the device. In order to adequately mimic the drop test conditions, a short-term external acceleration is applied and should be well below the fundamental period of system's free vibrations. Otherwise the response of the system can result in substantially higher curvatures and accelerations than that occurring during drop tests [57]. The maximum acceleration of PCB can reach to more than 1000G when subjected to drop impact loading. The induced stress depends on local acceleration, deformation and dynamic strength of the structure. In the drop test, the measured maximum acceleration is often used as a criterion of the strength of structure in microelectronic products. It is well known, however, that it is the maximum stress, not the maximum acceleration, which is responsible for the dynamic strength of a

ATTENTION: The Singapore Copyright Act applies to the use of this document. Nanyang Technological University Library

structure [120]. Two typical cases, a simple supported beam and a cantilever beam with an impacting concentrated mass were analyzed to find the dynamic response of a system subjected to shock loading during drop tests by Suhir [77]. From the results of the analysis, the maximum acceleration and the maximum dynamic stress are affected differently by different factors and therefore the use of the maximum acceleration as a strength criterion for dynamic strength is not adequate. So understanding of the maximum dynamic stress is required to characterize the dynamic response of electronic product to shock excitation.

The drop impact reliability of portable electronic equipment depends on several external and product factors, the forces and accelerations during impact [121]: drop height, housing material, weight, shape, orientation at impact, surface onto which it drops. Most drop heights used in the industry are 1m [74, 121, 122] and 1.5m [123, 124]. Typical the accidental drops of a portable product are randomly oriented. Yu et al. [125] showed that the horizontal impact case of PCB is the most dangerous case for reliability of solder joints. The first order mode vibration is more dominant in dynamic fracture of solder joints. It was shown from study by Wong et al. [126] that packages of larger size, stiffer construction, and lower stand-off are more vulnerable to drop impact and stress increases with increasing of drop height, PCB length, package stiffness, package size and decreases with increasing of solder bump height, solder bump size, solder bump number.

There are mainly three types of drop tests in the electronic industry: (a) free fall product level; (b) free fall board level; and (c) controlled pulse drop at board level. Board level drop test is convenient to characterize the solder joint performance, as it is more controllable than product level drop test. Some researchers had conducted board level drop tests to understand the response of solder joint to impact loading using

ATTENTION: The Singapore Copyright Act applies to the use of this document. Nanyang Technological University Library

different boundary conditions such as 4 or 6 screw support [69, 70] clamped-clamped boundary condition [71, 72] and free fall drop [73, 74]. Some researchers [75, 76, 127] had conducted product level drop tests due to real drop events.

Lead-free solder usually exhibits less drop impact life than lead-based solder from many test results [70, 72]. Amagai et al. [79, 80] proposed that the number of drop to failure decreased with Ag content increasing for SnAgCu solder and the drop failure performance could be improved by adding some optimum Indium and Nickel to SnAgCu solder because Indium could reduce Kirkendall void and Nickel affected IMC growth. The study of impact reliability for solder joint conducted by Date et al. [128] showed SnAgCu solder was more prone to fracture at interface than SnPb solder under impact test because of higher bulk strength.

Recently, more and more FEA simulations were carried out for drop impact reliability study. The dynamic material properties of solder are different from static ones because the dynamic material properties are dependent on strain rate. For solder of Sn-3.5Ag-0.7Cu, the yield stress at high strain rate is about 3 times higher than that at low strain rate. However, the elastic modulus of the solder joints varies less with strain rate. The solder constitutive model used in FEA simulation will affect stress-strain behavior of solder significantly. Some researchers [70, 129] modeled solder joints and other materials as linear elastic behavior, which would result in more error. Zhu [75, 130] considered rate-dependent bilinear plastic model for Sn/Pb solder in FEA simulation of drop impact loading. However, rate-dependent stress-strain behavior of lead-free solder was not documented from limited literatures in FEA simulation of drop impact load. In this study, FEA modeling and simulation of drop impact were conducted considering different constitutive models of solder containing elastic, bilinear plastic, rate dependent plastic models.

ATTENTION: The Singapore Copyright Act applies to the use of this document. Nanyang Technological University Library

6.2 BOARD LEVEL DROP TEST AND ANALYSIS

Drop test and result analysis for FCOB assembly, bare PCB and PCB assembly have been published earlier [71, 131] and the details are given in Appendix C. In this section, drop test and analysis of PCB assembly with Pb-free or Pb-based solder and Ni/Au or OSP finish will be discussed.

6.2.1 Test Setup and Measurement

The Lansmont test machine was used to provide the drop impact load for board-level specimen with different packages. This machine can provide half sine shock pulse. The acceleration level of the half sine pulse is related to the drop height and the mount of felt pads on drop base. The duration of the pulse is adjustable somewhat by the addition or subtraction of the felt pads. The basic drop machine structure consists of a steel base, two solid chrome plated guide rods, drop table and hoist positioning system as shown in Fig. 6-1. The drop table is an aluminum weldment with an assembled mass of 190.5kg. The table contains brakes and low-friction bearings, which rid on the guide rods. An integral brake pressure regulator in the main control panel supplies nitrogen pressure to the brake.

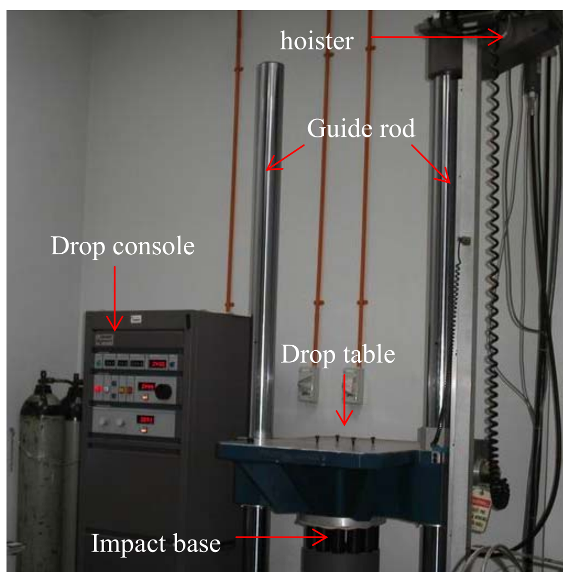

Fig. 6-1 Drop test setup.

ATTENTION: The Singapore Copyright Act applies to the use of this document. Nanyang Technological University Library

The specimen used in this experiment is shown in Fig. 6-2. The 35mmx35mm PBGA (312 balls), 28 mmx28mm PQFP (208 leads) and 7mmx7mm VQFN (48 leads) packages are mounted on PCB fixed on top of drop table with clamped-clamped boundary condition. All units are daisy chained for the purpose of solder joint failure monitoring. The solder compositions used in the test are 36Pb-62Sn-2Ag lead-based solder and Sn-4Ag-0.5Cu lead-free solder in order to investigate the effect of solder material on drop impact reliability of solder interconnects. Two different pad surface finishes of ENIG and OSP were used. Three labels were used for different specimens: Leg 1–Lead-free packages with ENIG finish; Leg 2–Lead-free packages with OSP finish and Leg 3–Lead based packages with OSP finish.

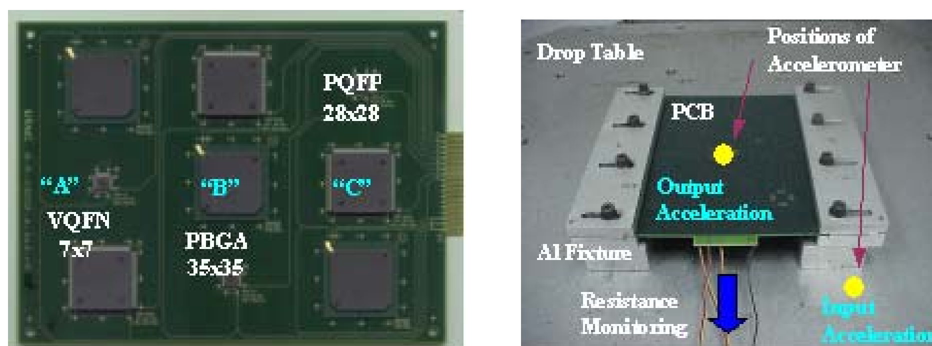

Fig. 6-2 PCB specimen with three different packages.

The drop height was set at 1m with the impact surface covered with felt pad. Six boards (sample size) were dropped for each of the three legs. The drop orientation is horizontal with facedown packages. The experiment was performed with an input peak acceleration of about 580G at the drop table. The acceleration of PCB center as shown in Fig. 6-3 is more than that of drop table due to deflection effect of PCB. As the PCB is experiencing maximum bending at the center during drop, only real time resistances of packages labeled "A", "B" and "C" as shown in Fig. 6-2 was monitored for drop impact reliability. Strain gauges were mounted on the PCB at the opposite side of the center PBGA package to measure the bending strain.

ATTENTION: The Singapore Copyright Act applies to the use of this document. Nanyang Technological University Library

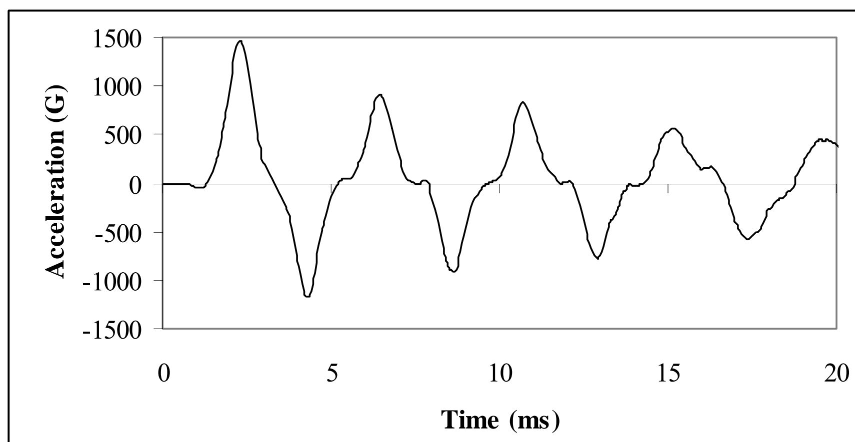

Fig. 6-3 Accelerations of PCB center.

6.2.2 Dynamic Response and Failure Detection

Because event detector usually captures an event (e.g., resistance more than 300Ω) and it may not be able to capture the continuous intermittent failure of solder joint during drop impact, the dynamic measurement method as shown in Fig. 6-4 was used to monitor resistance of daisy-chained solder joints in real-time during drop impact. According to this method, a constant resistor, R_0, is placed in series with the daisy chain of *Rx* and connected to a DC power supply. The oscilloscope was used to measure the dynamic voltage dropped on daisy chain loop. The dynamic resistance of solder joints, *Rx*, can be expressed:

$$R_x = \frac{R_0 V_x}{U - V_x} \tag{6.1}$$

where *U* is the voltage of the DC power supply and 1.8volts was used in this test, V_x is the dynamic voltage of daisy chain measured by oscilloscope, R_0 is the constant resistance of 10Ω used in this test. When $V_x \rightarrow U$, $R_x \rightarrow \infty$ (implies an open circuit), it indicates the critical solder joint has failed. Three solder joint daisy-chained current loops for components labeled “A”, “B”, and “C” as shown in Fig. 6-2 were monitored by three oscilloscope channels for one test board.

ATTENTION: The Singapore Copyright Act applies to the use of this document. Nanyang Technological University Library

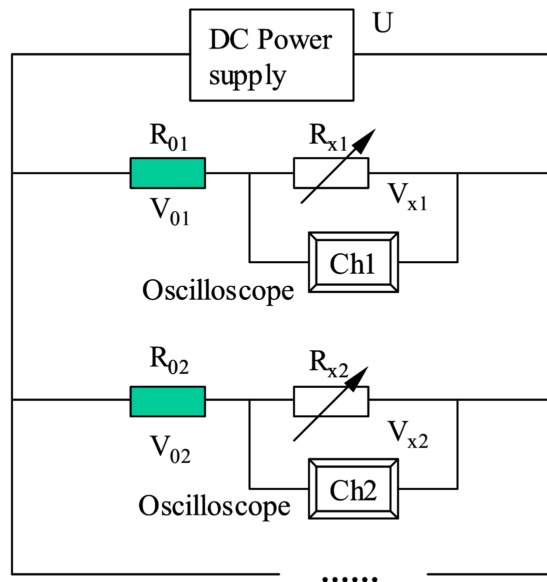

Fig. 6-4 Dynamic resistance measurement setup.

In a drop test, it is common to observe that the solder joint crack opens up resulting in a resistance discontinuity during drop impact and closes back to resume electrical continuity. The upward/downward deflection of the PCB leads to the opening/closing mode of the crack, which is known as an intermittent solder joint failure. When the crack becomes larger and cannot close back even after the impact test, a permanent solder joint failure occurs. In the current test, the permanent solder joint failure is identified as the failure criteria. Fig. 6-5 shows the typical dynamic response of resistance and PCB strain for lead-free assembly with OSP board finish. The resistance of PBGA solder daisy chain increases from an initial value of 1.4 volts (35Ω) to 1.8 volts (daisy chain open) after a rapid crack propagation. As for the VQFN package, some intermittent failures were observed from Fig 6-5. Dynamic voltage changes from initial value of 0.3volts (2Ω) to 1.0 volt (12.5Ω) then returns to 0.3volts, which shows that the crack is only partial and the partial crack probably closes up after vibration of board ceases. The resistance of PQFP daisy chain keeps constant after the impact from Fig. 6-5.

ATTENTION: The Singapore Copyright Act applies to the use of this document. Nanyang Technological University Library

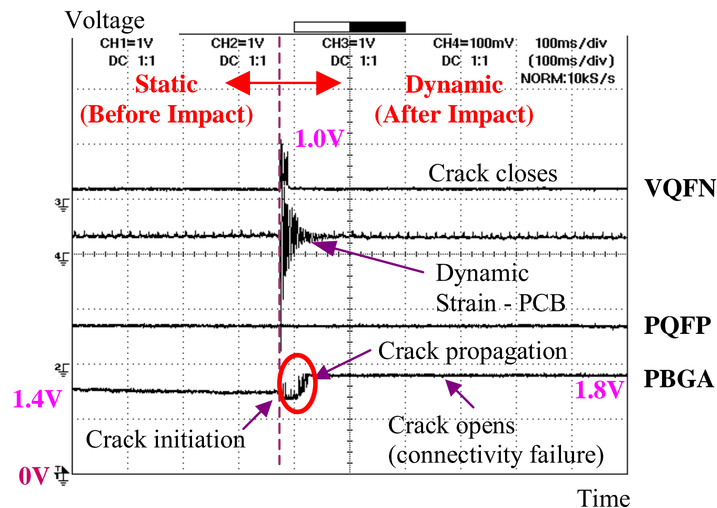

Fig. 6-5 Typical dynamic response during drop impact for leg2 specimen.

6.2.3 Drop Impact Results and Discussion

With a drop of 50 times conducted for each test board, the summary of the impact test results is given in Table 6-1. The sample size is 6 for each of the test package. It can be seen that PBGA component is more prone to drop impact failure than PQFP and VQFN components. Components with lead-free solder have less drop impact reliability than components with lead-based solder, which is consistent with drop impact result for a fine-pitch BGA packages tested by Tee et al. [70]. As for PBGA components, OSP board finish improves more impact reliability than Ni/Au finish. For PBGA component with lead-free solder and Ni/Au finish, five out of six failed units were detached away from the PCB. By examining the PCB where the PBGA detached from, solder ball to copper pad interface failure was found to be of majority. Clear solder joint cracks at the board side were found in the last remaining unit. However, for the PBGA package in Legs 2 & 3, PCB copper traces breakage and resin cracks were the contributing factor for connectivity failure [72]. Lall et al. [132] also reported PCB resin cracks in the drop test of chip scale package. As for the PQFP packages, failures were not due to solder joint crack but component failure with the lead fingers breaking off from the mold compound due to inertial force of component. As the

ATTENTION: The Singapore Copyright Act applies to the use of this document. Nanyang Technological University Library

smallest in size and lightest in weight, the VQFN components are the most resistant against impact forces among the three components.

Table 6-1 Drop impact test results.

Package	Test leg	Failure frequency	Numbers of drop to failure
PBGA	Lead-free Ni/Au	6/6	1, 1, 1, 2, 6, 24
	Lead-free OSP	5/6	15, 15, 19, 28, 47
	Lead-based OSP	3/6	12, 24, 40
PQFP	Lead-free Ni/Au	2/6	44, 45
	Lead-free OSP	2/6	16, 29
	Lead-based OSP	0/6	-
VQFN		0/18	-

6.3 FEA MODELING FOR DROP TEST

6.3.1 Drop Impact Modeling

The combination of numerical simulation and test is a desirable approach to obtain failure analysis and understand the dynamic response of the electronic assembly under drop impact load. It is a significant advantage for FEA simulation that it can pick up complete mechanical information at any location of analyzed object. Impact response is a typically transient phenomenon. In transient analysis with FEA, there are two basic algorithms for time integration methods: implicit and explicit methods.

For implicit time integration, inertia effects of mass and damping ([*C*] and [*M*]) are typically not included. Average acceleration-displacements evaluated at time $t+\Delta t$ are given by [133]:

$$\{U_{t+\Delta t}\} = [K]^{-1}\{F^{a}_{t+\Delta t}\} \tag{6.2}$$

For linear problems, the solution is unconditionally stable when the stiffness matrix [*K*] is linear, and large time steps can be taken. But for nonlinear problems, the

ATTENTION: The Singapore Copyright Act applies to the use of this document. Nanyang Technological University Library

solution requires inversion of the nonlinear stiffness matrix [K], at the same time small iterative time steps are required to achieve convergence and the convergence is not guaranteed for highly nonlinear problems.

For the explicit time integration, a central difference time integration method is used. Accelerations evaluated at time t are given by:

$$\{a_t\} = [M]^{-1}\left[\{F_t^{ext}\} - \{F_t^{\text{int}}\}\right] \tag{6.3}$$

where $[M]$ is a mass matrix, $\{F_t^{ext}\}$ is the external force vector, and $\{F_t^{\text{int}}\}$ is the internal force vector. The velocities and displacements can be evaluated after acceleration is known. The geometry is then updated by adding the displacement increments to the initial geometry.

For nonlinear problems, no inversion of the stiffness matrix is required and very small time steps are required to maintain the stability limit for explicit time integration method. Therefore, with tiny step, the implicit method is more time-consuming than the explicit because of its matrix integration and inversion. The explicit method becomes the optimal algorithm for the impact problem. ANSYS has a LS-DYNA module for explicit-based problems and is selected for the FEA simulation for drop impact test in this study to investigate the stress strain behavior of solder joint.

6.3.2 FEA Study of Drop Test for PBGA Assembly

In FEA modeling and simulation for drop impact test of board-level electronic assembly, three methods are usually used: full drop modeling event (full model), hybrid experiment-modeling event with input displacement (Input-D model) and with input acceleration (Input-G model). These three methods were conducted in FEA simulation for FCOB assembly in Appendix C. It was shown that Input-G method is a suitable and accurate method in drop simulation. In this section, Input-G modeling method is used for drop simulation of PBGA assembly.

ATTENTION: The Singapore Copyright Act applies to the use of this document. Nanyang Technological University Library

6.3.2.1 FEA model and material properties

The FEA modeling and simulation for PBGA assembly with lead-free solder joint as shown in Fig. 6-2 was conducted. Some assumptions were made in FEA modeling. Dynamic response of each component mounted on PCB is not affected by other components. The effect of components on global response of PCB can be ignored. Therefore, the quarter model can be created due to symmetry when only considering center PBGA component. Fig. 6-6 shows the quarter FEA model for PBGA assembly with total 16029 elements and 20913 nodes. The materials considered in FEA simulation contain FR4 PCB, SnAgCu solders, copper pads on both board side and package side, BT substrate, silicon die and mold compound.

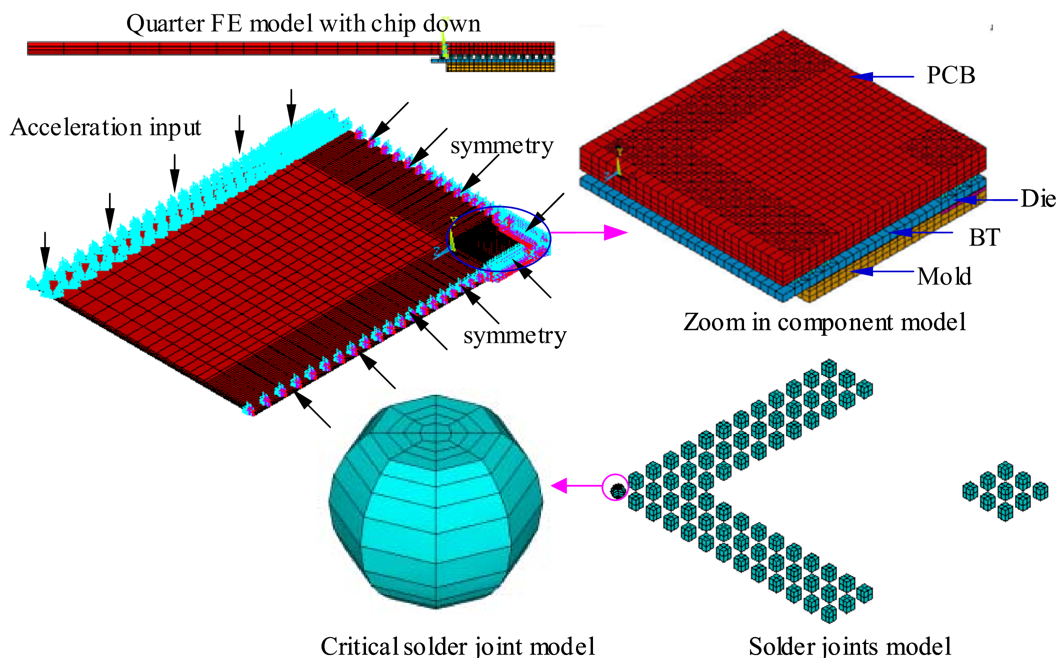

Fig. 6-6 Quarter FEA model and boundary condition for PBGA assembly.

Table 6-2 gives the material properties used in FEA simulation. In order to reduce element size, effective solder joint model developed in Chapter 3 was implemented except critical solder joint of corner solder ball for which the fine meshing was used. Symmetry boundary conditions were used in quarter model. The input acceleration as shown in Fig. 6-7 was applied on clamped PCB edge. Total 15 microseconds were

ATTENTION: The Singapore Copyright Act applies to the use of this document. Nanyang Technological University Library

simulated with 150 substeps for general result file and 750 substeps for history result file. Subcycling and mass scaling are effective techniques in explicit time integration method for reducing solving time without losing accuracy. The time step of –2e-8 and scale factor of 0.9 for scaled solution were used in FEA simulation so that achieving more than 70% decrease in CPU time while adding only 0.014% mass to the model.

Table 6-2 Material properties of FEA drop model for PBGA assembly.

Materials	Young's modulus (GPa)	Yield stress (MPa)	Tangent modulus (MPa)	Poisson’s ratio	Density (kg/m^3)
SnAgCu solder	Table 6-3	Table 6-3	Table 6-3	0.35	7500
FR4 PCB	20 (x,z), 9.8(y)	-	-	0.11(x,z),0.28(y)	1900
BT substrate	26 (x,z), 11(y)	-	-	0.11(x,z),0.39(y)	2000
Copper pad	155.2	120	1000	0.34	8900
Silicon chip	131	-	-	0.278	2330
Mold compound	16	-	-	0.24	1970

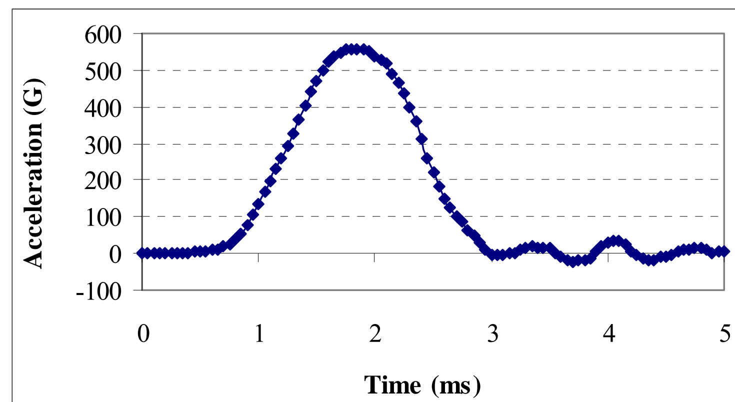

Fig. 6-7 Input acceleration in drop impact FEA simulation for PBGA assembly.

6.3.2.2 Elastic model for SnAgCu solder

In FEA modeling and simulation for drop test of PBGA assembly with lead free solder joint, the important and critical material is solder. Therefore, it is important for solder dynamic response how to model solder material in high strain rate loading condition. From limited publications [70, 75, 130], elastic and elastic-plastic models were simulated for Sn/Pb solder under drop impact load. In this study, elastic model and

ATTENTION: The Singapore Copyright Act applies to the use of this document. Nanyang Technological University Library

inelastic models were applied for lead-free solder in order to investigate the effect of constitutive model on dynamic response of solder joint. In this section, elastic model was first considered for solder joint material. It was known that damping effect is important for dynamic behavior of PCB under drop impact load and it is difficult to obtain accurate damping parameter from experiment. Therefore, trial and error was carried out in FEA simulation to achieve suitable damping parameter. The damping ratio varies from 0.01 to 0.1 with a step of 0.01 was simulated. The optimal damping ratio of 0.02 was achieved by comparing the output acceleration of PCB center as shown Fig. 6-8 from simulation result with acceleration as shown in Fig. 6-3 measured from drop impact.

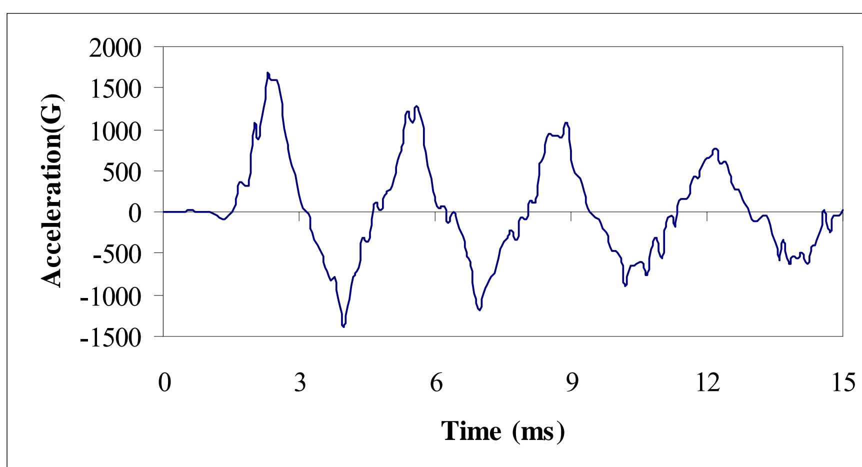

Fig. 6-8 Acceleration of PCB center node from FEA simulation.

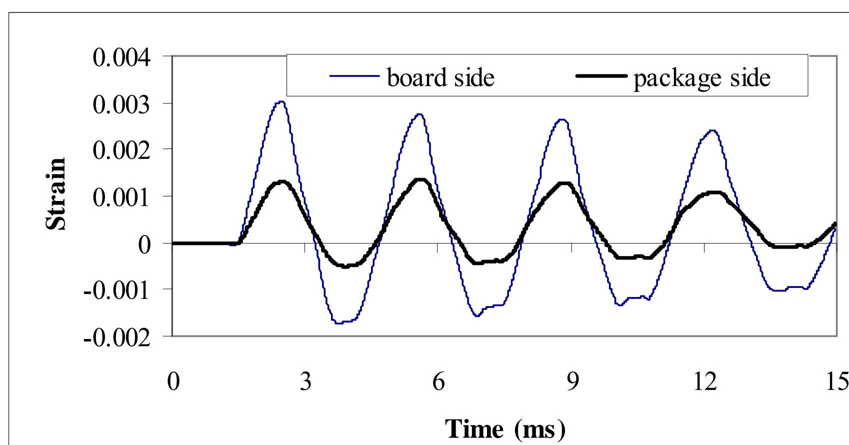

Fig. 6-9 Strain in drop direction for critical node on board and package sides.

ATTENTION: The Singapore Copyright Act applies to the use of this document. Nanyang Technological University Library

Fig. 6-9 shows the vertical strain comparisons between critical nodes on board side and package side. It is obvious that strain on board side is more than that on package side due to PCB deflection effect which indicates solder/PCB interface is prone to fail.

Fig. 6-10 shows the component stress in drop direction and first principal stress of critical node on board side. It can be seen that peak stress between component peel stress and first principal stress is quite close, which implies that the peel stress is the dominant part in inducing crack initiation and propagation of solder/PCB interface. The impact fatigue model was presented by Tee et al. [70] using peel stress as damage parameter for TFBGA package with Sn/Pb solder. However, the limitation of this impact model is that just elastic behavior was modeled for solder joints.

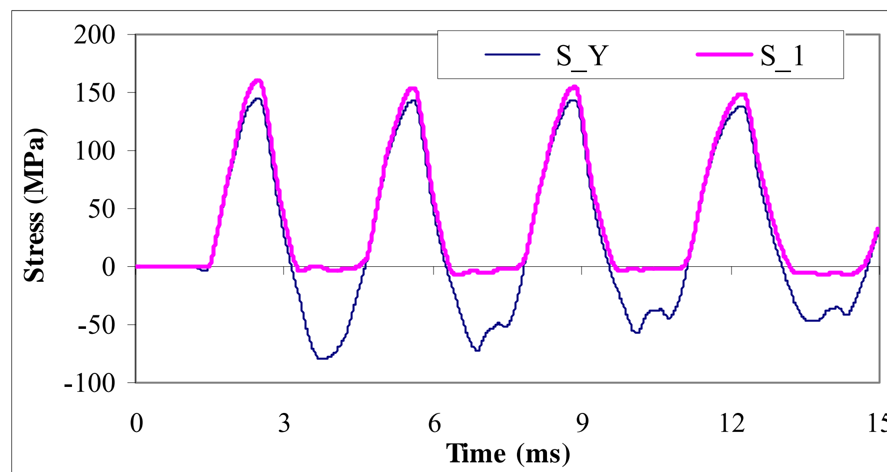

Fig. 6-10 Peel and 1st principal stress for critical node on board side.

6.3.2.3 Bilinear kinematic plastic model for SnAgCu solder

Plastic deformation of solder joint can be expected in dramatically dynamic loading such as drop impact load. In this section, the bilinear kinematic plastic model was implemented for solder and other materials have the same material properties as elastic model. The material properties of solder were extracted from static tensional test with slow strain rate, which is always used in thermal cycling simulation. Fig. 6-11 shows

ATTENTION: The Singapore Copyright Act applies to the use of this document. Nanyang Technological University Library

the component stress in drop direction from FEA results of elastic model and bilinear plastic model. It can be seen that the peak value of peel stress reduces by 30% when considering solder plastic behavior compared to elastic model. Fig. 6-12 shows von Mises stress comparison of critical node on board side between elastic model and plastic model. The error of peak von Mises stress between elastic and plastic is more than 100%. Therefore, consideration of plastic behavior is necessary in FEA modeling and simulation of electronic assembly under drop impact load. However, the strain rate of solder is not constant during drop impact test. In order to obtain more accurate stress strain result of solder, strain rate dependent plastic model is essential.

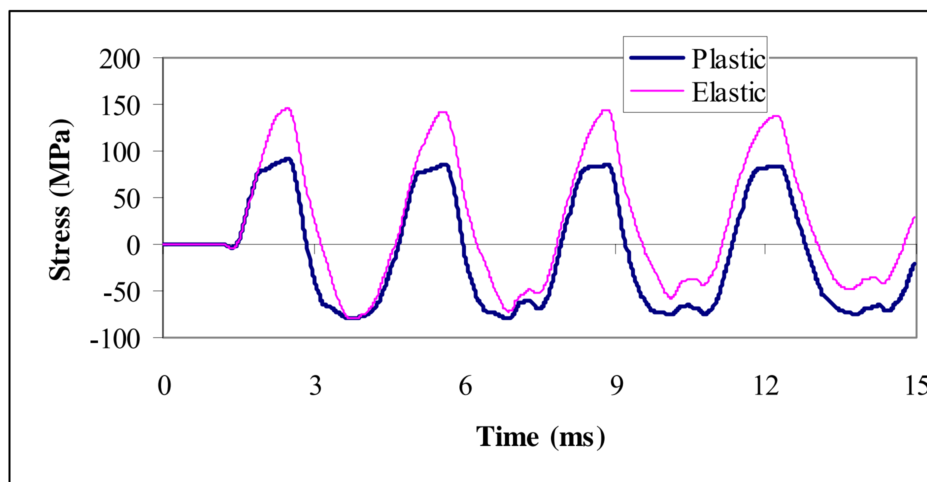

Fig. 6-11 Peel stress of critical node on board side from elastic and plastic models.

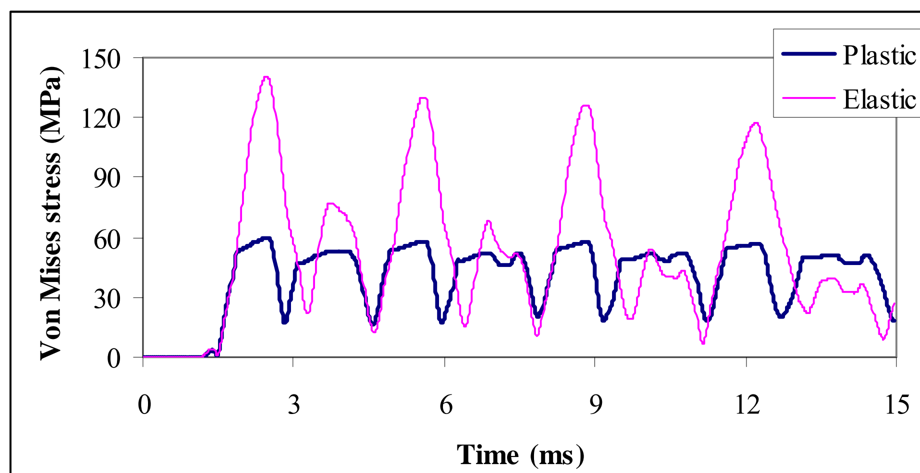

Fig. 6-12 Von Mises stress from elastic model and plastic model.

ATTENTION: The Singapore Copyright Act applies to the use of this document. Nanyang Technological University Library

6.3.2.4 Strain rate dependent plastic model for SnAgCu solder

Fig. 6-13 shows the stress strain curves for SnAgCu solder under different strain rates. It can seen that strain rate effect on solder material properties is significant. The rate dependent material properties were extracted from Fig. 6-13 and tabulated in Table 6-3. The Young's modulus, yield stress and tangent modulus increase with strain rate increasing. Strain rate effect on yield stress and tangent modulus are more significant than on Young's modulus. The load curves based on data in Table 6-3 were used to define the material properties as a function of strain rate in FEA simulation.

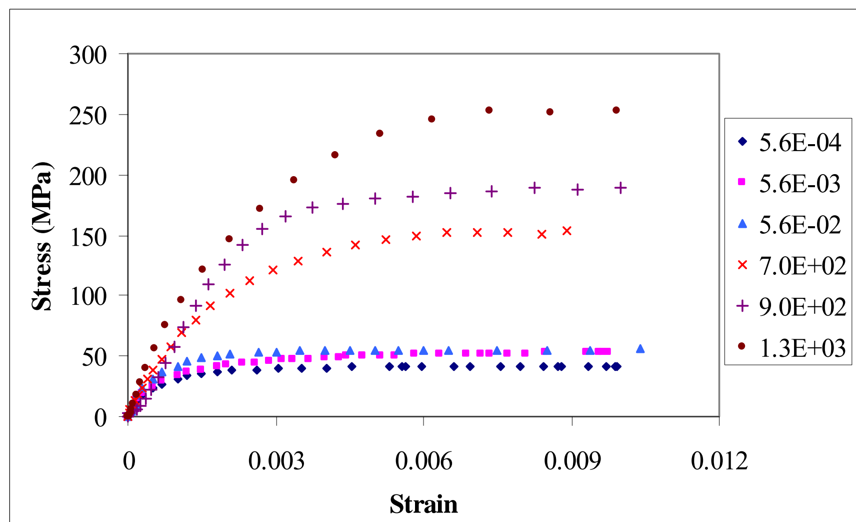

Fig. 6-13 Stress strain curves of SnAgCu solder under different strain rates.

Table 6-3 Strain rate dependent material properties of SnAgCu solder.

Strain rate	5.6E-4	5.6E-3	5.6E-2	7.0E+2	9.0E+2	1.3E+3
Young's modulus (GPa)	41.8	48.3	52.8	53.3	54	55.1
Yield stress (MPa)	35.1	42.9	53.1	129	175	230
Tangent modulus (MPa)	127	146	230.7	976	1662	2165

Fig. 6-14 shows the von Mises stress from two different plastic models. The von Mises stress from rate dependent plastic model is higher than that from bilinear plastic model because strain rate effect increases the yield stress level in rate dependent plastic model. High yield stress level reduces the effective plastic strain increment as

ATTENTION: The Singapore Copyright Act applies to the use of this document. Nanyang Technological University Library

shown in Fig. 6-15 where effective plastic strain of critical node on board side from rate dependent plastic model is lower than that from bilinear plastic model.

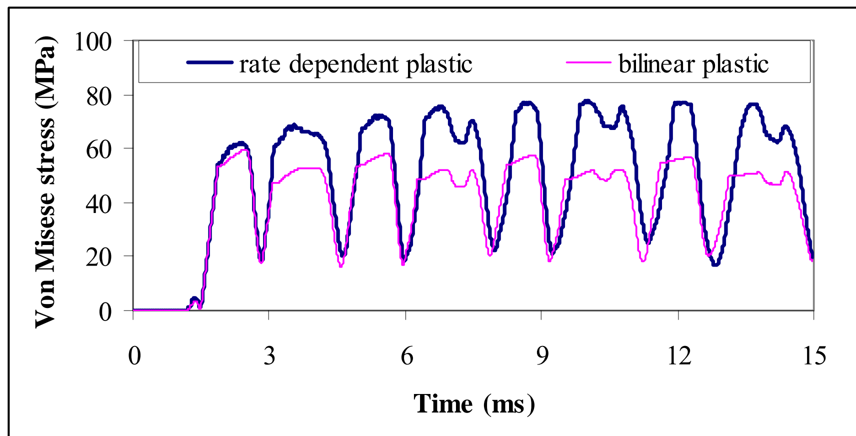

Fig. 6-14 Von Mises stress from different plastic models.

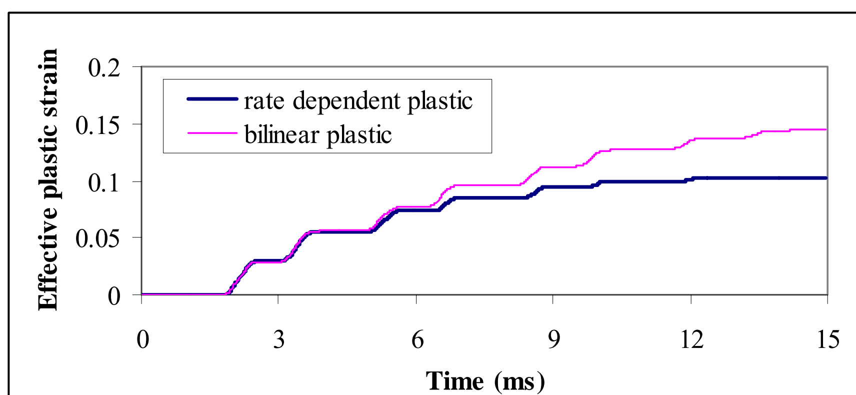

Fig. 6-15 Effective plastic strain from different plastic models.

6.3.2.5 Intermetallic compound consideration in FEA simulation

The 3µm layer of tertiary CuNiSn IMC was modeled on both chip and board sides. IMC were modeled as elastic behavior. Young's modulus, Poisson's ratio, and density of CuNiSn IMC used in FEA model are 160GPa, 0.25 and 8440kg/m^3, respectively. It is the first time to investigate the IMC effect on solder under drop impact load using FEA simulation. Fig. 6-16 shows the effective plastic strain of critical node on board side for both FEA models with and without IMC consideration when solder was modeled as bilinear plastic behavior. IMC layer consideration in FEA model reduces the effective plastic strain compared to FEA model without modeling IMC layer. The

ATTENTION: The Singapore Copyright Act applies to the use of this document. Nanyang Technological University Library

IMC layer is harder than copper pad so that it constrains the plastic deformation of solder, which results in lower effective plastic strain. It was known that IMC layer consideration in thermal cycling simulation increases solder plastic deformation due to larger CTE mismatch between IMC and solder. However, existing IMC layer reduces the impact reliability of electronic package from drop tests. Therefore, just considering deformation and solder stress strain behavior is not sufficient for investigating impact reliability of electronic assembly subjected to drop impact load. Interface failure and copper trace fracture are also important failure mode encountered in drop test [72].

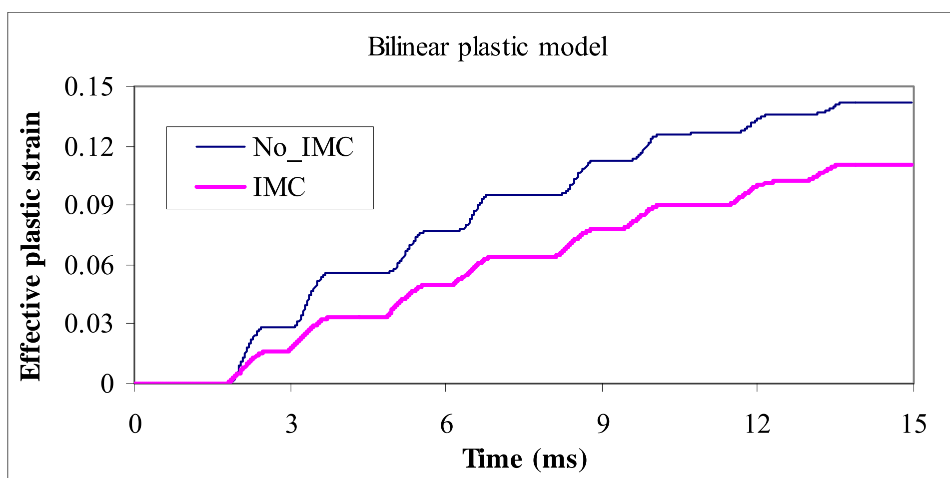

Fig. 6-16 Effective plastic strain from bilinear plastic model for both with and without IMC consideration.

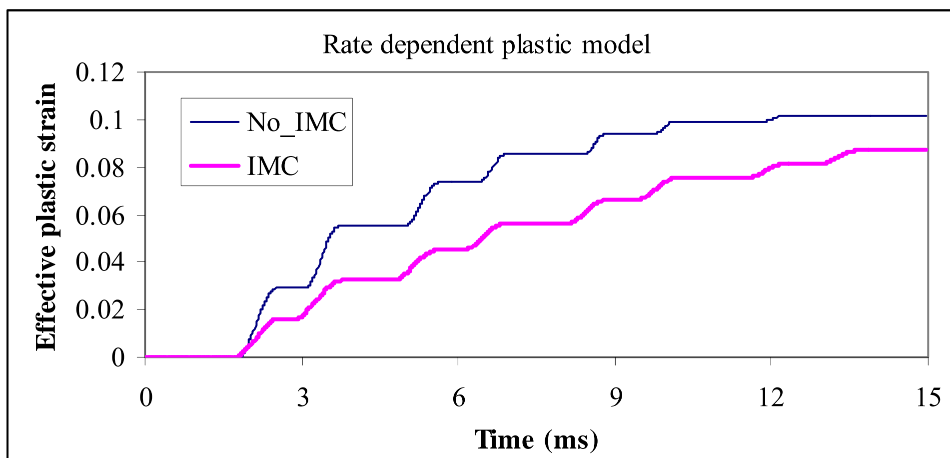

Fig. 6-17 Effective plastic strain from rate dependent plastic model for both with and without IMC consideration.

ATTENTION: The Singapore Copyright Act applies to the use of this document. Nanyang Technological University Library

Fig. 6-17 shows the effective plastic strain of critical node on board side for both FEA models with and without IMC layer consideration when solder was modeled as rate dependent plastic behavior. The results from rate dependent plastic model are similar to that from bilinear plastic model. Fig. 6-18 shows von Mises stress comparison between FEA models with and without modeling IMC layer. The von Mises stress is also lower for the case of modeling IMC layer than without considering IMC layer in FEA simulation.

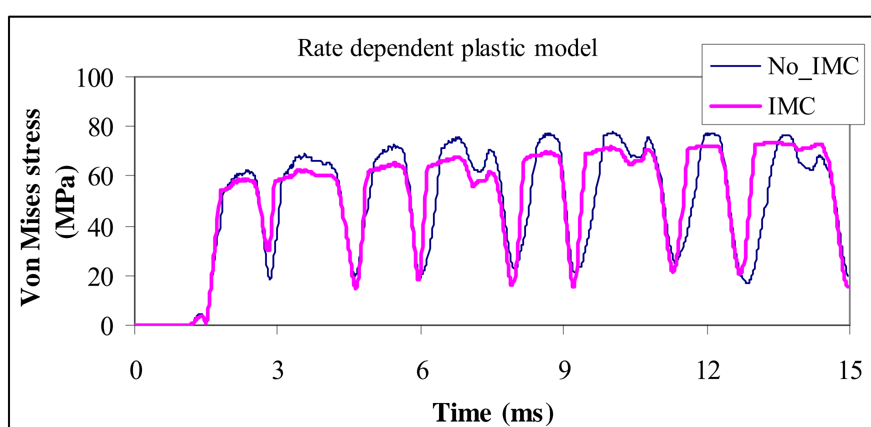

Fig. 6-18 Von Mises stress from rate dependent plastic model for both with and without IMC consideration.

6.4 CHARPY IMPACT TEST AND ANALYSIS

The Charpy impact test helps determine the impact energy absorbed and failure mode. Two different Charpy specimens of bulk SnAgCu specimen and soldered specimen as shown in Fig. 6-19 were used in this test. For soldered specimen, two copper blocks were soldered together with 1mm SnAgCu solder after reflow process. Two cases were studied for soldered specimen: copper block with and without Ni/Au plating. Three specimens (sample size) were used for each type of Charpy specimen.

Soldered specimen Bulk specimen

Fig. 6-19 Charpy specimens.

ATTENTION: The Singapore Copyright Act applies to the use of this document. Nanyang Technological University Library

Fig. 6-20 shows the fracture modes for different specimens. The bulk specimen exhibits ductile failure and soldered specimen shows all brittle interface failure. Table 6-4 lists the impact toughness for different specimens. The bulk specimen has the largest toughness value. The impact toughness of soldered specimen without Ni/Au plating is twice higher than that with Ni/Au plating. It implies that electronic assembly with SnAgCu solder and Ni/Au finish is liable to impact failure compared to the case without Ni/Au finish, which is consistent with drop test result for PBGA assembly mentioned earlier. Cu_6Sn_5 was formed between copper block and SnAgCu solder while CuNiSn was formed when Ni/Au plating was used. The fracture toughness for Cu_6Sn_5 and Cu_3Sn were reported by Balakrisnan et al. [134] using the controlled buckling test.

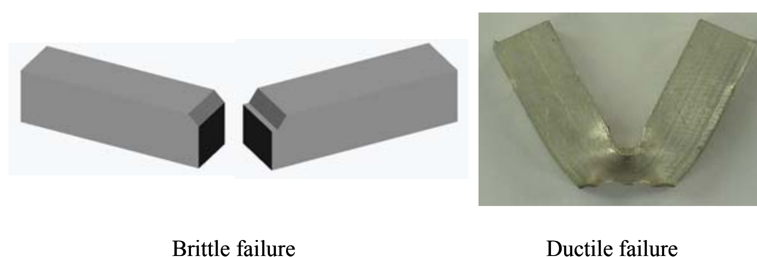

Brittle failure Ductile failure

Fig. 6-20 Fracture mode for different specimens.

Table 6-4 Impact toughness for different specimens.

Specimens	Bulk SnAgCu	Soldered	Soldered with Ni/Au plating
Impact toughness (J)	74	0.261	0.118

6.5 SUMMARY

Board-level drop impact tests were conducted for electronic assembly with different components. Drop impact FEA modeling and simulation for PBGA assembly with SnAgCu solder joints were carried out using Input-G modeling method with considering different solder constitutive models including elastic, bilinear kinematic plastic and strain rate dependent plastic model. IMC layer was modeled to investigate

ATTENTION: The Singapore Copyright Act applies to the use of this document. Nanyang Technological University Library

IMC effect on dynamic response of solder. Charpy impact tests were conducted for bulk solder specimen and soldered specimen.

A new and simple dynamic resistance monitoring setup can capture instantaneous and permanent drop impact failure. The PBGA component is more prone to drop impact failure than PQFP and VQFN components because leads in PQFP package are shock compliant and smaller size of VQFN causes it to be most robust under drop test. Components with lead-free solder have less drop impact reliability than components with lead-based solder. The PBGA component with OSP board finish exhibits more impact reliability than that with Ni/Au finish.

FEA modeling and simulation for PBGA assembly with SnAgCu solder show that peel stress in drop direction is a dominant component stress. The stress and strain of solder on board side are more than those on package side due to PCB deflection and inertial effect. Strain rate dependent plastic model was presented and it could lead to more reasonable and accurate results than elastic model and bilinear plastic model.

IMC layer modeled in FEA simulation reduces the plastic deformation of solder due to constraint effect of hard IMC layer on deformation of solder.

Bulk Charpy specimen shows the ductile fracture with higher impact toughness, while soldered Charpy specimen exhibits brittle fracture at IMC/solder interface with lower impact toughness. The Ni/Au plating on copper block reduces the fracture energy of soldered Charpy specimen compared to the case without Ni/Au plating, which is consistent with drop test results of components with OSP finish exhibiting more impact reliability than components with Ni/Au finish.

ATTENTION: The Singapore Copyright Act applies to the use of this document. Nanyang Technological University Library

CHAPTER 7 VIBRATION TEST AND ANALYSIS

7.1 INTRODUCTION

Electronic equipment can be subjected to many different forms of vibration over wide frequency ranges and acceleration levels [119]. Vibration, in a broad sense, is considered as an oscillating motion where structure or body moves back and forth. The simplest form of periodic motion is harmonic motion, which is usually represented by a continuous sine wave on a plot of displacement versus time, and this type of vibration is often selected for testing electronic equipment.

Vibration-induced stress can usually lead to fatigue failure for electronic assemblies. Vibration fatigue failure of solder joints is often assessed for reliability in electronic assemblies subjected to vibration load. There are three steps in vibration fatigue analysis of electronic assembly. Firstly, modal analysis of PCB; secondly, dynamic analysis of PCB; thirdly, stress analysis of the individual soldered component.

In order to obtain the mode shape and its related frequency, experimental and numerical methods are usually used. The most critical variable in the FEA modal analysis of PCB with electronic components is an accurate description of the boundary conditions because the frequency of PCB is very sensitive to the boundary conditions. Typical PCB edge conditions include clamped, simple support, and free conditions. Barker and Chen [135] introduced the rotational spring to model the wedge lock as elastic support for accurate natural frequency calculations. Lim, et al. [136] also used the rotational spring stiffness to simulate the support effect. For surface mounted microelectronic components, an approximation of PCB modal analysis can be made by considering the PCB as a bare unpopulated thin plate because the increase in stiffness

ATTENTION: The Singapore Copyright Act applies to the use of this document. Nanyang Technological University Library

of PCB due to the mounting of the components is approximately offset by the increase in total mass of the populated PCB [137]. But this approximation can lead to different errors for different packages, such as BGA, PGA, FCOB, and QFP etc.

The second step in vibration fatigue life calculation is dynamic analysis where the response of the PCB is calculated due to the vibrating load. The first few mode shapes are used since they represent the largest deflections and curvatures of the PCB and will account for the majority of the fatigue damage. The dynamic analysis provides information about the PCB deflection at each component location and for each mode shape. Then FEA simulation was used to determine the stress of the solder joint to predict the fatigue life of electronic component subjected to vibration load. Due to the complication of the geometry of electronic assembly, full simulation of electronic assembly will be very time-consuming and expensive. So the two-level submodeling approach has been used [138, 139].

The vibration analyses by Basaran and Chandaroy [140, 141], Zhao et al. [142] showed that solder joints respond elastically mainly at room temperature vibration loading. So, vibration fatigue failure of solder joints is often assessed for reliability using high cycle fatigue model, which is represented by an S-N curve.

In order to assess the reliability of FCOB assembly, it is necessary to conduct the modal analysis, stress-strain analysis and dynamic analysis. The submodeling method [37, 143, 144] was commonly used for board level FEA simulation. In this study, the constant G-level and block G-level vibration tests for FCOB assembly were conducted. Four different cases were considered in FEA modal analysis of FCOB assembly. The quasi-static analysis was conducted for FCOB assembly to calculate the stress strain of flip chip solder joints. Fatigue life comparisons were conducted among test results, quasi-static analysis and harmonic analysis results.

ATTENTION: The Singapore Copyright Act applies to the use of this document. Nanyang Technological University Library

7.2 VIBRATION TEST

Details of the vibration tests have been published earlier [82, 86] and summarized in Appendix D. In this section, vibration test and analysis is presented briefly.

In this study, sinusoidal vibration test was conducted for FCOB assembly as shown in Fig. 7-1 using constant G-level and block G-level of 3G, 5G and 10G (G is gravity acceleration) loadings. A clamped-clamped boundary condition along two long opposite PCB edges was used in test. In this study, 50% increase of resistance of daisy chain loop was used as a rule to determine the failure by Event Detector. The vibration transmissibility of the PCB was determined using two accelerometers mounted on the fixture and PCB. The frequency-scanning test was conducted with sweep sine frequency from 20Hz to 1000Hz first and the fundamental natural frequency of 194Hz was determined for FCOB specimen. Nonlinear vibration effects were obtained at different acceleration inputs for FCOB assembly.

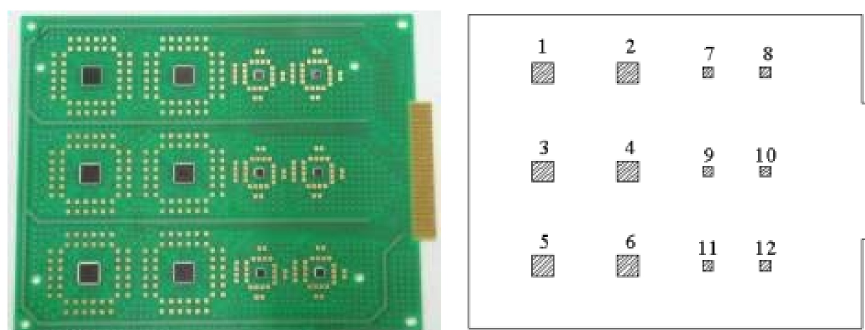

Fig. 7-1 Flip chip on board assembly and die number.

After frequency scanning test, then reliability test was conducted with frequency from 175Hz to 215Hz. The test results for outer chain on the large component satisfying two-parameter Weibull distribution and Weibull parameters are listed in Table 7-1. The fatigue life of flip chip solder joint reduces rapidly with vibration acceleration increasing.

ATTENTION: The Singapore Copyright Act applies to the use of this document. Nanyang Technological University Library

Table 7-1 Weibull parameters, MTTF and FTTF under vibration.

G_{in}	Char. life η (10^6cycles)	Slope β	MTTF (10^6 cycles)	FTTF (10^6 cycles)
3G	65.30	2.22	57.84	32.30
5G	23.28	1.20	21.91	4.93
10G	12.89	1.41	11.73	2.47

7.3 FINITE ELEMENT ANALYSIS FOR VIBRATION TEST

7.3.1 Modal Analysis of FCOB Assembly

PCB was modeled as shell element in FEA modal analysis because its thickness was very quite small compared with its length and width. The clamped-clamped boundary condition was simulated according to the test condition. First, the bare PCB without Flip Chip components was simulated for modal analysis to study the different variables effect such as material properties, element size (see Appendix D). The first ten mode shapes for bare PCB were put in Appendix D. It is found that the mode shape becomes more complicated when the order of mode increases. In general, the first order mode has the most significant effect on the reliability of the electronic devices.

In order to obtain the more accurate modal analysis result for FCOB assembly, four detailed modal analyses were conducted. In case 1, the Flip Chip components were modeled as distributed masses on the PCB. In case 2, the components were modeled as concentrated masses at the center locations of the components on the PCB. In case 3, the components were modeled as solid part. In case 4, the IC chips were modeled as shell and the solder joints were modeled as effective two-node beam elements with equivalent stiffness discussed in Chapter 3 for GLB modeling technique. According to Steinberg [119], the fundamental frequency for a PCB with the Clamped-Clamped boundary condition can be obtained from the following equation:

ATTENTION: The Singapore Copyright Act applies to the use of this document. Nanyang Technological University Library

$$f_n = \frac{3.55}{a^2}\sqrt{\frac{D}{\rho}} \tag{7.1}$$

where $D = Eh^3/12(1-\mu^2)$, $\rho = Mass/Area$, E=22000N/mm2, (Young's modulus),μ =0.28, (Poisson's ratio), h=1.13mm, (thickness of the PCB), a=140mm, (free side length of the PCB), ρ =2.147kg/m^2 =2.147e-9Ns^2/mm^3 (area mass density).

Table 7-2 shows the first mode natural frequency of the PCB obtained from different methods. The frequency obtained from bare PCB has a good agreement with theoretical result. The result of modal analysis using global-local beam (GLB) model has a good agreement with test result. A good approximation of FCOB assembly modal response can be made by considering the PCB as a bare unpopulated thin plate as the increase in stiffness of PCB due to the mounting of the components is offset by the increase in total mass of flip chip modules. The same approximation could introduce more error for PCB with BGA assemblies [145] because the contribution of the masses and stiffness of the BGA modules for PCB can not be ignored as the BGA modules have the larger volume and mass than flip chip modules.

Table 7-2 Comparison of the natural frequencies results.

Methods	Bare PCB	Eq. (7.1)	Case 1	Case 2	Case 3	Case 4	Test
Frequency (Hz)	208.6	209.4	206.8	206.8	209.6	201.9	194.1

7.3.2 Quasi-Static Analysis for Vibration Fatigue

7.3.2.1 Determining quasi-static load

In this study, a quasi-static analysis method was developed to calculate the stress strain behavior of the solder joints, which can be used for fatigue life prediction using stress-based fatigue model. The dynamic loading due to vibration was replaced by effective static loading in this method. According to Newton's second law, the pressure acting

ATTENTION: The Singapore Copyright Act applies to the use of this document. Nanyang Technological University Library

on the PCB or component can be obtained:

$$p = \frac{F}{A} = \frac{mG_{out}}{A} = \frac{\rho v G_{out}}{A} = \rho t G_{out} g \qquad (7.2)$$

where m, ρ, v, A, t are mass, density, volume, area, thickness of PCB or chip, respectively. G_{out} is output acceleration in G.

For constant G level test, the pressure load can be obtained when transmissibility is known. It is observed that transmissibility is not a constant value along transverse locations. The transmissibility was measured only for the half of the PCB due to symmetry. Eight locations uniformly distributed along PCB transverse direction shown in the Fig. 7-2 were selected to measure transmissibility of the PCB. Fig. 7-3 shows the transmissibility for different location at natural frequency for 10G test and a linear relationship between transmissibility and location is clear.

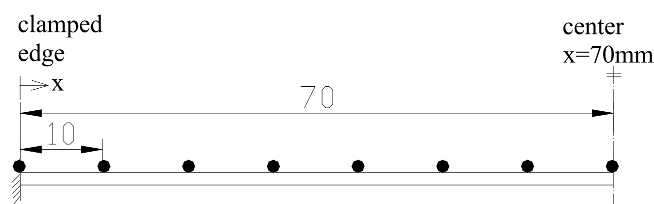

Fig. 7-2 Schematic of the location for transmissibility measurement.

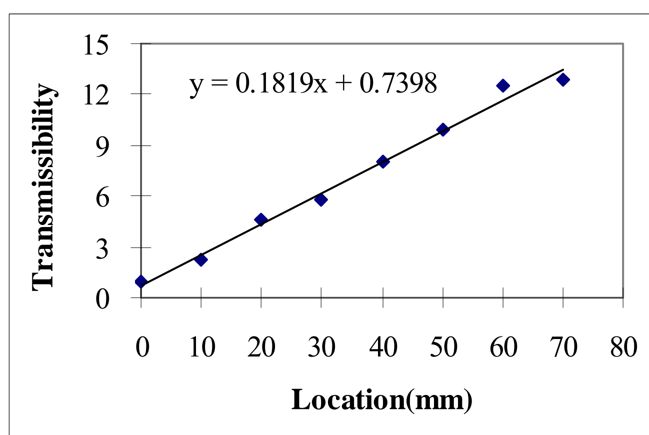

Fig. 7-3 Transmissibility at natural frequency for 10G input test.

7.3.2.2 Determination of stress amplitude

Submodeling technique was used in quasi-static analysis because it is difficult to take

ATTENTION: The Singapore Copyright Act applies to the use of this document. Nanyang Technological University Library

board level simulation for FCOB assembly using fine 3D model. Submodel consists of chip, underfill, solder ball, copper pad and FR4 PCB as shown in Fig. 7-4. For the whole model, only chip3 and 4 were modeled, and clamped-clamped boundary condition along two opposite longer sides was applied. Elastic-plastic constitutive model for solder joint was used and no plastic strain occurs from result.

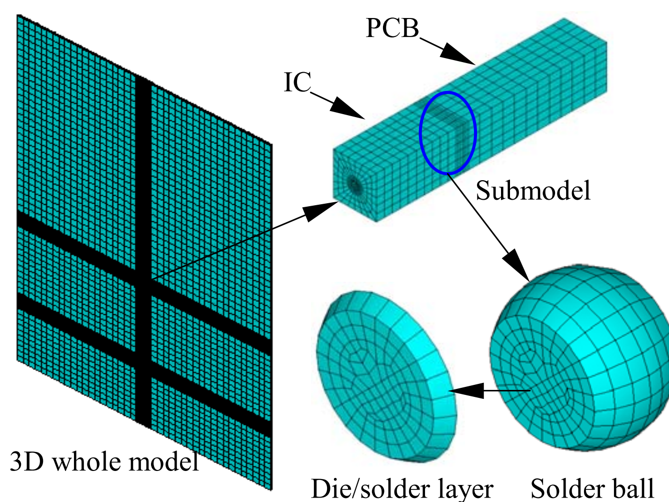

Fig. 7-4 Global and local models for FCOB assembly.

Table 7-3 Material properties used in FEA analysis for FCOB assembly.

Materials	Solder	FR4 PCB	Silicon	Underfill	Copper pad
E (GPa)	30.67	22(x, y), 9.8(z)	131	5.6	76
G (GPa)	-	3.5(xy), 2.5(xz, yz)	-	-	-
ν	0.35	0.11(xy), 0.28(xz, yz)	0.3	0.3	0.35
ρ (kg/m^3)	8500	1900	2300	1700	8900
σ_{yield} (MPa)	80	-	-	-	-

Table 7-3 lists material properties used in FEA simulation. The stress strain distribution for two chips was almost same from FEA results, so only chip 3 was selected for analysis. The outmost corner solder joint has the maximum stress. Thus, submodel was used to simulate the outmost corner solder joint. For multi-axes stress situation, the equivalent von Mises stress is commonly used to output stress in solder joint:

ATTENTION: The Singapore Copyright Act applies to the use of this document. Nanyang Technological University Library

$$\sigma_{eff} = \frac{1}{\sqrt{2}}\sqrt{(\sigma_1-\sigma_2)^2+(\sigma_2-\sigma_3)^2+(\sigma_3-\sigma_1)^2} \tag{7.3}$$

In order to minimize the effect of stress concentration, the volume-weight method was used to calculate the equivalent von Mises stress in the die/solder interface layer in which the failure more commonly occurs first. Volume-averaged stress can be obtained by:

$$\sigma_{ave} = \frac{\sum \sigma \cdot V}{\sum V} \tag{7.4}$$

The volume-averaged von Mises stresses were calculated for different G level tests and are shown in Table 7-4. The linear relationship of G_{out} and von Mises stress amplitude is shown in Fig. 7-5.

Table 7-4 Stress amplitudes for different G-level tests (at natural frequency).

G_{in} (G)	10	5	3
G_{out} (G)	128.5	77.25	53.22
Stress amplitude (MPa)	4.35	2.63	1.87

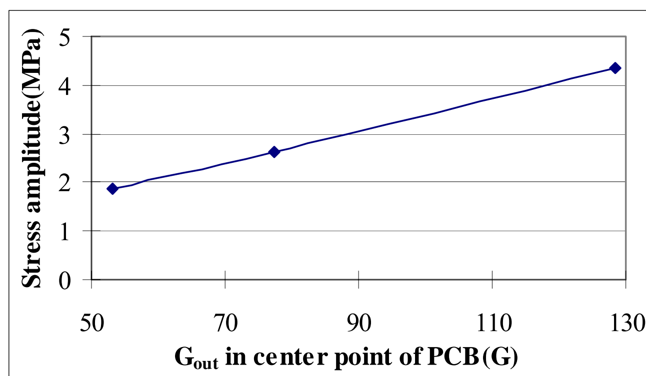

Fig. 7-5 Plot of G_{out} vs. von Mises stress amplitude at natural frequency.

The frequency range from 175Hz to 215Hz was used for vibration test. Different transmissibility occurs at different frequencies as shown in Fig. 7-6. Therefore, specimen was subjected to different effective pressures with different slope triangle distribution during test, thus different stress amplitudes will be applied on the solder

ATTENTION: The Singapore Copyright Act applies to the use of this document. Nanyang Technological University Library

joint during sweep sine vibration test from 175Hz to 215Hz. The stress amplitude can be determined using linear relationship as shown in Fig. 7-5 when G_{out} or transmissibility of PCB center point is known. The stress amplitude can be calculated for different G level test using following equation:

$$\sigma_a = \frac{4.35e6 \times G_{out}}{128.5} = \frac{4.35e6 \times 10 \times T}{128.5} \quad for 10G$$
$$\sigma_a = \frac{2.65e6 \times G_{out}}{77.25} = \frac{2.65e6 \times 5 \times T}{77.25} \quad for\ 5G \tag{7.5}$$
$$\sigma_a = \frac{2.65e6 \times G_{out}}{53.22} = \frac{2.65e6 \times 3 \times T}{53.22} \quad for\ 3G$$

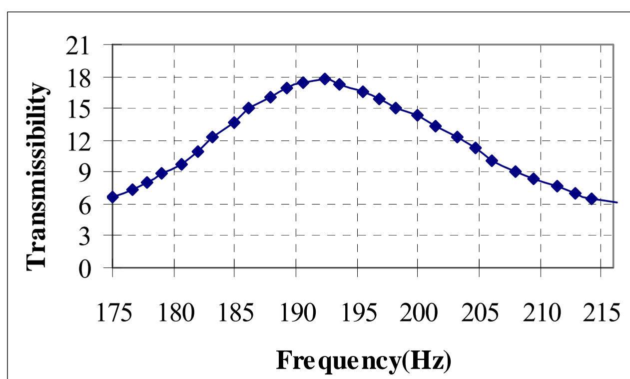

Fig. 7-6 Plot of transmissibility vs. frequency for 3G level test.

7.3.2.3 Fatigue life prediction using Miner's law

The stress-based high cycle fatigue approach was used to predict the fatigue life of component subjected to vibration load as shown below:

$$\sigma_a = \sigma_f^{'} \left(2N_f\right)^b \tag{7.6}$$

For eutectic Pb/Sn solder, the material constant $\sigma_f^{'}$ and b can be determined by curve fitting shown in Fig. 7-7 using test data by Yao et al. [40] and they are 177.15MPa and –0.2427, respectively. Then fatigue life can be determined by Eq. (7.6) when stress amplitude was known from above section analysis. From above analysis, different stress amplitude will be applied on solder joints during sweep vibration test with frequency range from 175Hz to 215Hz, which causes different cycles to failure at different frequency. Miner's law was used and fatigue life can be predicted by

ATTENTION: The Singapore Copyright Act applies to the use of this document. Nanyang Technological University Library

combining with Eq. (7.6). The detailed procedure for calculating fatigue life of solder joint subjected to vibration with different frequency is put in Appendix D.

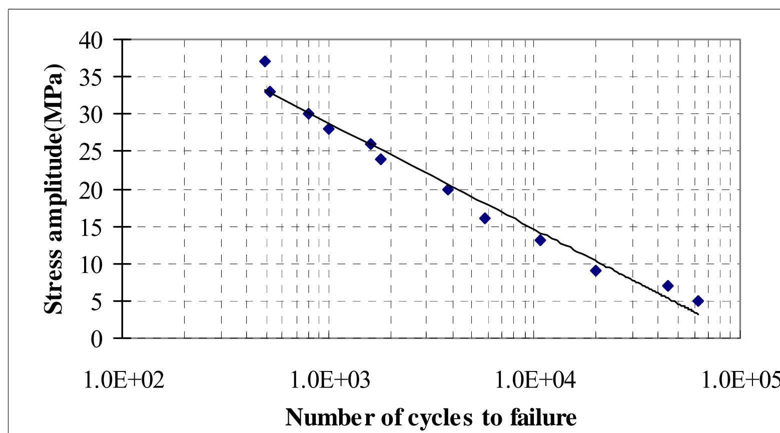

Fig. 7-7 Eutectic Sn/Pb solder S-logN curve.

Table 7-5 Fatigue life comparisons for chip 3.

G level	Test (1)	Prediction (2)	Factor (2/1)
3G	8.34E7	1.10E8	1.32
5G	3.34E7	2.57E7	0.77
10G	1.62E7	2.61E6	0.16

The fatigue life result comparisons between quasi-static method using CDI of 0.5 and test for chip3 are listed in Table 7-5. It can be seen that the quasi-static can give reasonable fatigue life prediction result compared to test result, especially for lower G level vibration test. Different CDIs were used to predict the solder fatigue life in order to investigate the CDI effect on solder fatigue life for sweep vibration load. The factor is defined as the ratio of fatigue predicted by quasi-static FEA result to experimental data. Different factors were calculated and shown in Fig. 7-8 when considering four CDIs of 1, 0.7, 0.5, and 0.33. The predicted fatigue life for 4 different CDIs has a good agreement with test data for 5G test. For lower G level test such as 3 G, lower CDI of 0.5 or 0.33 predicts reasonable fatigue life compared to test result. For 10G level test, the quasi-static analysis results in conservative fatigue life compared to test result.

ATTENTION: The Singapore Copyright Act applies to the use of this document. Nanyang Technological University Library

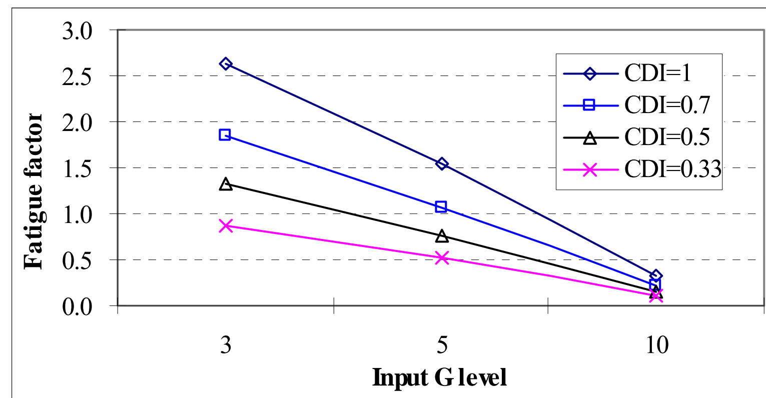

Fig. 7-8 CDI effect on fatigue life prediction.

7.3.3 Harmonic Response Analysis

Harmonic response analysis is a technique used to determine the steady-state response of a linear structure to loads that vary sinusoidally (harmonically) with time. In this study, harmonic response analysis for FCOB assembly was conducted for fatigue life prediction of solder joint in order to compare with quasi-static analysis result. The FEA model shown in Fig. 7-4 and material properties listed in Table 7-3 are same for quasi-static and harmonic analysis in FEA simulation. For global model, the displacement amplitude added on clamped-clamped boundary can be obtained according to Eq. (7.7) considering transmissibility T as unity because output G is same as input G in clamped boundary.

$$Z_{\max} = \frac{\ddot{Z}_{\max}}{\Omega^2} = \frac{9.8 G_{in} T}{4\pi^2 f^2} = \frac{0.248 G_{in} T}{f^2} \qquad (7.7)$$

Damping in some form should be specified in harmonic analysis; otherwise, the response will be infinity at the resonant frequencies. In this study, a constant damping ratio was used. The trial and error of damping ratios from 0.01 to 0.1 was conducted to find suitable damping ratio value by comparing displacement amplitude between simulation result and test result. The desirable damping ratio of 0.02 used in harmonic analysis was obtained. The frequency range used in harmonic response analysis was

ATTENTION: The Singapore Copyright Act applies to the use of this document. Nanyang Technological University Library

same as that used in reliability vibration test and the load steps were chosen based on frequency spacing recorded in vibration test. Volume-averaged von Mises stresses based on die/solder interface layer elements were calculated from submodel result and is shown in Fig. 7-9. It can be seen that stresses increase with increasing of frequency before natural frequency while stresses decrease with increasing of frequency after natural frequency. Fatigue life prediction of solder joint based on harmonic analysis results was carried out according to similar procedure used in quasi-static analysis. Table 7-6 lists fatigue life comparisons for test, quasi-static and harmonic analysis results considering CDI as 0.5. It can be seen that both harmonic and quasi-static analysis can give satisfactory fatigue life prediction result compared to test result, especially for lower G level test. It is very important and sometimes difficult for harmonic analysis to select desired damping ratio. Therefore, quasi-static analysis can be used to calculate the stress amplitude for fatigue life prediction of solder joint subjected to vibration load without damping ratio requirement.

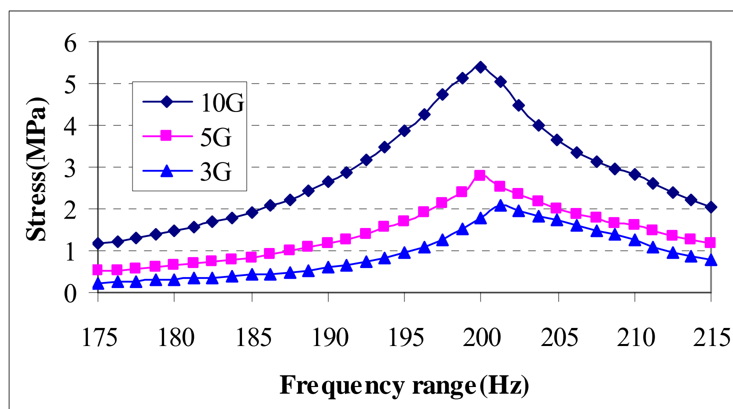

Fig. 7-9 Stress amplitudes at different frequencies for three G level tests.

Table 7-6 Fatigue life comparison for test, quasi-static and harmonic analysis.

G level	Test (A)	Quasi-static (B)	Harmonic (C)	Ratio (C/A)	Ratio (C/B)
3G	8.34E+07	1.10E+08	1.43E+08	1.71	1.30
5G	3.34E+07	2.57E+07	4.27E+07	1.28	1.66
10G	1.62E+07	2.61E+06	2.45E+06	0.15	0.94

ATTENTION: The Singapore Copyright Act applies to the use of this document. Nanyang Technological University Library

7.4 SUMMARY

FCOB assemblies were tested under sinusoidal vibration with clamped-clamped boundary condition. The non-linear effect in the FCOB assembly is found. The fatigue life reduces rapidly when the sinusoidal vibration acceleration input increases. The CDI of unity is unconservative and a safety factor of 2-3 is recommended when using CDI to predict the fatigue life of FCOB solder joint subjected to varying vibration load.

Considering the PCB as a bare unpopulated thin plate for the FCOB assembly can give more satisfactory modal response compared to the PBGA assembly, which requires modeling of the PBGA modules. The result of modal analysis using global-local beam model gave satisfactory agreement with experimental result.

A quasi-static analysis method was developed to calculate the stress strain behavior of the solder joints using submodeling technique. Harmonic analysis for FCOB assembly was conducted with reasonable damping ratio, which was obtained by trial and error FEA simulation study. Fatigue life was predicted based on calculated stress using high cycle fatigue model and Miner's law. Different CDI effect on fatigue life prediction was study and the fatigue life prediction results with CDI of 0.5 are reasonable compared to test results. Comparing fatigue life results from test, quasi-static analysis and harmonic analysis, the good agreement was obtained. An important advantage of quasi-static analysis is that damping ratio is not needed in FEA simulation while it is very important for harmonic analysis.

ATTENTION: The Singapore Copyright Act applies to the use of this document. Nanyang Technological University Library

CHAPTER 8 CONCLUSIONS

8.1 CONCLUSIONS

In this study, failure assessment methodology for Pb-free soldered electronic assembly has been investigated. A global-local finite element modeling technique was developed and compared with conventional fine 3D model results. Thermal cycling test and FEA analyses were carried out for PBGA, PQFP and TSSOP components with SnAgCu Pb-free solder. Cyclic three-point and four-point bend tests and FEA analyses were investigated for VQFN assembly with SnAgCu Pb-free solder. Drop impact tests and FEA simulations were performed for soldered electronic assemblies. Vibration tests containing constant G level and varying G level and FEA analyses were conducted for FCOB assemblies. Based on the analyses carried out in the previous chapters, specific conclusions can be drawn in the following sub-sections.

8.1.1 Global-Local Modeling Technique

The global-local modeling method containing submodeling and GLB modeling technique has been developed and calibrations for these models have been presented. Specific conclusions can be made as follows:

1. Comparisons between submodel and fine 3D model were conducted to investigate submodel effect on FEA results which cannot be found from literature where submodel was used without validation. Two different submodels have been developed for comparison and the results show that submodel with hybrid solid in one pitch area including solder joint, PCB and component is better than submodel with only solder joint. The key feature of the submodel technique is that it

ATTENTION: The Singapore Copyright Act applies to the use of this document. Nanyang Technological University Library

significantly reduces elements size and computing resources requirement without losing accuracy compared to fine 3D model.

2. The developed submodeling method has been successfully used for FEA modeling and simulation of electronic assembly subjected to different load conditions such as thermal cycling, isothermal cyclic bending, and vibration with different DOF transfer procedure between global model and submodel. The appropriate cut boundaries were presented for different package types such as FCOB with or without underfill, PBGA, PQFP, and VQFN.
3. The detailed procedure of global-local-beam (GLB) model has been developed using two-node beam element to replace real solder joint. Solid-beam-solid global model with error less than 25% is better than shell-beam-shell global model. The solid-beam-solid model with constrain equation has been presented for the first time. Effective solder model with the cubic cross-section solder joint having the similar stiffness as the real solder joint has also been developed. The effective solder model can lead to more accurate result with considering solder plastic deformation compared to effective two-node beam model. The developed GLB modeling method has been used successfully for modal analysis of FCOB assembly, thermal cycling and drop impact simulation for PBGA assembly.

8.1.2 Thermal Cycling Test and Analysis

Thermal cycling test and FEA simulation were conducted for Pb-free (SnAgCu) electronic assemblies. Specific conclusions can be obtained as follows:

1. PBGA assembly is more sensitive to thermal cycling failure than leaded assemblies such as PQFP and TSSOP, which was also verified by FEA simulation results. Assemblies with Ni/Au finish have longer fatigue life than those with OSP or Ag finish. Failure mode of PBGA solder joint exhibits solder fatigue failure with

ATTENTION: The Singapore Copyright Act applies to the use of this document. Nanyang Technological University Library

failure site close to solder/IMC interface at component side due to CTE mismatch.

2. For PBGA FEA modeling and simulation, 3D Quarter model or octant model can give more accurate results than 2D model and 3D slice model as expected. Consistent results can be obtained for different solder constitutive models such as EPC model, creep model and viscoplastic Anand's model. When using EPC model, plastic strain is small compared to creep strain for PBGA assembly, while plastic strain is similar to creep strain for FCOB assembly.
3. Fatigue life of solder decreases with higher stress-free temperature (150°C) and using room temperature (25°C) as stress-free condition is satisfactory. Solder fatigue life under thermal shock (TS) has similar trend to thermal cycling (TC). Fatigue life of solder decreases with larger temperature range (ΔT). For the same temperature range, fatigue life with higher maximum temperature (T_{max}) is slightly less than that with lower maximum temperature (T_{max}).
4. Predicted fatigue life of solder decreases when considering IMC effect and with increasing IMC layer thickness. It is the first time to simulate the IMC effect on solder fatigue life using FEA modeling and simulation.
5. Fatigue life of solder decreases significantly when CTE of solder mask is quite different from CTE of solder. When CTE of solder mask is close to CTE of solder, fatigue life of solder can be improved significantly.
6. Outermost ring volume averaging method is reasonable when using our fatigue model reported by Pang et al. [24] and this model is suitable for both PBGA solder and flip chip solder fatigue life prediction. It is the first time to introduce the different ring volumes to investigate the averaging volume effect on solder fatigue life prediction.

ATTENTION: The Singapore Copyright Act applies to the use of this document. Nanyang Technological University Library

8.1.3 Cyclic Bend Test and Analysis

Cyclic bend tests were conducted for VQFN assembly with Pb-free solder at 25°C and 125°C, respectively. Specific conclusions can be made as follows:

1. The correlation between three-point bend and four-point bend was developed and validated by test and simulation results. Failure data were given in two-parameter Weibull distribution. The cycle to failure increases when bending displacement range decreases. Fatigue life of VQFN solder joint is larger for OSP finish case than for Ni/Au finish case. The acceleration factor of cycle to failure due to high temperature (125°C) effect is compared to room temperature (25°C) test result. It is the first time to conduct the bending test at 125°C and investigate temperature effect on bend fatigue of solder.
2. The one-level submodeling method is effective and sufficient for FEA simulation compared with two-level submodeling technique. Fifteen simulation cycles are needed for cyclic bending loading effects to get converged results. Accumulated energy density per cycle at 125°C is more than that at 25°C for the same deflection condition, which indicates that higher temperature (125°C) accelerates bending fatigue failure of solder more significantly.
3. Energy-based fatigue models were developed for VQFN assembly with SnAgCu solder under cyclic bend at 25°C and 125°C, respectively. The fatigue exponent in fatigue model at 125°C is about twice that of fatigue model at 25°C.

8.1.4 Drop Test and Analysis

Board-level drop impact tests using clamped-clamped boundary condition have been conducted for electronic assemblies with Pb-free or Pb-based solders. FEA simulations were performed using different modeling methods and solder constitutive models. Specific conclusions can be made as follows:

ATTENTION: The Singapore Copyright Act applies to the use of this document. Nanyang Technological University Library

1. The boundary condition used in this work is different from others' work. The clamped-clamped boundary can ensure the first mode is dominant for PCB transient vibration after drop impact. The PBGA component is more prone to drop impact failure than PQFP and VQFN components because leaded assemblies have flexible solder joints. Components with Pb-free solder have less drop impact reliability than those with Pb-based solder. The PBGA component with OSP board finish exhibits better impact reliability than component with Ni/Au finish which fails earlier.
2. Strain rate dependent plastic model was developed for use and it is more realistic than elastic model. The solder/board interface is prone to failure for PBGA assemblies subjected to drop impact load.
3. IMC layer reduces the plastic deformation of solder under drop impact load due to constraint effect of hard IMC layer on deformation of solder, which differs from IMC effect on solder deformation under thermal cycling condition.

8.1.5 Vibration Test and Analysis

Sinusoidal vibration test and FEA modeling and simulation were conducted for board-level electronic assembly. Specific conclusions can be obtained as follows:

1. A novel vibration fatigue test method using constant G-level test to predict variable G-level test result was proposed. The fatigue life reduces rapidly when the vibration acceleration input increases.
2. Considering FCOB assembly as a bare plate can give satisfactory modal response compared to PBGA assembly. GLB model can give accurate modal analysis result.
3. A quasi-static analysis method has been developed to calculate the stress strain behavior of solder joints. Fatigue life was predicted based on FEA result using stress-based fatigue model and Miner's law. Different CDI effect on fatigue life

ATTENTION: The Singapore Copyright Act applies to the use of this document. Nanyang Technological University Library

prediction was studied and the fatigue life prediction results with CDI of 0.5 are satisfactory compared to test results. Harmonic analysis was conducted and fatigue life was predicted accordingly. Comparing fatigue life from test, quasi-static analysis and harmonic analysis, the good agreement was obtained. In this thesis, the comparison between quasi-static analysis and harmonic analysis is the first time to present for vibration reliability of electronic assembly.

8.1.6 Design-for-Reliability and Failure Assessment

The features of design-for-reliability and failure assessment developed have some similarities and differences for Pb-free and Pb-based solders under different loadings and are discussed below.

1. Fatigue failure is the dominant failure mode for both Pb-free and Pb-based solders subjected to thermal cycling, cyclic bending and vibration. For drop impact test, the dominant failure mode is IMC brittle rupture or copper trace crack. New material properties, material constants in constitutive models and fatigue models are necessary for Pb-free solders to do FEA simulation and fatigue life prediction. In this work, temperature dependent material properties have been implemented in FEA simulation, especially for Pb-free solders.
2. Pb-free solders have higher strain energy density accumulation than Pb-based solders under thermal cycling condition but this must be linked to energy based solder fatigue life prediction model which gives longer fatigue lives despite higher strain energy density for Pb-free solder. After reflow, different IMCs are formed between Pb-free or Pb-based solders and copper pad with different board finishes, then IMC will affect reliability of electronic assembly. For example, electronic assembly with SnAgCu Pb-free solder and Ni/Au finish has the worst drop impact life due to brittle CuNiSn IMC effect compared to Pb-based electronic assembly.

ATTENTION: The Singapore Copyright Act applies to the use of this document. Nanyang Technological University Library

3. Low cycle fatigue model (energy-based or strain-based) is used for thermal cycling test or bending test for both Pb-free and Pb-based solders. However, high cycle fatigue model (stress-based) is used for vibration test. Different coefficient and exponent constants are needed for different fatigue models for Pb-free and Pb-based solder. For drop impact test, impact fatigue model should be developed (this model is not available currently). Our fatigue model [24] of equation (4.26) is recommended for thermal fatigue life prediction of Sn-3.8Ag-0.7Cu solder.
4. In FEA modeling and simulation, quarter model of component can be used for thermal cycling loading due to symmetry of boundary condition. However, board-level FEA model must be used for bending test, vibration test and drop impact test. EPC model and Anand's viscoplastic model are consistent when they are used in thermal cycling simulation. However, Anand's model is recommended for cyclic bending simulation. In order to obtain converged result, three cycles are enough for TC test simulation while fifteen cycles are needed for bending test simulation. It is necessary to model temperature dependent material properties for TC test and model strain rate dependent material properties for drop impact test. Damping effect must be considered for harmonic analysis and drop impact simulation.

8.2 ACHIEVEMENTS AND RECOMMENDATIONS

8.2.1 Achievements and Contributions

The major achievements and new contributions of this project are summarized as follows:

1. A global-local modeling technique containing submodeling and GLB model was developed and successfully implemented in FEA simulation for different electronic assemblies such as PBGA, PQFP, TSSOP and VQFN when subjected to different

ATTENTION: The Singapore Copyright Act applies to the use of this document. Nanyang Technological University Library

loadings such as thermal cycling, cyclic bend, drop impact and vibration loads. Some unique researches and contributions different from others' work include: in-depth comparison between submodel and fine 3D model in order to obtain a satisfactory cut boundary; error analysis of submodeling application for different package types such as FCOB with or without underfill, PBGA assembly; comparison between solid-beam-solid model and shell-beam-shell model in GLB modeling method and their applications, etc.

2. A series of experiments containing thermal cycling, cyclic bend, repeated drop impact and vibration were conducted and investigated comprehensively for different types of electronic package. Corresponding FEA simulations for different testing conditions were performed using global-local modeling technique to investigate stress-strain response of solder under different loading types. Unique features different from other's work in reliability tests involve: different packages with different board finishes were tested and compared with respect to thermal fatigue life; four-point bend test was carried out at 125°C for the first time; clamped-clamped boundary condition was applied for both drop and vibration tests; a novel vibration fatigue test method using constant G-level test to predict variable G-level test result.
3. Intermetallic compound (IMC) was considered in FEA modeling and simulation for PBGA assembly under thermal cycling and drop impact loads. It is the first time to model IMC layer in FEA simulation for Pb-free electronic assemblies because it is difficult to model thin IMC layer. Different IMCs and IMC thickness effects on thermal fatigue life of Pb-free solder were proposed.
4. Bending fatigue models were developed for VQFN component with SnAgCu solder subjected to bending load at 25°C and 125°C, respectively. The correlation

ATTENTION: The Singapore Copyright Act applies to the use of this document. Nanyang Technological University Library

between three-point bend and four-point bend was addressed and validated by test and simulation results for the first time. Temperature effect (125°C vs. 25°C) on bending fatigue life of Pb-free solder was investigated, which cannot be found from publications. Bending fatigue life must be developed because fatigue life equations for thermal cycling test cannot be directly used to predict solder bending fatigue life in terms of following different factors: thermal cycling load vs. isothermal condition; dominant creep deformation in TC test due to longer dwell time vs. neglectable creep deformation in bend test due to shorter cycle time; IMC growth and its effect on solder fatigue life in TC test.

5. A quasi-static analysis method has been developed for electronic assembly when subjected to sinusoidal vibration load. A reasonable cumulative damage index was presented for failure assessment of electronic assembly under vibration load for the first time based on test results and simulation results with of quasi-static analysis and harmonic analysis.
6. Systematic studies of FEA calibration and thermal fatigue life prediction for PBGA component were carried out considering many effect factors: 2D or 3D FEA model, solder constitutive models and fatigue models, solder mask definition, volume-averaged methods, different IMCs, stress-free temperature conditions, thermal loading profiles. It is the first time to do the comprehensive investigation of FEA geometry models impact on solder fatigue life considering all possibly encountered 2D or 3D models from literature. The in-depth comparison among all commonly used solder constitutive models is new for fatigue life prediction of Pb-free electronic assembly. Volume-averaging method based on outer ring elements was proposed for the first time in this work.
7. Different solder constitutive models containing elastic model, bilinear kinematic

ATTENTION: The Singapore Copyright Act applies to the use of this document. Nanyang Technological University Library

plastic model and strain rate dependent plastic model were implemented and compared in FEA modeling and simulation of drop impact load. It is the first time to simulate Pb-free solder using strain rate dependent plastic model and investigate its effect on solder stress strain behavior. In addition, three drop impact modeling methods involving in full drop event, Input-D and Input-G models were investigated systematically.

8.2.2 Recommendations

Some recommendations for future work to improve the developments of failure assessment for Pb-free assembly subjected to thermomechanical or mechanical loadings are as follows:

1. More drop impact reliability tests and FEA modeling and simulations are needed in order to develop an impact fatigue model for soldered electronic assembly with Pb-free solders. Failure mode and mechanism of electronic assembly with Pb-free solder is a big concern and more studies are needed for design-for-reliability of electronic products subjected to drop impact load.
2. Mechanical tests with different strain rates are needed for Pb-free solder material in order to create more accurate rate dependent material properties of solder used for FEA modeling and simulation of drop impact load.
3. Four-point bend tests with positive to negative deflection at different temperatures are needed to correlate Pb-free solder thermal fatigue life and bending fatigue life.

ATTENTION: The Singapore Copyright Act applies to the use of this document. Nanyang Technological University Library

REFERENCES

[1] Pecht, M., (1991), "Handbook of Electronic Package Design", *Marcel Dekker*, Inc, New York.

[2] Tummala, R. R., (2001), "Fundamentals of Microsystems Packaging", *Mc Graw Hill*.

[3] Lau, J.H., (1993), "Thermal Stress and Strain in Microelectronics Packaging", *Van Nostrand Reinhold*, New York.

[4] Chan, H. A., and Englert, P. J., (2001), "Accelerated Stress Testing Handbook-Guide for Achieving Quality Products", *IEEE Press*.

[5] Pecht, M.G., Agarwal, R., McCluskey, P., et al., (1999), "Electronic Packaging Materials and Their Properties", *CRC Press LLC*.

[6] Lee, J.C., and Rassaian, M., (2002), "Effective Local Flexural Stiffness of Ball Grid Array Assemblies", *Journal of Electronic Packaging*, Vol. 124, pp.192-197.

[7] Gustafsson, G., Guven, I., Kradinov, V., et al., (2000), "Finite Element Modeling of BGA Packages for Life Prediction", *Proceedings of 50th Electronic Components and Technology Conference*, May 21-24, Las Vegas, pp.1059-1063.

[8] Cheng, Z.N., Wang, G.Z., Chen, L., et al., (2000), "Viscoplastic Anand Model for Solder Alloys and Its Application", *Soldering & Surface Mount Technology*, 12/2, pp.31-36.

[9] Han, J.B., (2001), "Flip-Chip BGA Design to Avert Die Cracking", *Journal of Electronic Packaging*, Vol.123, pp.58-62.

[10] Darbha, K., and Dasgupta, A., (2001), "a Nested Finite Element Methodology (NFEM) for Stress Analysis of Electronic Products-Part II: Durability Analysis of Flip Chip and Chip Scale Interconnects", *Journal of Electronic Packaging*, Vol.123, pp.147-155.

ATTENTION: The Singapore Copyright Act applies to the use of this document. Nanyang Technological University Library

[11] Chiang, K. N., and Liu, C.M., (2001), "a Comparison of Thermal Stress/Strain Behavior of Elliptical/Round Solder Pads", *Journal of Electronic Packaging*, Vol.123, pp.127-131.

[12] Aihara, T., Ito, S., Sasajima, H., et al., (2001), "Development of Reliability and Moldability on Fine Pitch Ball Grid Array by Optimizing Materials", *Journal of Electronic Packaging*, Vol.123, pp.88-94.

[13] Pang, H.L.J., Chong, D.Y.R., and Low, T.H, (2001), "Thermal Cycling Analysis of Flip-Chip Solder Joint Reliability", *IEEE Transaction on Components and Packaging Technologies*, Vol. 24, No.4, pp.705-712.

[14] Yao, Q., and Qu, J., (1999), "Three-Dimensional Versus Two-Dimensional Finite Element Modeling of Flip-Chip Packages", *Journal of Electronic Packaging*, Vol. 121, pp.196-201.

[15] Dowling, N.E., (1993), "Mechanics Behavior of Materials: Engineering Methods for Deformation, Fracture, and Fatigue", *Prentice-Hall International Editions*.

[16] Miric, A.Z., and Grusd, A., (1998), "Lead-Free Alloys", *Soldering & Surface Mount Technology*, 10/1, pp.19-25.

[17] Pyland, J., Pucha, R. V., and Sitaraman, S.K., (2002), "Thermomechanical Reliability of Underfilled BGA Packages", *IEEE Transactions on Electronics Packaging Manufacturing*, Vol. 25, No. 2, pp.100-106.

[18] Wen, S., Keer, L. M., Vaynman, S., et al., (2002), "a Constitutive Model for a High Lead Solder", *IEEE Transactions on Components and Packaging Technologies*, Vol. 25, No. 1, pp.23-31

[19] Wiese, S., Meusel, E., and Wolter, K.J., (2003), "Microstructural Dependence of Constitutive Properties of Eutectic SnAg and SnAgCu Solders", *Proceedings of 53rd Electronic Components and Technology Conference*, New Orleans, pp.197-206.

[20] Lau, J.H., and Lee, S.-W.R., (2002), "Modeling and Analysis of 96.5Sn-3.5Ag Lead-Free Solder Joints of Wafer Level Chip Scale Package on Buildup Microvia Printed Circuit Board", *IEEE Transactions on Electronics Packaging Manufacturing*, Vol. 25, No. 1, pp.51-58.

ATTENTION: The Singapore Copyright Act applies to the use of this document. Nanyang Technological University Library

[21] Darveaux, R., and Banerji, K., (1992), "Constitutive Relations for Tin-Based Solder Joints", *IEEE Transactions on Components, Hybrids and Manufacturing Technology*, Vol.15, pp.1013-1024.

[22] ANSYS Version 7.0 Manual, (2002), *Ansys Inc*.

[23] Wiese, S., Schubert, A., Walter, H., et al., (2001), "Constitutive Behavior of Lead-free Solders vs. Lead-containing Solders -Experiments on Bulk Specimens and Flip-Chip Joints", *Proceedings of 51st Electronic Components and Technology Conference*, May 29- June 1. Orlando, pp.890-902

[24] Pang, H.L.J., Xiong, B.S. and Low, T.H., (2004) "Creep and Fatigue Characterization of Lead Free 95.5Sn-3.8Ag-0.7Cu Solder", *Proceedings of 54th Electronic Components and Technology Conference*, June 1-4, Las Vegas, pp.1333-1337.

[25] Wang, G. Z., Cheng, Z. N., Becker, K., et al., (2001), "Applying Anand Model to Represent the Viscoplastic Deformation Behavior of Solder Alloys", *Journal of Electronic Packaging*, Vol. 123, pp.247-253.

[26] Darveaux, R., (2000), "Effect of Simulation Methodology on Solder Joint Crack Growth Correlation", *Proceedings of 50th Electronic Components and Technology Conference*, May 21-24, Las Vegas, pp.1048-1058.

[27] Anand, L., (1985), "Constitutive Equations for Hot-Working of Metals", *International Journal of Plasticity*, Vol. 1, pp.213-231.

[28] Brown, S. B., Kim, K. H., and Anand, L., (1989), "an Internal Variable Constitutive Model for Hot Working of Metals", *International Journal of Plasticity*, Vol. 5, pp.95-130.

[29] Pang, H.L.J., Seetoh, C.W., and Wang, Z.P., (2000), "CBGA Solder Joint Reliability Evaluation Based on Elastic-Plastic-Creep Analysis", *Journal of Electronic Packaging*, Vol. 122, pp.255-261.

[30] Krieg, R.D. and Key, S.W., (1976), "Implementation of a Time Dependent Plasticity Theory into Structural Computer Programs", Vol. 20 of Constitutive Equation in Viscoplasticity: *Computational and Engineering Aspects* (ASME. New York, N.Y.), pp.125-137.

ATTENTION: The Singapore Copyright Act applies to the use of this document. Nanyang Technological University Library

[31] de Kluizenaar, E.E., (1990), “Reliability of Soldered Joints: a Description of the State of the Art Part 2”, *Soldering & Surface Mount Technology*, No. 5, pp.56-66.

[32] de Kluizenaar, E.E., (1990), “Reliability of Soldered Joints: a Description of the State of the Art Part 3”, *Soldering & Surface Mount Technology*, No. 6, pp. 18-27.

[33] Pang, H.L.J, Xiong, B.S., and Kurniawijaya, H., (2002), “Mechanical Strength of Lead-Free Solders”, *Proceedings of GlobalTRONICS Technology Conference*, Singapore, pp.113-118.

[34] Pang, H.L.J., Xiong, B. S., Neo, C. C., et al., (2003), “Bulk Solder and Solder Joint Properties for Lead Free 95.5Sn-3.8Ag-0.7Cu Solder Alloy”, *Proceedings of 53rd Electronic Components and Technology Conference*, New Orleans, pp.673-679.

[35] Turbini, L.J, Munie, G.C., Bernier, D., et al., (2001), “Examining the Environment Impact of Lead-Free Soldering Alternatives”, *IEEE Transactions on Packaging Manufacturing*, Vol. 24, No. 1, pp.4-9.

[36] Lee, W.W., Nguyen, L.T., and Selvaduray, G.S., (2000) “Solder Joint Fatigue Models: Review and Application to Chip Scale Packages”, *Microelectronics Reliability*, (40), pp.231-244.

[37] Wong, T.E., Reed, B.A., Cohen, H.M., et al., (1999), “Development of BGA Solder Joint Vibration Fatigue Life Prediction Model”, *Proceedings of 49th Electronic Components and Technology Conference*, pp.149-154.

[38] Wong, T.E., Palmieri, F.W., and Reed, B.A., (2000), “Durability/Reliability of BGA Solder Joints under Vibration Environment”, *Proceedings of 50th Electronic Components and Technology Conference*, pp.1083-1088.

[39] Wong, T.E., Palmieri, F.W., and Fenger, H.S., (2002), “Under-Filled BGA Solder Joint Vibration Fatigue Damage”, *Proceedings of Inter Society Conference on Thermal Phenomena*, pp.961-966.

[40] Yao, Q.Z., Qu, J.M., and Xu, S.X., (1999), “Solder Fatigue Life in Two Chip Scale Packages”, *Proceedings of IEEE-IMAPS International Symposium on Microelectronics*, October, Chicago, pp.563-570.

ATTENTION: The Singapore Copyright Act applies to the use of this document. Nanyang Technological University Library

[41] Lau, J.H., (1996), "Solder Joint Reliability of Flip Chip and Plastic Ball Grid Array Assemblies under Thermal Mechanical, and Vibrational Conditions", *IEEE Transactions on Components, packaging, and Manufacturing Technology-Part B*, Vol. 19, No.4, pp.728-735.

[42] Shi, X.Q., Pang, H.L.J., Zhou, W., et al., (1999), "A Modified energy-based Low Cycle Fatigue Model for Eutectic Solder Alloy", *Scripta Material*, Vol. 41, No.3, pp.289-296.

[43] Wong, T. E., Kachatorian, L.A., and Cohen, H.M., (1999), "J-Lead Solder Joint Thermal Fatigue Life Model", *Journal of Electronic Packaging*, Vol. 121, pp.186-190.

[44] Pang, H.L.J., Tan, T., and Sitaraman, S.K., (1998), "Thermo-Mechanical Analysis of Solder Joint Fatigue and Creep in a Flip Chip on Board Package Subjected to Temperature Cycling Loading", *Proceedings of 48th Electronic Components and Technology Conference*, May 25-28, Seattle, pp.878-883.

[45] Knecht, S., and Fox, L., (1991), "Integrated Matrix Creep: Application to Accelerated Testing and Lifetime Prediction. In: Lau, J.H., Editor. Solder Joint Reliability Theory and Applications. *Van Nostrand Reinhold*, New York.

[46] Syed, A., (2004), "Accumulated Creep Strain and Energy Density Based Thermal Fatigue Life Prediction Models for SnAgCu Solder Joints", *Proceedings of 54th Electronic Components and Technology Conference*, June 1-4, Las Vegas, pp.737-746.

[47] Schubert, A., Dudek, R., Auerswald, E., et al., (2003), "Fatigue Life Models for SnAgCu and SnPb Solder Joints Evaluated by Experiments and Simulation", *Proceedings of 53rd Electronic Components and Technology Conference*, New Orleans, pp.603-610.

[48] Engelmaier, W., (1983), "Fatigue Life to Leadless Chip Carrier Solder Joints during Power Cycling,' *IEEE Transactions on Components, Hybrids and Manufacturing Technology*, Vol. CHMT-6, No.3, pp.52-57.

[49] Shi, X.Q., Pang, H.L.J, Zhou, W., et al., (2000), "Low Cycle Fatigue Analysis of Temperature and Frequency Effects in Eutectic Solder Alloy", *International Journal of Fatigue*, 22, pp.217-228.

ATTENTION: The Singapore Copyright Act applies to the use of this document. Nanyang Technological University Library

[50] Solomon, H.D., and Tolksdorf, E.D., (1995), "Energy Approach to the Fatigue of 60/40 Solder: Part I-Influence of Temperature and Cycle Frequency", *Journal of Electronic Packaging*, Vol. 117, No. 2, pp.130-135.

[51] Solomon, H.D., and Tolksdorf, E.D., (1996), "Energy Approach to the Fatigue of 60/40 Solder: Part II-Influence of Hold Time and Asymmetric Loading", *Journal of Electronic Packaging*, Vol. 118, No. 2, pp.67-71.

[52] Akay, H.U., Paydar, N.H., and Bilgic, A., (1997), "Fatigue Life Prediction for Thermally Loaded Solder Joints Using a Volume-Weighted Averaging Technique", *Journal of Electronic Packaging*, Vol.119, pp.228-235.

[53] Tu, P.L., Chan, Y.C., and Lai, J.K.L., (1997), "Effect of Intermetallic Compounds on the Thermal Fatigue of Surface Mount Solder Joints", *IEEE Transactions on Components, Packaging, and Manufacturing Technology-Part B*, Vol. 20, No.1, pp.87-93.

[54] Pang, H.L.J, Tan, K.H., Shi, X.Q., et al., (2001), "Microstructure and Intermetallic Growth effects on Shear and Fatigue of Solder Joints Subjected to Thermal Cycling Aging", *Materials Science and Engineering*, A307, pp.42-50.

[55] Kim, D.H., Elenius, P., and Barrettt, S., (2002), "Solder Joint Reliability and Characteristics of Deformation and Crack Growth of Sn-Ag-Cu Versus Eutectic Sn-Pb on a WLP in a Thermal Cycling Test", *IEEE Transactions on Electronics Packaging Manufacturing*, Vol. 25, No. 2, pp.84-90.

[56] Yao, D., and Shang, J.K., (1997), "Effect of Load-Mix on Fatigue Crack Growth in 63Sn-37Pb Solder Joints", *Journal of Electronic Packaging*, Vol. 119, pp.114-118.

[57] Suhir, E., (2002), "Could Shock Test Adequately Mimic Drop Test Conditions?", *Journal of Electronic Packaging*, Vol. 24, pp.170-177.

[58] Nelson, W., (1990), "Accelerated Testing: Statistical Models, Test Plans, and Data Analyses", *John Willey and Sons Publication*, New York.

[59] Norris, K.C., and Landzberg, A.H., (1969), "Reliability of Controlled Collapse Interconnections", *IBM Journal of Research & Development*, Vol. 13, pp.266-271.

ATTENTION: The Singapore Copyright Act applies to the use of this document. Nanyang Technological University Library

[60] Lau, J.H., Dauksher, W., and Vianco, P., (2003), "Accelerated Models, Constitutive Equations, and Reliability of Lead-Free Solders and Joints", *Proceedings of 53rd Electronic Components and Technology Conference*, New Orleans, pp.229-236.

[61] JEDEC STANDARD, (2000), JESD22-A104-B: Temperature Cycling.

[62] JEDEC STANDARD, (1995), JESD22-A106-A (Revision of Test Method A106): Thermal Shock, April.

[63] Shetty, S., Lehtinen, V., Dasgupta, A., et al., (2001), "Fatigue of Chip Scale Package Interconnects Due to Cyclic Bending", *Journal of Electronic Packaging*, Vol. 123, pp.302-308.

[64] Shetty, S., and Reinikainen, T., (2003), "Three- and Four-Point Bend Testing for Electronic Packages", *Journal of Electronic Packaging*, Vol. 125, pp.556-561.

[65] Wu, J.D., Ho, S.H., Zheng, P.J., et al., (2001), "an Experimental Study of Failure and Fatigue Life of a Stacked CSP Subjected to Cyclic Bending", *Proceedings of 51st Electronic Components and Technology Conference*, pp.1081-1086.

[66] Skipor, A., and Leicht L., (2001), "Mechanical Bending Fatigue Reliability and Its Application to Area Array Packaging", *Proceedings of 51st Electronic Components and Technology Conference*, pp.606-612.

[67] Mercado, L.L., Philips, B., Sahasrabudhe, S., et al., (2004), "Use-Condition-Based Cyclic Bend Test Development for Handheld Components", *Proceedings of 54th Electronic Components and Technology Conference*, June 1-4, Las Vegas, pp.1279-1287.

[68] Geng, P., Chen, P., and Ling Y., (2002), "Effect of Strain Rate on Solder Joint Failure under Mechanical Load", *Proceedings of 52nd Electronic Components and Technology Conference*, pp.974-978.

[69] Tee, T.Y., Ng, H.S., Lim, C.T., et al., (2003), "Board Level Drop Test and Simulation of TFBGA Packages for Telecommunication Applications", *Proceedings of 53rd Electronic Components and Technology Conference*, New Orleans, pp.121-129.

ATTENTION: The Singapore Copyright Act applies to the use of this document. Nanyang Technological University Library

[70] Tee, T.Y., Ng, H.S., Lim, C.T., et al., (2004), "Impact Life Prediction Modeling of TFBGA Packages under Board Level Drop Test", *Microelectronics Reliability*, (44), pp.1131-1142.

[71] Wang, Y.Q., Low, K.H., Che, F.X., et al., (2003), "Modeling and Simulation of Printed Circuit Board Drop Test", *Proceedings of 5th Electronics Packaging Technology Conference*, December 10-12, Singapore, pp.263-268.

[72] Chong, D.Y.R., Ng, K., Low, T.H., et al., (2004), "Drop Test Reliability Assessment of Leaded & Lead-Free Solder Joints for IC Packages", *Proceedings of 6th Electronics Packaging Technology Conference*, December, 8-10, Singapore, pp.210-217.

[73] Xie, D.J., Arra, M., Yi, S., et al., (2003), "Solder Joint Behavior of Area Array Packages in Board Level Drop for Handheld Devices", *Proceedings of 53rd Electronic Components and Technology Conference*, New Orleans, pp.130-135.

[74] Mishiro, K., Ishikawa, S., Abe, M., et al., (2002), "Effect of the Drop Impact on BGA/CSP Package Reliability", *Microelectronics Reliability*, (42), pp.77-82.

[75] Zhu, L.P., (2003), "Modeling Technique for Reliability Assessment of Portable Electronic Product Subjected to Drop Impact Loads", *Proceedings of 53rd Electronic Components and Technology Conference*, New Orleans, pp.100-104.

[76] Lim, C.T., Ang, C.W., Tan, L.B., et al., (2003), "Drop Impact Survey of Portable Electronic Products", *Proceedings of 53rd Electronic Components and Technology Conference*, New Orleans, pp.113-120.

[77] Suhir, E., (1997), "Is the Maximum Acceleration an Adequate Criterion of Dynamic Strength of a Structural Element in an Electronic Product?", *IEEE Transactions on Components, Packaging, and Manufacturing Technology-Part A*, Vol.20, No.4, pp.513-517.

[78] Keltie, R.F., and Falter, K.J., (1993), "Guidelines for the Use of Approximations in Shock Response Analysis of Electronic Assemblies", *Journal of Electronic Packaging*, Vol. 115, pp.124-130.

[79] Amagai, M., and Tajima, T., (2003), "High Solder Joint Reliability with Lead Free Solders", *Proceedings of 53rd Electronic Component and Technology Conference*, New Orleans, pp.317-322.

ATTENTION: The Singapore Copyright Act applies to the use of this document. Nanyang Technological University Library

[80] Amagai, M., Toyoda, Y., Ohnishi, T., et al., (2004) "High Drop Test Reliability: Lead-free Solders", *Proceedings of 54th Electronic Components and Technology Conference*, June 1-4, Las Vegas, pp.1304-1309.

[81] He, X.L., and Fulton, R., (2000), "Modeling and Simulation of the Dynamic Response of the Electronic Packaging", *Proceedings of 50th Electronic Components and Technology Conference*, pp.1535-1547.

[82] Che, F.X., Pang, H.L.J., Wong, F.L., et al., (2003), "Vibration Fatigue Test and Analysis for Flip Chip Solder Joints", *Proceedings of 5th Electronics Packaging Technology Conference*, December 10-12, Singapore, pp.107-113.

[83] Perkins, A., and Sitaraman, S.K., (2004), "Vibration-Induced Solder Joint Failure of a Ceramic Column Grid Array (CCGA) Package", *Proceedings of 54th Electronic Components and Technology Conference*, June 1-4, Las Vegas, pp.1271-1278.

[84] Yang, Q. J., Wang, Z.P., Lim, G.H., et al., (2002), "Reliability of PBGA Assemblies under out-of-Plane Vibration Excitation", I*EEE Transaction on Component and Packaging Technologies*, Vol. 25, No.2, pp.293-300.

[85] Kim, Y.B., Noguchi, H., and Amagai, M., (2003), "Vibration Fatigue Reliability of BGA-IC Package with Pb-free Solder and Pb-Sn Solder", *Proceedings of 53rd Electronic Components and Technology Conference*, New Orleans, pp.891-897.

[86] Pang, H.L.J., Che, F.X., and. Low, T.H., (2004), "Vibration Fatigue Analysis for FCOB Solder Joints", *Proceedings of 54th Electronic Components and Technology Conference*, June 1-4, Las Vegas, pp.1055-1061.

[87] Clough, R.W., (1960), "The Finite Element Method in Plane Stress Analysis", *Proceedings American Society of Civil Engineers, 2nd Conference on Electronic Computation*, Pittsburgh, Pennsylvania, 23, pp.345-378.

[88] Pang, H.L.J., and Chong, Y.R., (2001), "Flip Chip on Board Solder Joint Reliability Analysis Using 2-D and 3-D FEA Models", *IEEE Transaction on Advanced Packaging*, Vol.24, No.4, pp.499-506.

ATTENTION: The Singapore Copyright Act applies to the use of this document. Nanyang Technological University Library

[89] Akay, H.U., Liu, Y., and Rassaian, M., (2003), "Simplification of Finite Element Models for Thermal Fatigue Life Prediction of PBGA Packages", *Journal of Electronic Packaging*, Vol.125, pp.347-353.

[90] Anderson, T., and Guven, E.M., (1999), "the Necessity of Reexamining Previous Life Prediction Analyses of Solder Joints in Electronic Packages", *Proceedings of 49th Electronic Components and Technology Conference*, pp.1010-1014.

[91] Anderson, T., Barut, A., Guven, I., et al., (2000), "Revisit of Life-Prediction Model for Solder Joints", *Proceedings of 50th Electronic Components and Technology Conference*, May 21-24, pp.1064-1069.

[92] Dudek, R., Doring, R., and Michel B., (2003), "Reliability Prediction of Area Array Solder Joints", *Journal of Electronic Packaging*, Vol.125, December, pp.562-568.

[93] Cheng, H.C., Chiang, K.N., and Lee, M.H., (1998), "an Effective Approach for Three-Dimensional Finite Element Analysis of Ball Grid Array Typed Packages", *Journal of Electronic Packaging*, Vol. 120, pp.129-134.

[94] Yuan, C.A., and Chiang, K.N., (2003), "Micro to Macro Thermomechanical Simulation of Wafer Level Packaging", *Journal of Electronic Packaging*, Vol. 125, pp.576-581.

[95] Yu, Q., Shiratori, M., and Wang, S.B., (1993), "Stress Analysis of Surface-Mount Assembly by an Influence Function Method", *EEP-Vol. 4-1, Advanced in Electronic Packaging, ASME International Electronic Conference*, Binghamton, Sept. 29-Oct.2, New York, pp.227-232.

[96] Zhu, J., (1999), "Three-Dimensional Effects of Solder Joints in Micro-Scale BGA Assembly", *Journal of Electronic Packaging*, Vol. 121, pp.297-302.

[97] Zhu, J., Quander, S., and Reinikainen, T., (2001), "Global/Local Modeling for PWB Mechanical Loading", *Proceedings of 51th Electronic Components and Technology Conference*, May 29-June 1, Orlando, pp.1164-1169.

[98] Saito, N., Sasaki, K., and Hata, N., (1999), "Effective Stress and Displacement Analysis Method for Area-Array Structures", *EEP-Vol. 26-1, Advanced in Electronic Packaging, ASME International Electronic Conference*, pp.21-25.

ATTENTION: The Singapore Copyright Act applies to the use of this document. Nanyang Technological University Library

[99] Yang, Q. J., Lim, G.H., Pang, H.L.J., et al., (1999), "Vibration Reliability Analysis of a PBGA Assembly under Foundation Excitations", *EEP-Vol. 26-1, Advances in Electronic Packaging, Vol. 1, ASME International Electronic Conference*, pp.705-711.

[100] Chen, L., Zhang, Q., Wang G.Z., et al., (2001), " the Effects of Underfill and Its Material Models on Thermomechanical Behaviors of a Flip Chip Package", *IEEE Transactions on Advanced Packaging*, Vol. 24, No. 1, pp.17-24.

[101] Petyt, M., (1990), "Introduction to Finite Element Vibration Analysis", *Cambridge University Press*.

[102] Pang, H.L. J., Xiong, B.S**.,** and Low, T.H., (2004), "Low Cycle Fatigue Study of Lead Free 99.3Sn-0.7Cu Solder Alloy," *International Journal of Fatigue*, Vol. 26, No. 8, pp.865-872.

[103] Che, F.X., Low, T.H., Pang, H.L.J., et al., (2004), "Modeling Thermo-Mechanical Reliability of Bumpless Flip Chip Package", *Proceedings of 54th Electronic Components and Technology Conference*, June 1-4, Las Vegas, pp.421-426.

[104] Terashima, S., Kariya, Y., Hosoi, T., et al., (2003), "Effect of Silver Content on Thermal Fatigue Life of Sn-xAg-0.5Cu Flip-Chip Interconnects", *Journal of Electronic Materials*, Vol. 32, No. 12, pp.1527-1533.

[105] Pang, H.L.J., Xiong, B.S. and Che, F.X., (2004) "Modeling Stress Strain Curves for Lead-Free 95.5Sn-3.8Ag-0.7Cu Solder", *proceedings of Eurosim2004*, May 9-12, Brussels, Belgium, pp.449-453.

[106] Amagai, M., Watanaba, M., Omiya, M., et al., (2002), "Mechanical Characterization of Sn-Ag-based Lead-free Solders", *Microelectronics Reliability* (42), pp.951-966.

[107] Pang, H.L.J., Low, T.H., Xiong, B.S. et al., (2003), "Design for Reliability (DFR) Methodology for Electronic Packaging Assemblies", *Proceedings of 5th Electronic Packaging Technology Conference*, December 10-12, Singapore, pp.470-478.

[108] Amagai, M., (1999), "Characterization of Chip Scale Packaging Materials," *Microelectronics Reliability* (39), pp.1365-1377.

ATTENTION: The Singapore Copyright Act applies to the use of this document. Nanyang Technological University Library

[109] Che, F.X., and Pang, H.L.J., (2004) "Thermal Fatigue Reliability Analysis for PBGA with Sn-3.8Ag-0.7Cu Solder Joints", *Proceedings of* 6th *Electronics Packaging Technology Conference*, December 8-10, Singapore, pp.787-792.

[110] Lucas, J.P., Rhee, H., Guo, F., et al., (2003), "Mechanical Properties of Intermetallic Compounds Associated with Pb-Free Solder Joints using Nanoindentation", *Journal of Electronic Materials*, Vol. 32, No.12, pp.1375-1383.

[111] Frear, D.R., Burchett, S.N., Morgan, H.S., et al., (1994), "the Mechanics of Solder Alloy Interconnects", *Van Nostrand Reinhold*, New York, pp.60-61.

[112] Deng, X., Koopman, M., Chawla, N., et al., (2004), "Young's Modulus of (Cu, Ag)-Sn Intermetallics Measured by Nanoindentation", *Materials Science and Engineering A* 364, pp.240-243.

[113] Deng, X., Chawla, N., Chawla, K.K., et al., (2004), "Deformation Behavior of (Cu, Ag)-Sn Intermetallic by Nanoindentation", *Acta Materialia*, 52, pp.4291-4303.

[114] Ume I.C., Martin T., and Gatro J.T., (1997), "Finite Element Analysis of PWB Warpage Due to the Solder Masking Process", *IEEE Transactions on Component, Packaging, and Manufacturing Technology-Part A*, Vol. 20, No. 3, pp.295-306.

[115] Pang, J. H.L., Yeo, A., Low, T.H., et al., (2004), "Lead-Free 96.5Sn-3.5Ag Flip Chip Solder Joint Reliability Analysis", *Proceedings of 2004 Inter Society Conference on Thermal Phenomena*, June 1-4, Las Vegas, pp.160-164.

[116] Kariya, Y., Hosoi, T., Kimura, T., et al., (2004), "Fatigue Life Enhancement of Low Silver Content Sn-Ag-Cu Flip-Chip Interconnects by Ni Addition", *Proceedings of 2004 Inter Society Conference on Thermal Phenomena*, June 1-4, Las Vegas, pp.103-108.

[117] JEDEC STANDARD, (2003), JESD22-B111: Board Level Drop Test Method of Components for Handheld Electronic Products.

[118] JEDEC STANDARD, (2004), IPC/JEDEC-9702: Monotonic Bend Characterization of Board-Level Interconnects.

ATTENTION: The Singapore Copyright Act applies to the use of this document. Nanyang Technological University Library

[119] Steinberg, D. S., (1988), "Vibration Analysis for Electronic Equipment", 2nd Edition, *John Wiley & Sons*, New York.

[120] Weaver, W. Jr., Timoshenko, S.P., and Young, D.H, (1990), "Vibration Problems in Engineering", 5th Edition, *Wiley*.

[121] Sidharth, V., Gannamani, R., and Zhang, M.L., (2000), "Characterization of a Novel Fine-Pitch Ball Grid Array Package for Flash Memory Application", *Proceedings of 50th Electronic Components and Technology Conference*, pp. 353-357.

[122] Wu, J., Song, G.S., Yeh, C.P., et al., (1998), "Drop/Impact Simulation and Test Validation of the Telecommunication Products", *Proceedings of InterSociety Conference on Thermal Phenomena*, pp.330-336.

[123] Seah, S.K.W., Lim, C.T., Wong, E.H., et al., (2002), "Mechanical Response of PCBs in Portable Electronic Products during Drop Impact", *Proceedings of 4th Electronics Packaging Technology Conference*, Singapore, pp.120-125.

[124] Arra, M., Xie, D., and Shangguan, D., (2002), "Performance of Lead-Free Solder Joints under Dynamic Mechanical Lading", *Proceedings of 52nd Electronic Components and Technology Conference*, pp.1256-1262.

[125] Yu, Q., Kikuchi, H., Ikeda, S., et al., (2002), "Dynamic Behavior of Electronics Package and Impact Reliability of BGA Solder Joints", *Proceedings of InterSociety Conference on Thermal Phenomena*, pp.953-960.

[126] Wong, E.H., Lim, K.M., Lee, N., et al., (2002), "Drop Impact Test-Mechanics & Physics of Failure", *Proceedings of 4th Electronics Packaging Technology Conference*, Singapore, pp.327-333.

[127] Ju, R., and Hsiao, B., (2004), "Drop Simulation for Portable Electronic Products", *Proceedings of 8th International LS-DYNA Users Conference*, May 2-4, Dearborn, Michigan, pp.14-1-14-5.

[128] Date, M., Shoji, M., Fujiyoshi, K., et al., (2004), "Impact Reliability of Solder Joints", *Proceedings of 54th Electronic Components and Technology Conference*, June 1-4, Las Vegas, pp.668-674.

ATTENTION: The Singapore Copyright Act applies to the use of this document. Nanyang Technological University Library

[129] Sillanpää, M, Okura J.H., (2004), "Flip Chip on Board: Assessment of Reliability in Cellular Phone Application", *IEEE Transaction on Components and Packaging Technologies*, Vol. 27, No.3 pp.461-467.

[130] Zhu, L.P., (2001), "Submodeling Technique for BGA Reliability Analysis of CSP Packaging Subjected to an Impact Loading", *Proceedings of IPACK'01*, July 8-13, Kauai, Hawaii, IPACK2001-15873: 1-9.

[131] Che, F.X., and Pang, H.L.J., (2004), "Harsh Solder Joint Reliability Tests by Impact Drop and Highly Accelerated Life Test (HALT)", *Proceedings of* 6th *Electronics Packaging Technology Conference*, December 8-10, Singapore, pp.205-209.

[132] Lall, P., Panchaged, D., Liu, Y., et al., (2004), "Models for Prediction of Fin-Pitch BGAs and CSPs in Shock and Drop-Impact', *Proceedings of 54th Electronic Components and Technology Conference*, June 1-4, Las Vegas, pp.1296-1303.

[133] ANSYS/LS-DYNA User's Guide, (2002), Release 7.0, *ANSYS, Inc*.

[134] Balakrisnan, B., Chum, C.C., Li, M., et al., (2003), "Fracture Toughness of Cu-Sn Intermetallic Thin Flims", *Journal of Electronic Materials*, Vol. 32, No. 3, pp.166-171.

[135] Barker, D. B., and Chen, Y. S., (1993), "Modeling the Vibration Restraints of Wedge Lock Card Guides", *Journal of Electronic Packaging*, Vol. 115, pp.189-194.

[136] Lim, G. H., Ong, J. H., and Penny, J. E. T., (1999), "Effect of Edge and Internal Point Support of a Printed Circuit Board under Vibration", *Journal of Electronic Packaging*, Vol. 121, pp.122-126.

[137] Barker, D. B., Chen, Y. S., and Dasgupta, A., (1993), "Estimating the Vibration Fatigue Life of Quad Leaded Surface Mount Components", *Journal of Electronic Packaging,* Vol. 115, pp.195-200.

[138] Pitarresi, J. M., and Akanda, A., (1993), "Random Vibration Response of a Surface Mount Lead/Solder Joint", *ASME EEP, V4-1, Advances in Electronic Packaging*, pp.207-215.

ATTENTION: The Singapore Copyright Act applies to the use of this document. Nanyang Technological University Library

[139] Lee, S. B., and Ham, S. J., (1999), "Fatigue Life Assessment of Bump Type Solder Joint under Vibration Environment", *ASME EEP-Vol. 26-1, Advances in Electronic Packaging*, Vol.1, pp.699-704.

[140] Basaran, C., and Chandaroy, R., (1999), "Nonlinear Dynamic Analysis of Surface Mount Interconnects: Part I-Theory", *Journal of Electronic Packaging*, Vol. 121, pp.8-11.

[141] Basaran, C., and Chandaroy, R., (1999), "Nonlinear Dynamic Analysis of Surface Mount Interconnects: Part II-Application", *Journal of Electronic Packaging*, Vol. 121, pp.12-17.

[142] Zhao, Y., Basaran, C., Cartwright, A., et al., (2000), "Thermomechanical Behavior of Micron Scale Solder Joints under Dynamic Loads", *Mechanics of Materials*, Vol. 32, pp.161-173.

[143] Barker, D. B., Dasgupta, A., and Pecht, M. G., (1992), "PWB Solder Joint Life Calculations under Thermal and Vibrational Loading", *Journal of The IES*, January/February, pp.17-25.

[144] Li, R. S., (2001), "A Methodology for Fatigue Prediction of Electronic Components under Random Vibration Load", *Journal of Electronic Packaging*, Vol. 123, pp.394-400.

[145] Yang, Q. J., Pang, H. L.J., Wang, Z. P., et al., (2000), "Vibration Reliability Characterization of PBGA Assemblies", *Microelectronics Reliability*, (40), pp.1097-1107.

[146] Johnson, W., (1972), "Impact Strength of Materials", *Edward Arnold*, London.

[147] Ng, H.S., Tee, T.Y., and Luan, J.E., (2004), "Design for Standard Impact Pulse of Drop Tester using Dynamic Simulation", *Proceedings of 6th Electronics Packaging Technology Conference*, December 8-10, Singapore, pp.793-799.

[148] Meirovitch, L., (1986), "Elements of Vibration Analysis", 2nd edition, *McGraw-Hill*.

ATTENTION: The Singapore Copyright Act applies to the use of this document. Nanyang Technological University Library

APPENDIX A GLB MODELING TECHNIQUE

A.1 EQUIVALENT BEAM STIFFNESS ANALYSIS

The two-node beam element has 12 DOFs, three translational and three rotational at each node. The relation between the generalized nodal force vector $\{F\}$ and the displacement vector $\{u\}$ of beam is expressed in matrix form as follows:

$$\{F\} = \{K\}\{u\} \tag{A.1}$$

$$\{F\} = \begin{bmatrix} F_{x1} & F_{y1} & F_{z1} & M_{x1} & M_{y1} & M_{z1} & F_{x2} & F_{y2} & F_{z2} & M_{x2} & M_{y2} & M_{z2} \end{bmatrix}^T \tag{A.2}$$

$$\{u\} = \begin{bmatrix} u_{x1} & u_{y1} & u_{z1} & \theta_{x1} & \theta_{y1} & \theta_{z1} & u_{x2} & u_{y2} & u_{z2} & \theta_{x2} & \theta_{y2} & \theta_{z2} \end{bmatrix}^T \tag{A.3}$$

where $[K]$ is the stiffness matrix of two-node beam. F_{ij} in Eq. (A.2) means a nodal force in the i-th direction at the j-th node and M_{ij} means a nodal moment around the i-th direction axis at the j-th node. The definitions of u_{ij} and θ_{ij} in Eq. (A.3) are similar to F_{ij} and M_{ij}

According to the beam theory, the stiffness matrix of a beam element corresponding to X, Y directions can be expressed as:

$$\begin{Bmatrix} M_{x1} \\ M_{x2} \end{Bmatrix} = \begin{bmatrix} B & D \\ D & B \end{bmatrix} \begin{Bmatrix} \theta_{x1} \\ \theta_{x2} \end{Bmatrix} \tag{A.4}$$

$$\begin{Bmatrix} M_{y1} \\ M_{y2} \end{Bmatrix} = \begin{bmatrix} A & C \\ C & A \end{bmatrix} \begin{Bmatrix} \theta_{y1} \\ \theta_{y2} \end{Bmatrix} \tag{A.5}$$

where $B = \frac{4EI_x}{L}$, $D = \frac{2EI_x}{L}$, $A = \frac{4EI_y}{L}$, $C = \frac{2EI_y}{L}$, I and E are the moment of inertia and elastic modulus, respectively, L is the length of the beam.

The torsional stiffness with respect to Z direction can be expressed as:

$$\begin{Bmatrix} M_{z1} \\ M_{z2} \end{Bmatrix} = \frac{JG}{L} \begin{bmatrix} 1 & -1 \\ -1 & 1 \end{bmatrix} \begin{Bmatrix} \theta_{z1} \\ \theta_{z2} \end{Bmatrix} = \begin{bmatrix} Q & -Q \\ -Q & Q \end{bmatrix} \begin{Bmatrix} \theta_{z1} \\ \theta_{z2} \end{Bmatrix} \tag{A.6}$$

ATTENTION: The Singapore Copyright Act applies to the use of this document. Nanyang Technological University Library

where J and G are polar moment of inertia and shear elastic modulus, respectively.

The axial stiffness can be expressed as:

$$\begin{Bmatrix} F_{z1} \\ F_{z2} \end{Bmatrix} = \frac{EA}{L}\begin{bmatrix} 1 & -1 \\ -1 & 1 \end{bmatrix}\begin{Bmatrix} u_{z1} \\ u_{z2} \end{Bmatrix} = \begin{bmatrix} H & -H \\ -H & H \end{bmatrix}\begin{Bmatrix} u_{z1} \\ u_{z2} \end{Bmatrix} \tag{A.7}$$

where A is the cross-section area. Combining Eq. (A.4) to Eq. (A.7) yields:

$$\begin{Bmatrix} M_{x1} \\ M_{y1} \\ F_{z1} \\ M_{z1} \\ M_{x2} \\ M_{y2} \\ F_{z2} \\ M_{z2} \end{Bmatrix} = \begin{bmatrix} B & 0 & 0 & 0 & D & 0 & 0 & 0 \\ 0 & A & 0 & 0 & 0 & C & 0 & 0 \\ 0 & 0 & H & 0 & 0 & 0 & -H & 0 \\ 0 & 0 & 0 & Q & 0 & 0 & 0 & -Q \\ D & 0 & 0 & 0 & B & 0 & 0 & 0 \\ 0 & C & 0 & 0 & 0 & A & 0 & 0 \\ 0 & 0 & -H & 0 & 0 & 0 & H & 0 \\ 0 & 0 & 0 & -Q & 0 & 0 & 0 & Q \end{bmatrix}\begin{Bmatrix} \theta_{x1} \\ \theta_{y1} \\ u_{z1} \\ \theta_{z1} \\ \theta_{x2} \\ \theta_{y2} \\ u_{z2} \\ \theta_{z2} \end{Bmatrix} \tag{A.8}$$

or

$$\{\overline{F}\} = [S_I]\{\overline{u}\} \tag{A.9}$$

As Fig. 3-17 illustrates, the following relationships can be derived:

$$F_{y2} = \frac{M_{x1} + M_{x2}}{L}, F_{y1} = \frac{-M_{x1} - M_{x2}}{L}, F_{x2} = \frac{-M_{y1} - M_{y2}}{L}, F_{x1} = \frac{M_{y1} + M_{y2}}{L} \tag{A.10}$$

Rewriting Eqs. (A.10) in matrix form yields:

$$\{F\} = \begin{Bmatrix} F_{x1} \\ F_{y1} \\ F_{z1} \\ M_{x1} \\ M_{y1} \\ M_{z1} \\ F_{x2} \\ F_{y2} \\ F_{z2} \\ M_{x2} \\ M_{y2} \\ M_{z2} \end{Bmatrix} = \frac{1}{L}\begin{bmatrix} 0 & 1 & 0 & 0 & 0 & 1 & 0 & 0 \\ -1 & 0 & 0 & 0 & -1 & 0 & 0 & 0 \\ 0 & 0 & L & 0 & 0 & 0 & 0 & 0 \\ L & 0 & 0 & 0 & 0 & 0 & 0 & 0 \\ 0 & L & 0 & 0 & 0 & 0 & 0 & 0 \\ 0 & 0 & 0 & L & 0 & 0 & 0 & 0 \\ 0 & -1 & 0 & 0 & 0 & -1 & 0 & 0 \\ 1 & 0 & 0 & 0 & 1 & 0 & 0 & 0 \\ 0 & 0 & 0 & 0 & 0 & 0 & L & 0 \\ 0 & 0 & 0 & 0 & L & 0 & 0 & 0 \\ 0 & 0 & 0 & 0 & 0 & L & 0 & 0 \\ 0 & 0 & 0 & 0 & 0 & 0 & 0 & L \end{bmatrix}\begin{Bmatrix} M_{x1} \\ M_{y1} \\ F_{z1} \\ M_{z1} \\ M_{x2} \\ M_{y2} \\ F_{z2} \\ M_{z2} \end{Bmatrix} = [S]\begin{Bmatrix} M_{x1} \\ M_{y1} \\ F_{z1} \\ M_{z1} \\ M_{x2} \\ M_{y2} \\ F_{z2} \\ M_{z2} \end{Bmatrix} \tag{A.11}$$

Substituting Eq. (A.8) and Eq. (A.9) into Eq. (A.11) yields:

ATTENTION: The Singapore Copyright Act applies to the use of this document. Nanyang Technological University Library

$$\{F\} = [S][S_I][S]^T\{u\} = [K]\{u\} \tag{A.12}$$

$$[K] = \begin{bmatrix}
\frac{2(A+C)}{L^2} & 0 & 0 & 0 & \frac{A+C}{L} & 0 & \frac{-2(A+C)}{L^2} & 0 & 0 & 0 & \frac{A+C}{L} & 0 \\
0 & \frac{2(B+D)}{L^2} & 0 & \frac{-(B+D)}{L} & 0 & 0 & 0 & \frac{-2(B+D)}{L^2} & 0 & \frac{-(B+D)}{L} & 0 & 0 \\
0 & 0 & H & 0 & 0 & 0 & 0 & 0 & -H & 0 & 0 & 0 \\
0 & \frac{-(B+D)}{L} & 0 & B & 0 & 0 & 0 & \frac{B+D}{L} & 0 & D & 0 & 0 \\
\frac{A+C}{L} & 0 & 0 & 0 & A & 0 & \frac{-(A+C)}{L} & 0 & 0 & 0 & C & 0 \\
0 & 0 & 0 & 0 & 0 & Q & 0 & 0 & 0 & 0 & 0 & -Q \\
\frac{-2(A+C)}{L^2} & 0 & 0 & 0 & \frac{-(A+C)}{L} & 0 & \frac{2(A+C)}{L^2} & 0 & 0 & 0 & \frac{-(A+C)}{L} & 0 \\
0 & \frac{-2(B+D)}{L^2} & 0 & \frac{B+D}{L} & 0 & 0 & 0 & \frac{2(B+D)}{L^2} & 0 & \frac{B+D}{L} & 0 & 0 \\
0 & 0 & -H & 0 & 0 & 0 & 0 & 0 & H & 0 & 0 & 0 \\
0 & \frac{-(B+D)}{L} & 0 & D & 0 & 0 & 0 & \frac{B+D}{L} & 0 & B & 0 & 0 \\
\frac{A+C}{L} & 0 & 0 & 0 & C & 0 & \frac{-(A+C)}{L} & 0 & 0 & 0 & A & 0 \\
0 & 0 & 0 & 0 & 0 & -Q & 0 & 0 & 0 & 0 & 0 & Q
\end{bmatrix}$$

The $[K]$ is symmetric matrix which can be rewritten by simple upper triangle form:

$$[K] = \begin{bmatrix}
S_{11} & 0 & 0 & 0 & S_{15} & 0 & -S_{11} & 0 & 0 & 0 & S_{15} & 0 \\
 & S_{22} & 0 & -S_{24} & 0 & 0 & 0 & -S_{22} & 0 & -S_{24} & 0 & 0 \\
 & & H & 0 & 0 & 0 & 0 & 0 & -H & 0 & 0 & 0 \\
 & & & B & 0 & 0 & 0 & S_{24} & 0 & D & 0 & 0 \\
 & & & & A & 0 & -S_{15} & 0 & 0 & 0 & C & 0 \\
 & & & & & Q & 0 & 0 & 0 & 0 & 0 & -Q \\
 & & & & & & S_{11} & 0 & 0 & 0 & -S_{15} & 0 \\
 & & & & & & & S_{22} & 0 & S_{24} & 0 & 0 \\
 & & sym & & & & & & H & 0 & 0 & 0 \\
 & & & & & & & & & B & 0 & 0 \\
 & & & & & & & & & & A & 0 \\
 & & & & & & & & & & & Q
\end{bmatrix} \tag{A.13}$$

where $S_{11} = \frac{2(A+C)}{L^2}$, $S_{15} = \frac{A+C}{L}$, $S_{22} = \frac{2(B+D)}{L^2}$, $S_{24} = \frac{B+D}{L}$. When the cross-section of the beam is axisymmetric or square, yields A=B, C=D, then $S_{11}=S_{22}$, $S_{15}=S_{24}$.

In order to extract the stiffness of the solder joint, unit translational and rotational displacement were applied on the solder joint surface as a boundary condition. Here

ATTENTION: The Singapore Copyright Act applies to the use of this document. Nanyang Technological University Library

10^{-6}m and 10^{-6}rad were selected as unit translational and rotational then the reactions were amplified by 10^6 to obtain the solder joint stiffness matrix. The 1m and 1rad were not selected as unit displacements because these values were far greater than the solder joint geometry, thus leading to some errors in stiffness extraction analysis due to distortion. Therefore, a boundary value problem of $\{u\} = \{10^{-6}, 0, 0, \cdots 0\}^T$ was solved by FEA simulation. From the solutions the generalized forces imposed at two end surfaces can be obtained, and these generalized forces form the first column or the first row elements in the solder joint stiffness matrix. By the same process, when 12 different boundary value problems with unit displacement were solved, all the terms in the stiffness can be obtained. When the original stiffness matrix was obtained, it is modified according to the form of [*K*] in Eq. (A.13) and the resultant stiffness matrix of FC solder ball is given in Table A-1. The units in Table are N/m for tensional and shear force or N·m/Radian for moment and torsion.

Table A-1 Stiffness matrix of solder joint as two-node beam element.

	X_1	Y_1	Z_1	θ_{x1}	θ_{y1}	θ_{z1}	X_2	Y_2	Z_2	θ_{x2}	θ_{y2}	θ_{z2}
X_1	1.26E6	0	0	0	6.31E1	0	-1.26E6	0	0	0	6.31E1	0
Y_1		1.26E6	0	-6.31E1	0	0	0	-1.26E6	0	-6.31E1	0	0
Z_1			5.19E6	0	0	0	0	0	-5.19E6	0	0	0
θ_{x1}				9.82E-3	0	0	0	6.31E1	0	-3.51E-3	0	0
θ_{y1}					9.82E-3	0	-6.31E1	0	0	0	-3.51E-3	0
θ_{z1}						4.59E-3	0	0	0	0	0	-4.59E-3
X_2							1.26E6	0	0	0	-6.31E1	0
Y_2			Sym					1.26E6	0	6.31E1	0	0
Z_2									5.19E6	0	0	0
θ_{x2}										9.82E-3	0	0
θ_{y2}											9.82E-3	0
θ_{z2}												4.59E-3

ATTENTION: The Singapore Copyright Act applies to the use of this document. Nanyang Technological University Library

A.2 CONSTRAIN EQUATION

The node in solid element has 3 DOFs while the node in beam element has 6 DOFs which results in inconsistent of nodal DOFs when connecting beam element to solid element. The constraint equation can be used to solve this DOF inconsistent problem as illustrated in Fig. A-1 for 2D element example. In this example, node 2 is a common node used by beam element and solid element. In order to transfer moment between beam and solid elements through node 2, the following constraint equation can be used:

$$ROT_{Z2} = (U_{Y3} - U_{Y1})/10 \tag{A.14}$$

where ROT_{Z2}, U_{Y3} and U_{Y1} are rotational displacement of node 2, translational displacement of node 3 and node 1, respectively. For 3D FEA model case, the similar constraint equation can be developed.

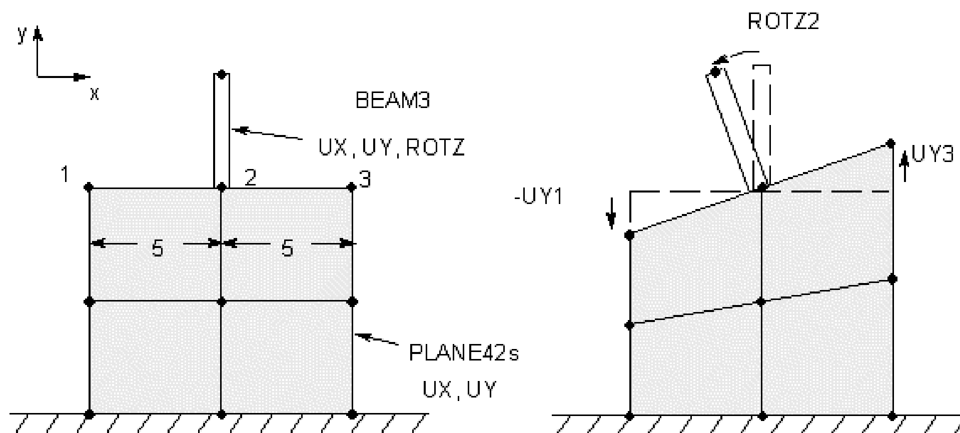

Fig. A-1 Relationship between rotation and translation DOF [22].

ATTENTION: The Singapore Copyright Act applies to the use of this document. Nanyang Technological University Library

APPENDIX B AG CONTENT EFFECT ON FATIGUE LIFE OF FLIP CHIP SOLDER

B.1 THERMAL CYCLING TEST FOR FCOB ASSEMBLY

Thermal cycling test result for FCOB assemblies without underfill reported by Terashima et al. [104] is used for validation of FEA simulation study of the effect of Ag content on solder fatigue life. In FCOB assembly, an 8mm×8mm×0.4mm silicon chip and a 50mm×50mm×0.7mm FR4 PCB were joined by 240 flip-chip (Sn-xAg-0.5Cu) solder balls with diameter of 0.3mm, standoff height of 0.2mm and ball pitch of 0.45mm. Four Ag contents (x=1, 2, 3 and 4 in mass%) were used. Thermal cycling test with –40°C/125°C and cycle time of 46 minutes was conducted. Two types of electrodes on the substrates were employed: one was Cu pad and the other was Cu pad with Ni/Au surface finish. Test results show that thermal fatigue failure of Sn-xAg-0.5Cu was dependent on the Ag content of solder but independent of the surface finish. The solder joints with lower Ag content (x=1 and 2) have a faster failure rate than those with higher Ag content (x=3 and 4). The MTTF is listed in Table B-1 [104].

Table B-1 Fatigue cycles for FCOB assembly with different Ag contents [104].

Specimen	FCOB with 3-4Ag solder	FCOB with 1-2Ag solder
MTTF (cycles)	570	320

B.2 AG CONTENT EFFECT ON FATIGUE LIFE

The FEA simulation and fatigue life prediction were performed for FCOB assembly to compare with Terashima's test result to study Ag content effect on solder

ATTENTION: The Singapore Copyright Act applies to the use of this document. Nanyang Technological University Library

fatigue life. Fig. B-1 shows the 2D FEA model for FCOB assembly. Four materials containing FR4 PCB, silicon chip, Cu pad and solder joint were modeled in FEA simulation. For convenience, solder with 1% and 2% Ag in mass is termed as low Ag solder using material properties of Sn-1Ag-0.5Cu solder, and solder with 3% and 4% Ag is termed as high Ag solder using material properties of Sn-3.8Ag-0.7Cu.

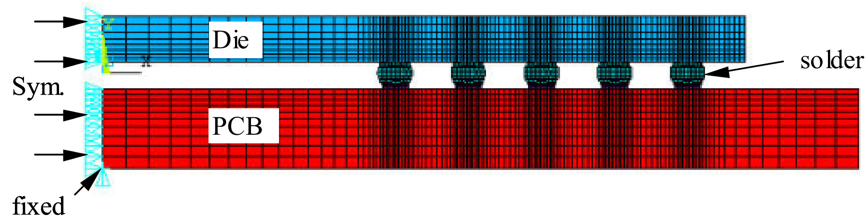

Fig. B-1 2D axisymmetric FEA model of FCOB assembly.

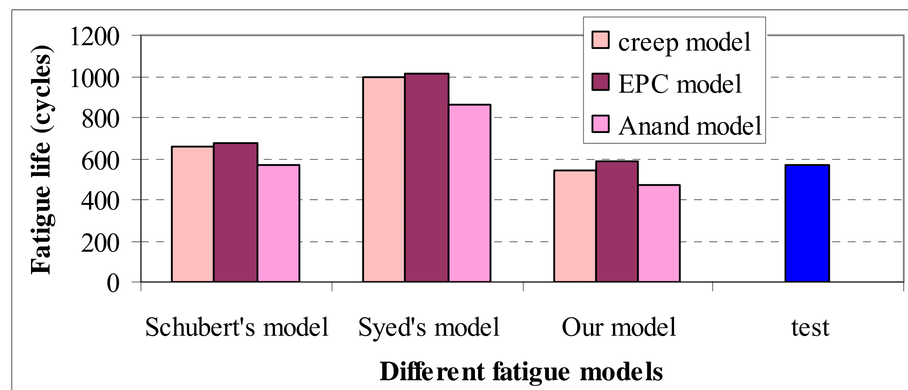

(Note: our model refers to Pang et al [24])

Fig. B-2 Fatigue life of FCOB assembly with high Ag content solders.

In FEA simulation for FCOB assembly with high Ag solders, different solder constitutive models such as creep model, EPC model and Anand's model were used. Fatigue life predicted by different fatigue models of Eq. (4.6), Eq. (4.8) and Eq. (4.10) are shown in Fig. B-2. The averaged energy densities based on whole layer elements for Schubert's and Syed's model and based on outermost elements for our model were calculated for fatigue life prediction. It can be seen that fatigue life predicted by Schubert's model and our model is more accurate than by Syed's model compared to test result. From previous discussion in Chapter 4, Syed's model was developed from

ATTENTION: The Singapore Copyright Act applies to the use of this document. Nanyang Technological University Library

different BGA assemblies with larger solder ball while Schubert's model was developed from BGA assemblies and FCOB assemblies so Schubert's model can lead to more accurate life prediction for FCOB assembly than Syed's model.

From FEA result when using EPC model, the accumulated plastic strain energy density of 0.248MPa was close to accumulated creep strain energy density of 0.27MPa on whole solder/chip interface layer, which is different from PBGA assembly where creep part is dominant. High-level stress inducing more plastic strain occurs in FCOB solder joint and lower level stress occurs in PBGA solder joint when assembly subjected to similar thermal cycling load. Therefore, plastic part must be considered in fatigue life prediction for FCOB solder joint when using EPC model in FEA modeling.

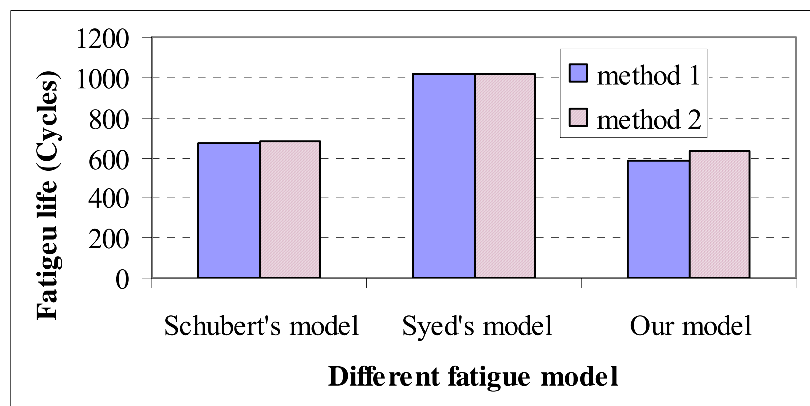

(Note: our model refers to Pang et al [24])

Fig. B-3 Fatigue life prediction for FCOB with high Ag content by energy-base model and creep-fatigue model.

Two methods were used for fatigue life prediction when solder was simulated by EPC model. The first method is summing plastic part and creep part as total inelastic strain energy density used for fatigue life estimation. The second method is predicting fatigue life separately using plastic part and creep part, then calculate total fatigue life using combined creep-fatigue life prediction model of Eq. (4.11). Fig. B-3 shows the comparison for two methods. Two methods result in same fatigue life for Syed's fatigue model because the fatigue ductility exponent in Syed's model is unity. Two

ATTENTION: The Singapore Copyright Act applies to the use of this document. Nanyang Technological University Library

fatigue life prediction methods also result in similar fatigue lire when using Schubert's model [47] and our model [24].

FEA simulation was also conducted for FCOB assembly with low Ag content solder joint using reported constitutive model. Fatigue models from Eq. (4.5) to Eq. (4.10) cannot be used to predict low Ag content solder fatigue life because they were developed for Sn-(3-4)Ag-Cu solder. Strain-based fatigue models for high Ag and low Ag content solders were given by Kariya et al. [116] and expressed as follows:

For Sn-1Ag-0.5Cu: $$\Delta\varepsilon_{in} \cdot N_f^{0.62} = 1.4 \quad \text{(B.1)}$$

For Sn-3Ag-0.5Cu: $$\Delta\varepsilon_{in} \cdot N_f^{0.45} = 0.78 \quad \text{(B.2)}$$

The maximum inelastic strain was used in developing above equations. Therefore, the inelastic strain from outermost element on solder/chip interface with maximum strain value was used in fatigue life prediction. Fig. B-4 shows predicted fatigue life and test results for FCOB assemblies with different Ag content solders and they agree well. Low Ag content solder has shorter fatigue life than high Ag solder from test results as well as predicted results. Predicted fatigue life in this study is consistent with Terashima's test results.

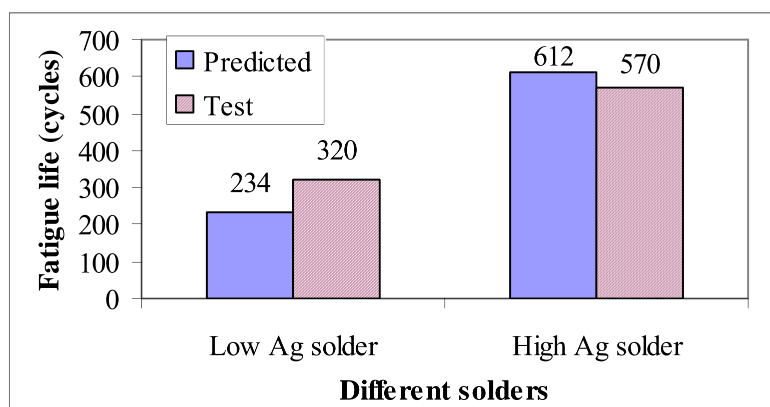

Fig. B-4 Fatigue life comparison for SAC solders with high Ag and low Ag.

ATTENTION: The Singapore Copyright Act applies to the use of this document. Nanyang Technological University Library

APPENDIX C DROP TEST AND SIMULATION

C.1 DROP TEST AND ANALYSIS

C.1.1 Drop Test and Analysis for FCOB Assembly

The Lansmont test machine was used for board-level drop test. This machine can provide half sine shock pulse. The duration of the pulse is adjustable somewhat by the addition or subtraction of the felt pads. The FCOB assembly specimen as shown in Fig. C-1 was attached to a drop table with chip down and horizontal to the table through aluminum fixture providing clamped-clamped boundary condition.

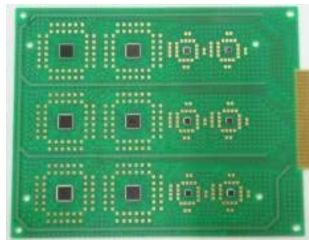

Fig. C-1 FCOB specimen.

During impact, the longitudinal stress wave will travel in the table, when the wave travels into the PCB, it turns into the bending wave. The propagation velocity of the longitudinal stress wave in the table and fixture can be expressed as [146]:

$$C_L = \sqrt{E/\rho} \tag{C.1}$$

where E is the Young's modulus, and ρ is the material density.

The velocity of the bending wave in the specimen can be expressed as

$$C_b = \pi\gamma / L \tag{C.2}$$

where $\gamma = \sqrt{D/\rho_a}$, D is the flexural modulus of $Eh^3/12$, h is thickness, $\rho_a = \rho \cdot h$ is the area density, L is the beam length.

ATTENTION: The Singapore Copyright Act applies to the use of this document. Nanyang Technological University Library

In this test, in order to measure the dynamic response of the specimen to the drop impact loading, the strain gauges and accelerometer affixed exactly to the surface of the PCB desired locations were used to measure the dynamic strain and acceleration of the specimen. During the drop test, a high-speed camera with recording rate of 4500 frames/s was used to capture the images of the specimen movements. Before the drop test, 4 marks were attached on the PCB free edge, which can make the data record easily by high-speed camera. Mark 4 is a reference point attached on the fixture, and mark 1, 2, and 3 are located on the left quarter point, center point and right quarter point of PCB free edge, respectively. After 40 drops, no solder joint failure was found.

In the drop test with 1m height, four felt pads were placed on the impact base surface to prevent metal-to-metal impact. The vertical relative displacements obtained from the high-speed camera were extracted for analysis considering displacement of fixture as a reference. Fig. C-2 shows the relative displacement comparison between center point of mark 2 and quarter point of mark 3. It can be seen from Fig. C-2 that the motion of the specimen during the drop test is similar to the harmonic motion, suggesting the existence of a dominant fundamental deformation mode. The displacement of center point is more than that of quarter point. The vibration displacement range (2×amplitude) of the mark 2 is 5.2mm approximately. The vibration period of the specimen is about 5.2ms, which is equivalent to the frequency of 192Hz and is consistent with the fundamental frequency of 195Hz from FEA result.

A wooden plate was placed above the felt pads in order to change the effect of the impact surface on the specimen dynamic response. The relative displacement of center mark is shown in Fig. C-3 for two different bases. It is obvious that the soft base reduces the maximum vibration displacement and increases vibration period of the specimen, thus the maximum acceleration of the specimen will be reduced.

ATTENTION: The Singapore Copyright Act applies to the use of this document. Nanyang Technological University Library

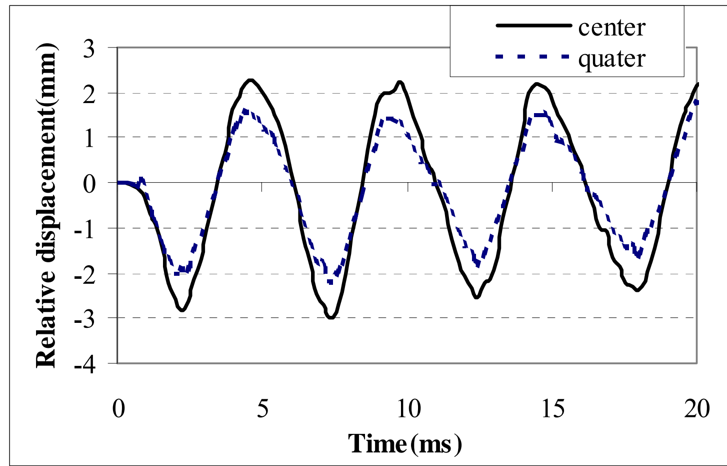

Fig. C-2 Relative displacement comparison for center mark and quarter mark.

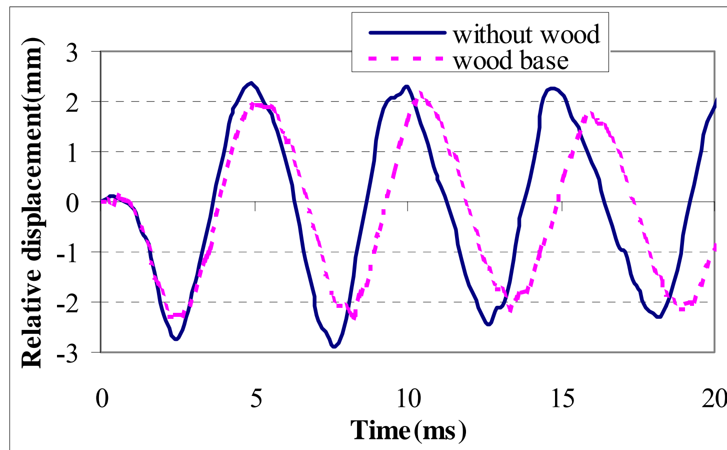

Fig. C-3 Relative displacement comparison for two different drop bases.

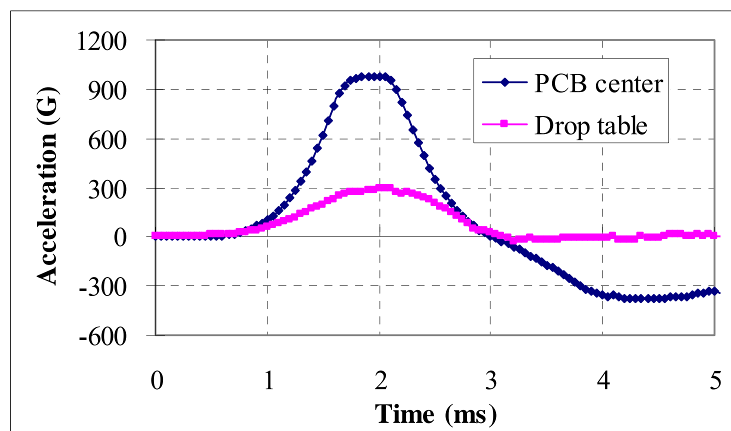

Fig. C-4 Acceleration results from accelerometer.

The peak acceleration of mark2 from high-speed camera result is 981G. Fig. C-4 shows the acceleration of the drop table and specimen center measured by

ATTENTION: The Singapore Copyright Act applies to the use of this document. Nanyang Technological University Library

accelerometer during the impact. It can be seen that the PCB center has a higher acceleration than the drop table due to PCB deflection. Comparing acceleration from the high-speed camera and the accelerometer, the consistent result was obtained. Otherwise, the maximum acceleration of PCB center reduces by 30% after adding wooden plate on drop base.

C.1.2 Drop Test and Analysis for Bare PCB and PCB Assembly

Bare PCB and PCB assembly with clamped-clamped boundary condition along the longer edge were tested. PCB assembly as shown in Fig. C-5 has one PBGA, one TSSOP and two PQFPs with SnAgCu lead-free solders. Three different surface finishes containing Ag, Ni/Au and OSP are used for PCB assembly. In the drop test, accelerometers and strain gauges as shown in Fig. C-5 were used to measure the dynamic response of the specimen.

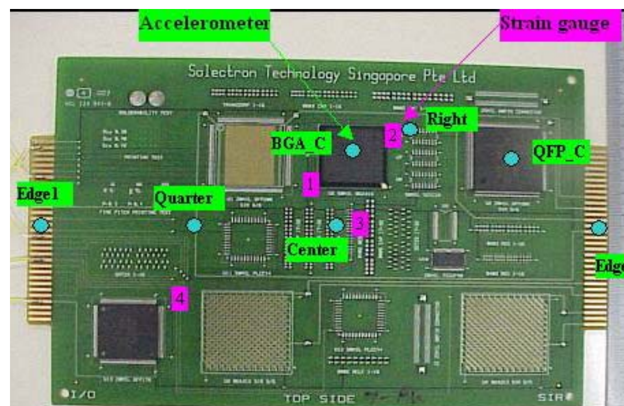

Fig. C-5 Specimen and measurement locations.

C.1.2.1 Bare PCB drop test and analysis

Four different drop heights of 0.4m, 0.6m, 0.8m and 1m were selected in bare PCB drop test to study the drop height effect on the dynamic response of the PCB. One layer felt pad was added on drop base. Fig. C-6 shows the accelerations of drop table for different drop heights. The peak acceleration of drop table increases with drop height increasing. The duration of impact pulse, however, keeps a constant value of

ATTENTION: The Singapore Copyright Act applies to the use of this document. Nanyang Technological University Library

2ms for different drop heights. Therefore, drop height affects the peak acceleration significantly but hardly affects the impact pulse duration, while drop base affects both the peak acceleration and the impact pulse duration. This result is consistent with the simulation result done by Ng et al. [147]. Fig. C-7 shows the accelerations of bare PCB center for different drop heights. It can be seen that transient vibration of PCB occurs after drop impact and the first peak acceleration has the maximum value, then consequent peak values reduce due to damping effect. The transient vibration duration of bare PCB has a constant value for different drop heights, which corresponds to the natural frequency of 302Hz for bare PCB determined by FEA simulations.

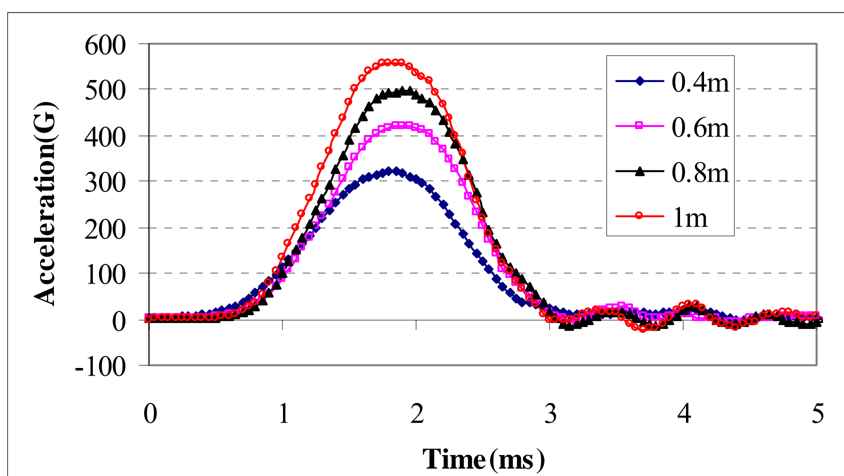

Fig. C-6 Acceleration of drop table in different drop heights.

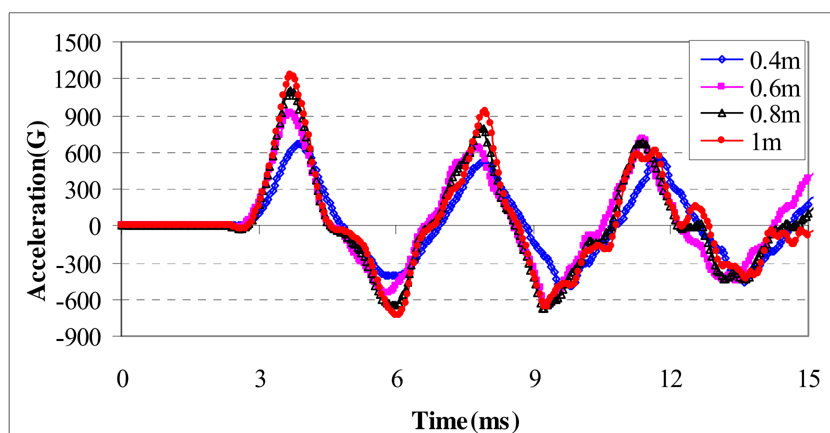

Fig. C-7 Acceleration of bare PCB center in different drop heights.

ATTENTION: The Singapore Copyright Act applies to the use of this document. Nanyang Technological University Library

Fig. C-8 shows the accelerations for different locations. The PCB center has higher acceleration than drop table. The peak acceleration of PCB center lags behind that of drop table about 2ms due to dynamic wave propagation. The velocity of the bending wave in the specimen can be calculated as 35.9m/s by Eq. (C.2) when E=22GPa, ρ =1900kg/m^3, h=1.63e-3m and L=0.14m. Therefore, the wave propagation time from drop table to PCB center is calculated as 1.95ms, which is consistent with the test result. The power law relationship in Fig. C-9 has a good curve fitting between fist peak acceleration and drop height. According to perfect elastic impact theory, the exponent of power law curve should be 0.5. Because some energy was absorbed by drop base during impact, the exponent of power law is less than 0.5 for real drop events.

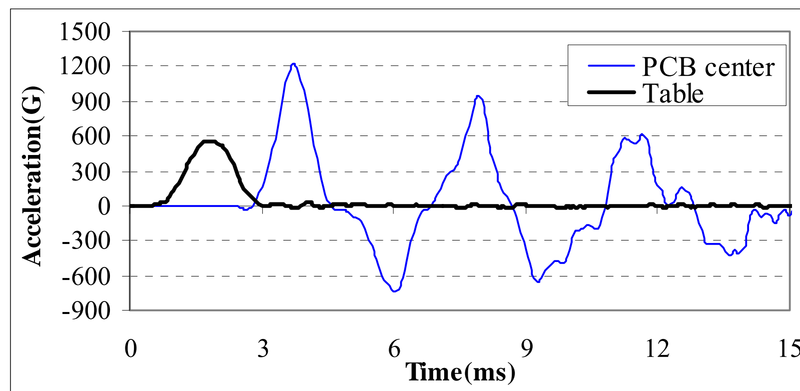

Fig. C-8 Acceleration of different locations at drop height of 1m.

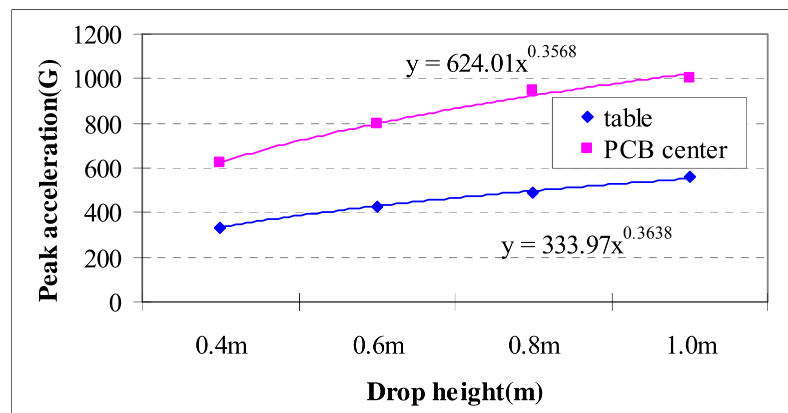

Fig. C-9 Relationship between peak acceleration and drop height.

ATTENTION: The Singapore Copyright Act applies to the use of this document. Nanyang Technological University Library

Fig. C-10 shows the strains measured by different strain gauges in Fig. C-5. It can be seen that the PCB center has the highest strain value due to the largest deflection. When PCB bends down, not all strain gauges on PCB upper surface experience compressive strain for clamped-clamped boundary condition. It can be seen that the strain gauge 2 near the clamped edge experiences tensile strain while other strain gauges experience compressive strain. The peak strain value decreases with time due to damping effect in transient vibration.

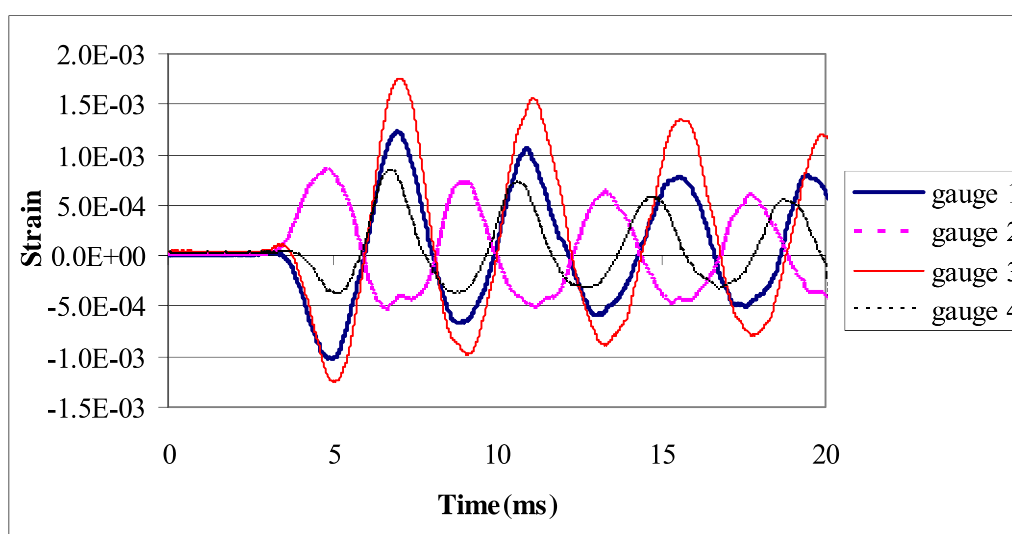

Fig. C-10 Strain comparison for different strain gauges with drop height of 1m.

C.1.2.2 PCB assembly drop test and analysis

In PCB assembly drop test, drop height of 1m was fixed. Thirty drops were conducted for each surface finish component and no failure was found. From acceleration measurement, different surface finishes effect on acceleration can be ignored because it hardly affects the PCB assembly structure, stiffness and mass. Different surface finishes, however, can affect the fatigue failure of solder joint due to different interface material properties. Fig. C-11 shows the acceleration of different locations on PCB with Ag surface finish. It can be seen that the largest acceleration occurs at PCB free edge center.

ATTENTION: The Singapore Copyright Act applies to the use of this document. Nanyang Technological University Library

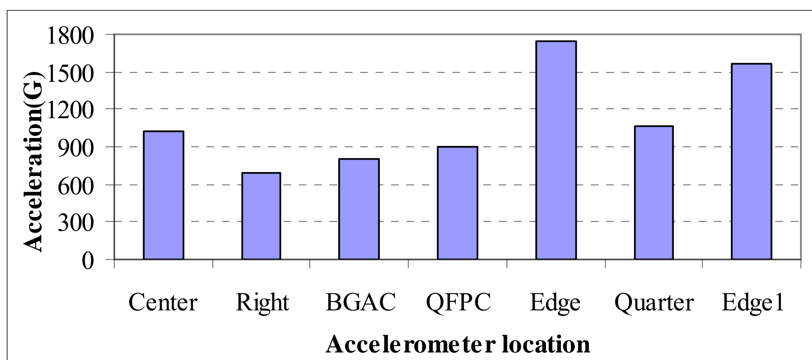

Fig. C-11 Acceleration at different locations on PCB assembly board.

C.1.2.3 Bare PCB versus PCB assembly

Fig. C-12 shows the comparison of acceleration on the PCB center between bare PCB and PCB assembly. It can be seen that the acceleration of bare PCB center is higher than that of PCB assembly center for same drop condition and the frequency of acceleration for bear PCB is more than that for PCB assembly, which was verified by FEA results. Attenuation of acceleration for PCB assembly is faster than that of bare PCB due to more flexible of bare PCB than PCB assembly. Fig. C-13 shows the strain comparisons between bear PCB and PCB assembly for strain gauge 1 located at PBGA corner. The strain on the PCB assembly is slightly higher than that on bear PCB due to local stiffening effect of PBGA package.

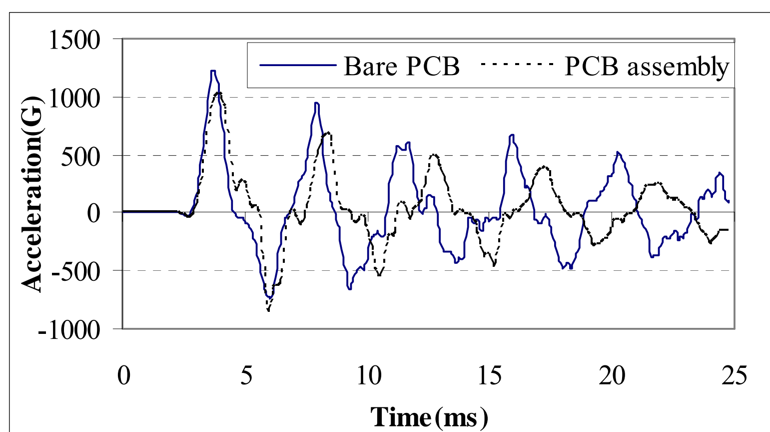

Fig. C-12 Acceleration comparisons between bare PCB and PCB assembly.

ATTENTION: The Singapore Copyright Act applies to the use of this document. Nanyang Technological University Library

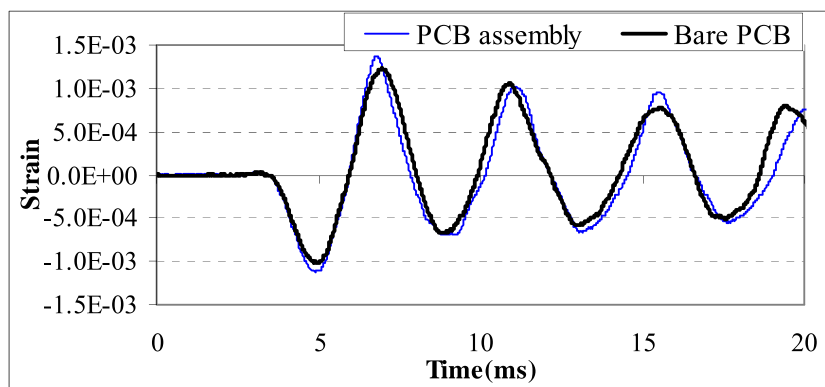

Fig. C-13 Strain comparisons between bare PCB and PCB assembly at strain gauge1.

C.2 FEA SIMULATION FOR DROP TEST

In FEA simulation for drop impact test of board-level electronic assembly, three methods are usually used: full drop modeling event (full model), hybrid experiment-modeling event with input displacement boundary condition (Input-D model) and with input acceleration boundary condition (Input-G model). In this study, these three methods were conducted in FEA simulation for FCOB assembly.

C.2.1 Full Drop Event Model

In this full model analysis, the specimen, fixture, table and impact base are all simulated. The detailed full FEA model is shown in Fig. C-14. Some assumptions and simplifications were made in full model in order to reduce element size and CPU time. The rectangular parallelepiped drop table was meshed with the same mass as real drop table. A rigid behavior of the drop base was assumed. Bare PCB was modeled instead of physical FCOB assembly because the effect of flip chip components on dynamic response of global PCB can be ignored. During the free fall stage, the table and specimen are simply accelerated due to gravity. To save CPU time, an initial velocity of 4.43m/s is used to approximately simulate 1m drop height using $v = \sqrt{2gh}$, where v is the impact velocity, g is the acceleration due to gravity, and h is 1m drop height.

ATTENTION: The Singapore Copyright Act applies to the use of this document. Nanyang Technological University Library

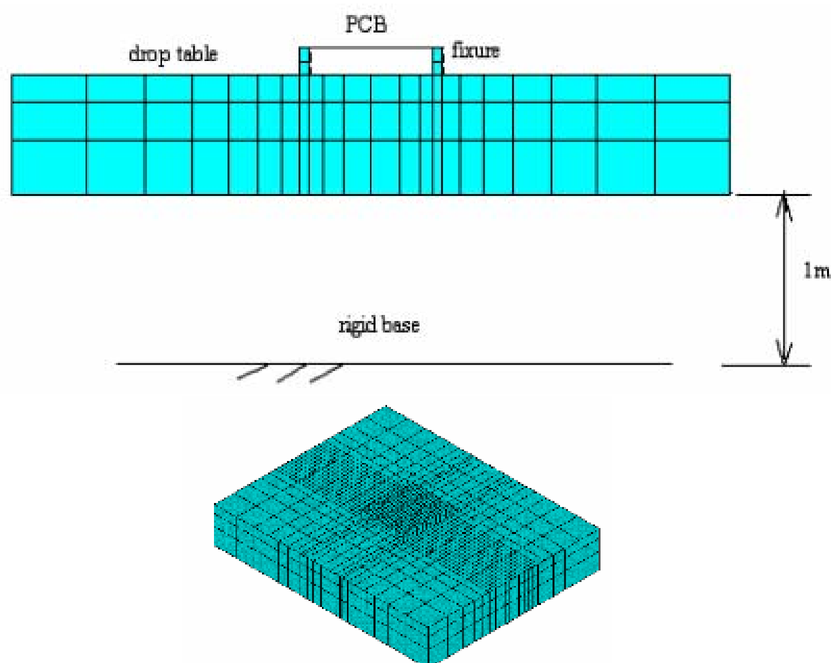

Fig. C-14 Full drop impact FEA model.

Fig. C-15 shows the displacement results of PCB free edge at maximum downward deflection. It can be seen that the maximum deflection of PCB center is consistent with test result and first vibration mode during drop impact is verified. Fig. C-16 shows the acceleration history of PCB center. The first peak acceleration during impact is much higher than test result due to rigid base used in FEA simulation. In physical test condition, felt pad was added on steel drop base. However, it is difficult to accurately simulate material properties of drop base. In full model, the geometry size mismatch between drop table and specimen is significant, especially between drop table and component. If small part such as solder joint is modeled in full drop model, it is not practical because the element size used in full model is dramatically large. Therefore, full model is not a suitable and reasonable model in drop impact simulation for studying stress strain behavior of solder joint.

ATTENTION: The Singapore Copyright Act applies to the use of this document. Nanyang Technological University Library

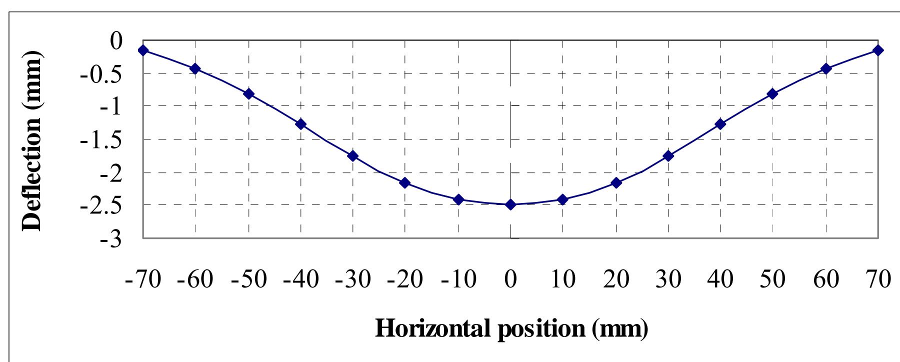

Fig. C-15 Maximum deflection of free edge of PCB during drop impact.

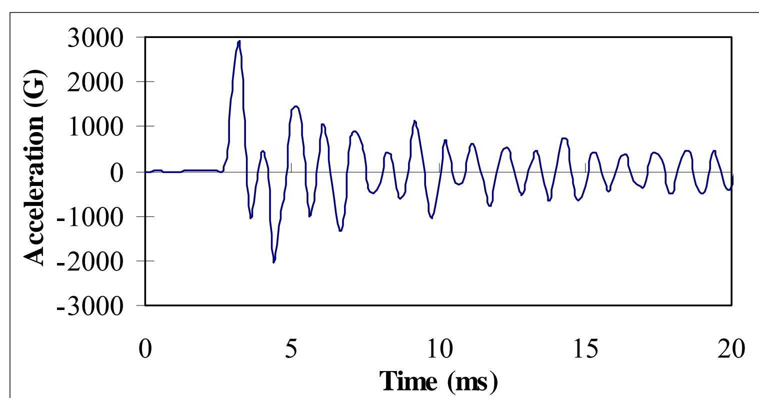

Fig. C-16 Acceleration of PCB center from full model.

C.2.2 Input-D Modeling Method

This method simulates the FCOB assembly including the PCB and component as shown in Fig. C-17. This approach avoids simulations of the drop table, fixture, and the contact between drop base and drop table, as well as the damping effects of the table-to-foundation contact event. The geometry mismatch between large drop table and specimen can be avoided and it is practical to model flip chip package including small solder joints. In this study, only on large flip chip component close to PCB center was modeled. The bilinear plastic material behavior was modeled for solder joint and elastic material properties were used for remaining materials. The input displacement boundary applied on the nodes of the fixed edges with width of 5mm was shown in Fig. C-18 obtained from the high-speed camera measurements.

ATTENTION: The Singapore Copyright Act applies to the use of this document. Nanyang Technological University Library

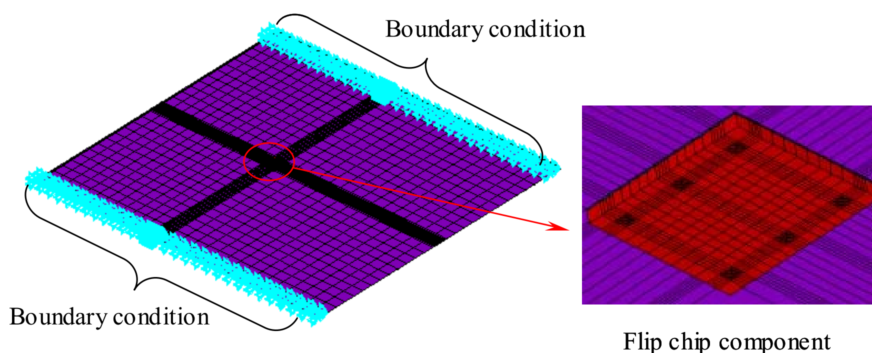

Fig. C-17 Hybrid experiment-modeling FEA model.

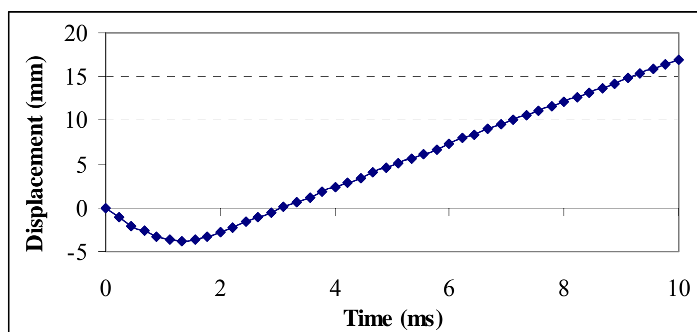

Fig. C-18 Displacement boundary condition used in Input-D method.

Fig. C-19 shows the acceleration and relative displacement history of PCB center node from FEA results. The displacement result is more accurate than acceleration result compared with test results. Input-D method leads to more accurate results compared with full model. Fig. C-20 shows the effective plastic strain of critical nodes on both solder interfaces of board side and chip side. It can be seen that effective plastic strain of solder/PCB side is larger than that of solder/chip side due to PCB bending effect, which indicates that solder/PCB interface is prone to cracking failure under drop impact load. Input-D modeling method requires an expensive high-speed camera to monitor the displacement of support during drop impact. Higher data recording rate is needed if more accurate FEA results are expected. Otherwise, only displacement of specimen edge can be easily measured and it is difficult to measure displacement of PCB center using high-speed camera.

ATTENTION: The Singapore Copyright Act applies to the use of this document. Nanyang Technological University Library

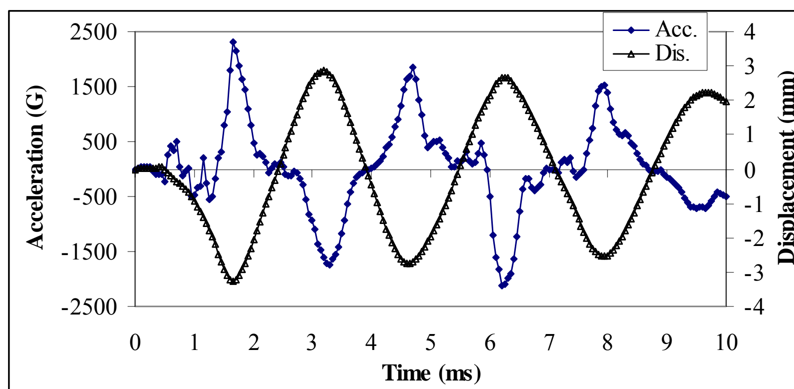

Fig. C-19 Acceleration and displacement history from Input-D FEA model.

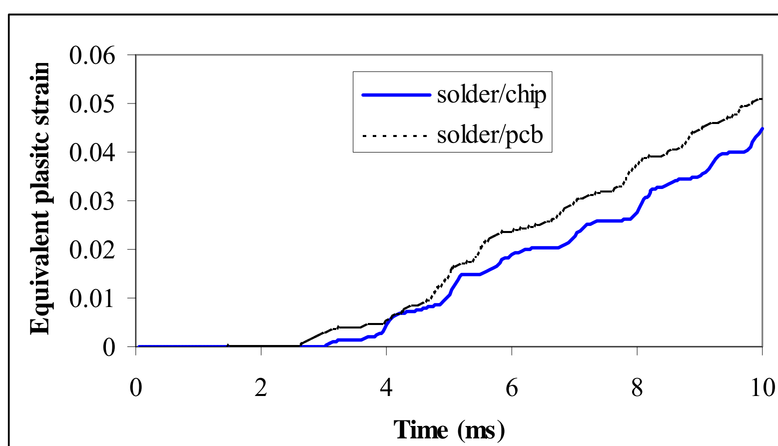

Fig. C-20 Effective plastic strain from Input-D FEA model.

C.2.3 Input-G Modeling Method

In this modeling method, FEA model is the same as that used in Input-D modeling method. The only difference between Input-D and Input-G methods is boundary condition. The acceleration along drop direction was used as input parameter applied on clamped PCB edges in Input-G method while displacement was used for Input-D method. The acceleration of drop table as shown in Fig. C-21 was used as boundary condition imposed on nodes along clamped edges. Fig. C-22 shows the acceleration and relative displacement history of PCB center node from FEA results. Comparing FEA results as shown in Fig. C-16 for full model, Fig. C-19 for Input-D method and Fig. C-22 for Input-G method, it is obvious that Input-G modeling method is a

ATTENTION: The Singapore Copyright Act applies to the use of this document. Nanyang Technological University Library

desirable and accurate simulation approach. Accelerometer with high frequency is much cheaper than high-speed camera and can be mounted on any expected position of specimen to measure the dynamic response. In this study, the accelerometer has the recording frequency of 20kHz while high-speed camera just has frequency of 4.5kHz.

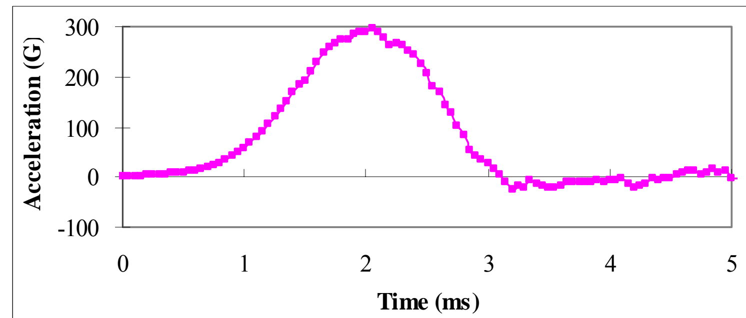

Fig. C-21 Acceleration boundary condition used in Input-G method.

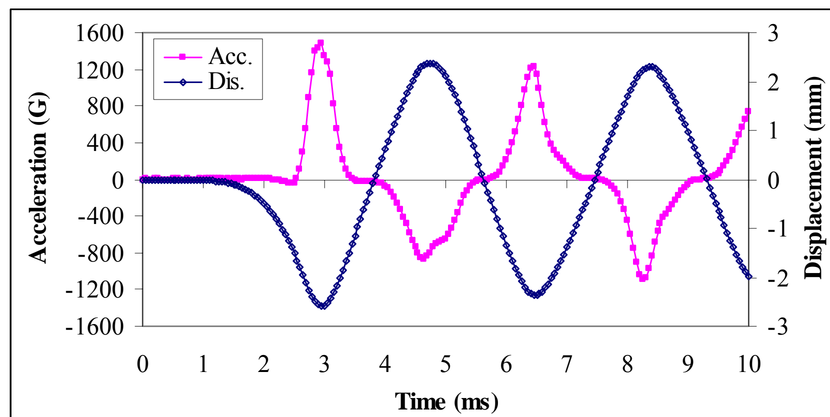

Fig. C-22 Acceleration and displacement history from Input-G FEA model.

Three FEA modeling methods and result comparisons were carried out for FCOB assembly subjected to drop impact loading. It can be seen that three methods can lead to accurate relative displacement results and vibration mode. However, the difference of acceleration results among different modeling methods is significant. Compared to test result, the Input-G modeling method is a desirable modeling approach.

ATTENTION: The Singapore Copyright Act applies to the use of this document. Nanyang Technological University Library

APPENDIX D VIBRATION TEST AND ANALYSIS

D.1 VIBRATION TEST AND ANALYSIS

D.1.1 Test Vehicle and Setup

Vibration test was conducted for FCOB assembly as shown in Fig. D-1. Six larger flip chip modules of 8.5mm×8.5mm×0.65mm(L×W×H) silicon die and six smaller flip chip modules of 3.5mm×3.5mm×0.65mm (L×W×H) silicon die were mounted on the FR-4 PCB of 185mm×150mm×1.13mm(L×W×H). The solder joints are eutectic 63Sn/37Pb solder with a diameter of 0.16mm, ball pitch of 0.35mm and standoff of height of 0.1mm. A total of 4 test boards were tested in different acceleration levels to assess the reliability of FCOB assembly subjected to constant G-level and block G-level loading of 3G, 5G and 10G. The sinusoidal vibration tests were conducted because it is the simple and representative type of the vibration.

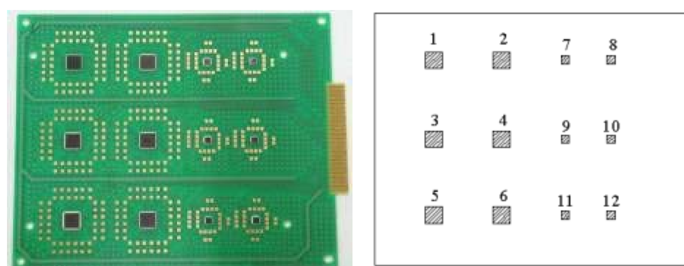

Fig. D-1 Flip chip on board assembly and die number.

Two accelerometers were used in the test, one for fixture and the other for PCB, thus the vibration transmissibility of the PCB can be determined when evaluated at different acceleration levels. The specimen was clamped along two longer opposite sides using aluminum fixture, which was bolted to the shaker header. The resistance change of the daisy chain loops connecting the solder joints was used to determine the failure of the solder joints. There are three loops for the larger flip chip with outer,

ATTENTION: The Singapore Copyright Act applies to the use of this document. Nanyang Technological University Library

middle and inner loops, while there is only one outer loop for each smaller flip chip. Total 22 loops were monitored simultaneously by the Event Detector during vibration test. Any resistance change exceeding a preset threshold with minimum duration of 0.1μs can be detected by the Event Detector. In this study, 50% increase of resistance was used as a rule to determine the failure. Fig. D-2 shows the vibration test setup.

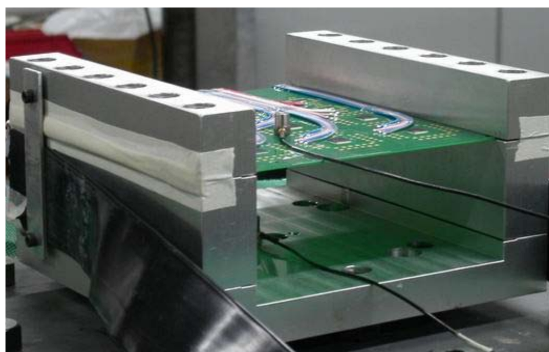

Fig. D-2 Setup of the vibration test.

D.1.2 Natural Frequency Scanning Test and Analysis

The frequency-scanning test was conducted with sweep sine frequency from 20Hz to 1000Hz in order to determine the fundamental resonance frequency of the specimen. The transmissibility of the specimen can be estimated using the following equation:

$$T = \frac{G_{out}}{G_{in}} \tag{D.1}$$

where G_{out} is the maximum acceleration measured at the specimen center, and G_{in} is the acceleration amplitude of the sinusoidal excitation. The fundamental resonance frequency of 194Hz was determined by scanning test with 0.5G level.

The screening test was conducted at 0.5, 1, 2, 3, 4, 5, 6, 7, 8, 10, 12, 14, 16, 18 and 20 G-levels with the same frequency range from 20Hz to 1000Hz. According to Meirovitch [148], for a linear vibration system, its transmissibility should remain constant regardless of any input change. However, the varying transmissibility, T, at different acceleration input shows nonlinear relationship as shown in Fig. D-3 for

ATTENTION: The Singapore Copyright Act applies to the use of this document. Nanyang Technological University Library

FCOB assembly subjected to vibration load. A nonlinear vibration effect was found by Perkins and Sitaraman [83] for CCGA assemblies and by Yang et al. [84] for PBGA assemblies.

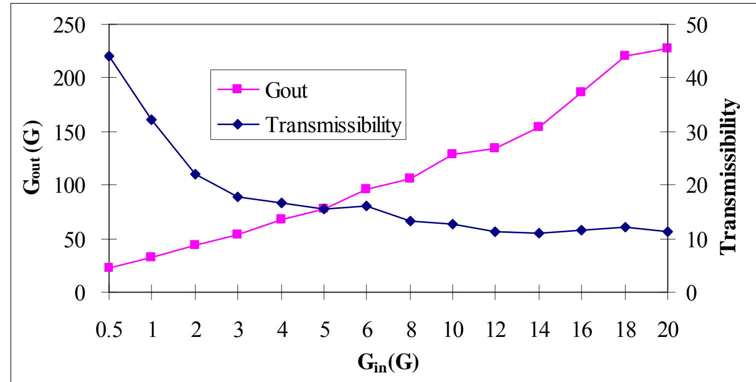

Fig. D-3 Nonlinear relationship between G_{in} and G_{out}.

For a vibration system subjected to a harmonic excitation, its displacement response at any location can be expressed as [148]:

$$Z = Z_{\max} \sin(\Omega t + \phi) \quad \text{(D.2)}$$

where Z_{max} is the maximum displacement and Ω is the natural frequency in radians per second, which can be changed into natural frequency in Hertz by:

$$\Omega = 2\pi f \quad \text{(D.3)}$$

Differentiating Eq. (D.2) twice with respect to time, obtained:

$$\ddot{Z} = -Z_{\max}\Omega^2 \sin(\Omega t + \phi) \quad \text{(D.4)}$$

Hence, maximum acceleration of $\ddot{Z}_{\max}$ can be expressed as:

$$\ddot{Z}_{\max} = Z_{\max}\Omega^2 \quad \text{(D.5)}$$

And the maximum displacement can be determined as:

$$Z_{\max} = \frac{\ddot{Z}_{\max}}{\Omega^2} = \frac{9.8 G_{in} T}{4\pi^2 f^2} = \frac{0.248 G_{in} T}{f^2} \quad \text{(D.6)}$$

where G_{in} has a unit of G, and Z_{max} in meter. According to Eq. (D.6), the maximum displacements for different G-level tests can be estimated.

ATTENTION: The Singapore Copyright Act applies to the use of this document. Nanyang Technological University Library

D.1.3 Reliability Test and Analysis

The fundamental natural frequency was found from natural frequency scanning test, then reliability test can be conducted based on known natural frequency. In reliability vibration test, the sweep frequency range was 10% around natural frequency of 194Hz, that is, from 175Hz to 215Hz. The sine sweep vibration swept from low frequency to high frequency and then from high frequency to low frequency and repeated until a preset time was reached. For the varying block G-level vibration test, 3G, 5G, 10G level vibration tests were conducted in turn for same specimen and 5 hours was used for each acceleration level. Constant G level vibration tests at 3G, 5G, and 10G were conducted for 200, 100, 36 hours, respectively. The vibration cycles to failure were calculated based on the duration time recorded by the Event Detector and the average frequency of the sweep sinusoidal excitation. The test results for outer chain of the large component satisfy two-parameter Weibull distribution well as shown in Fig. D-4. No failure results were found for the small components. Fig. D-4 also shows the Weibull plot of PBGA test result from Yang's work [84] where the PCB has the same length and width as that used in this study and the clamped-clamped boundary condition at two shorter edges was used.

Table D-1 shows the Weibull parameters, MTTF and FTTF for FCOB and PBGA assemblies. It can be seen from Table D-1 that the fatigue life of FCOB solder joint reduces rapidly with sinusoidal vibration acceleration amplitude increasing. It was shown that the PBGA solder joint fatigue life of, however, are much lower than FCOB solder joint fatigue life. This is due to the fact that components in FCOB assembly have less mass and smaller size than those in PBGA assembly and underfill is used in FCOB assembly which improves FCOB solder joint fatigue life.

ATTENTION: The Singapore Copyright Act applies to the use of this document. Nanyang Technological University Library

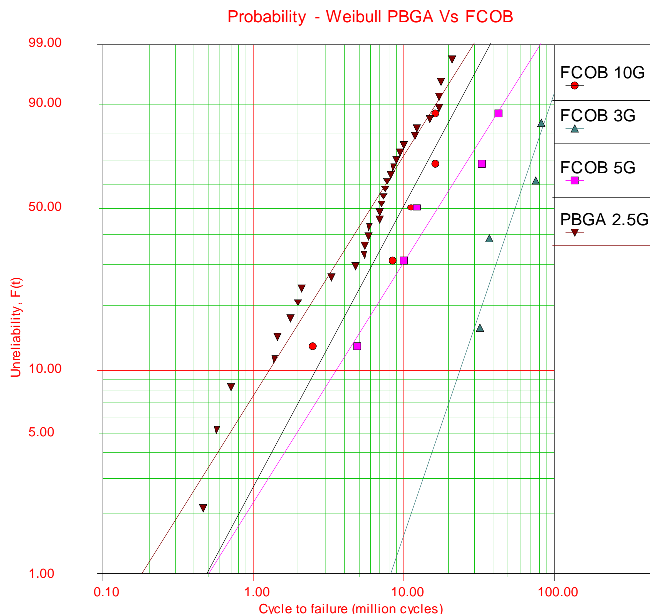

Fig. D-4 Weibull plots of test results for FCOB and PBGA assembly.

Table D-1 Weibull parameters, MTTF and FTTF for FCOB and PBGA.

G_{in}	η (10^6cycles)	β	MTTF (10^6 cycles)	FTTF (10^6 cycles)
FCOB 3G	65.30	2.22	57.84	32.30
FCOB 5G	23.28	1.20	21.91	4.93
FCOB 10G	12.89	1.41	11.73	2.47
PBGA 2.5G	8.31	1.20	7.82	0.46

The high-speed camera able to record up to 4500 frames/s was used to capture the dynamic response of specimen. The displacement was measured at the PCB free edge. The relative displacement of free edge can be calculated using mark at fixture as reference point. The theoretical maximum displacement can be calculated using Eq. (D.6). Table D-2 gives the displacement results comparison between high-speed camera and theoretical data. It can be seen that high-speed camera can give good result without contact effect on specimen.

Table D-2 Displacement results comparison.

G_{in} (G)	Eq. (D.6)(mm)	Camera (mm)	Difference (%)
3	1.07	0.96	-10.3
10	2.18	2.36	8.3

ATTENTION: The Singapore Copyright Act applies to the use of this document. Nanyang Technological University Library

D.2.4 Cumulative Damage Index Fatigue Analysis

For the electronic assembly subjected to different block G-level vibration tests, the fatigue damage due to each G-level can be superimposed using the linear superposition method by Miner's law:

$$CDI = D_{total} = \sum_{i=1}^{n} \frac{n_i}{N_i} \tag{D.7}$$

Failure is assumed to occur at a more conservative value such as D_{total}=0.7 for electronic assemblies. For the varying G-level test, chip 3 and 4 were selected for the CDI analysis. The values of n_i were obtained from the varying G-level test result as shown in Fig. D-5 for chip 3 and chip 4, while N_i was equal to MTTF shown in Table D-1. Substituting the data as shown in Fig. D-5 and Table D-1 into Eq. (D.7), obtain:

$$CDI_{die3} = \frac{n_1}{N_1} + \frac{n_2}{N_2} + \frac{n_3}{N_3} = \frac{3.42}{57.84} + \frac{3.42}{21.91} + \frac{2.7597}{11.73} = 0.451$$

$$CDI_{die4} = \frac{n_1}{N_1} + \frac{n_2}{N_2} + \frac{n_3}{N_3} = \frac{6.84}{57.84} + \frac{6.84}{21.91} + \frac{3.6539}{11.73} = 0.742$$

From above CDI values, fatigue failure occurs for FCOB solder joints when the CDI is 0.451 and 0.742 for outer chain of chip 3 and 4, respectively. Using the CDI of unity is nonconservative and a safety factor of 2-3 is recommended for FCOB solder joint fatigue failure assessment when subjected to varying sinusoidal vibration load.

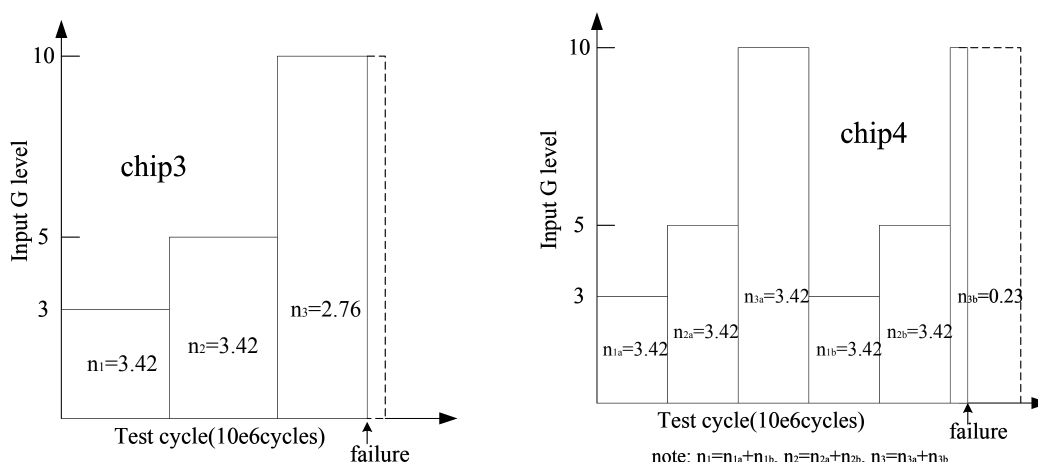

Fig. D-5 Schematic of varying G-level tests for chip3 and chip4.

ATTENTION: The Singapore Copyright Act applies to the use of this document. Nanyang Technological University Library

D.2 MODAL ANALYSIS

PCB was modeled as shell element in modal analysis because its thickness was quite small compared with its length and width. The clamped-clamped boundary condition was simulated according to the test condition. The bare PCB without Flip Chip components was simulated for modal analysis to study the different parameter effects such as material properties, element size. Table D-3 shows the natural frequency results of first three modes for bare PCB. It can be seen that the element size and considering PCB with orthotropic material properties affect slightly the PCB natural frequency. In the subsequent analysis, the 5mm×5mm element size and PCB with Young's modulus of 22GPa, Poisson's ratio of 0.28 were used. Fig. D-6 shows the first ten mode shapes for bare PCB. It is obvious that the mode shape becomes more complicated when the order of mode increases. Generally, the first order mode has the most significant effect on the reliability of the electronic assembly.

Table D-3 Natural frequencies for bare PCB modal analysis.

No.	E (GPa)	ν	f1	f2	f3	Element size (mm×mm)
1	22	0.28	208.75	232.86	324.0	2.5×2.5
2	22	0.28	208.61	232.51	323.17	5×5
3	22	0.28	208.59	232.44	322.9	7.5×7.5
4	22	0.28	208.57	232.34	322.51	10×10
5	22	0.28	208.5	232.07	321.48	15×15
6	E_x=22 E_y=22 E_z=10	ν_{xy}=0.28 ν_{yz}=0.11 ν_{zx}=0.11	208.51	232.36	322.88	5×5

ATTENTION: The Singapore Copyright Act applies to the use of this document. Nanyang Technological University Library

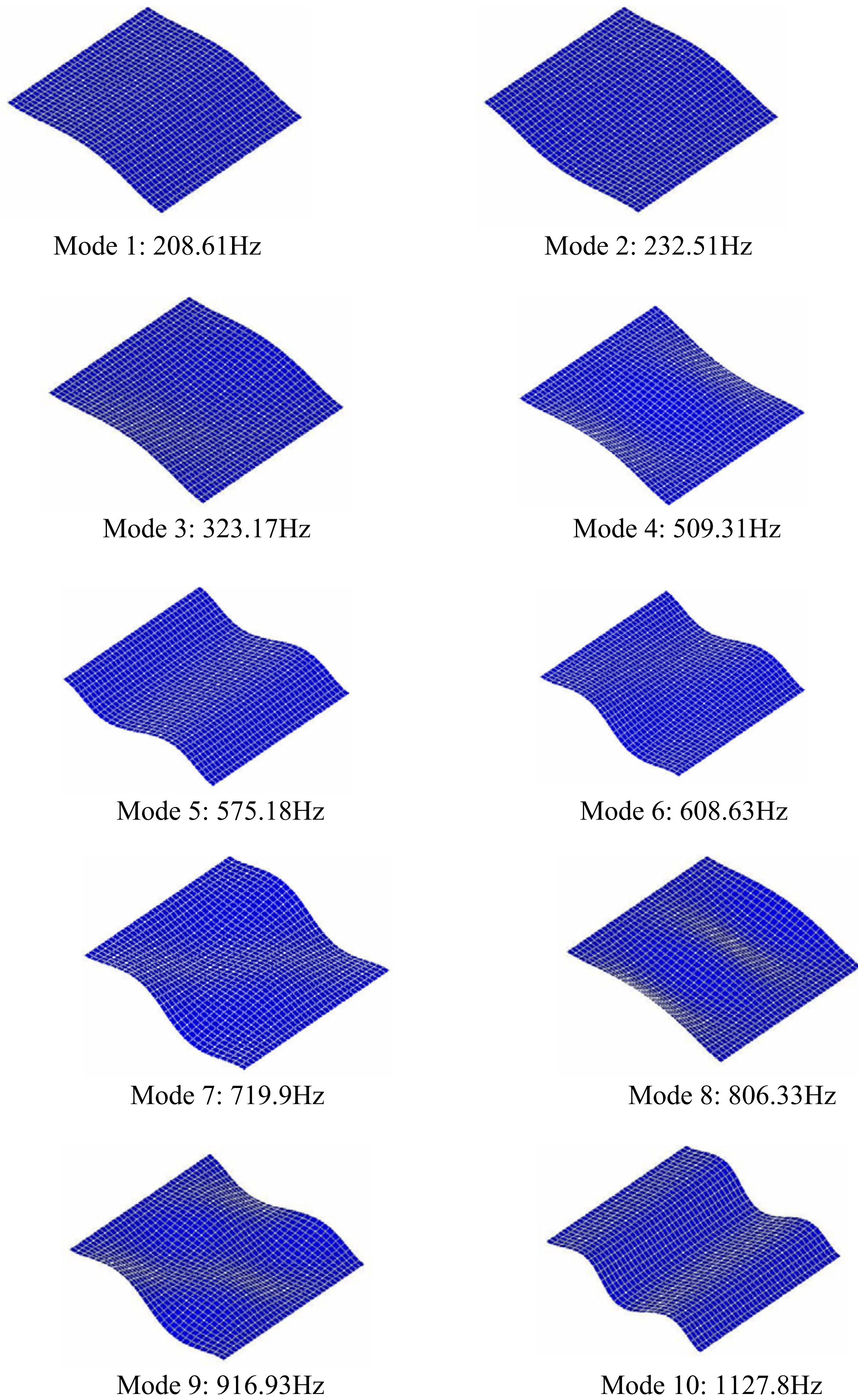

Fig. D-6 Mode shapes and corresponding natural frequency for the bare PCB.

ATTENTION: The Singapore Copyright Act applies to the use of this document. Nanyang Technological University Library

D.3 FATIGUE LIFE CALCULATION FOR VIBRATION TEST

As known, different stress amplitude will be applied on solder joints during sweep vibration test with frequency range from 175Hz to 215Hz. Different stress amplitudes caused by vibration loads with different frequency induce different solder fatigue life. Solder fatigue life can be predicted by combining fatigue model with Miner's law for solder joint subjected to sweep vibration test. The detailed procedure is given below for calculating fatigue life of solder joint subjected to sweep vibration test.

Assuming the failure time is t (in second) for specimen subjected to sine sweep vibration, the fatigue cycle N can be determined using mean frequency of 195Hz when FCOB assembly subjected to vibration test with frequency from 175 Hz to 215Hz:

$$N = 195 \times t \tag{D.8}$$

Total 28 individual frequencies were recorded in vibration test from 175Hz to 215Hz. Because the sweep velocity is constant, same period of time (t/28) is consumed for each frequency. Then the actual cycle (n_i) at each frequency (f_i) can be determined:

$$n_i=(t/28) \times f_i=N \times f_i/(195 \times 28) \tag{D.9}$$

The CDI can be obtained by:

$$CDI = \sum_{i=1}^{28} \frac{n_i}{N_i} = \sum_{i=1}^{28} \frac{N \times f_i/(195 \times 28)}{N_i} = N \bullet \sum_{i=1}^{28} \frac{f_i/(195 \times 28)}{N_i} \tag{D.10}$$

So, the fatigue life for solder joint subjected to constant G-level vibration with frequency from 175Hz to 215Hz can be obtained:

$$N = CDI \Big/ \sum_{i=1}^{28} \frac{f_i/(195 \times 28)}{N_i} \tag{D.11}$$

where f_i is frequency recorded in sweep frequency range and N_i is its corresponding cycle to failure. Therefore, the fatigue cycle, N, can be obtained using Eq. (D.11) when CDI, f_i and corresponding N_i are known.

ATTENTION: The Singapore Copyright Act applies to the use of this document. Nanyang Technological University Library

APPENDIX E PUBLICATIONS

The following papers are related to the present research:

Wang, Y.Q., Low, K.H., **Che, F.X.**, Pang, H.L.J., and Yeo, S.P., **2003**, Modeling and Simulation of Printed Circuit Board Drop Test, *Proceedings of 5th Electronics Packaging Technology Conference (EPTC),* December 10-12, 2003, Singapore, pp.263-268.

Che, F.X., Pang, H.L.J., Wong, F.L., Lim, G.H., and Low, T.H., **2003**, Vibration Fatigue Test and Analysis for Flip Chip Solder Joints, *Proceedings of 5th EPTC*, December 10-12, 2003, Singapore, pp.107-113.

Pang, H.L.J., **Che, F.X**., and. Low, T.H., **2004**, Vibration Fatigue Analysis for FCOB Solder Joints, *Proceedings of 54th Electronic Components and Technology Conference (ECTC)*, June 1-4, 2004, Las Vegas, pp.1055-1061.

Che, F.X., Low, T.H., Pang, H.L.J., Lin, W. C.C., Chiang, C. L.S., and Yang T. K. A., **2004**, Modeling Thermo-Mechanical Reliability of Bumpless Flip Chip Package, *Proceedings of 54th ECTC*, June 1-4, 2004, Las Vegas, pp.421-426.

Che, F.X., and Pang, H.L.J., **2004**, Harsh Solder Joint Reliability Tests by Impact Drop and Highly Accelerated Life Test (HALT), *Proceedings of 6th EPTC*, December 8-10, 2004, Singapore, pp.205-209.

Che, F.X., and Pang, H.L.J., **2004**, Thermal Fatigue Reliability Analysis for PBGA with Sn-3.8Ag-0.7Cu Solder Joints, *Proceedings of 6th EPTC*, December 8-10, 2004, Singapore, pp.787-792.

Che, F. X., Pang, H.L.J., Xiong, B.C., Xu, L.H., and Low, T.H., **2005**, Lead Free Solder Joint Reliability Characterization for PBGA, PQFP and TSSOP Assemblies**,** *Proceedings of 55th ECTC*, May 31-June 3, 2005, Florida.

Chong, D.Y.R., **Che, F.X**., Pang, J.H.L., Ng, K., Tan, J.Y.N., and Low, P. T.H., **2005,** Drop Impact Reliability Testing for Lead-free and Leaded Soldered IC Packages, *Microelectronics Reliability*, (Accepted).